



**COMPARISON OF THE REFRACTIVE INDEX STRUCTURE CONSTANT
DERIVED FROM NUMERICAL WEATHER PREDICTION (NWP) MODELS
AND THERMOSONDE DATA**

THESIS

De Leon C. Narcisse, Captain, USAF

AFIT/GM/ENP/03-04

**DEPARTMENT OF THE AIR FORCE
AIR UNIVERSITY**

AIR FORCE INSTITUTE OF TECHNOLOGY

Wright-Patterson Air Force Base, Ohio

APPROVED FOR PUBLIC RELEASE; DISTRIBUTION UNLIMITED

The views expressed in this thesis are those of the author and do not reflect the official policy or position of the United States Air Force, Department of Defense or the United States Government.

AFIT/GM/ENP/03-04

**COMPARISON OF THE REFRACTIVE INDEX STRUCTURE CONSTANT
DERIVED FROM NUMERICAL WEATHER PREDICTION (NWP) MODELS
AND THERMOSONDE DATA**

THESIS

Presented to the Faculty

Department of Engineering Physics

Graduate School of Engineering and Management

Air Force Institute of Technology

Air University

Air Education and Training Command

In Partial Fulfillment of the Requirements for the

Degree of Master of Science in Meteorology

De Leon C. Narcisse, BS

Captain, USAF

March 2003

APPROVED FOR PUBLIC RELEASE; DISTRIBUTION UNLIMITED

COMPARISON OF THE REFRACTIVE INDEX STRUCTURE CONSTANT
DERIVED FROM NUMERICAL WEATHER PREDICTION (NWP) MODELS AND
THERMOSONDE DATA

De Leon C. Narcisse, BS

Captain, USAF

Approved:



Lt Col Michael K. Walters (Chairman)

28 Feb 03

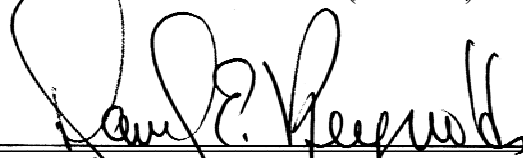
Date



Dr. Glen P. Perram (Member)

28 Feb 03

Date



Prof. Daniel E. Reynolds (Member)

28 Feb 03

Date

Acknowledgments

I would like to thank many people who made this thesis work possible. I would like to thank God and next my wife, children and friends without whose support this would not have been accomplished. I would like to thank my thesis advisor, Lt Col Michael K. Walters, for his technical assistance and his mentorship during this process. I would like to thank all other members in my committee, Dr. Glen Perram, Professor Dan Reynolds for their expertise they provided in their fields of study. Additionally, I would like to thank Dr. Frank Ruggiero for his unwavering support, Dr. Don Walters, Lt. Col. Randy Lefevre, Major Matthew Goda, 1st Lt. Steve Early, Capt. Elizabeth Boll, 1st Lt. Ed Amrhein, Capt. Richard Benz, Capt. Mark Allen, Capt. Richard Gonzalez, Capt. Mark Gasbarro, Mr. Jeff Sitler, and many colleagues that all contributed scientific advice into this thesis.

De Leon C. Narcisse

Table of Contents

	Page
Acknowledgments	iv
Table of Contents.....	v
List of Figures.....	vii
List of Tables	xv
Abstract.....	xvi
 I. Introduction	 1
1.1 Motivation.....	1
1.2 Significance of Problem.....	1
1.3 Statement of Problem.....	3
1.4 Benefit of Solving the Problem	4
1.5 General Approach	4
1.6 Organizational Overview	7
1.7 Summary of Results.....	8
 II. Literature Review.....	 12
2.1 Issues with directed energy traveling through the atmosphere.....	12
2.2 Issues with directed energy and the airborne laser	15
2.3 Optical Turbulence	17
2.3.1) Definition of Turbulence	17
2.3.2) Definition of Optical Turbulence	20
2.4 Thermosonde	29
2.5 Fifth Generation Mesoscale Model.....	31
2.7 Advanced Climate Modeling and Environmental Simulations (ACMES).....	35
2.8 Synoptic Data.....	37
2.9 Recent Work	37

III. Data Description	38
3.1 Thermosonde Data Description	38
3.2 2 X CLEAR I profile	40
3.3 MM5 Data Description	40
3.4 ACMES Data Description	42
3.5 COAMPS Data Description.....	43
3.6 Synoptic Data Description	44
IV. Data Analysis.....	45
4.1 Binning Data	45
4.2 Thermosonde Data	45
4.3 MM5 Data.....	47
4.4 ACMES Data	50
4.5 COAMPS Data	51
4.6 CLEAR I.....	51
4.7 Synoptic Analysis	53
V. Statistical Analysis.....	64
5.1 Objective Metrics.....	64
5.2 Contingency Tables	69
5.3 Paired-t test	73
5.4 COAMPS Paired-t test results	78
5.5 MM5 Paired-t test results.....	81
5.6 ACMES Paired-t test results	81
5.7 Model to Model paired-t tests.....	82
5.8 Thermosondes	86
VI. Conclusions	87
6.1 Summary.....	87
6.2 Recommendations.....	89
Appendix A. Synoptic Charts	91
Appendix B. Statistical Charts.....	152
References.....	162
Vita	166

List of Figures

	Page
Figure 1. ABL concept diagram [Adapted from GAO 1997].....	3
Figure 2. Diagram of Laser Beam Generation Components [Adapted from Golnik 1993].....	12
Figure 3. Atmospheric effects on Laser Beam Propagation [Adapted from Pries 1980].....	14
Figure 4. Wave front error due to Atmospheric effects [Adapted from Pries 1980].....	15
Figure 5. Inertial Sub-range of Turbulence [Adapted from Andrews and Phillips 1998]	22
Figure 6. Structure Function vs. Inertial Sub-Range indicating 2/3rds slope or “2/3rds power law” [Adapted from Tatarski 1961].....	25
Figure 7. Thermosonde Image with Balloon attached [Adapted from Air Force Research Lab 1998]	30
Figure 8. MM5 Model Domain for this thesis [adapted from Ruggiero and DeBenedictis 2002].....	32
Figure 9. ACMES map [adapted from AFCCC]	36
Figure 10. Example layered mean vs. single point in layer	46
Figure 11. Model Output Interpolation Diagram.....	47
Figure 12. Entire Domain profile of Modeled Output	49
Figure 13. Example of binned data for all models vs. thermosonde and 2 X CLEAR I	52
Figure 14. Temperature profiles for 24/0114Z Launch	53
Figure 15. Surface Weather Chart for 12Z 18 Oct 01 [Adapted from NCDC 2001].....	55

Figure 16. 00Z 21 Oct 01 500 mb analysis chart [Adapted from NCDC 2001].....	55
Figure 17. 12Z 200 mb 19 Oct 01 chart [Adapted from NCDC 2001].....	56
Figure 18. 12Z 300 mb 19 Oct 01 chart [Adapted from NCDC 2001].....	57
Figure 19. 12Z 300 mb 21 October 2001 chart [Adapted from NCDC 2001].....	58
Figure 20. 12Z 200 mb chart 21 October 2001 [Adapted from NCDC 2001].....	58
Figure 21. Thermosonde profile with model comparisons for 20 October 2001 for 2320Z Launch.....	59
Figure 22. Thermosonde profile with model comparisons for 21/0235Z Launch.....	60
Figure 23. Skew-T profile for Vandenberg AFB, CA. at 00Z on 22 Oct 01 [Adapted from UW 2002].....	61
Figure 24. Infrared Satellite image of Low pressure system off the west coast 12Z 19 October 2001 [Adapted from NCDC 2001]	62
Figure 25. Water vapor image of low pressure system of west coast of U.S. 12Z 19 October 2001 [Adapted from NCDC 2001].....	63
Figure 26. Example Normal Distribution. Plot of Model-Observations Differences for 20/0300Z ACMES-Observed data.....	74
Figure 27. Example of Autocorrelation plot. Plot for 20/0300Z ACMES-Observed data	75
Figure 28. Example of paired-t test with a significant difference between model and observed data at .05 alpha level for ACMES and Observed data of the 20/0300Z Launch	77
Figure A.1 Surface Analysis 00Z 21 October 2001, inverted trough to the east of Vandenberg AFB, CA. [Adapted from NCDC 2001]	91
Figure A.2 Surface Analysis 12Z 21 October 2001, inverted trough moving eastward [Adapted from NCDC 2001]	92
Figure A.3 Surface Analysis 00Z 22 October 2001, high pressure becoming dominant [Adapted from NCDC 2001].....	92

Figure A.4 Surface Analysis 12Z 22 October 2001, ridging to the west [Adapted from NCDC 2001]	93
Figure A.5 Surface Analysis 00Z 23 October 2001, northerly flow around high pressure to the west [Adapted from NCDC 2001]	93
Figure A.6 Surface Analysis 12Z 23 October 2001, inverted trough axis to the east [Adapted from NCDC 2001].....	94
Figure A.7 500 mb Analysis Chart 00Z 21 October 2001, weak ridging with trough to NW [Adapted from NCDC 2001]	94
Figure A.8 500 mb Analysis Chart 12Z 21 October 2001, zonal flow [Adapted from NCDC 2001].....	95
Figure A.9 500 mb Analysis 00Z 22 October 2001, zonal flow with trough to the west [Adapted from NCDC 2001].....	95
Figure A.10 500 mb Analysis 12Z 22 October 2001, trough axis near Vandenberg AFB, CA. [Adapted from NCDC 2001]	96
Figure A.11 500 mb Analysis 00Z 23 October 2001, ridge beginning to build into region [Adapted from NCDC 2001].....	96
Figure A.12 500 mb Analysis 12Z 23 October 2001, NW flow around Pacific High [Adapted from NCDC 2001]	97
Figure A.13 300 mb Analysis 00Z 21 October 2001, jet maximum moving eastward into region [Adapted from NCDC 2001].....	97
Figure A.14 300 mb Analysis 12Z 21 October 2001, jet maximum over Vandenberg AFB, CA. [Adapted from NCDC 2001].....	98
Figure A.15 300 mb Analysis 00Z 22 October 2001, jet maximum moving out of region [Adapted from NCDC 2001].....	98
Figure A.16 300 mb Analysis 12Z 22 October 2001, trough axis in place as jet maximum moves south [Adapted from NCDC 2001].....	99
Figure A.17 300 mb Analysis 00Z 23 October 2001, weak trough axis with jet to SE [Adapted from NCDC 2001]	99
Figure A.18 300 mb Analysis 12Z 23 October 2001, NW flow around N. Pacific High [Adapted from NCDC 2001].....	100
Figure A.19 200 mb Analysis 00Z 21 October 2001, jet maximum moving eastward [Adapted from NCDC 2001]	100

Figure A.20 200 mb Analysis 12Z 21 October 2001, jet maximum moving in place over Central and S. CA [Adapted from NCDC 2001]	101
Figure A.21 200 mb Analysis 00Z 22 October 2001, jet maximum near Vandenberg AFB, CA [Adapted from NCDC 2001]	101
Figure A.22 200 mb Analysis 12Z 22 October 2001, jet maximum south of region [Adapted from NCDC 2001]	102
Figure A.23 200 mb Analysis 00Z 23 October 2001, trough axis moving to SE of region [Adapted from NCDC 2001]	102
Figure A.24 200 mb Analysis 12Z 23 October 2001, NW flow around N. Pacific High [Adapted from NCDC 2001]	103
Figure A.25 Skew-T profile 00Z 21 October 2001, 85 kt jet maximum above tropopause near 200 mb [Adapted from University of Wyoming 2001]	104
Figure A.26 Skew-T profile 12Z 21 October 2001, 95 kt jet maximum near 200 mb and tropopause [Adapted from University of Wyoming 2001]	104
Figure A.27 Skew-T profile 00Z 22 October 2001, 100 kt jet maximum near 200 mb and below tropopause [Adapted from University of Wyoming 2001]	105
Figure A.28 Skew-T profile 12Z October 2001, 50 kt decrease in jet maximum at 200 mb with tropopause height lowering to just above 300 mb [Adapted from University of Wyoming 2001]	105
Figure A.29 Infrared Satellite Image 12Z 19 October 2001, weakening upper front with embedded vorticity maximum to the west [Adapted from NCDC 2001]	106
Figure A.30 Infrared Satellite Image 00Z 20 October 2001, weakening front moving inland as vorticity maximum decays to west [Adapted from NCDC 2001]	106
Figure A.31 Infrared Satellite Image 12Z 20 October 2001, moisture plume from SW [Adapted from NCDC 2001]	107
Figure A.32 Infrared Satellite Image 00Z 21 October 2001, moisture plume from SW [Adapted from NCDC 2001]	107
Figure A.33 Infrared Satellite Image 12Z 21 October 2001, jet axis just north of moisture plume [Adapted from NCDC 2001]	108

Figure A.34 Infrared Satellite Image 00Z 22 October 2001, high pressure builds as jet axis moves southward [Adapted from NCDC 2001]	108
Figure A.35 Infrared Satellite Image 12Z 22 October 2001, high pressure dominant [Adapted from NCDC].....	109
Figure A.36 Water Vapor Satellite Image 12Z 19 October 2001, upper front bringing moisture from SW [Adapted from NCDC 2001].....	109
Figure A.37 Water Vapor Satellite Image 00Z 20 October 2001, upper boundary moving inland [Adapted from NCDC 2001]	110
Figure A.38 Water Vapor Satellite Image 12Z 20 October 2001, moisture plume moving from SW around weakening vorticity maximum in Pacific [Adapted from NCDC 2001]	110
Figure A.39 Water Vapor Satellite Image 00Z 21 October 2001, moisture plume from SW evident as jet becomes more prominent from SW [Adapted from NCDC 2001].....	111
Figure A.40 Water Vapor Satellite Image 12Z 21 October 2001, jet evident over top of ridge outlining moisture plume [Adapted from NCDC 2001].....	111
Figure A.41 Water Vapor Satellite Image 00Z 22 October 2001, maximum moving over region [Adapted from NCDC 2001].....	112
Figure A.42 Water Vapor Satellite Image 12Z 22 October 2001, jet maximum moving southward over S. California [Adapted from NCDC 2001].....	112
Figure A.43 Water Vapor Satellite Image 00Z 23 October 2001, zonal flow as jet maximum south of region [Adapted from NCDC 2001].....	113
Figure A.44 Water Vapor Satellite Image 12Z 23 October 2001, jet maximum well south of region [Adapted from NCDC 2001]	113
Figure A.45 Binned Vertical data Profiles for 19/0322Z Launch	114
Figure A.46 Potential Temperature Profiles for 19/0322Z Launch.....	115
Figure A.47 Binned Vertical data Profiles for 19/0508Z Launch	116
Figure A.48 Potential Temperature Profiles for 19/0508Z Launch.....	117
Figure A.49 Binned Vertical data Profiles for 19/2323Z Launch	118

Figure A.50 Binned Vertical data Profiles for 20/0115Z Launch	119
Figure A.51 Binned Vertical data Profiles for 20/0300Z Launch	120
Figure A.52 Binned Vertical data Profiles for 20/0444Z Launch	121
Figure A.53 Binned Vertical data Profiles for 20/2320Z Launch	122
Figure A.54 Binned Vertical data Profiles for 21/0235Z Launch	123
Figure A.55 Binned Vertical data Profiles for 21/0413Z Launch	124
Figure A.56 Binned Vertical data Profiles for 23/0115Z Launch	125
Figure A.57 Binned Vertical data Profiles for 23/0254Z Launch	126
Figure A.58 Binned Vertical data Profiles for 24/0114Z Launch	127
Figure A.59 Binned Vertical data Profile for 24/0248Z Launch	128
Figure A.60 Binned Vertical data Profile for 24/0430Z Launch	129
Figure A.61 Binned Vertical data Profile for 25/0115Z Launch	130
Figure A.62 Binned Vertical data Profile for 25/0253Z Launch	131
Figure A.63 Binned Vertical data Profiles for 26/0111Z Launch	132
Figure A.64 Binned Vertical data Profiles for 26/0249Z Launch	133
Figure A.65 Domain Average Profiles for 19/0322Z Launch	134
Figure A.66 Domain Average Profiles for 19/0508Z Launch	135
Figure A.67 Domain Average Profiles for 19/2323Z Launch	136
Figure A.68 Domain Average Profiles for 20/0115Z Launch	137
Figure A.69 Domain Average Profiles for 20/0300Z Launch	138
Figure A.70 Domain Average Profiles for 20/0444Z Launch	139
Figure A.71 Domain Average Profiles for 20/2320Z Launch	140
Figure A.72 Domain Average Profiles for 21/0235Z Launch	141
Figure A.73 Domain Average Profiles for 21/0413Z Launch	142

Figure A.74 Domain Average Profiles for 23/0115Z Launch	143
Figure A.75 Domain Average Profiles for 23/0254Z Launch	144
Figure A.76 Domain Average Profiles for 24/0114Z Launch	145
Figure A.77 Domain Average Profiles for 24/0248Z Launch	146
Figure A.78 Domain Average Profiles for 24/0430Z Launch	147
Figure A.79 Domain Average Profiles for 25/0115Z Launch	148
Figure A.80 Domain Average Profiles for 25/0253Z Launch	149
Figure A.81 Domain Average Profiles for 26/0111Z Launch	150
Figure A.82 Domain Average Profiles for 26/0249Z Launch	151
Figure B.1 Distribution Plot for differences between thermosonde data and COAMPS20/00Z data for 19/2323Z Launch	152
Figure B.2 Time Series Plot for differences between thermosonde data and COAMPS 20/00Z data for 19/2323Z Launch	153
Figure B.3 Matched Pairs Plot for paired-t test of differences between thermosonde data and COAMPS 20/00Z data for 19/2323Z Launch.....	153
Figure B.4 Distribution Plot for differences between thermosonde data and COAMPS 20/00Z data for the 20/0444Z Launch.....	154
Figure B.5 Time Series Plot for differences between thermosonde data and COAMPS 20/00Z data for the 20/0444Z Launch.....	154
Figure B.6 Matched Pairs Plot for paired-t test of differences between thermosonde data and COAMPS 20/00Z data for 20/0444Z Launch.....	155
Figure B.7 Distribution Plot for differences between thermosonde data and COAMPS20/00Z data for 23/0115Z Launch	155
Figure B.8 Time Series Plot for differences between thermosonde data and COAMPS 23/00Z data for the 23/0115Z Launch.....	156
Figure B.9 Matched Pairs Plot for paired-t test of differences between thermosonde data and COAMPS 23/00Z data for 23/0115Z Launch.....	156
Figure B.10 Distribution Plot for differences between thermosonde data and ACMES data for the 21/0235Z Launch	157

Figure B.11 Time Series Plot for differences between thermosonde data and ACMES data for the 21/0235Z Launch.....	157
Figure B.12 Matched Pairs Plot for paired-t test of differences between thermosonde data and ACMES data for 21/0235Z Launch	158
Figure B.13 Distribution Plot for differences between thermosonde data and ACMES data for the 25/0115Z Launch.....	158
Figure B.14 Time Series Plot for differences between thermosonde data and ACMES data for the 25/0115Z Launch.....	159
Figure B.15 Matched Pairs Plot for paired-t test of differences between thermosonde data and ACMES data for 25/0115Z Launch	159
Figure B.16 Distribution Plot for differences between thermosonde data and ACMES data for the 25/0253Z Launch.....	160
Figure B.17 Time Series Plot for differences between thermosonde data and ACMES data for the 25/0253Z Launch.....	160
Figure B.18 Matched Pairs Plot for paired-t test of differences between thermosonde data and ACMES data for 25/0253Z Launch	161

List of Tables

Table 1. MM5 Domains	32
Table 2. Thermosonde Launches	39
Table 3. MM5 Model Runs and Thermosonde Launches.....	41
Table 4. ACMES Model Runs	42
Table 5. COAMPS Data	43
Table 6. Mean Absolute Error (MAE).....	65
Table 7. Root Mean Square Error (RMSE)	66
Table 8. Mean Error (ME)	67
Table 9. Correlations.....	69
Table 10. Contingency Table Results	71
Table 11. Paired-t Test Results for Alpha level .05.....	76
Table 12. Paired-t Test Results for Alpha level of .10.....	79
Table 13. Paired-t Test Results Alpha level .01.....	80
Table 14. Between Model Paired-t Test Results.....	83
Table 15. Vertically Integrated Values of Profiles	85

Abstract

An accurate depiction of atmospheric turbulence is required for successful employment of a viable airborne laser for the Department of Defense (DOD). The Airborne Laser (ABL) System Program Office (SPO), which is tasked by the Missile Defense Agency (MDA), has not designated any particular numerical weather model that is used exclusively to model optical turbulence. This research compares the Critical Laser Enhancing Atmospheric Research (CLEAR) I, 2 X CLEAR I and thermosonde derived values of the refractive index structure constant (C_n^2) to C_n^2 values derived from several numerical weather prediction models currently in use by the DOD. The models used were the Fifth Generation Mesoscale Model (MM5), the Coupled Ocean Atmosphere Prediction System (COAMPS), and the Advanced Climate Modeling and Environmental Simulation (ACMES) method. Comparisons are presented using thermosonde data collected at Vandenberg AFB, California during the period 19-26 Oct 2001 Universal Time Coordinated (UTC). Results indicate that the model-derived C_n^2 and the thermosonde derived C_n^2 values are statistically different in many cases.

The methodology employed used thermosonde derived values for the refractive index structure parameter (C_n^2) as truth to which the other data sets were compared. Latitude and longitude points from the thermosonde trajectories were used to plot model derived optical turbulence values along a path mapping the trajectory of the balloon using linear and temporal interpolation between vertical levels. These data sets were vertically

integrated and a layered mean was calculated for both the observed and model derived output and then compared, using objective metrics, contingency tables, and the paired-t statistical test.

The objective metrics showed that the 3-hour COAMPS forecasts yield the best scores when compared to the actual thermosonde data. The other models all suggest comparable ME, RMSE, MAE, and correlation results. Contingency table results suggest the 3-hour COAMPS had the best scores. The other models had comparable contingency table results. The paired-t test indicated the ACMES and COAMPS 3-hour forecast each suggested a lack of significant differences between the means of observed and model data for alpha levels of .01, .05, and .10 for several comparisons. The MM5, ACMES, and COAMPS models were compared to each other using paired-t tests with an alpha level of .05. The COAMPS 3-hour forecasts are statistically different when compared to the other models based on this statistical analysis. Vertically path integrated values of optical turbulence were produced for each launch and all models valid for the same time. The MM5 forecasts yielded values closest to the thermosonde values for these comparisons. The path-integrated values are generated assuming an isotropic atmosphere for each layer. A synoptic analysis was also conducted to help account for any variations that might occur, which did help account for large optical turbulence values between 21/00Z and 23/00Z.

COMPARISON OF THE REFRACTIVE INDEX STRUCTURE CONSTANT
DERIVED FROM INSTRUMENTS AND NUMERICAL WEATHER PREDICTION
(NWP) MODELS

I. Introduction

1.1 Motivation

Accurately measuring and forecasting optical turbulence is a necessary prerequisite for successful airborne laser program operations. The ABL has a requirement to work in an environment where optical turbulence can be multiples of CLEAR I. The CLEAR I profile is a standard atmospheric profile of optical turbulence in the Earth's atmosphere. This thesis will examine how C_n^2 values derived based on data from the MM5, ACMES, and COAMPS models compares to derived C_n^2 values from thermosonde measurements taken from 18-25 October 2001 at Vandenberg AFB, CA. C_n^2 characterizes the strength or weakness of refractive index fluctuations.

1.2 Significance of Problem

Operation Desert Storm demonstrated that the U.S. military and other allied forces have limited capability against theater ballistic missiles. No operational airborne laser system exists with the capability to destroy enemy ballistic missiles in the boost phase (GAO 1997). The Airborne Laser (ABL) Program is a Department of Defense sponsored program tasked with meeting this threat (ABL 2002).

The ABL program involves civilian and military cooperation, which will integrate three major components for successful employment. Boeing is the prime contractor and has produced a modified 747-400 freighter aircraft to host the ABL. Various contractors are working on other components for the ABL. The concept is depicted in Figure 1.

Critical to the success of the ABL program is the ability to accurately compensate for optical turbulence effects in the atmosphere, so that adaptive optics on the ABL can refocus the laser beam once it's deformed due to atmospheric effects. Prediction of optical turbulence using forecast models will help to optimize the deployment of the ABL.

The CLEAR I profile models the variation of optical turbulence with altitude (Weaver et al. 2002). CLEAR I was developed in 1984 for the ground based laser/free electron laser program, which took non-optical measurements using thermosonde data from White Sands Missile Range (WSMR), New Mexico (White et al. 1985). CLEAR I is used for normalizing optical performance properties. This profile has become analogous to the standard atmosphere profile used by meteorologists (Ruggiero and DeBenedictis 2002). CLEAR I estimates of C_n^2 are between $10^{-14} \text{ m}^{-2/3}$ and $10^{-20} \text{ m}^{-2/3}$.

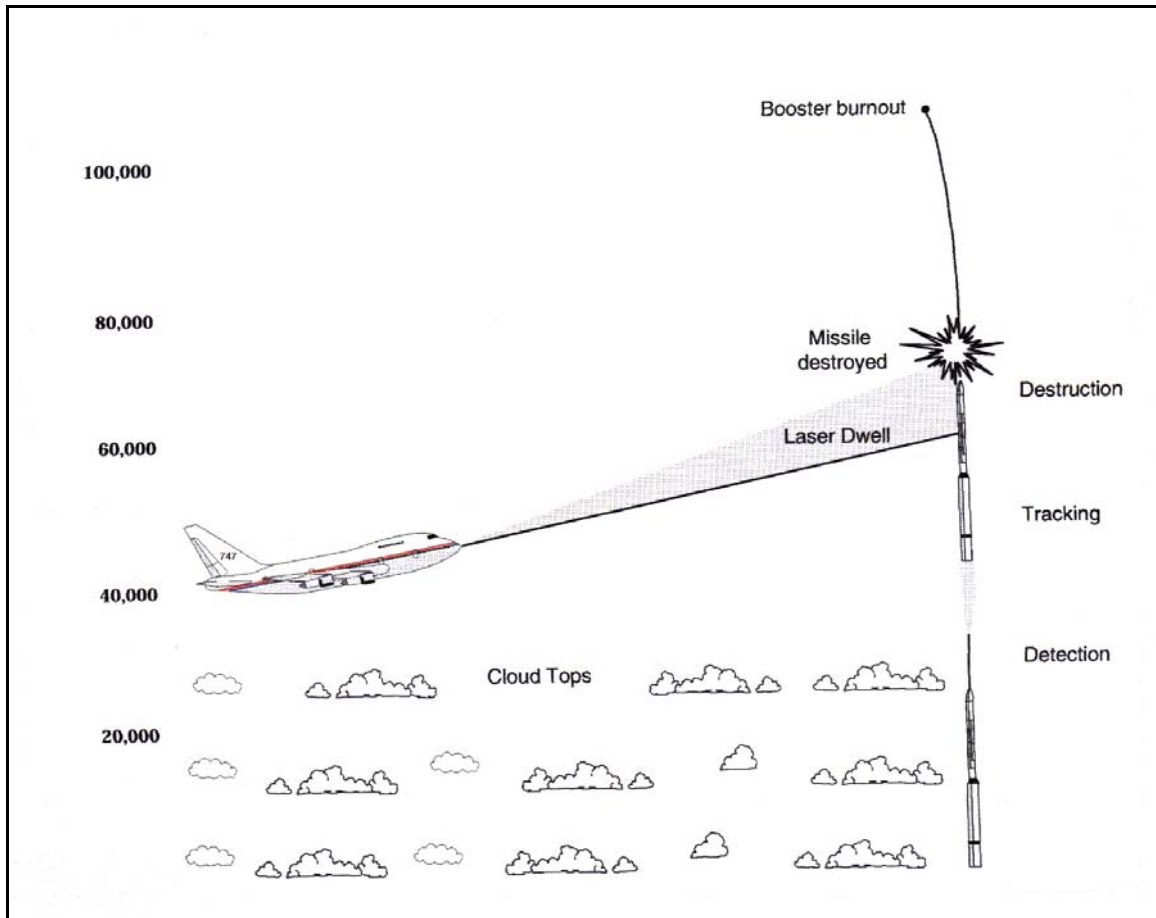


Figure 1. ABL concept diagram [Adapted from GAO 1997]

1.3 Statement of Problem

How do observed values of C_n^2 derived from thermosonde data and C_n^2 derived from numerical weather prediction models compare? The comparison among the model data and the thermosonde data are the central focus of this research.

1.4 Benefit of Solving the Problem

Giving the war-fighter the best first guess possible of the operational environment before the ABL gets airborne for each mission is the paramount goal of modeling optical turbulence. This thesis will help to characterize these models using statistics. The statistical analysis of the models when compared to the thermosonde data and each other will help lead to a better understanding of how each model is different. Understanding how each model characterizes the atmosphere is essential to making them better at forecasting optical turbulence. The differences among these models need to be understood so that possible strengths of the current models can be used in future versions to better characterize optical turbulence. It has been noted that there is substantial room for improvement in the parameterizations used to predict optical turbulence in the current forecast models (Ruggiero and DeBenedictis 2002).

1.5 General Approach

Many steps were required in order to complete this research. First, model data were obtained from many sources. Model output was post-processed to predict optical turbulence. These model data sets include MM5 data, COAMPS data, ACMES data, and thermosonde data from Vandenberg AFB, California. The ABL is concerned with propagation along a horizontally integrated path. The data are integrated into equal sized layers to try and assess a statistical average value for each layer. This idea of an integrated layered mean value extends from the work of Dr. Frank Ruggiero and Dan DeBenedictis (Ruggiero and DeBenedictis 2002). These vertically path integrated layer averages, also referred to as binned data, assume a homogeneous or “onion skin”

atmosphere. The “onion skin” model assumes a constant value within a layer. This idea of a mean layer value relates a vertically integrated path to a horizontally integrated path assuming a homogeneous atmosphere. A statistical mean of each layer will give insight into how optical turbulence (C_n^2) is modeled and observed within a layer of the atmosphere.

Thermosonde data were collected at Vandenberg AFB, California, for this campaign and were provided by the Air Force Research Laboratory (AFRL) at Hanscom AFB, Massachusetts. The thermosonde data are used as the baseline from which to assess the other modeled data sets. The thermosonde data are not captured all at once or exactly on the hour. The launch dates used in this thesis are from 19 Oct 01 UTC – 26 Oct 01 UTC. These observed thermosonde data sets were vertically integrated in 500 m increments at the Air Force Institute of Technology (AFIT). Linear interpolation is used to calculate the levels that aren’t represented in the data, but are needed to vertically integrate the data properly.

Optical turbulence data are processed using algorithms after the models have generated the initial fields; this is called post-processing. The post-processed model C_n^2 data are interpolated both spatially and temporally to the location of the thermosonde or balloon path for comparison.

AFRL at Hanscom AFB, Massachusetts, has processed the MM5 data to produce C_n^2 values at 500 m increments up to 25 km (Duhdia et al. 2001). The C_n^2 values derived are produced using seven 24-hour forecasts, initialized at 12Z, and output is produced

every 3-hours for each model run. The time period for these model runs encompassed a period from 19 Oct 01 UTC– 26 Oct 01 UTC.

COAMPS data have been processed by the Naval Postgraduate School (NPS) in Monterey, California (COAMPS 1999). This particular data set contains a single value for C_n^2 at each of the 47 levels in the model up to 10 mb, and is not in 500 m increments. Complete model runs are not available for this thesis, but NPS calculated C_n^2 along a mean path of the thermosonde in these model runs. This data set is valid from 19 Oct 01 UTC – 26 Oct 01 UTC. These data have been vertically integrated at AFIT for this thesis to get a mean layer average in 500 m increments to match the other data sets.

The Air Force Combat Climatology Center (AFCCC) has provided ACMES data. These data have been post-processed by AFCCC to produce C_n^2 values at each grid point in the model. ACMES method output data have been vertically integrated at AFIT to match the other data sets (ACMES 2001). This post-processed model output has been interpolated both temporally and spatially using linear interpolation to the location of the thermosonde. This data set has also been used to get a layered mean value over the entire grid, which is a little less than 9 degrees by 11 degrees.

Data were vertically integrated the same for all models and mapped to the path of the actual thermosonde profiles for each launch. Objective metrics, contingency tables and paired-t statistical tests were conducted using each of these data sets.

A meteorological analysis for this campaign was studied. This analysis was completed to provide insights into associations between values of optical turbulence that might be high or low at certain locations due to meteorological phenomena. Analysis

data used for this thesis comes from AFCCC and the National Climatic Data Center (NCDC) (NCDC 2001).

1.6 Organizational Overview

Chapter 2 begins by reviewing the issues surrounding optical turbulence research in this thesis. First, an understanding of the general issues associated with directed energy is discussed. Next, issues are discussed that relate directed energy and turbulence. This discussion also includes a general description of optical turbulence, to gain insight into how C_n^2 was derived. Next, a description of the models used to predict C_n^2 is discussed. A description of the thermosonde and how it uses temperature to infer optical turbulence is provided. Lastly, an overview of related work will be discussed, which serves as the baseline for this research.

Chapter 3 describes each of the data sets used for comparisons between the models and observed optical turbulence.

Chapter 4 covers the analysis of the data used in this thesis, which includes the meteorological analysis. This chapter describes how and why the data are vertically integrated in 500 m layers for comparison.

Chapter 5 describes the statistical results of this thesis using both objective metrics, contingency tables and the paired-t test. Vertically path integrated values were also calculated for each model output valid time and compared to the vertically path integrated values from the thermosonde data.

Chapter 6 focuses on conclusions of this thesis. It also includes recommendations for future work in the area of modeling optical turbulence.

1.7 Summary of Results

Objective metrics used for this research include the mean error (ME), mean absolute error (MAE), mean squared error (MSE), and correlations. The COAMPS 3-hour data for this October 2001 Vandenberg AFB campaign has consistently smaller error, compared to thermosonde data measurements of C_n^2 from the other models based on objective metrics. The 3-hour ACMES, 15-hour MM5, and 15-hour COAMPS models had comparable ME, MAE, and RMSE results. All models had similar correlation scores when compared to thermosonde data.

Contingency tables were used to analyze the data. Hit rate (HR), threat score (TS), probability of detection (POD), false alarm rate (FAR), Heidke skill score (HSS), and bias were computed for each 2 X 2 contingency table. The contingency tables were computed for model and thermosonde values greater than 2 X CLEAR I, and greater than CLEAR I for the entire thermosonde profile, above the boundary level, and above flight level. The COAMPS 3-hour forecasts yielded the best overall scores in all categories, followed by the ACMES 3-hour forecasts. The MM5 15-hour data and COAMPS 15-hour data had similar results for the contingency table results. Contingency tables were also produced for the model domain profiles with the MM5 15-hour forecasts and the ACMES 3-hour forecasts. The model domains were not available for the COAMPS data sets. The ACMES 3-hour data results produced better overall scores compared to the MM5 15-hour data for the model domain comparisons.

The paired-t test had some surprising results. Paired-t tests were initially conducted with an alpha level of .05. The paired-t tests conducted with an alpha level of

.05 suggested a significant difference between vertically integrated C_n^2 using the models and thermosonde data in many cases. Based on the paired-t test results using an alpha level of .05, it was decided to try the same paired-t tests using alpha levels of .10 and .01. Using a .10 alpha level the two COAMPS and two ACMES model runs suggested a lack of significant difference for several comparisons when compared to thermosonde data. Using a .05 alpha level resulted in three COAMPS and three ACMES model data sets indicating a lack of significant differences between the means when compared to thermosonde data. When the alpha level was set to .01, the COAMPS model showed a lack of a significant difference between the observed and forecasted means in nine comparisons. For an alpha level of .01 the ACMES model data suggests a lack of significant differences for five cases and the MM5 data indicated a lack of significant differences between the means for one case.

Paired-t tests were also conducted to test the differences between means of the various models used in this research, all using an alpha level of .05. The ACMES 3-hour data when compared to the COAMPS 15-hour data indicates a lack of significant difference between these two models. ACMES 3-hour data when compared to the MM5 15-hour data also suggests a lack of significant difference between these two models. The COAMPS 15-hour data and the MM5 15-hour data don't indicate a significant difference between these models. All models that were compared with the COAMPS 3-hour data using the paired-t test, suggest that the COAMPS 3-hour forecasts are different from the other models.

Data were also vertically integrated or summed up for each entire profile in both the models and the thermosonde data for comparisons. The summed values of C_n^2 suggest that the MM5 15-hour data values were closer to the thermosonde values. The COAMPS 3-hour data yielded the next best results, followed by the ACMES 3-hour forecasts, and lastly the COAMPS 15-hour forecasts.

The results of this research show that statistically the COAMPS 3-hour model profiles compare favorably to the thermosonde data based on the ME, MAE, RMSE, and contingency table scores. The MM5 15-hour data indicated it had the closest path integrated values when compared to thermosonde data.

Averages of optical turbulence over the entire domain, whether using the MM5 or ACMES, identified higher values in the overall structure compared with the thermosonde data. These domain averages also indicated the highest values of optical turbulence above 12 km with regularity when compared to the thermosonde data. The domain average profiles yield an outline similar to the thermosonde profile. This result is interesting considering the scale over which entire grid layer averages are computed.

The synoptic evaluation for this thesis indicates the importance of identifying and forecasting meteorological features. The strong jet stream event was indicated by several thermosonde launches. Forecasting techniques for synoptic scale phenomena related to optical turbulence should be an area of continued focus.

A greater understanding of how these models assimilate, initialize, and parameterize physical processes they can't resolve should be an area of continued investigation. The effect of lateral boundary conditions (LBC) is another area of concern and can have a significant impact on how the predicted fields in the models evolve. The

LBC's can propagate boundary errors into the interior of the domain (Warner et. al. 1997). There may be significant differences between the models, which cannot be accounted for, which includes but is not limited to different domains, differences in terrain, and different physics schemes, etc. Further study is emphasized for all models used in this thesis because there is no simple way to pinpoint the differences in C_n^2 between models.

II. Literature Review

2.1 Issues with directed energy traveling through the atmosphere

First, let us understand the key elements of a directed energy system.

Directed energy in this case refers to a laser beam generated somewhere and directed towards a target. The laser beam must first be created, which requires a generation mechanism of some type. After the beam is formed, it is transferred to a beam expander. This beam expansion system can be a telescope or mirror and may be as large or as small as necessary. Lastly, a directed energy system may include a tracking system, which points the beam at a specific target as shown Figure 2. There are many other components that can be included in a laser system, but these are the core elements for any system (Golnik 1993).

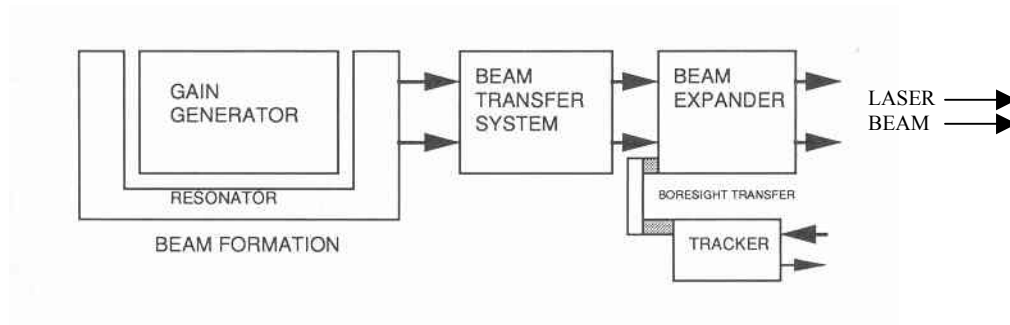


Figure 2. Diagram of Laser Beam Generation Components [Adapted from Golnik 1993]

The goal of any directed energy system, as the name implies, is to place power on a target, for a specified period of time in order to create a desired effect. Beam quality is a way of describing power or irradiance on a target. Beam quality is defined as the square root of the ratio of ideal power on a target to actual power on a target (BQ),

$$BQ = \left(\frac{IdealPower}{ActualPower} \right)^{1/2}, \quad (1)$$

which is dimensionless. Ideal power represents the power of the beam within a defined radius that reaches a diffraction-limited spot. Actual power in Equation 1 refers to the power that reaches a spot within the same defined radius. This formula indicates a beam of perfect quality hitting a target would have a BQ of 1.0. Anything greater than one indicates a degraded beam (Golnik 1993).

Another way to describe power on target is the Strehl ratio, which is considered by many as the measure of merit for highly focused optical systems. This Strehl ratio represents the ratio of on-axis mean irradiance in turbulence or diffraction-limited spot-size at the image plane (numerator) to the on-axis mean irradiance or diffraction-limited spot-size in the absence of turbulence (denominator). A Strehl ratio of 1.0 represents a perfect beam. A Strehl ratio of less than 1.0 represents a degraded beam (Andrews and Phillips 1998).

There are several factors which contribute to beam quality including wave front error, boresight/drift, jitter, diffraction, propagation, and other (miscellaneous) effects. Examples of beam wander and spreading are seen in Figure 3 and Figure 4. One of the concerns in this research will be on the beam after it leaves the expander, on its way to the target, during the propagation phase. Power losses during propagation are mainly the

result of absorption due to the atmosphere. Diffraction, scattering and nonlinear effects also can play a significant role, depending on the aerosol density of the medium and beam intensity (Golnik 1993).

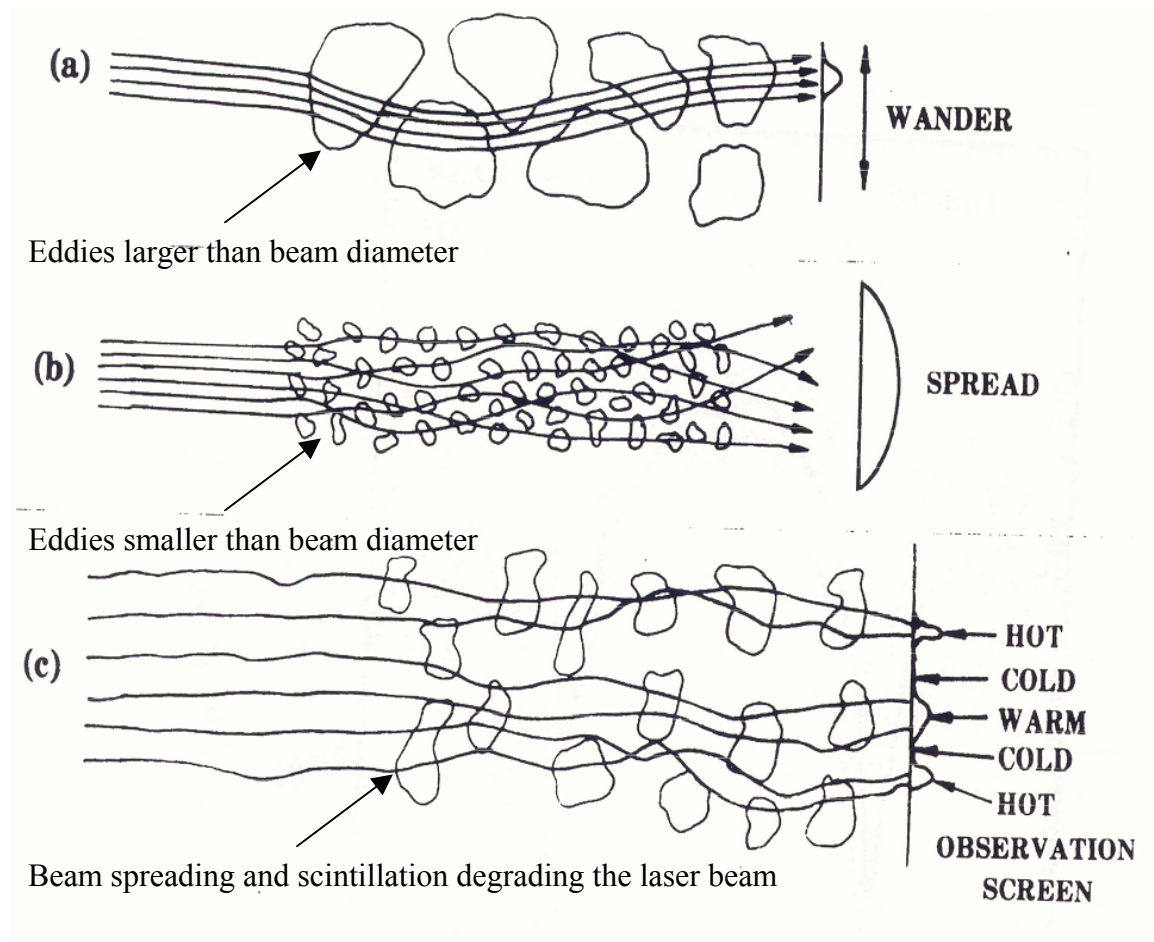


Figure 3. Atmospheric effects on Laser Beam Propagation [Adapted from Pries 1980]

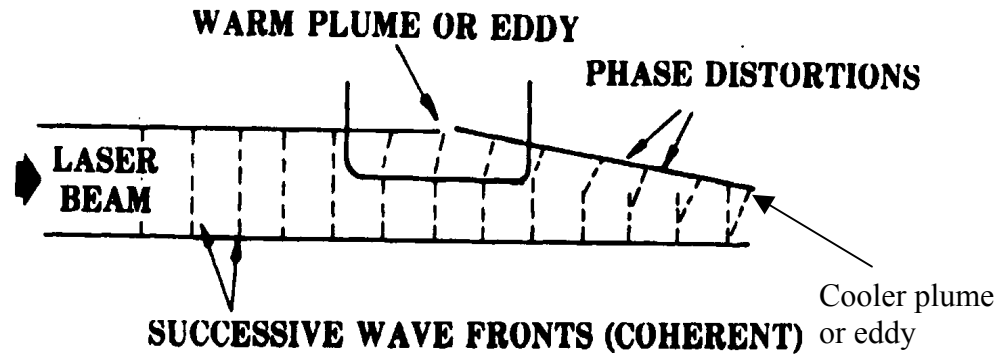


Figure 4. Wave front error due to Atmospheric effects [Adapted from Pries 1980]

2.2 Issues with directed energy and the airborne laser

One concern with the ABL is directing a HEL towards a target while maintaining an effective lock on the target. The ABL wavelength is 1.315 microns. This near-infrared wavelength is advantageous for the ABL, because it travels easily throughout the Earth's atmosphere, thus having greater destructive power on target. Inherent in this effort is maintaining beam intensity incident on the target that is the same as when it left the source.

Since the HEL will be traveling long horizontal distances in the Earth's atmosphere there are many meteorological factors that must be taken into consideration. One of the major concerns for HEL travel includes mechanical turbulence (which may vibrate the aircraft itself as well as affect the HEL). In regions of strong mechanical turbulence the temperature gradients necessary for optical turbulence are minimized due to mixing. Strong mechanical turbulence occurs near the ground where turbulence produces near perfect mixing. Experimental observations support the occurrence of strong optical turbulence where temperature gradients are large enough in the presence of

velocity fluctuations (Beland 1993). Other meteorological considerations include knowing what features in the atmosphere are likely to be places where temperature gradients are likely to occur and thus optical turbulence can be expected to occur with a high degree of confidence. Previous works have shed light on these efforts to help numerical modelers and forecasters do a better job of predicting optical turbulence (C_n^2). Higher values of C_n^2 have been shown to occur north of the jet core, with lower values to the south of the jet core in the Northern Hemisphere. Also, higher values of C_n^2 can be expected just above inversions, on the warm side. Other features include higher C_n^2 values in regions of strong vertical wind shear, higher C_n^2 underneath inversions during the approach of jets that are associated with gravity waves, higher values of C_n^2 above and below tropopause boundaries and during trough passage (Budai 2001).

Optical turbulence in the boundary layer, which is the region of the Earth where the atmospheric dynamics are dominated by the exchange and interaction of heat with the Earth's surface, is one of two regions that must be considered in modeling the Earth's atmosphere. The upper or free atmosphere is a region above the planetary boundary layer where the dynamics and turbulence depends more on synoptic-scale meteorology, wind shear, and gravity waves (Beland 1993).

Optical turbulence in the atmosphere contributes to degrading the quality of the laser beam as it approaches its intended target. The two main issues concerning an airborne directed energy system are clear air turbulence (CAT), which is a type of atmospheric turbulence that leads to optical turbulence, and thermal blooming (MacGovern et al. 2000). CAT is defined as a higher altitude (6-15 km) turbulence

phenomenon occurring in cloud-free regions, associated with wind shear, particularly between the core of a jet stream and the surrounding air (Glickman et al. 2000). Thermal blooming is another factor, which causes the beam to expand. Thermal blooming refers to self-induced spreading, distortion, and bending of a HEL beam that occurs due to the energy of the HEL, which is absorbed by molecular and aerosol constituents in the medium in which the HEL travels. The absorption of the HEL by the medium, in this case air, causes heating of the air thus leading to density or refractive index gradients, which distorts and degrades the beam (Pries 1980). Clear air turbulence and thermal blooming both act to degrade the effectiveness of the laser beam (MacGovern et al. 2000). Thermal blooming is a phenomenon that will not be a focus of this thesis, but was mentioned for completeness.

2.3 Optical Turbulence

2.3.1) Definition of Turbulence

Turbulence is a random, rotational state of fluid motion that arises when shear instabilities from the nonlinear terms in the momentum equation overcome viscous damping at small scales to form eddy like motions (Gibson 1991). This random, irregular fluid flow in which the particles of the fluid move in a disordered manner creates an exchange of momentum from one portion of a fluid to another. Turbulence is fundamentally characterized in terms of velocity fluctuations (Beland 1993).

Some of the characteristics of turbulence include the following (Tennekes and Lumley 1972):

1. Irregularity: Randomness is a characteristic of all turbulent flows, which is why statistical methods are used to try and solve turbulence problems. A deterministic approach to these types of problems is practically impossible.
2. Diffusivity: Another important feature of all turbulent flows is rapid mixing and increased rates of momentum, heat, and mass transfer caused by diffusivity (particles becoming widely dispersed or spread out).
3. Large Reynolds numbers: Turbulent flows occur at high Reynolds numbers. Large Reynolds numbers indicate turbulence, which occurs when laminar flow becomes unstable. The Reynolds number is a dimensionless number used in fluid dynamics to describe instabilities from laminar flow. The Reynolds number is described by the equation,

$$Re = \frac{UL}{\nu}, \quad (2)$$

where, U is the scale of variation of velocity in a length scale L , and ν is the fluid viscosity (Kundu 1990). The interaction of viscous terms and nonlinear inertia terms in the equations of motion are related to the instability of laminar flow. Randomness and non-linearity make the equations of turbulence very difficult to solve.

4. Three-dimensional vorticity fluctuations: Turbulence is three-dimensional and rotational. High levels of fluctuating vorticity characterize turbulence. Random vorticity fluctuations that characterize turbulence could not maintain themselves if the velocity fluctuations were

two dimensional, since vortex stretching, an important vorticity-maintenance mechanism is absent in two-dimensional flow.

5. Dissipation: Turbulent flows are always dissipative. Deformation work increases the internal energy of the fluid at the expense of kinetic energy of the turbulence due to viscous shear stresses. Turbulence needs a continuous supply of energy to make up for the losses due to viscosity. If there is no energy supplied, the turbulence will decay rapidly. Random motions such as gravity waves and sound waves have insignificant viscous losses and are not turbulent. The major distinction between random waves and turbulence is that waves are non-dissipative (though they are dispersive), while turbulence is essentially dissipative.

6. Continuum: Even the smallest scales occurring in a turbulent flow are ordinarily far larger than any molecular length scale.

7. Turbulent flows are flows: Turbulence is a feature of fluid flows not fluids themselves. Since the equations of motion are nonlinear, each individual flow pattern has certain unique characteristics that are associated with its initial and boundary conditions. No general solutions to problems in turbulent flow are available.

Turbulent processes characterize the atmosphere of the Earth, and since the HEL of the ABL will travel through this medium we must be concerned with its effects.

2.3.2) Definition of Optical Turbulence

Optical turbulence is defined as temporal and spatial fluctuations in the index of refraction that result from atmospheric turbulence. Optical turbulence is caused by the presence of adjacent parcels of air, at slightly different indices of refraction, moving about in the path of propagating electromagnetic waves (Jumper and Beland 2000).

These adjacent parcels of high or low refractive index can be thought of as eddies, which act as lenses of various sizes and shapes moving randomly in the atmosphere (Strohbehn 1978). These eddies can be thought of as very weak lenses with very long focal lengths (Dewan 1980), similar to pancake like layers in the atmosphere. Fluctuations in the refractive index that result from turbulent mixing are random in nature. These turbulent fluctuations cause phase distortions in the wave front along the propagation path in the atmosphere as it passes through the turbulence, which further distorts the beam as it continues to travel (Beland 1993).

Atmospheric turbulence, which leads to optical turbulence, is not completely understood and is chaotic in its behavior. Statistics are used to describe chaotic processes, which is why statistics are used to explain optical turbulence. A. N. Kolmogorov (1941) developed a universal structure tensor, which helps to describe the random motions in velocities between two points in space separated by some distance. This led him to describe the distance r , between the outer-scale of turbulence (L_0) and the inner-scale of turbulence (l_0) known as the inertial sub-range for turbulence

$$D_{rr} = C_v^2 r^{2/3}, \quad (3)$$

where, D_{rr} represents the universal structure tensor and, C_v^2 is the velocity structure constant, a measure of the total amount of energy in turbulence. C_v^2 measures the strength or weakness of velocity turbulence and is called the velocity structure coefficient or constant (Strohbehn 1978). Equation 3 is only valid for values of r , the displacement vector between l_o and L_o . This theory requires isotropic turbulence structure (i.e. the turbulence does not vary with direction), for the inertial sub-range. Energy input into the turbulence process from L_o cascades down adiabatically through the inertial sub-range until it is lost as heat through viscous effects when it becomes less than l_o (Bufton 1975). The structure function, C_v^2 , is used as the basic statistical quantity to describe turbulence.

The length scales of optical turbulence can be thought of as an energy cascade. The source of energy at large scales is either wind shear or convection. Under energy cascade theory, the wind velocity increases until it reaches a point at which the critical Reynolds number is exceeded. Once this critical Reynolds number is reached, local unstable eddies with characteristic dimensions slightly smaller than, and independent of the parent flow are created. Under the influence of inertial forces, larger eddies break up into smaller eddies to form a continuum of eddy sizes for the transfer of energy from the macro-scale (the outer-scale of turbulence, L_o) to the micro-scale (the inner-scale of turbulence, l_o). The family of eddies bounded by these two regions can be thought of as the inertial sub-range of turbulent eddies. Scale sizes smaller than the inner-scale of turbulence are considered in the viscous dissipation range. In the viscous dissipation range the turbulent eddies disappear and the remaining energy in the fluid motion is dissipated as heat. The outer-scale of turbulence denotes the scale sizes below which the

turbulent eddies are independent of the parent flow. Eddies below the outer-scale are assumed to be statistically homogeneous and isotropic. Eddy sizes above the outer-scale of turbulence are non-isotropic and not well defined (Andrews and Phillips 1998). The inertial sub-range is depicted in Figure 5.

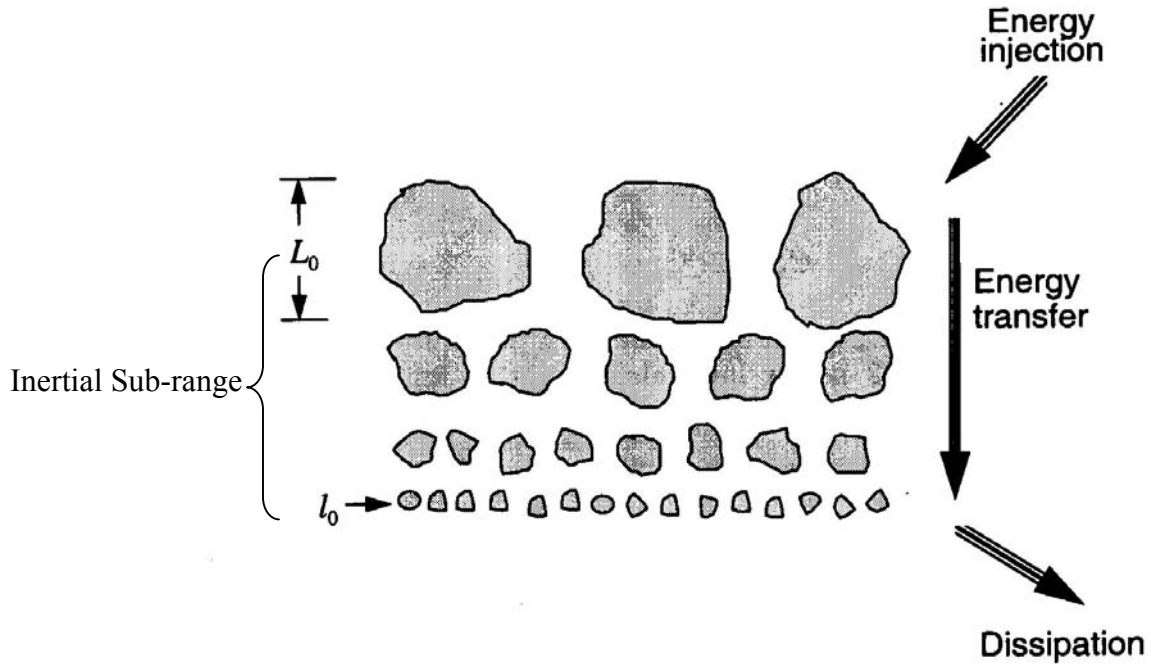


Figure 5. Inertial Sub-range of Turbulence [Adapted from Andrews and Phillips 1998]

Tatarski (1961) related Kolmogorov's (1961) work on turbulence to the refractive index. He used the concept of a conservative passive additive quantity to relate turbulence to the refractive index. Conservative properties are such that the values do not change in the course of a particular series of events (Glickman et al. 2000). To relate the ambient temperature to velocity fluctuation statistics we use potential temperature. Potential temperature is used because the difference between the absolute temperature and the change in temperature with height caused by a dry adiabatic lapse rate yields a

conservative quantity, which is what's needed for Kolmogorov theory to be valid (Strohbehn 1978).

Turbulence effects occur because of mixing of atmospheric parameters, such as temperature, water vapor, and the index of refraction. Temperature, water vapor and the index of refraction are passive quantities since their dynamics do not affect turbulence (Beland 1993). Temperature fluctuations are considered passive because they don't exchange energy with velocity turbulence (Andrews and Phillips 1997). Passive additives are quantities that do not affect turbulence dynamics. When passive additives are inserted into a turbulent medium they do not affect its statistics (Strohbehn 1978). Based on Kolmogorov theory, the structure function for potential temperature variations can be described by

$$D_{\theta}(r) = C_{\theta}^2 r^{2/3}. \quad (4)$$

In equation 4, D_{θ} is the structure function for potential temperature, and C_{θ}^2 is the potential temperature structure constant. Equation 4 leads to the development of the structure function for the refractive index (n) by relating the equation for refractive index of air at optical frequencies, which is

$$n-1 = 77.6 (1 + 7.52 \times 10^{-3} \lambda^{-2}) (p/T) 10^{-6}, \quad (5)$$

written in terms of temperature and pressure, where λ is wavelength, to potential temperature θ (Strohbehn 1978). Any vertically displaced parcel will produce a temperature change, because the parcel will try to equalize its pressure with that of the surrounding medium. The pressure change in the parcel as a result of the parcel being vertically displaced produces a temperature change assuming adiabatic conditions. The

potential temperature can be described by $\theta = T - \Gamma_a z$, where Γ_a is the dry adiabatic lapse rate of 9.8 degrees C/km, z is height, and T is ambient temperature (Strohbehn 1978). Corrsin (1951) showed that conservative passive additives obey the 2/3 law, which implies the slope of the curve relating the structure function and the inertial sub-range has approximately this slope. The two-thirds law indicates that no general behavior about the structure function can be predicted for values greater than the outer length scale, because the structure function becomes dependent on an-isotropic eddies and the two-thirds law theory no longer holds. The slope of the structure function asymptotically approaches $2\sigma^2$ as r becomes greater than L_o , where σ^2 is the variance of the fluctuations if the random field is homogeneous and isotropic (Beland 1993), which is approximately near the outer length scale as shown in Figure 6 (Tatarski 1961). The inertial sub-range is indicated to exist based on experimental evidence by Tsvang (1969), which lends support to the validity of the 2/3 power law. Validity of the 2/3 power law for the structure function in the inertial range, the -11/3 power law associated with the power spectrum in three dimensions, and the -5/3 power law for a one dimensional power spectrum have been established over a wide range of experiments (Andrews and Phillips 1997). Turbulence scale sizes for the inner length scales, outer length scales, and the magnitude of turbulence intensity changes with altitude (h) depending on the size of the eddies. The assumption of isotropy previously indicated must be modified to one of local isotropy. The inner length scale l_o is on the order of a few cm near the ground and in the stratosphere increases to tens of cm. The outer length scale L_o is thought to be roughly equal to altitude above the surface. The scale sizes that have the largest impact on optical

propagation are generally within the inertial sub-range at all altitudes and are weighted most heavily towards the inner length scales (Bufton 1975).

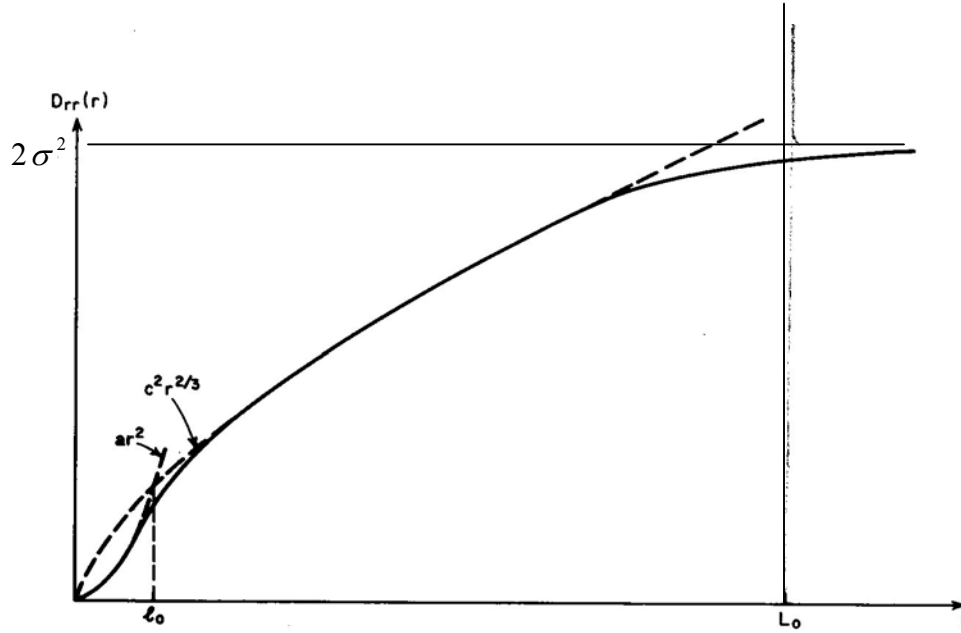


Figure 6. Structure Function vs. Inertial Sub-Range indicating 2/3rds slope or “2/3rds power law” [Adapted from Tatarski 1961]

The refractive index structure coefficient C_n^2 describes optical turbulence strength and distribution. Experimentally, it has been shown that turbulence strength and distribution enters optical propagation theory through $C_n^2(h)$, which depends on micro-scale temperature fluctuations specified by the temperature structure coefficient, $C_T^2(h)$ (Bufton 1975).

C_n^2 variations with altitude constitute a vertical profile of the optical strength of turbulence in the atmosphere. Changes in the refractive index (n) must therefore be related through changes in temperature and pressure as a result of these changes in height. The differential of the index of refraction δn is described by

$$\delta n = \frac{79P}{T} \left(\frac{\delta P}{P} - \frac{\delta T}{T} \right) \times 10^{-6}, \quad (6)$$

where, P is pressure, and T is temperature. Since the pressure fluctuations are measured at a fixed point with respect to the ground they can be considered relatively small and rapidly dispersed. As a result of this small contribution of pressure, the observed refractive index variations will be almost exclusively due to temperature fluctuations, so the $\delta P / P$ term can be neglected. The neglecting of the pressure term in Equation 6 will force the refractivity variations at a fixed height to be almost completely due to temperature fluctuations (Strohbehn 1978). Using the differential of potential temperature $\delta\theta$ instead of the differential of ambient temperature δT , because it is a conservative quantity, allows Equation 6 to be rewritten as

$$\delta n = -79P \frac{\delta\theta}{T^2} \times 10^{-6}, \quad (7)$$

The differential of potential temperature $\delta\theta$ is a conservative passive additive, so the differential of the refractive index will be a function of $\delta\theta$ (Strohbehn 1978). Since $\delta\theta$ is a conservative passive additive and δn is as well, the two-thirds law for refractivity fluctuations can be written as

$$D_n(r) = C_n^2 r^{2/3}. \quad (8)$$

This allows us to write the refractive index structure constant C_n^2 in terms of C_θ^2 ,

$$C_n^2 = \left(\frac{79}{T^2} \times 10^{-6} \right)^2 \times C_\theta^2. \quad (9)$$

From here on C_T^2 will be used in place of C_θ^2 , where the subscript T represents potential temperature (Strohbehn 1978). Also, the structure constants are not really constants, but

change both temporally and spatially. The variation of $C_n^2(h)$ as a function of altitude (h) characterizes the vertical distribution of turbulence (MacGovern et al. 2000). C_n^2 is not directly measured but is inferred from the temperature structure constant, C_T^2 , which is really the potential temperature structure constant as mentioned previously, temperature is (T) measured in kelvins, and pressure (p) measured in millibars using the equation

$$C_n^2 \approx (79 \times 10^{-6} (P/T^2))^2 C_T^2, \quad (10)$$

where, the wavelength is known.

C_n^2 can also be directly related to the Brunt-Vaisala frequency (N^2) by the following equation,

$$C_n^2 = 2.8 L_o^{4/3} (79 \times 10^{-6} P / gT)^2 N^4, \quad (11)$$

which describes the strength of temperature gradients (Beland 1993) where,

$$N^2 = \left(\frac{g}{\theta} \right) \left(\frac{\partial \theta}{\partial z} \right), \quad (12)$$

and g is the acceleration due to gravity, θ is the potential temperature, z is height and $L_o^{4/3}$ refers to the largest scale of inertial range turbulence.

Observed values from the thermosonde and derived values from the numerical models must be concerned with path integrated C_n^2 values for a standard ABL scenario exceeding twice the CLEAR I profile. Values of C_n^2 that are greater than twice the CLEAR I profile are areas of concern and may indicate areas of enhanced Rytov variance. Rytov variance is a measure of the fluctuations in amplitude intensity or

scintillation of the laser beam energy due to path integrated turbulence (Roadcap 2002). Numerical models need to be able to predict high optical turbulence events ($10^{-15} \text{ m}^{-2/3}$ or greater) with a minimum of false alarms (Ruggiero 2002). C_n^2 values of 20 percent or less than the CLEAR I profile may indicate a problem with the measurement devices or models used to characterize it and should be checked (Roadcap 2002).

Rytov variance, along with Fried's Coherence length, isoplanatic angle and the Greenwood frequency are the four commonly used parameters used to describe the atmospheric effects of optical turbulence. Fried's Coherence length describes the effective aperture size due to phase distortions of the optical wave front caused by path-integrated turbulence. The smaller the effective aperture, the less coherent the beam is and the less energy that will be available to get to the target. The isoplanatic angle describes the angular width for application of the adaptive optics wave front correction that will correct for the turbulence on the outgoing path. If the target subtends an angle greater than this angle, the wave front correction becomes invalid. The Greenwood frequency is a measure of the required bandwidth for the adaptive optics system produced by the beams atmospheric path. A higher Greenwood frequency requires more bandwidth for the adaptive optics to work (Roadcap 2002). This frequency can be thought of as a relative measure of how fast the atmosphere is changing (Goda 2002). This thesis will only be concerned with Rytov variance assuming an "onion skin" model, but the other three parameters were mentioned for completeness. The "onion skin"

model assumes that the fields of C_n^2 are horizontally homogeneous and that C_n^2 is only a function of height (Ruggiero and DeBenedictis 2002).

2.4 Thermosonde

The thermosonde relays temperature information to a ground station, which calculates C_n^2 as a function of height, as a result of fine scale temperature measurements (Bufton 1975). The thermosonde system measures the mean square temperature fluctuations across a one-meter distance as a function of altitude using the Obukhov-Kolmogorov (Obukhov 1941, Kolmogorov 1941) turbulence theory equation,

$$C_T^2(h) = \left\{ \frac{[T(r_1) - T(r_2)]^2}{r^{2/3}} \right\}_h, \quad (13)$$

where $r = |r_2 - r_1|$, r is the absolute value of the scalar distance between two points, r_1 and r_2 where the temperature is measured. These temperature fluctuations represent a “potential temperature”, which adjusts for the difference in temperature with height due to adiabatic expansion (Jumper et al. 1997). Equation 13 is used to compute the temperature structure constant, which is then used to compute the index of refraction structure constant $C_n^2(h)$ described by

$$C_n^2 = \left[\frac{80P(h)}{T(h)^2} \times 10^{-6} \right]^2 C_T^2(h). \quad (14)$$

The index of refraction depends almost exclusively upon temperature for some electromagnetic frequencies (for optical frequencies). For radar frequencies it depends on both temperature and specific humidity (Dewan 1980). This thesis is focused on optical frequencies.

Thermosondes are instrument packages carried by balloons as seen in Figure 7. These instrument packages carry probes at both ends of a 1m long styrofoam boom to measure temperature. The changing resistance of a thin wire between the two probes is used to calculate the root mean square (rms) temperature difference and this result is sent to a ground station. The thermosonde measures from the surface to 30 km at 20 m intervals as it ascends and usually requires about 2 hours before it completes a mission.

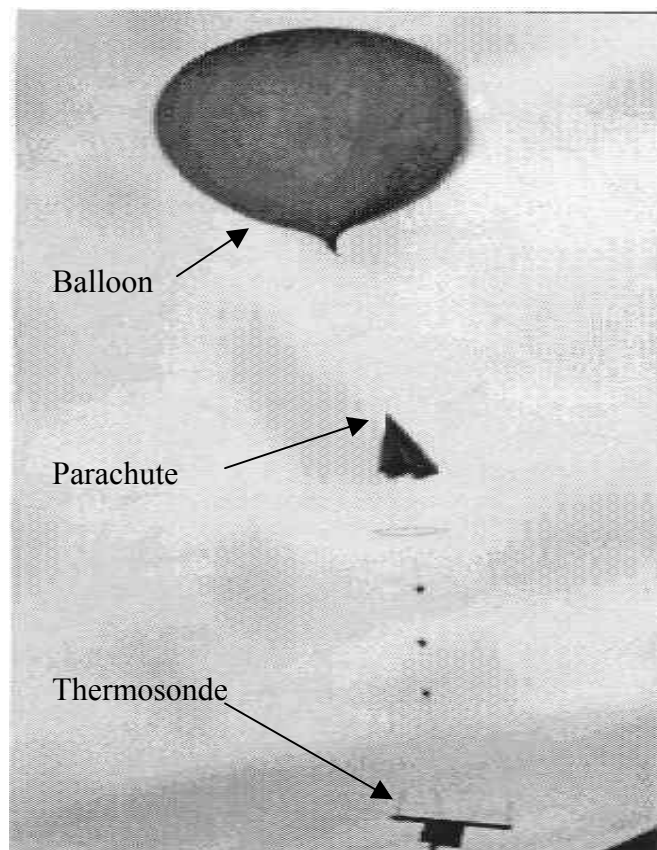


Figure 7. Thermosonde Image with Balloon attached [Adapted from Air Force Research Lab 1998]

The balloon pops at about 30 km and then descends with the parachute slowing its fall. Data are only recorded during ascent, and not during descent. The thermosonde is hung about 110 meters below the balloon in order to mitigate wake turbulence from the balloon. Optical turbulence is integrated over a 20-meter spatial scale, which is referred

to as a turbulent spectrum. Optical turbulence values are then transmitted and recorded every 1.5s. The electronics are capable of measuring layers down to approximately .005m with a 5 m/s ascent rate (Robinson 2002).

2.5 Fifth Generation Mesoscale Model

Air Force Research Labs uses the Fifth Generation Mesoscale Model (MM5) (Dudhia et al. 2001) at Hansom AFB, Massachusetts to model optical turbulence. The MM5 model used for this thesis is a modified version of the MM5 used by the Air Force Weather Agency (AFWA). The MM5 is a grid point model that uses non-hydrostatic sigma levels for its vertical coordinates. This version of the MM5 has a horizontal resolution of 45, 15, and 5 km using 81 vertical levels as shown in Figure 8, and it uses the same parameterizations as the AFWA version of the MM5. These model runs all used one-degree horizontal resolution data from the National Center for Environmental Prediction (NCEP) analysis and Aviation (AVN) models. AVN was used to update the lateral boundary conditions of the outermost nest of the MM5 during model integration. MM5 ran non-hydrostatically for all the runs. This version of the MM5 model initializes using the standard Cressman (1959) analysis scheme. The MM5 data used for this thesis were post-processed using the Dewan Equation

$$C_n^2 = 2.8 \left(\frac{(79 \times 10^{-6} P)}{T^2} \right)^2 L_o^{4/3} \left(\frac{\partial T}{\partial z} + \gamma \right)^2, \quad (15)$$

to compute optical turbulence (Ruggiero and DeBenedictis 2002). The post-processed MM5 data were provided by AFRL in 500 m intervals. All the terms are the same as

mentioned previously, and γ is the dry adiabatic lapse rate of 9.8 C/km. Each domains horizontal grid information and time steps are listed in Table 1. The model top is defined as 10 mb.

Table 1. MM5 Domains

Domain 1 73 73 (45km grid spacing)	Time step length 90 s
Domain 2 88 88 (15km grid spacing)	Time step length 30 s
Domain 3 121 121 (5 km grid spacing)	Time step length 10 s

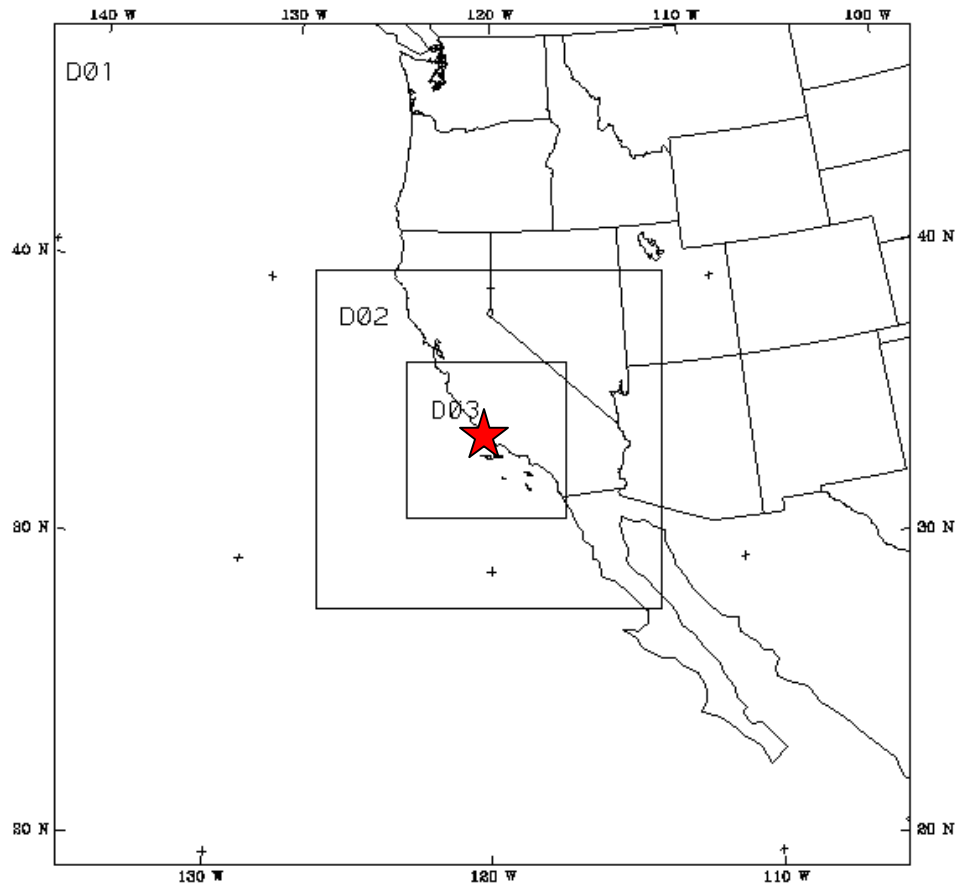


Figure 8. MM5 Model Domain for this thesis [adapted from Ruggiero and DeBenedictis 2002]

2.6 Coupled Ocean Atmosphere Prediction System (COAMPS)

The Naval Postgraduate School (NPS) working with the Naval Research Laboratory (NRL) uses the COAMPS model to predict optical turbulence (COAMPS 1999). The COAMPS model is a non-hydrostatic grid point mesoscale model. COAMPS uses primitive equations with non-hydrostatic sigma levels for vertical coordinates and the parameterization schemes that are default with the model. This model is triple nested with 81, 27, and 9 km horizontal resolution. It uses 47 vertical levels with the top of the model being 10 mb. COAMPS uses the 39 level ETA data for initialization coupled with a 2-D multi-quadratic interpolation. The horizontal grid uses the Arakawa-C grid. The COAMPS analysis is performed using an un-staggered Arakawa-A grid. Bicubic spline interpolation is used to interpolate the forecast model initialized fields to the horizontal Arakawa-C grid. The COAMPS model is run in continuous update cycle, with the first-guess fields coming from the previous COAMPS forecast.

NPS runs two versions of the COAMPS model to forecast optical turbulence. One version of the COAMPS model accounts for turbulent kinetic energy (TKE) at all altitudes by modifying the source code to match experimental measurements (Walters 2002a). The version of the COAMPS model used for this thesis uses model output to calculate optical turbulence based on the gradient Richardson number length scale.

The Dewan equation, which is used in the MM5 and ACMES models to compute optical turbulence, is not used in these COAMPS model runs. The gradient Richardson number and TKE algorithms give similar results for low to moderate turbulence situations. The Richardson number technique gives more conservative results, while the TKE buoyancy technique is more sensitive to neutral potential temperature gradients that

occur with strong jet streams (Walters 2002a). The optical turbulence equation used in the COAMPS model is from the combined works of Tjernstrom (1993), (Walters and Kunkel 1981), Bougeault et al. (1995), Parker (2002) and is as follows:

$$C_n^2 = (2.8) l_h l_\epsilon^{1/3} \left(\frac{79 \times 10^{-6} P \frac{d\theta}{dz}}{T\theta} \right)^2, \quad (16)$$

where,

$$l_h = l_o \left[1 + 15 Ri_g (1 + 5 Ri_g)^{1/2} \right]^{-1/2}, \quad (17)$$

and,

$$l_\epsilon = l_o \left[1 + 50 Ri_g \right]^{-1/4}, \quad (18)$$

where,

$$Ri_g = \frac{g}{\theta_v} \frac{\partial \theta_v}{\partial z} \left[\left(\frac{\partial \bar{U}}{\partial z} \right)^2 + \left(\frac{\partial \bar{V}}{\partial z} \right)^2 \right]^{-1}. \quad (19)$$

All terms have the usual meanings and θ_v represents virtual potential temperature.

Virtual potential temperature is the theoretical temperature dry air would have with the same density as moist air (Glickman et al. 2000). The length scale of sensible heat is represented by l_h , and l_ϵ represents the length scale for the dissipation of turbulent kinetic energy (TKE). The gradient Richardson number (Ri_g), represents a ratio between the buoyancy term (numerator) and a wind shear term (denominator) in Equation 19. When the gradient Richardson number is < 0.25 everywhere in the flow of a fluid then linear instability occurs and the atmosphere becomes turbulent (Kundu 1990).

2.7 Advanced Climate Modeling and Environmental Simulations (ACMES)

ACMES is a method of generating high-resolution climate statistics for any location on Earth (Amrhein 2002). The method used in ACMES is called CLIMOD and uses climate statistics in a dynamic model. The mesoscale numerical model it uses is the Mesoscale Atmospheric Simulation System (MASS) model, which was developed at MESO, Inc (MASS 2001). The MASS model can produce 6 to 36 hour forecasts on the meso-alpha and meso-beta scales. The window used for these model runs has a horizontal resolution of 11 km with 60 vertical levels from the surface up to 100 mb and is shown in Figure 9. ACMES, MM5, and COAMPS use NCEP and National Center for Atmospheric Research (NCAR) meteorological data for reanalysis, along with surface characteristics for initial conditions.

The NCEP/NCAR reanalysis data produces a global field of meteorological data (Kalnay et al. 1996). The NCEP/NCAR reanalysis project takes in global meteorological data, quality controls this data and runs a data assimilation on these data. These fields cover the entire continental United States and provide an excellent way of observing synoptic features in the atmosphere with reliability (Budai 2001).

The MASS model for this thesis is initialized at 00Z and 12Z. Reanalysis data, rawinsonde data, and surface observations are used to initialize the model. The reanalysis data are read in every 6 hours to update the boundary conditions. At the 12-hour point the model stops so it can be reinitialized with rawinsonde and surface observations. Incremental analysis update (IAU) is performed in order to nudge the previous solution of the model to match the observations at this re-initialization point.



Figure 9. ACMES map [adapted from AFCCC]

During IAU the previous 3 hours of diagnostic files are adjusted so that model data more closely matches the rawinsonde and surface data at the 12-hour point. IAU is performed to avoid discontinuities in variables; moisture is a variable where these discontinuities usually occur. After IAU is complete the model runs again for 12 hours and this process is again repeated until the model run is complete (Amrhein 2002). Incremental analysis update is used to ingest the surface and rawinsonde data. This technique allows for the introduction of observed data into the model while it's running. ACMES data are post-processed using the Dewan equation to calculate optical turbulence.

The MASS model for 15-30 Oct 01 campaign was given a few days to “spin up” in an attempt to avoid a cold start for the period of the campaign. The model was cold started on 1 Oct 01 for the 15-30 Oct 01 campaign. The ABL microphysics package was also maintained for the duration of the model run (Amrhein 2002).

2.8 Synoptic Data

NCDC supplied the synoptic data. These data sets include surface charts, upper air charts at standard levels, and observations for the period of this campaign. The University of Wyoming supplied the skew-t data (UW 2001).

2.9 Recent Work

Frank Ruggiero’s (Ruggiero and DeBenedictis 2002) work, which recently investigated the performance of three optical turbulence-forecasting techniques, serves as the framework for this thesis. His work compared several equations used to calculate optical turbulence and the CLEAR I profile. The thermosonde data were integrated or summed up into 500 m layers and averaged to produce a layered mean value. This model output was linearly interpolated to match the heights of the thermosonde observed heights at 500 m intervals. A root mean square (rms) error, bias, and correlation were then calculated for these profiles between 5 and 21 km.

III. Data Description

C_n^2 derived from four data sets were used for this thesis. Thermosonde data, MM5, ACMES, and COAMPS model runs were used as part of this analysis. The model runs mentioned previously were compared to optical turbulence values from thermosonde observations and 2 X CLEAR I.

Data collection was conducted at Vandenberg AFB, California which is situated along the coast and is heavily influenced by the dominant marine layer. The Santa Ynez Mountains are to the south and east of the base with peaks of 1228 m. The balloons were launched at 34.67 North, 120.42 West at 116 m elevation.

3.1 Thermosonde Data Description

The thermosonde data used for this thesis were obtained from the Air Force Research Laboratory at Hansom AFB, Massachusetts. Thermosonde data were collected for the period of 19-26 October 2001 UTC at Vandenberg AFB, California. The launch dates and times are shown in Table 2. The shaded cells in Table 2 indicate daytime launches.

Most of the launches were conducted at night to reduce the chances of differential error on each sensor due to daytime heating. The thermosonde data generates two files that are used for this thesis. A trajectory file is generated, which has time in seconds, height(m), windspeed(m/s), windir(deg), deltax(km), deltay(km), range(km), and azimuth(deg). The data in the trajectory files are produced every two seconds with

approximately 10 m vertical resolution. This trajectory output produces a 5 m/s vertical resolution of the launch data. Each trajectory file has over 2000 data points that extend

Table 2. Thermosonde Launches

Flight ID	Local Launch Date	Local Launch Time	UTC Launch Date	UTC Launch Time
VanFa002	18-Oct-01	20:22	19-Oct-01	3:22
VanFa003	18-Oct-01	22:08	19-Oct-01	5:08
VanFa004	19-Oct-01	16:23	19-Oct-01	23:23
VanFa005	19-Oct-01	18:15	20-Oct-01	1:15
VanFa006	19-Oct-01	20:00	20-Oct-01	3:00
VanFa007	19-Oct-01	21:44	20-Oct-01	4:44
VanFa008	20-Oct-01	16:20	20-Oct-01	23:20
VanFa010	20-Oct-01	19:35	21-Oct-01	2:35
VanFa011	20-Oct-01	21:13	21-Oct-01	4:13
VanFa012	22-Oct-01	18:15	23-Oct-01	1:15
VanFa013	22-Oct-01	19:54	23-Oct-01	2:54
VanFa015	23-Oct-01	18:14	24-Oct-01	1:14
VanFa016	23-Oct-01	19:48	24-Oct-01	2:48
VanFa017	23-Oct-01	21:30	24-Oct-01	4:30
VanFa018	24-Oct-01	18:15	25-Oct-01	1:15
Vanfa019	24-Oct-01	19:53	25-Oct-01	2:53
VanFa021	25-Oct-01	18:11	26-Oct-01	1:11
VanFa022	25-Oct-01	19:49	26-Oct-01	2:49

Shading = Daytime Launches

Flight ID = Thermosonde Launch Number

from the surface up to 30 km. The next file generated is a text file, which has height(m), pressure(mb), temp(c), RH(%), and C_n^2 ($\text{m}^{-2/3}$). Each of the text files has over 3000 data points, which extend up from the surface to 30 km. It is worthwhile to note that no launches were conducted from 00Z 22 October 2001 – 00Z 23 October 2001.

3.2.2 X CLEAR I profile

The CLEAR I profile was produced in the summer of 1984. Thirty-nine balloon launches were conducted at White Sands Missile Range (WSMR) in New Mexico to determine a profile of C_n^2 in the atmosphere. The CLEAR I profile is calculated using mean sea level (MSL) heights (Beland 1993). The launches were conducted both during the day and night. The night launches were used as the baseline for the CLEAR I profile because the night launches have higher values of optical turbulence due to less thermal mixing in the atmosphere at night. Higher rates of thermal mixing due to heating will create lower values of optical turbulence due to the atmosphere being well mixed (White et al. 1985).

3.3 MM5 Data Description

The Air Force Research Laboratory produced the MM5 model output for the 19-26 October 2001 UTC Vandenberg AFB, California campaign. Values of C_n^2 , ambient temperature (C), pressure (mb), mixing ratio, and the u, v wind components are interpolated to common points horizontally in the model domain from 500 m up to 25 km for each model run. Seven MM5 model runs were produced with each model run corresponding to different thermosonde launches as listed in Table 3. Shading in Table 3 indicates daytime launches.

Table 3. MM5 Model Runs and Thermosonde Launches

Model Run Start Date	Model Start Time UTC	Balloon #	Local Launch Date	Local Launch Time	UTC Launch Date	UTC Launch Time
18-Oct-01	12:00	VanFa002	18-Oct-01	20:22	19-Oct-01	3:22
		VanFa003	18-Oct-01	22:08	19-Oct-01	5:08
		VanFa004	19-Oct-01	16:23	19-Oct-01	23:23
19-Oct-01	12:00	VanFa005	19-Oct-01	18:15	20-Oct-01	1:15
		VanFa006	19-Oct-01	20:00	20-Oct-01	3:00
		VanFa007	19-Oct-01	21:44	20-Oct-01	4:44
20-Oct-01	12:00	VanFa008	20-Oct-01	16:20	20-Oct-01	23:20
		VanFa010	20-Oct-01	19:35	21-Oct-01	2:35
		VanFa011	20-Oct-01	21:13	21-Oct-01	4:13
22-Oct-01	12:00	VanFa012	22-Oct-01	18:15	23-Oct-01	1:15
		VanFa013	22-Oct-01	19:54	23-Oct-01	2:54
23-Oct-01	12:00	VanFa015	23-Oct-01	18:14	24-Oct-01	1:14
		VanFa016	23-Oct-01	19:48	24-Oct-01	2:48
		VanFa017	23-Oct-01	21:30	24-Oct-01	4:30
24-Oct-01	12:00	VanFa018	24-Oct-01	18:15	25-Oct-01	1:15
		Vanfa019	24-Oct-01	19:53	25-Oct-01	2:53
25-Oct-01	12:00	VanFa021	25-Oct-01	18:11	26-Oct-01	1:11
		VanFa022	25-Oct-01	19:49	26-Oct-01	2:49

Shading = Daytime Launches

Balloon # = Thermosonde Launch Number

The MM5 output is stored in successive time-series with the model output post-processed every 3 hours for the entire 24-hour period. This post-processing produces nine output times for single model run. Each of the MM5 model runs are initialized at 12Z. Optical turbulence values were checked for consistency between model output times. No significant differences in C_n^2 values were noted between successive model output times.

3.4 ACMES Data Description

ACMES model runs were produced for each day of the October 2001 Vandenberg AFB, CA. campaign. ACMES model output was produced for each hour in the 24-hour period. ACMES output using the MASS model produces 54 variables for each model run in the entire domain. Ambient temperature (K), pressure (mb), C_n^2 ($m^{-2/3}$), and sigma heights(km) are used from these model runs. The ACMES model runs are used as listed for each launch in Table 4. The data between successive model output times were checked for consistency. Each hourly model output time and model output every 3 hours were checked for consistency. Shading indicates daytime launches in Table 4.

Table 4. ACMES Model Runs

Model Run Start Date	Model Start Time UTC	Balloon #	Local Launch Date	Local Launch Time	UTC Launch Date	UTC Launch Time
18-Oct-01	00:00	VanFa002	18-Oct-01	20:22	19-Oct-01	3:22
		VanFa003	18-Oct-01	22:08	19-Oct-01	5:08
		VanFa004	19-Oct-01	16:23	19-Oct-01	23:23
19-Oct-01	00:00	VanFa005	19-Oct-01	18:15	20-Oct-01	1:15
		VanFa006	19-Oct-01	20:00	20-Oct-01	3:00
		VanFa007	19-Oct-01	21:44	20-Oct-01	4:44
20-Oct-01	00:00	VanFa008	20-Oct-01	16:20	20-Oct-01	23:20
		VanFa010	20-Oct-01	19:35	21-Oct-01	2:35
		VanFa011	20-Oct-01	21:13	21-Oct-01	4:13
22-Oct-01	00:00	VanFa012	22-Oct-01	18:15	23-Oct-01	1:15
		VanFa013	22-Oct-01	19:54	23-Oct-01	2:54
23-Oct-01	00:00	VanFa015	23-Oct-01	18:14	24-Oct-01	1:14
		VanFa016	23-Oct-01	19:48	24-Oct-01	2:48
		VanFa017	23-Oct-01	21:30	24-Oct-01	4:30
24-Oct-01	00:00	VanFa018	24-Oct-01	18:15	25-Oct-01	1:15
		Vanfa019	24-Oct-01	19:53	25-Oct-01	2:53
25-Oct-01	00:00	VanFa021	25-Oct-01	18:11	26-Oct-01	1:11
		VanFa022	25-Oct-01	19:49	26-Oct-01	2:49

Shading = Daytime Launches

Balloon # = Thermosonde Launch Number

3.5 COAMPS Data Description

The Naval Postgraduate School processed the COAMPS data for this campaign. The C_n^2 output is derived using the mean trajectory of the balloon, using a mean ascent rate for the balloon and following the model's prediction for the balloon position (Walters 2002b). The COAMPS data are processed using a 00Z and 12Z run for each day, so that each launch uses two model output times for comparison as listed in Table 5. There are 47 optical turbulence values for each model output time, corresponding to each level of the model data along the path of the balloon. The shading indicates daytime launches in Table 5.

Table 5. COAMPS Data

Model Run Start Date	Model Start Time UTC	Balloon #	Local Launch Date	Local Launch Time	UTC Launch Date	UTC Launch Time
18-Oct-01	18/12 19/00	VanFa002	18-Oct-01	20:22	19-Oct-01	3:22
		VanFa003	18-Oct-01	22:08	19-Oct-01	5:08
19-Oct-01	19/12 20/00	VanFa004	19-Oct-01	16:23	19-Oct-01	23:23
		VanFa005	19-Oct-01	18:15	20-Oct-01	1:15
		VanFa006	19-Oct-01	20:00	20-Oct-01	3:00
		VanFa007	19-Oct-01	21:44	20-Oct-01	4:44
20-Oct-01	20/12 21/00	VanFa008	20-Oct-01	16:20	20-Oct-01	23:20
		VanFa010	20-Oct-01	19:35	21-Oct-01	2:35
		VanFa011	20-Oct-01	21:13	21-Oct-01	4:13
22-Oct-01	22/12 23/00	VanFa012	22-Oct-01	18:15	23-Oct-01	1:15
		VanFa013	22-Oct-01	19:54	23-Oct-01	2:54
23-Oct-01	23/12 24/00	VanFa015	23-Oct-01	18:14	24-Oct-01	1:14
		VanFa016	23-Oct-01	19:48	24-Oct-01	2:48
		VanFa017	23-Oct-01	21:30	24-Oct-01	4:30
24-Oct-01	24/12 25/00	VanFa018	24-Oct-01	18:15	25-Oct-01	1:15
		Vanfa019	24-Oct-01	19:53	25-Oct-01	2:53
25-Oct-01	25/12 26/00	VanFa021	25-Oct-01	18:11	26-Oct-01	1:11
		VanFa022	25-Oct-01	19:49	26-Oct-01	2:49

Shading = Daytime Launches

Balloon # = Thermosonde Launch Number

3.6 Synoptic Data Description

The NCDC supplied all the observations, charts and satellite images used in this thesis. The University of Wyoming supplied the skew-t data. The surface, 500 mb, 300 mb, 200 mb, water vapor, infrared satellite images, and skew-t diagrams are presented to emphasize optical turbulence areas in this thesis.

IV. Data Analysis

The data analysis compares thermosonde data and model data in layers to approximate the horizontal layers that the ABL might encounter in the atmosphere. Based on visual inspection, most of the thermosonde data and model data values were below 2 X CLEAR I values.

4.1 Binning Data

The ABL is tasked with projecting a laser beam along a horizontal path up to hundreds of kilometers in the atmosphere. Dr. Frank Ruggiero of AFRL developed a method of integrating thermosonde data and comparing these data to model data in layers. All data sets are vertically path integrated in 500 m layers to compute a mean layer value based on the “onion skin” model of the atmosphere. The other model data sets were matched to the resolution of the thermosonde data for similar comparisons.

4.2 Thermosonde Data

The thermosonde data were taken from the surface up to approximately 30 km. Thermosonde data were binned from the surface in 500 m increments and a mean value is taken from the entire layer including the top and bottom of the layer. In the thermosonde output, there are no values at exactly 500 m, 1000 m, etc. so these values are linearly interpolated using the nearest two values. This was accomplished for all 18 launches used in this thesis. The u and v wind components from the thermosonde data were used to determine the latitude and longitude of the balloon as it traveled along a path during its ascent. These latitude and longitude points at each 500 m level are used for horizontal

spatial interpolation of the gridded model output. A mean ascent rate for each launch was calculated using the start and end times of each balloon launch.

Each thermosonde launch traversed a horizontal distance of 45-55 km from west to east. The entire launch trajectory covered a period of approximately 2 hours and the time for the balloon to travel each 500 m increment was approximately between 90-100 seconds. All thermosonde comparisons are in Appendix A.

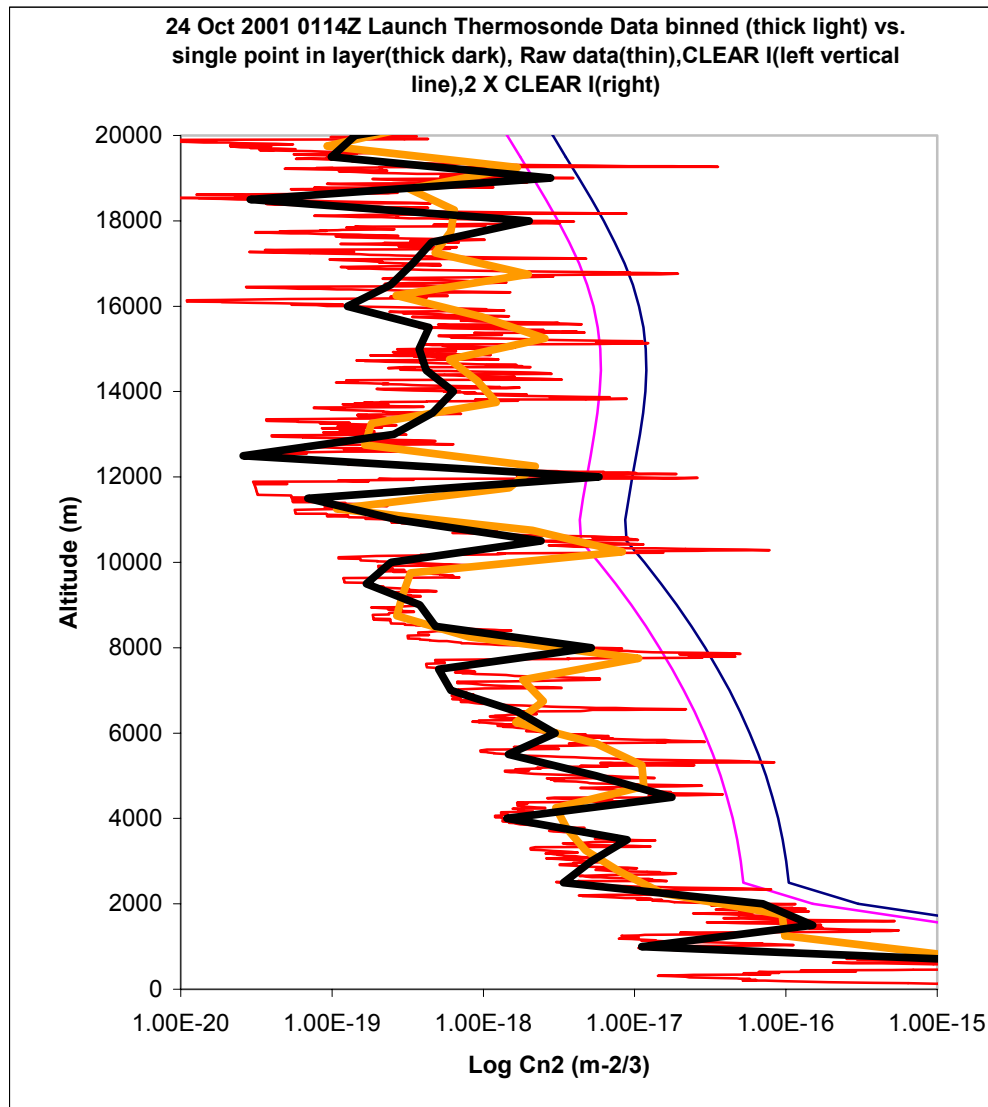


Figure 10. Example layered mean vs. single point in layer

4.3 MM5 Data

The MM5 data are linearly interpolated in space and time from the model grid points to the balloon trajectory points, using the vertically path integrated data. The appropriate model runs included the model output valid time before launch and model output valid time after launch for linear interpolation. The forecast length of the model data used was 24-hours.

These integrated model output data sets were then used to interpolate through time, starting with the initial launch time and using the end of the launch time to calculate a constant rate of ascent. The constant rate of ascent was used to determine which model output valid times were necessary for the temporal interpolation, so that the times between successive levels approximately matched those of the actual balloon flight as depicted in Figure 11.

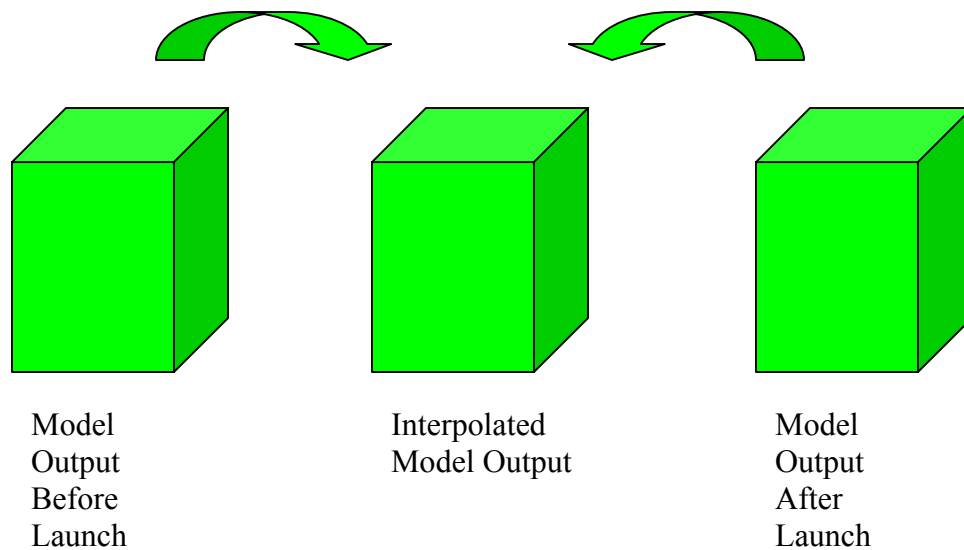


Figure 11. Model Output Interpolation Diagram

After temporal interpolation was completed, spatial interpolation was used on the interpolated model output. An average latitude and longitude was computed for each grid box in the model and the nearest neighbor method was employed to determine which values in the model were closest to the observed latitude and longitude values. Once this was accomplished, inverse distance weighted interpolation was used to determine a value for optical turbulence, temperature, and pressure at that point in the model to be compared with observed values from the thermosonde and 2 X CLEAR I.

For each of the eighteen launches, up to three model output valid times were binned for the MM5 data. From these three model output times an interpolated model output time was produced. This interpolated model output time was used to compute a domain average for C_n^2 and a weighted value of C_n^2 matched to the latitude and longitude of the thermosonde trajectory. A total of 54 model output valid times were produced.

Since the ABL is tasked with projecting laser-beams along quasi-horizontal paths long distances in the atmosphere, it was decided to see how the mean of the entire model domain would compare to the CLEAR I and 2 X CLEAR I profiles. An example of this profile is in Figure 12. All model domain profiles are in Appendix A.

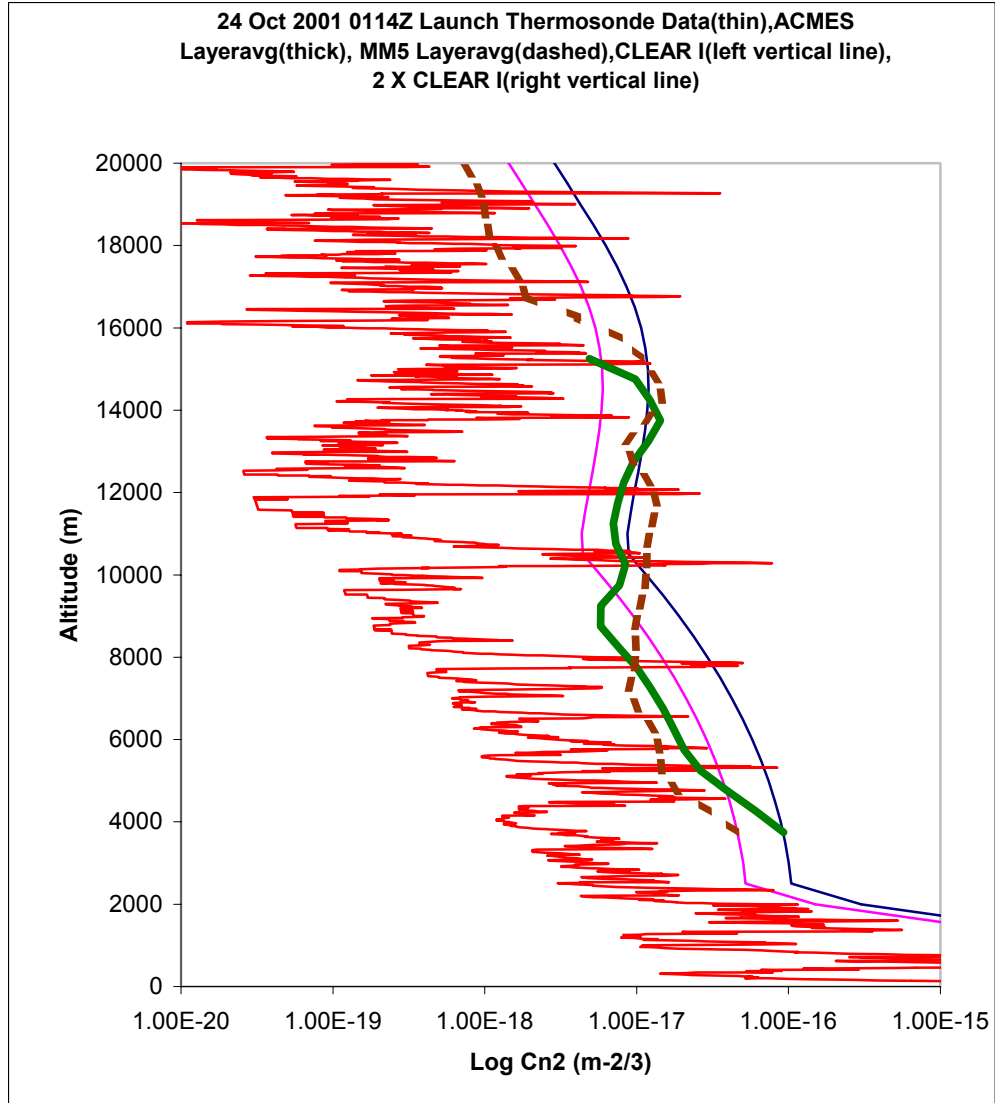


Figure 12. Entire Domain profile of Modeled Output

The domain averages seem to encompass most of the C_n^2 structure for most of the model output valid times based on visual inspection. This domain averaging may be another way to predict the overall structure of optical turbulence for large regions of the atmosphere. The domain averages were computed above all terrain features up to where the model data stopped. The domain covers a vast area of typically 9 degrees by 11

degrees or 1.2 million square km. These domain averages seem to encompass most of the higher values of C_n^2 compared to the thermosonde profiles.

4.4 ACMES Data

The same methods that were used on the MM5 model runs were used on the ACMES model runs. The exceptions are that the ACMES model run output was not at 500 m increment levels. These data had to be vertically path integrated and were done using the same method as used for the thermosonde data. Once binning was accomplished, temporal interpolation was completed using the same method as for the MM5 data. The ACMES model output valid times are produced every hour, so successive model output times had to be incorporated for an accurate linear temporal interpolation. The interpolation of ACMES data required up to four model output valid times per launch for a total of 72 model output data sets. Linear interpolation was then accomplished using these model output valid times. A domain average of the ACMES model output valid times was also computed for comparison. A weighted value for temperature, pressure, and C_n^2 was then computed using inverse distance weighted interpolation along the path of the actual thermosonde data. The path in the model was calculated using the latitude and longitude data from the thermosonde trajectory. These data have 31 levels up to 17 km and the other models are compared using these same levels.

4.5 COAMPS Data

The Naval Postgraduate School (NPS) supplied the COAMPS model output. The complete model runs were not available for this research, but the optical turbulence values along the path of the thermosonde computed by NPS are used for comparison. These model output valid times follow the mean path of the balloon, by using a mean ascent rate for the balloon and following the model's prediction for the balloon position (Walters 2002b).

The data have C_n^2 values for the 47 vertical levels in the model along the balloon path for both the 00Z and 12Z model runs. The COAMPS model output is not in 500 m increments and is binned using the same method as the thermosonde data for comparison. The COAMPS data are not interpolated through time, because there was only one output time. The COAMPS model output valid time closest to the balloon launch was used for comparison. In the absence of complete COAMPS model runs, temporal interpolation was not possible for this thesis.

4.6 CLEAR I

The equations used for the CLEAR I (White et. al. 1985) profile are from the IR/EO handbook (Beland 1993). These equations are computed at 500 m increments up to 30 km. Twice CLEAR I defines 2 X CLEAR I. Twice CLEAR I is the standard in the GAO report (GAO 1997) for the ABL environment, so it was added to the vertical profile plots for comparative purposes. All the data sets are binned in 500 m increments and compared to 2 X CLEAR I, to see how they match up to the established standard. An example of the CLEAR I and 2 X CLEAR I profile can be seen in Figure 13.

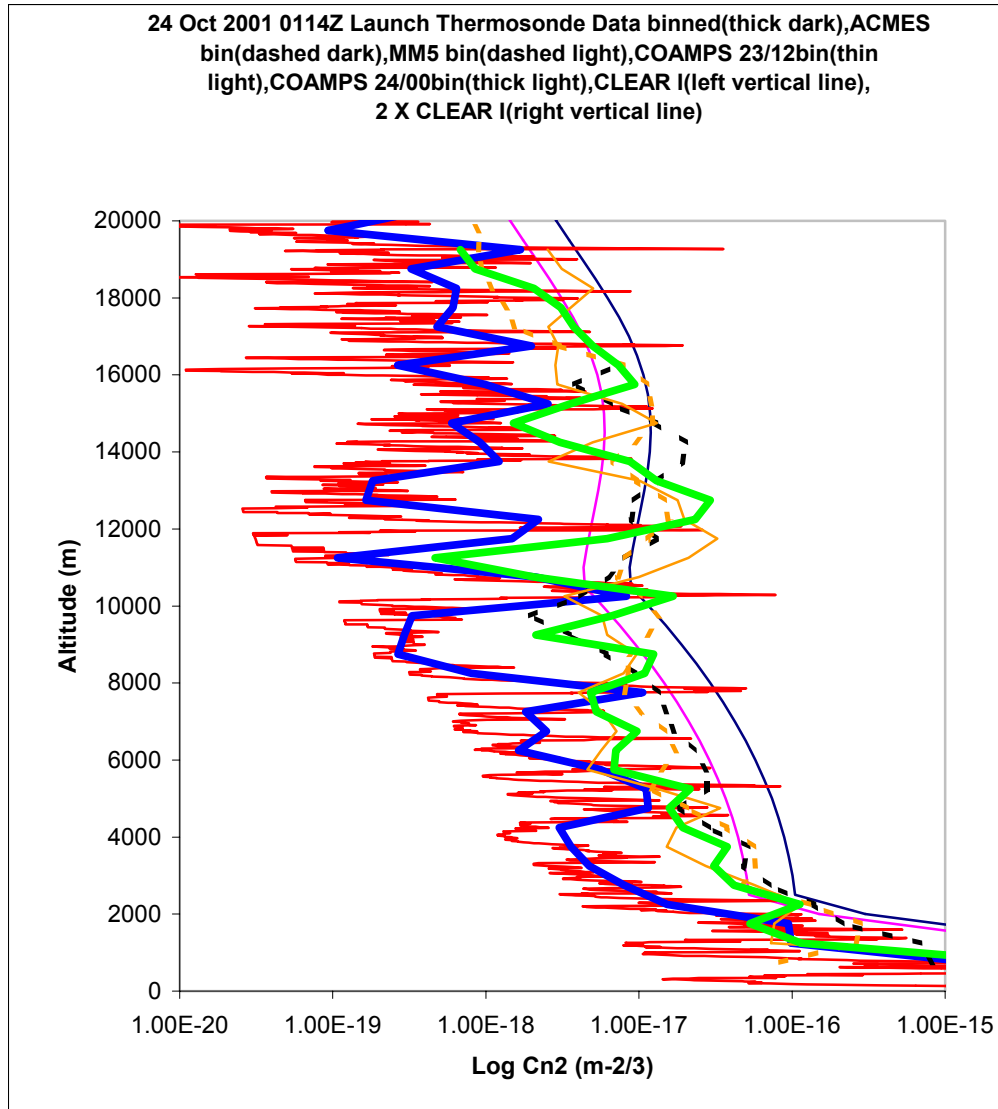


Figure 13. Example of binned data for all models vs. thermosonde and 2 X CLEAR I

Potential temperatures for all models were also profiled to see how consistent they were. An example of a temperature comparison is shown in Figure 14 and some are also in Appendix A for selected cases. Most of the model-produced temperature profiles appear to map very closely to the actual temperature profile from the thermosonde launches.

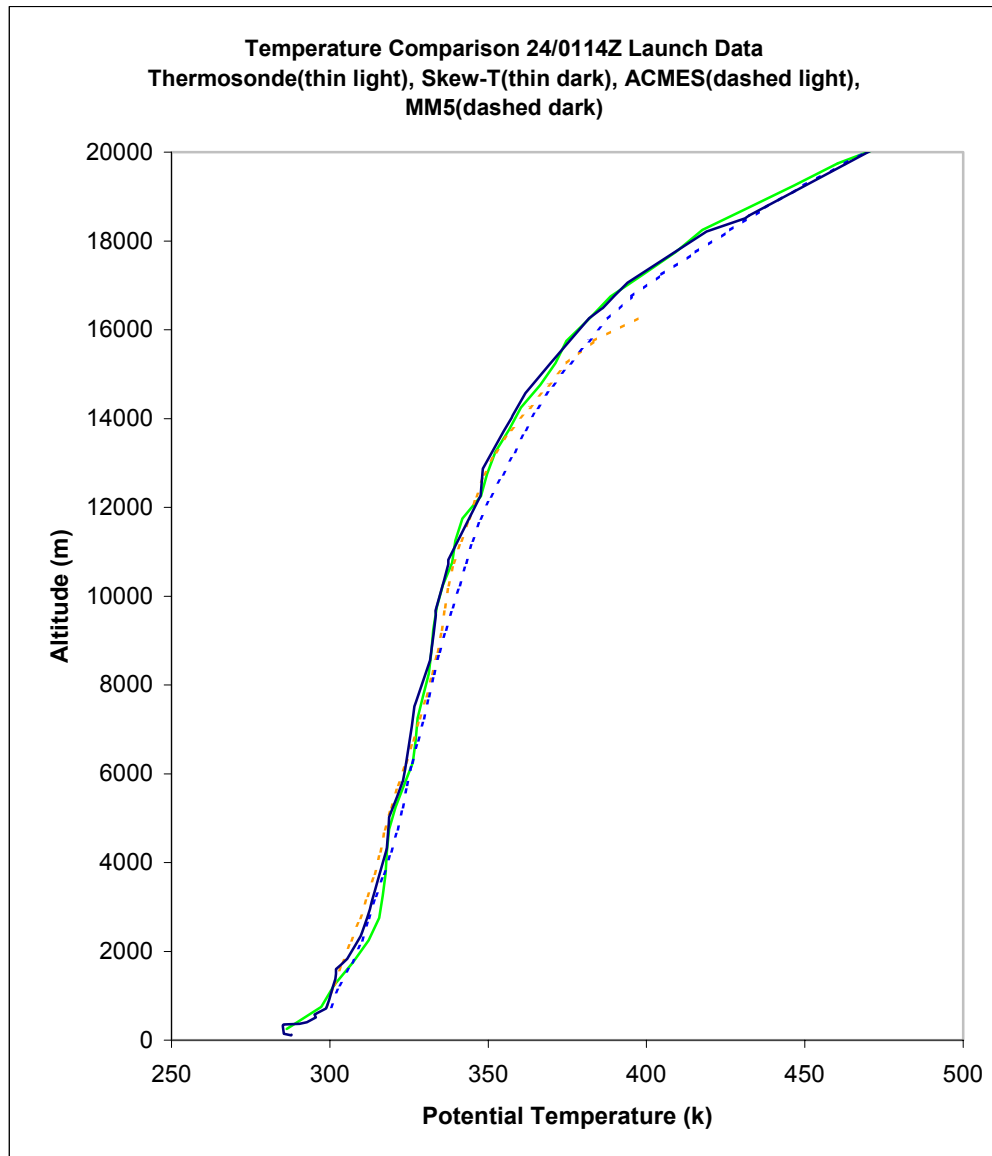


Figure 14. Temperature profiles for 24/0114Z Launch

4.7 Synoptic Analysis

Thermosonde measurements were taken from 18 October 2001 – 25 October 2001 at Vandenberg AFB, California. Weather reanalysis data from the National Climatic Data Center (NCDC) displays the surface, 500 mb, 300 mb, 200 mb, charts and satellite images for selected times of this campaign in Appendix A. Skew-t

profiles for these selected time periods were also be used from the University of Wyoming's website (UW 2002). Synoptic charts were used to highlight features that have been documented in previous works to indicate a relationship between synoptic features and high optical turbulence values, such as the boundary layer, jet streams and the tropopause.

The weather for this campaign was relatively uneventful. There was no precipitation recorded for the entire period of the campaign at Vandenberg AFB, California. The time period for this campaign was characterized by a strong jet stream between 21/00Z and 23/00Z (Roadcap et al. 2001). After this jet stream event the weather pattern became very zonal and benign for the remainder of the campaign.

The overall surface weather pattern began with an inverted trough to the east of Vandenberg AFB, California. This inverted trough extends from the S. California/Arizona border region northward up through the interior of California ending near the San Francisco area. No surface frontal systems moved through the launch area for the entire campaign. The inverted trough is illustrated in Figure 15.

The 500 mb chart shown in Figure 16 indicates a low pressure trough off the west coast of California and the influence of a high pressure center to the south of Vandenberg AFB, California prior to the start of this campaign. A weak high-pressure ridge was evident through the 21/00Z time period at 500 mb. A weak trough began to emerge at 21/12Z reaching its maximum extent on 22/12Z. Beginning on 23/00Z zonal flow became more pronounced as high pressure began to dominate at this level for the remainder of the campaign.

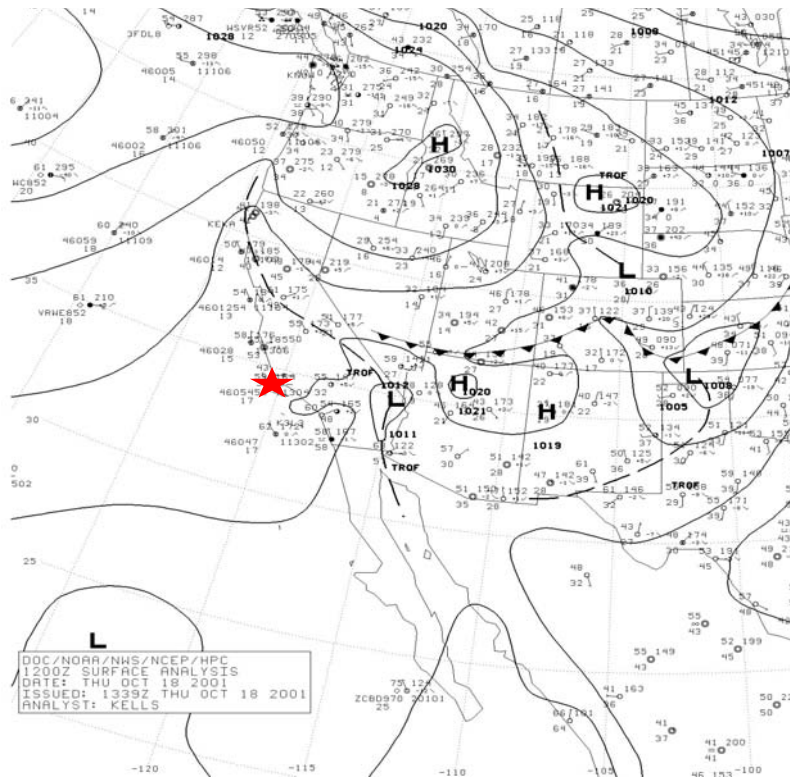


Figure 15. Surface Weather Chart for 12Z 18 Oct 01 [Adapted from NCDC 2001]

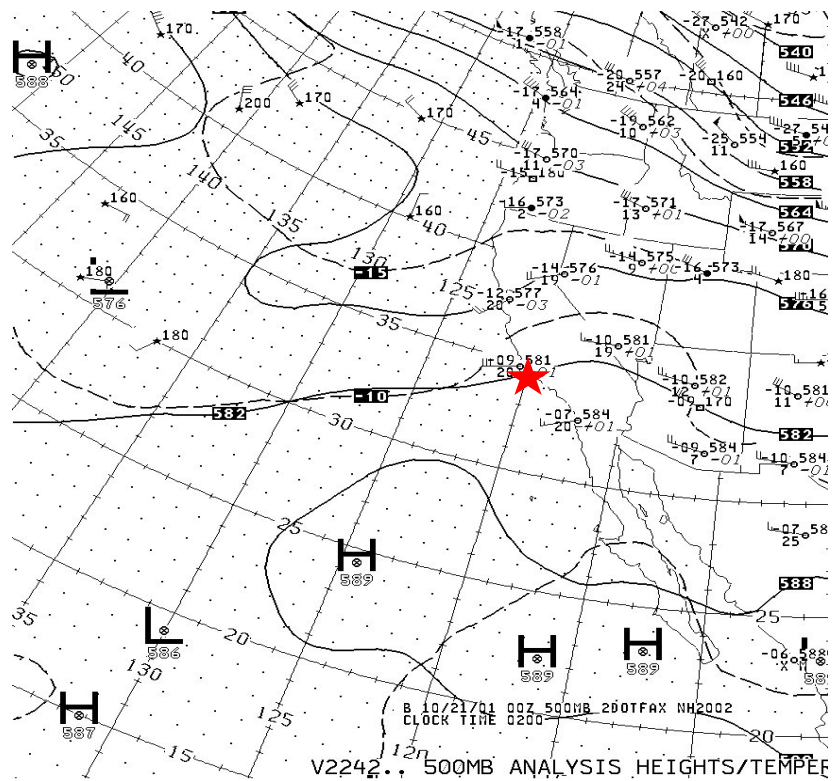


Figure 16. 00Z 21 Oct 01 500 mb analysis chart [Adapted from NCDC 2001]

The 300 mb and 200 mb charts shown in Figures 17 and 18 respectively, indicate the influence of the jet stream prior to the first launch. A persistent low pressure center is indicated off the west coast upstream of California. A ridge of high pressure is also evident, centered over California reaching its maximum extent on 19/12Z. The ridge maximum is more evident on the 200 mb chart Figure 17, and weaker on the 300 mb chart Figure 18.

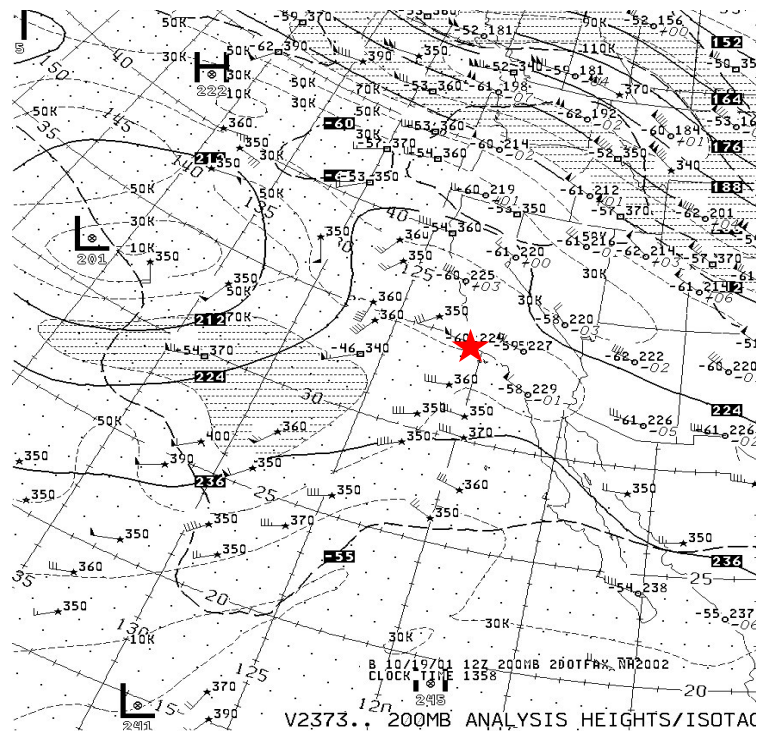


Figure 17. 12Z 200 mb 19 Oct 01 chart [Adapted from NCDC 2001]

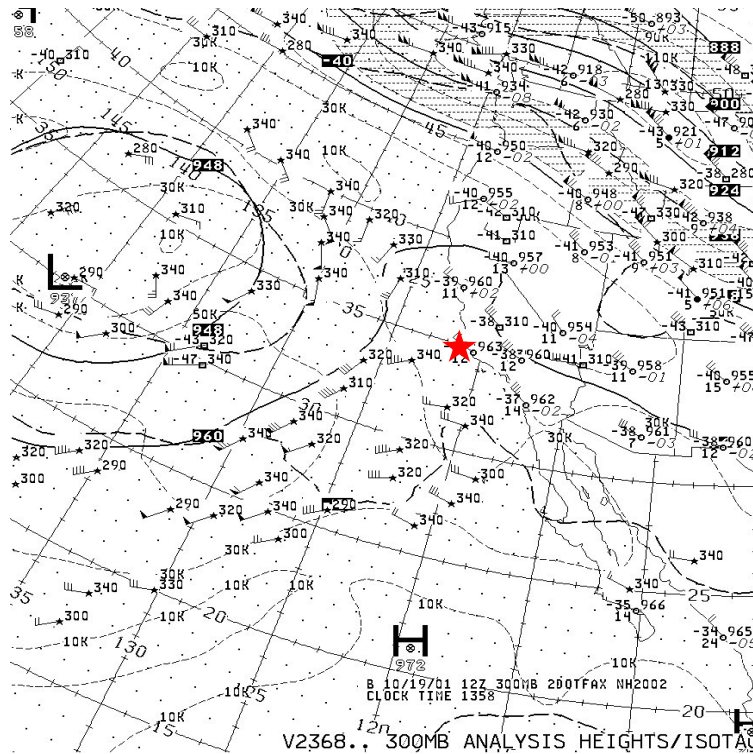


Figure 18. 12Z 300 mb 19 Oct 01 chart [Adapted from NCDC 2001]

As the ridge over California begins to weaken, a surge in jet stream strength is noticeable over the Pacific Ocean moving inland on 20/12Z. At 21/12Z the jet maximum is firmly in-place over Vandenberg AFB, California at both 300 mb, Figure 19, and 200 mb, Figure 20. The influence of this jet streak is dominant until 22/12Z, at which time it moves southward and eastward at both levels. High pressure becomes the main influence on the weather beginning at 23/00Z, with a strong ridge firmly in place by the end of the campaign.

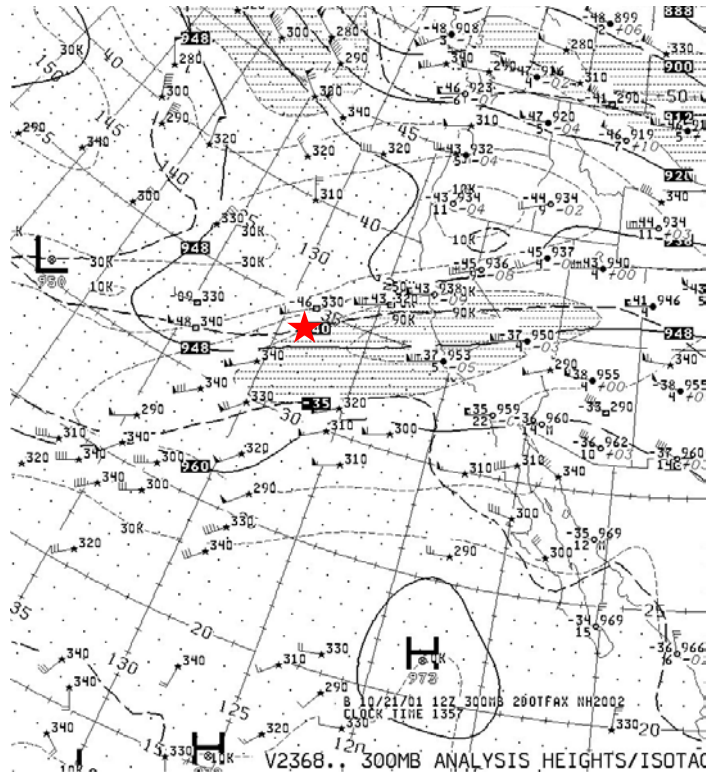


Figure 19. 12Z 300 mb 21 October 2001 chart [Adapted from NCDC 2001]

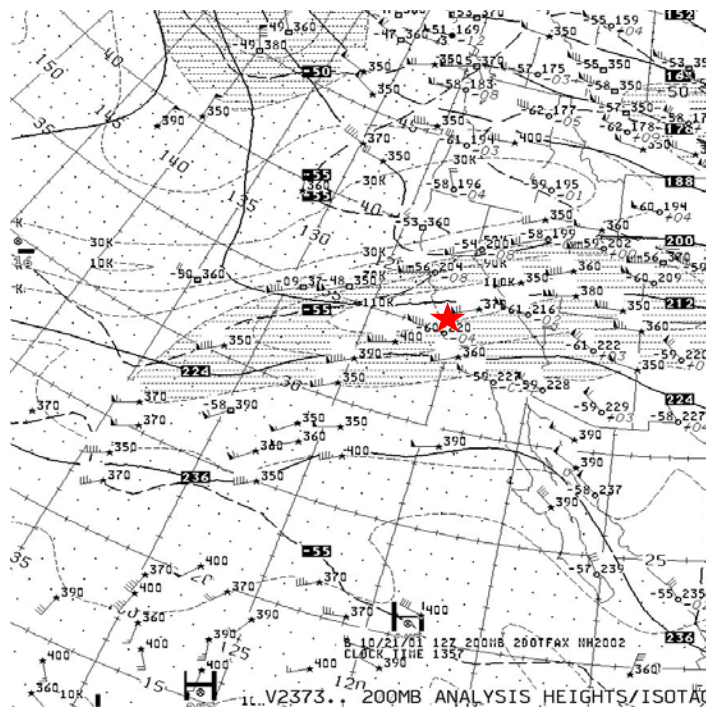


Figure 20. 12Z 200 mb chart 21 October 2001 [Adapted from NCDC 2001]

Comparisons between the thermosonde profiles for the same 0-6 hour time period were checked to see if the profiles were similar. Based on visual inspection the overall thermosonde profiles appeared similar. These thermosonde comparisons would be expected to depict overall equivalent vertical profiles for the same time period due to similar meteorological conditions. Thermosonde comparisons give an indication of how sensitive the instrumentation is to fluctuations within the atmosphere for the same time

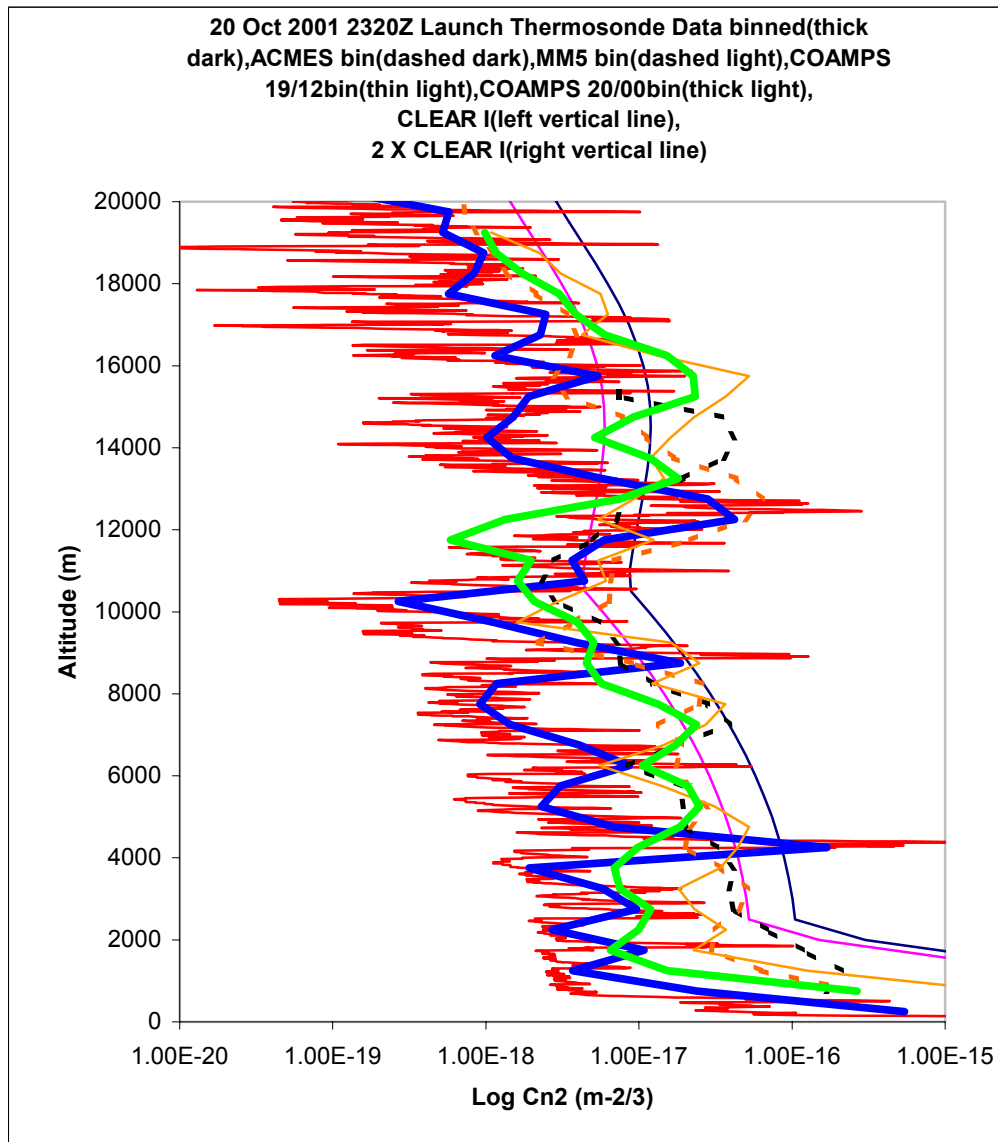


Figure 21. Thermosonde profile with model comparisons for 20 October 2001 for 2320Z Launch

period. Profiles for the 20/2320Z and 21/0235Z launches are in Figures 21 and 22.

Thermosonde observations indicate a noticeable increase in optical turbulence between 12 km and 14 km between 21/00Z and 24/00Z, which coincides with the enhanced jet stream activity and decreasing after this time period.

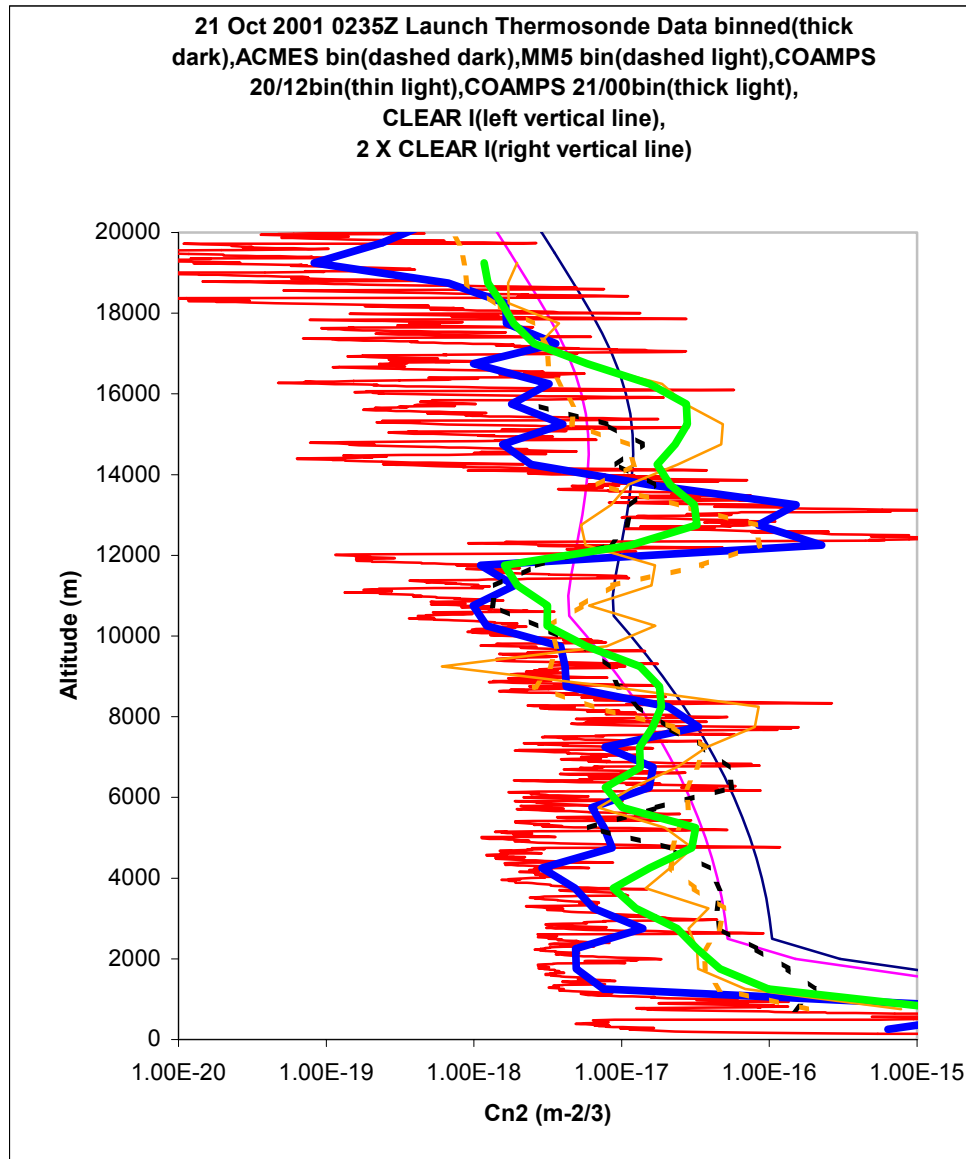


Figure 22. Thermosonde profile with model comparisons for 21/0235Z Launch

Tropopause heights, inversions and winds are indicated on the skew-t profile, and these features are looked at to see if they can help explain the structure in the vertical profiles of C_n^2 . The skew-t profiles for this campaign indicate an increase from 51 kt winds at 130 mb and 51 kts at 250 mb on 00Z, 20 October 2001. The winds increase to a maximum of 71 kts by 12Z, 20 October 2001 at 220 mb. Skew-t profiles indicate the winds progressively increase to 101 kts by 00Z on 22 October 2001 as shown in Figure 23. See Appendix A for selected skew-t profiles.

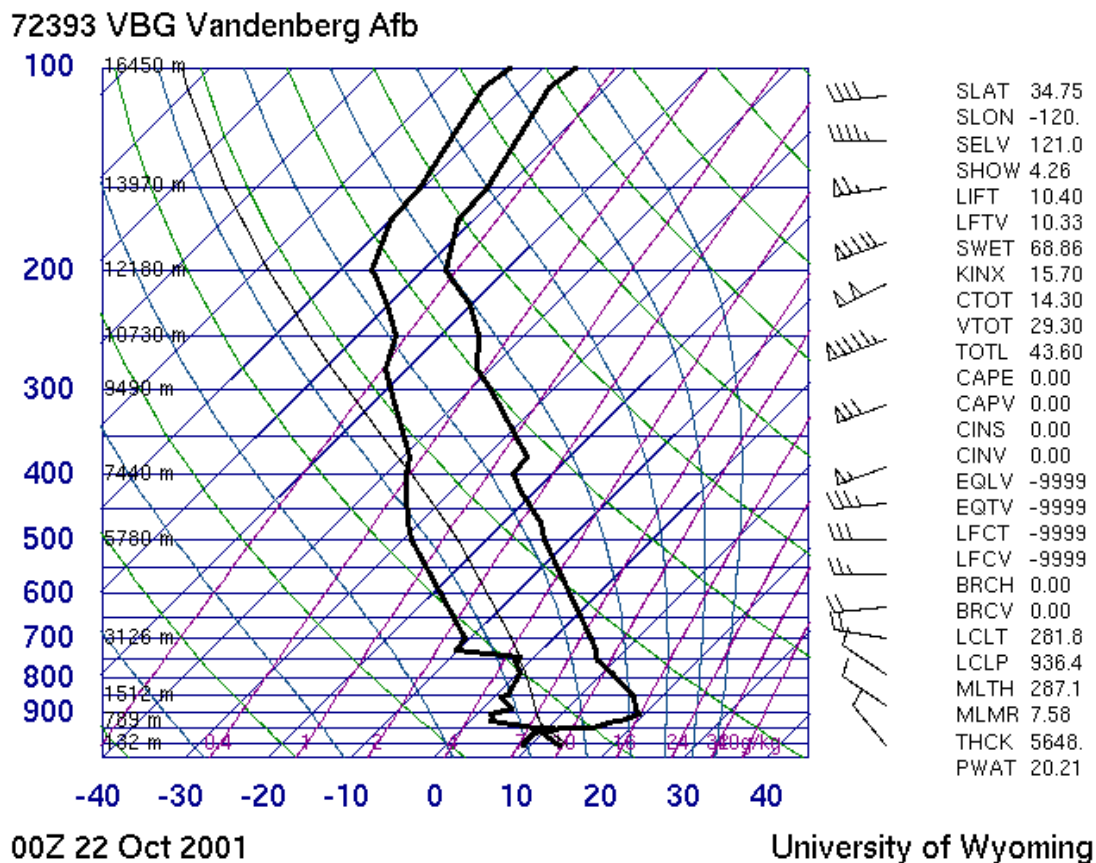


Figure 23. Skew-T profile for Vandenberg AFB, CA. at 00Z on 22 Oct 01 [Adapted from UW 2002]

Infrared satellite imagery and water vapor imagery show an upper level low pressure system off the west coast of the California with an embedded vorticity maximum developing by 12Z on 19 October 2001. Figure 24 shows the influence of this upper level low pressure system. The intensity of the low depicted in Figure 24 corresponds with the upper level cyclone reaching its lowest pressure as indicated on the 500 mb chart for 12Z on 19 October 2001.

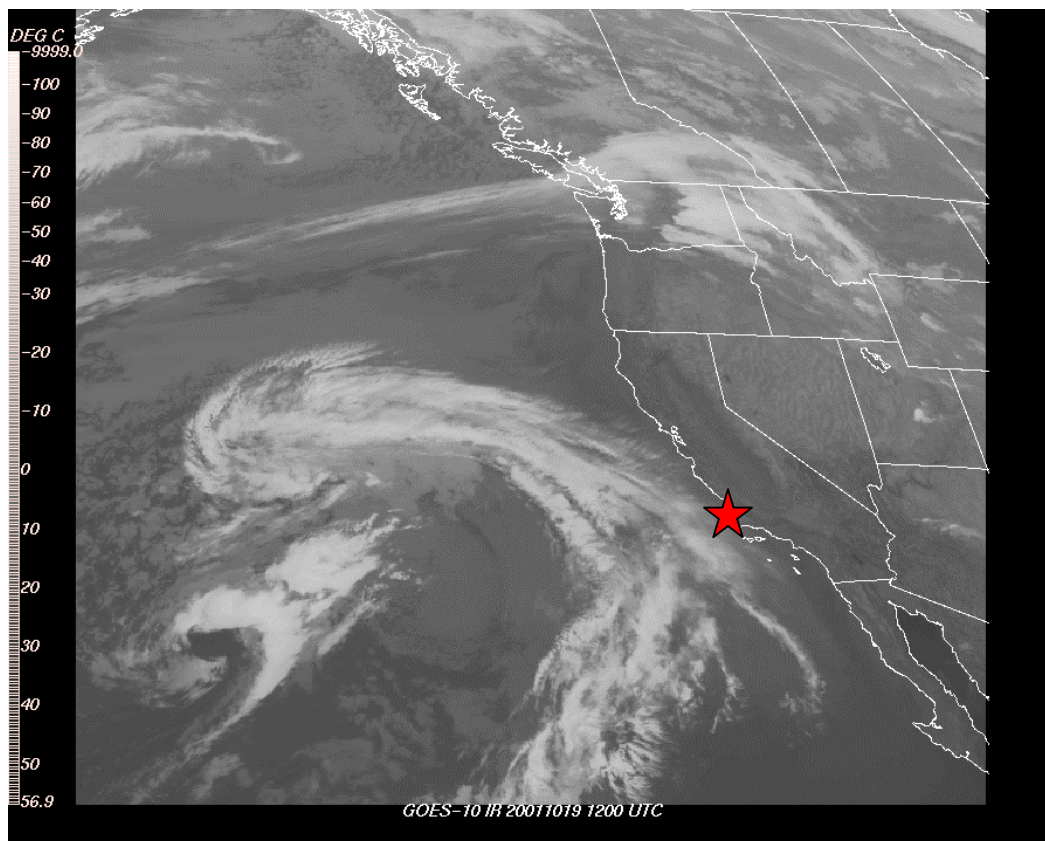


Figure 24. Infrared Satellite image of Low pressure system off the west coast 12Z 19 October 2001
[Adapted from NCDC 2001]

Water vapor imagery also highlights these same features and accentuates the locations of the jet stream in Figure 25. These features helped bring the strong jet stream winds into S. California by 00Z on 22 October 2001. Again, after this period the satellite imagery shows no significant features for the duration of the campaign.

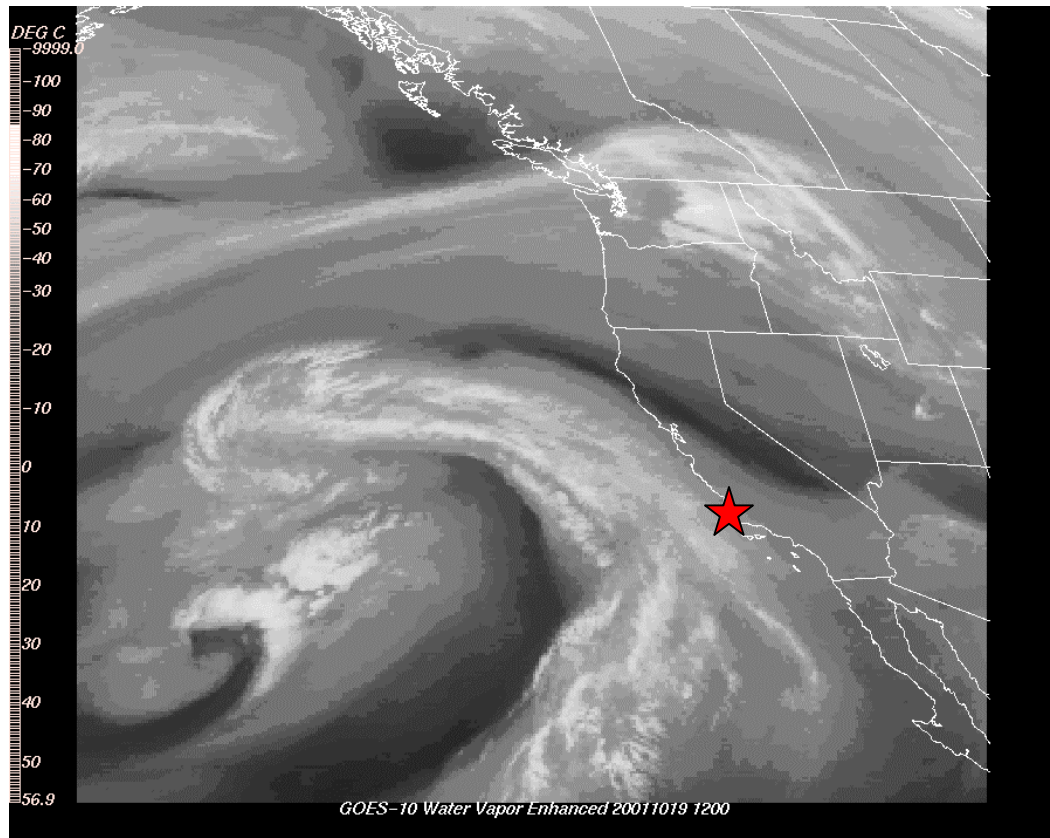


Figure 25. Water vapor image of low pressure system of west coast of U.S. 12Z 19 October 2001
[Adapted from NCDC 2001]

V. Statistical Analysis

5.1 Objective Metrics

The statistical analyses presented here were conducted using objective metrics. The C_n^2 values derived based on output from the MM5, ACMES, and COAMPS models were compared to observed thermosonde output and 2 X CLEAR I. The mean values of equivalent 500 m layers were compared (Devore 2000).

The mean absolute error (MAE) is a measure of accuracy, which measures the arithmetic average of the absolute values of the differences between the members of each pair of equivalent observed and forecasted values. If the forecasted model values are perfect then the MAE is zero (Wilks 1995). MAE is described by

$$\text{MAE} = \frac{1}{n} \sum_{k=1}^n |y_k - o_k|, \quad (20)$$

where y_k is the k th forecast point, and o_k is the k th observation point. The results of these comparisons are listed in Table 6. MAE for the COAMPS 3-hour data suggests that it's more accurate than the other models. The COAMPS 15-hour data indicate it's statistically more accurate than the MM5 data and ACMES data. The ACMES 3-hour data results indicate it's overall more accurate than the MM5 15-hour data. No ACMES 15-hour forecasts or MM5 3-hour forecasts were available for this thesis.

Table 6. Mean Absolute Error (MAE)

Launch	ACMES 3-hr	MM5 15-hr	COAMPS 15-hr	COAMPS 3-hr
19/0322Z	1.460	1.152	1.105	1.034
19/0508Z	1.377	1.464	1.184	0.912
19/2323Z	1.092	1.170	0.904	0.795
20/0115Z	1.398	1.344	1.166	
20/0300Z	1.619	1.759	1.820	1.252
20/0444Z	1.584	1.548	1.593	1.089
20/2320Z	1.867	1.699	1.852	1.565
21/0235Z	1.433	1.339	1.728	1.210
21/0413Z	1.381	1.648	1.628	1.675
23/0115Z	1.560	1.680	1.436	1.210
23/0254Z	2.298	2.373	1.936	1.288
24/0114Z	2.101	2.194	1.896	1.691
24/0248Z	1.699	1.828	1.601	1.245
24/0430Z	1.786	1.808	1.469	1.465
25/0115Z	1.229	2.108	2.079	1.502
25/0253Z	1.138	1.688	1.555	1.195
26/0111Z	1.992	1.848	1.688	1.077
26/0249Z	2.196	2.262	1.975	1.670

Launch = Thermosonde Launch date and time

Shading = Best score among all comparisons

The mean squared error (MSE), which is another measure of accuracy, was also computed. The mean squared error is also a measure of the variance. The MSE is computed by taking the averaged squared difference between the forecast and observation pairs. MSE increases from zero for perfect forecasts to larger positive values as the discrepancies between the forecasts and observed values become increasingly large. The COAMPS 3-hour data suggests that it has the least MSE among the models. The COAMPS 15-hour data indicates overall more accuracy than the ACMES 3-hour and MM5 15-hour data. The ACMES 3-hour data has the least MSE on two occasions. The MM5 15-hour data indicated the least MSE results on one occasion.

Forecasted values that are highly correlated to observed values will have a lower MSE. The correlation between the models and observations reflects a linear association, but does not account for biases that may be present in the forecasts (Wilks 1995). MSE is described by

$$\text{MSE} = \frac{1}{n} \sum_{k=1}^n (y_k - o_k)^2. \quad (21)$$

The square root of MSE was computed and is shown in Table 7.

Table 7. Root Mean Square Error (RMSE)

Launch	ACMES 3-hr	MM5 15-hr	COAMPS 15-hr	COAMPS 3-hr
19/0322Z	1.842	1.281	1.446	1.313
19/0508Z	1.872	1.653	1.560	1.057
19/2323Z	1.418	1.370	1.170	0.941
20/0115Z	1.799	1.726	1.455	
20/0300Z	1.932	1.951	2.155	1.483
20/0444Z	1.854	1.849	1.881	1.330
20/2320Z	2.167	1.927	2.157	1.775
21/0235Z	1.789	1.581	1.965	1.464
21/0413Z	1.721	1.957	1.914	2.027
23/0115Z	1.758	1.995	1.843	1.551
23/0254Z	2.429	2.611	2.254	1.531
24/0114Z	2.358	2.485	2.274	2.084
24/0248Z	1.889	2.035	1.857	1.559
24/0430Z	2.023	2.020	1.809	1.762
25/0115Z	1.664	2.403	2.369	1.783
25/0253Z	1.515	2.026	1.877	1.447
26/0111Z	2.194	2.063	1.971	1.315
26/0249Z	2.469	2.478	2.272	1.938

Launch = Thermosonde Launch date and time

Shading = Best score among all comparisons

The mean error (ME) is also computed and is shown in Table 8. The mean error is the difference between the average forecast and average observation, thus expressing the bias of the forecast. Forecasts that are too high will have a ME greater than zero, and

forecasts that are too low will have a ME less than zero. The ME gives no information about the typical magnitude of individual forecast errors, and is not a measure of accuracy (Wilks 1995). ME is described by

$$ME = \frac{1}{n} \sum_{k=1}^n (y_k - o_k) . \quad (22)$$

Table 8. Mean Error (ME)

Launch	ACMES-3hr	MM5 15-hr	COAMPS 15-hr	COAMPS 3-hr
19/0322Z	-1.185	0.935	0.554	0.635
19/0508Z	-0.673	1.204	0.972	0.564
19/2323Z	0.778	0.486	0.484	-0.075
20/0115Z	0.776	0.799	0.563	
20/0300Z	1.513	1.662	1.515	0.882
20/0444Z	1.030	1.299	1.442	0.456
20/2320Z	1.433	1.432	1.532	0.695
21/0235Z	0.579	0.718	0.835	0.663
21/0413Z	1.330	1.439	1.479	1.452
23/0115Z	1.266	1.518	0.923	0.195
23/0254Z	2.067	2.298	1.778	0.986
24/0114Z	2.021	1.996	1.732	1.604
24/0248Z	1.350	1.352	1.089	0.625
24/0430Z	1.538	1.580	1.318	1.278
25/0115Z	0.087	2.043	2.014	1.252
25/0253Z	-0.420	1.630	1.269	0.996
26/0111Z	1.801	1.829	1.571	0.592
26/0249Z	2.181	2.199	1.844	1.543

Launch = Thermosonde Launch date and time

Shading = Best score among all comparisons

ME for the data sets indicate that the ACMES model under-forecasts on three occasions, whereas the other three models consistently over-forecast optical turbulence. The ACMES model indicates a bias towards over-forecasting. The COAMPS 3-hour data suggests that it has the least amount of bias compared to the other models. The

COAMPS 15-hour data indicates it has the least amount of bias overall when compared to the MM5 15-hour data and the ACMES 3-hour data. The ACMES 3-hour data had the best ME scores on four occasions. The MM5 15-hour data had the highest bias of these models based on a computed average value. The bias of each of these models is statistically different from zero and positive.

Correlations were calculated using the Pearson product-moment correlation coefficient, which measures the strength of the linear relationship between two variables. A perfect positive correlation between two variables has a value of one and a perfect negative correlation is expressed by a value of negative one. High correlation doesn't imply high accuracy, and accurate results don't imply high correlations. Correlations are shown in Table 9. All models show a positive correlation with the observed data. All models show comparable results.

$$Corr = \frac{\sum_{i=1}^n (x_i - \bar{x})(y_i - \bar{y})}{\sqrt{\sum_{i=1}^n (x_i - \bar{x})^2} \sqrt{\sum_{i=1}^n (y_i - \bar{y})^2}} \quad (23)$$

The 3-hour COAMPS data had the best scores based on objective metrics using ME, MAE, and MSE when compared to the other models. The 3-hour ACMES, 15-hour MM5, and 15-hour COAMPS models were all comparable based on objective metrics.

Table 9. Correlations

Launch	ACMES 3-hr	MM5 15-hr	COAMPS 15-hr	COAMPS 3-hr
19/0322Z	0.5648	0.7674	0.5390	0.6580
19/0508Z	0.4552	0.6685	0.6502	0.8538
19/2323Z	0.3465	0.4112	0.5869	0.3713
20/0115Z	0.2876	0.3446	0.5582	
20/0300Z	0.5448	0.6306	0.3367	0.5862
20/0444Z	0.5292	0.7133	0.7354	0.7151
20/2320Z	0.1079	0.3983	0.2833	0.0794
21/0235Z	0.4308	0.6118	0.3271	0.6756
21/0413Z	0.6840	0.4704	0.5682	0.4452
23/0115Z	0.6427	0.5780	0.4450	0.4481
23/0254Z	0.5088	0.5396	0.5115	0.6845
24/0114Z	0.8089	0.7146	0.6877	0.7536
24/0248Z	0.6857	0.5420	0.5938	0.6260
24/0430Z	0.6260	0.6567	0.6830	0.6876
25/0115Z	0.4970	0.6706	0.7067	0.6625
25/0253Z	0.5208	0.6105	0.6386	0.6818
26/0111Z	0.5986	0.7199	0.6264	0.5563
26/0249Z	0.6007	0.5110	0.5940	0.5198

Launch = Thermosonde Launch date and time
Shading = Best score among all comparisons

5.2 Contingency Tables

Contingency tables were also produced for this thesis, and they are summarized in Table 10. Contingency tables require categorical forecasts. CLEAR I and 2 X CLEAR I were chosen as reference values. Model data and thermosonde data values greater than 2 X CLEAR I and CLEAR I were compared. The model and thermosonde comparisons for contingency tables were calculated for the same profile or layers, the same layers above the boundary level, and the same layers above flight level (40,000 ft). The boundary level is defined here as 3 km. All contingency tables were 2 X 2.

The null hypothesis for the contingency tables was a test of independence between observations and forecasts or to test that an observation occurring in row i is independent of that same observation occurring in column j for all i and j . Chi-squared tests were conducted on all contingency tables using one degree of freedom, and an alpha level of .05 to test the significance of the tables. Chi-squared tests yielded values much larger than 3.84, which was the critical value for this test with one degree of freedom. P-values for all contingency tables indicated strong evidence to reject the null hypothesis. The Fisher exact test was also conducted for each contingency table because some of the cell counts were very small or zero. Fisher exact tests compute the exact probability, given the observed marginal frequencies, of obtaining exactly the frequencies observed and any configuration with a smaller probability of occurrence in the same direction (Conover 1980). For this thesis same direction implies a one-tailed test, in the yes-yes or no-no direction, for a correct forecast. All Fisher exact test results were statistically significant.

Various parameters were calculated using the contingency tables as seen in Figure 10. They include hit rate, threat score, probability of detection, false alarm rate, Heidke skill score, and bias. Hit rate (HR) is the fraction of forecasting occasions when the categorical forecasts correctly anticipated the event or non-event. The best possible hit rate is one and the worst possible hit rate is zero. The threat score (TS) or critical success index is the number of correct “yes” forecasts divided by the total number of occasions on which that event was forecast and /or observed. The best possible threat score is one and the worst possible threat score is zero. The probability of detection (POD) is the fraction of those occasions when the forecast event occurred on which it was also

Table 10. Contingency Table Results

	HR	TS	POD	FAR	HSS	BIAS
ACMES 3hr > 2 X CLEAR I	0.873	0.237	0.733	0.741	0.329	2.833
MM5 15hr > 2 X CLEAR I	0.808	0.164	0.700	0.824	0.214	3.967
COAMPS 15hr > 2 X CLEAR I	0.815	0.202	0.867	0.792	0.272	4.167
COAMPS 3hr > 2 X CLEAR I	0.918	0.313	0.700	0.638	0.437	1.933
ACMES Lyravg > 2 X CLEAR I	0.907	0.245	0.481	0.667	0.346	1.444
MM5 Lyravg > 2 X CLEAR I	0.752	0.151	0.655	0.836	0.173	4.000
ACMES 3hr > CLEAR I	0.740	0.289	1.000	0.711	0.340	3.458
MM5 15hr > CLEAR I	0.638	0.223	0.983	0.776	0.233	4.390
COAMPS 15hr > CLEAR I	0.715	0.260	0.949	0.736	0.297	3.593
COAMPS 3hr > CLEAR I	0.835	0.338	0.797	0.630	0.422	
ACMES Lyravg > CLEAR I	0.734	0.315	0.898	0.673	0.349	2.746
MM5 Lyravg > CLEAR I	0.623	0.238	0.879	0.754	0.222	3.569
ACMES 3hr > 2 X CLEAR I bdry lvl	0.871	0.275	0.733	0.694	0.372	2.400
MM5 15hr > 2 X CLEAR I bdry lvl	0.762	0.164	0.700	0.824	0.196	3.967
COAMPS 15hr > 2 X CLEAR I bdry lvl	0.771	0.202	0.867	0.792	0.255	4.167
COAMPS 3hr > 2 X CLEAR I bdry lvl	0.898	0.313	0.700	0.638	0.427	1.933
ACMES 3hr > CLEAR I bdry lvl	0.753	0.347	1.000	0.653	0.398	2.881
MM5 15hr > CLEAR I bdry lvl	0.604	0.246	0.983	0.753	0.234	3.983
COAMPS 15hr > CLEAR I bdry lvl	0.647	0.260	0.949	0.736	0.262	3.593
COAMPS 3hr > CLEAR I bdry lvl	0.809	0.363	0.831	0.608	0.431	2.119
ACMES 3hr > 2 X CLEAR I flight lvl	0.744	0.258	1.000	0.742	0.313	3.875
MM5 15hr > 2 X CLEAR I flight lvl	0.528	0.158	1.000	0.842	0.142	6.313
COAMPS 15hr > 2 X CLEAR I flight lvl	0.639	0.198	1.000	0.802	0.213	5.063
COAMPS 3hr > 2 X CLEAR I flight lvl	0.833	0.348	1.000	0.652	0.443	2.875
ACMES 3hr > CLEAR I flight lvl	0.561	0.275	1.000	0.725	0.231	3.633
MM5 15hr > CLEAR I flight lvl	0.378	0.211	1.000	0.789	0.102	4.733
COAMPS 15hr > CLEAR I flight lvl	0.433	0.227	1.000	0.773	0.136	4.400
COAMPS 3hr > CLEAR I flight lvl	0.689	0.349	1.000	0.651	0.359	2.867

HR = Hit Rate

TS = Threat Score

POD = Probability of Detection

FAR = False Alarm Rate

HSS = Heidke Skill Score

Shading = indicates best score

forecasted. The best possible POD score is one and the worst POD score is zero. False alarm rate (FAR) is the proportion of forecasted events that fail to occur. The best FAR score possible is zero and the worst possible FAR score is one. Heidke skill score indicates that a perfect forecast has a score of one, a score of zero would be achieved by a random forecast, and a score of negative values that is worse than random, with negative one being the worst. Bias is a comparison between the average forecast and the average observation, computed using the ratio of the number of “yes” forecasts to the number of “yes” observations. Unbiased forecasts have a bias score of one (Wilks 1995).

The COAMPS 3-hour data suggests it has the best HR, TS, FAR, HSS, and bias scores when compared to the COAMPS 15-hour, MM5 15-hour, and ACMES 3-hour data sets for values greater than 2 X CLEAR I for the entire profile. The ACMES 3-hour data yielded better results than the COAMPS 15-hour data and MM5 15-hour data. The COAMPS 15-hour data had the best POD score for the entire profile.

The ACMES 3-hour data suggests it gave better results than the MM5 15-hour data when comparing the model domain data for values greater than 2 X CLEAR I. The COAMPS data could not be compared using this test.

The COAMPS 3-hour data implies it has the best HR, TS, FAR, HSS, and bias scores for values greater than CLEAR I compared for the entire profile to the other models. The ACMES 3-hour data yielded the next best scores and the highest POD among all models. Among the remaining two models the COAMPS 15-hour data gave better overall scores when compared to MM5 15-hour data, with the exception of the MM5 15-hour data having a better POD score.

The ACMES 3-hour data suggests it has better scores than the MM5 15-hour data when the model domain values are compared to values greater than CLEAR I.

For comparisons of the models above the boundary level greater than 2 X CLEAR I, the COAMPS 3-hour data suggests better HR, TS, FAR, HSS, and bias scores than the other models. The COAMPS 15-hour data had the best POD score among the models for values greater than 2 X CLEAR I above the boundary level. The ACMES 3-hour data yields the next best scores. The COAMPS 15-hour scores are slightly better than the MM5 15-hour data among the remaining two models.

Comparisons conducted above the boundary level for values greater than CLEAR I indicated the COAMPS 3-hour data had the best scores. The ACMES 3-hour data had the next best scores and the best POD score among the models. Among the remaining two models the COAMPS 15-hour scores are better than the MM5 15-hour scores.

The COAMPS 3-hour data had the best scores for comparisons greater than 2 X CLEAR I and CLEAR I above flight level. The ACMES 3-hour data yields the next best scores in both categories. The COAMPS 15-hour data has better scores than the MM5 15-hour data for both of these categories.

5.3 Paired-t test

The sample sizes of the modeled and observed pairs of differences had a minimum of 30 values, so the central limit theorem (CLT) is evoked. It's also assumed that each sample is a random sample. For completeness, a test of normality was produced for all model and observed difference pairs to see if they exhibited a normal

distribution. Figure 26, which shows how the differences between model and observed pairs are distributed for 20/0300Z comparison of ACMES model data and observed thermosonde data. This comparison is indicative of how all the pairs of differences were distributed for all the thermosonde-model pairs. The graph gives a strong indication that the pairs of differences are normally distributed.

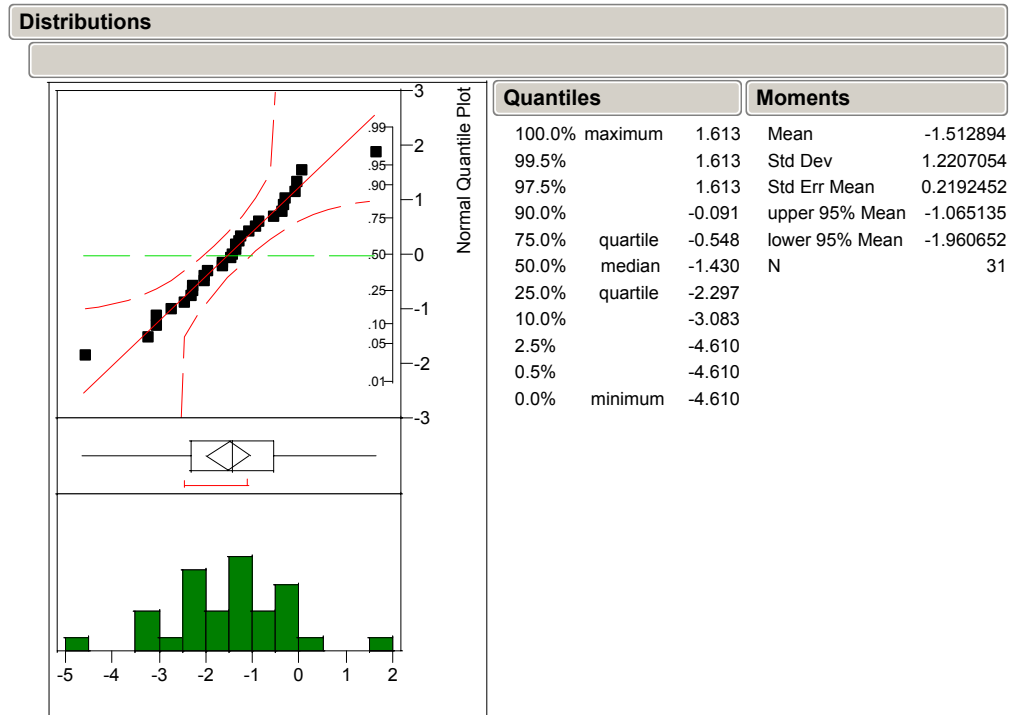


Figure 26. Example Normal Distribution. Plot of Model-Observations Differences for 20/0300Z ACMES-Observed data

Stationarity implies that the mean and auto-correlation function of the data series don't change with time. The correlation between variables in a stationary series is determined only by their separation in time or lag and not their absolute positions in time (Wilks 1995). Auto-correlations were conducted on the differences to see how the pairs of points are correlated spatially. If the auto-correlations decrease rapidly then we can

assume the differences are uncorrelated in space and a paired-t test can be conducted. The paired-t test is a test of the differences about the means between the instrumented data and the model data. Figure 27 represents how the auto-correlations for the differences between observed and modeled data appeared for all sets of pairs.

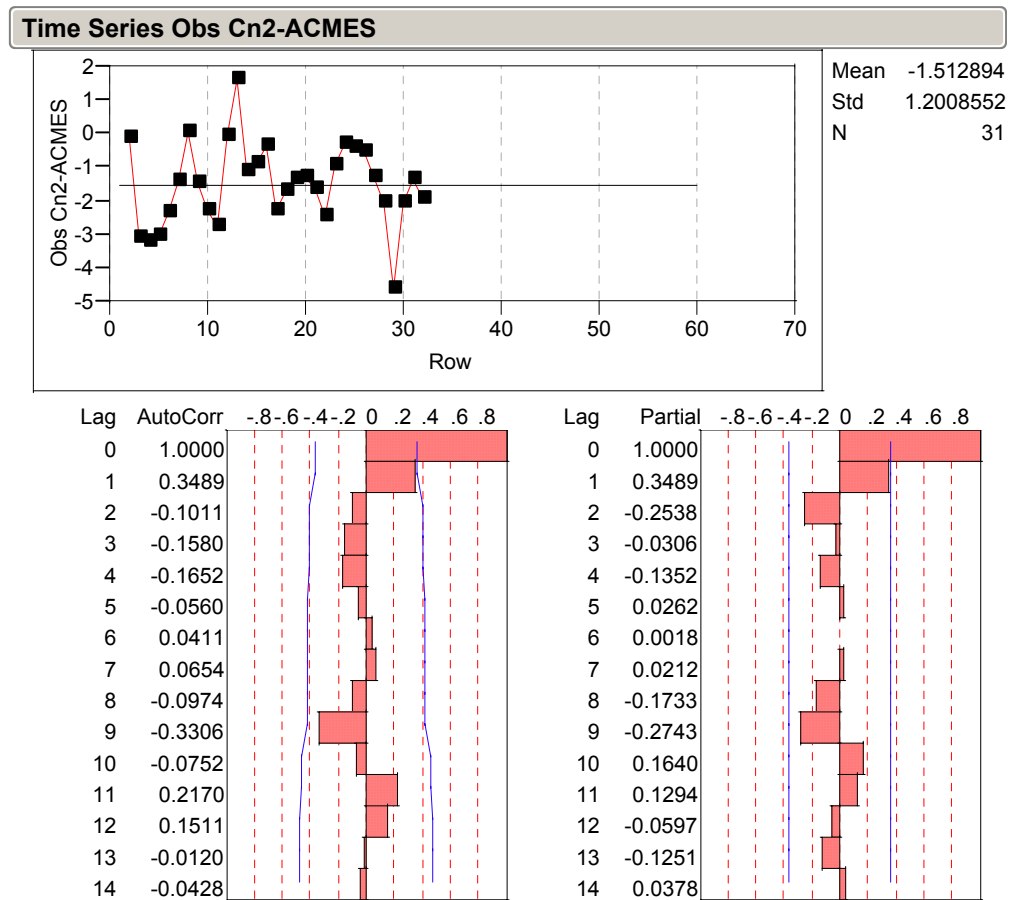


Figure 27. Example of Autocorrelation plot. Plot for 20/0300Z ACMES-Observed data

The auto-correlations drop off very rapidly after the first lag, which indicates that the differences become uncorrelated very rapidly as we move forward between levels. The bars indicate the auto-correlations and the solid line shows twice the large-lag (+ or – twice the standard error). This gives a strong indication that the differences of the pairs are independent of one another, which allows the paired-t test to be conducted.

Most of the comparisons indicate a significant difference exists between the means of the forecast and the model at the .05 alpha level. The results of all paired-t tests conducted at the .05 alpha level are shown in Table 11. In Table 11, “same” indicates a lack of significant difference between the model and observed data. A blank space in Table 11 indicates no data were available for comparison.

Table 11. Paired-t Test Results for Alpha level .05

Launch	ACMES 3hr	MM5 15hr	COAMPS 3hr	COAMPS 15hr
19/0322Z	DIFFERENT	DIFFERENT	DIFFERENT	DIFFERENT
19/0508Z	DIFFERENT	DIFFERENT	DIFFERENT	DIFFERENT
19/2323Z	DIFFERENT	DIFFERENT	SAME	DIFFERENT
20/0115Z	DIFFERENT	DIFFERENT		DIFFERENT
20/0300Z	DIFFERENT	DIFFERENT	DIFFERENT	DIFFERENT
20/0444Z	DIFFERENT	DIFFERENT	SAME	DIFFERENT
20/2320Z	DIFFERENT	DIFFERENT	DIFFERENT	DIFFERENT
21/0235Z	SAME	DIFFERENT	DIFFERENT	DIFFERENT
21/0413Z	DIFFERENT	DIFFERENT	DIFFERENT	DIFFERENT
23/0115Z	DIFFERENT	DIFFERENT	SAME	DIFFERENT
23/0254Z	DIFFERENT	DIFFERENT	DIFFERENT	DIFFERENT
24/0114Z	DIFFERENT	DIFFERENT	DIFFERENT	DIFFERENT
24/0248Z	DIFFERENT	DIFFERENT	DIFFERENT	DIFFERENT
24/0430Z	DIFFERENT	DIFFERENT	DIFFERENT	DIFFERENT
25/0115Z	SAME	DIFFERENT	DIFFERENT	DIFFERENT
25/0253Z	SAME	DIFFERENT	DIFFERENT	DIFFERENT
26/0111Z	DIFFERENT	DIFFERENT	DIFFERENT	DIFFERENT
26/0249Z	DIFFERENT	DIFFERENT	DIFFERENT	DIFFERENT

Launch = Thermosonde Launch date and time

Different = Model is Statistically Different from Thermosonde data

Same = Model shows a lack of Statistical Difference from Thermosonde data

Shading = Paired-t tests where model and thermosonde data are not different

Blank Space = No model data available for comparison

An example of the paired-t test is shown in Figure 28. A statistically significant difference between the model and observed data are indicated by whether the two dashed

lines in Figure 28 encompass the zero line. When both dashed lines surrounding the difference line don't include the zero line as in Figure 28, this indicates the means are significantly different at the .05 alpha level. There are three cases of the ACMES data and three cases for the COAMPS data showing no significant difference between the model and observed means at the .05 alpha level. The dates and times in which these two models did suggests a lack of significant differences between their means are all for different dates and times. An example of the ACMES 20/0300Z model data paired-t test is shown in Figure 28. Tests were conducted for alpha levels of .10 and .01 because very few cases showed a lack of significant difference between the means with an alpha level of .05.

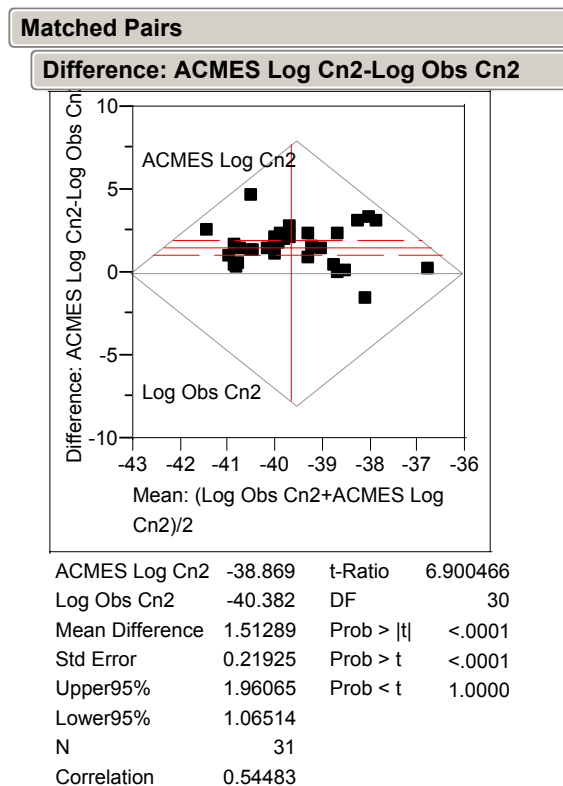


Figure 28. Example of paired-t test with a significant difference between model and observed data at .05 alpha level for ACMES and Observed data of the 20/0300Z Launch

The normal distribution plots, auto-correlations, and matched pairs results of the paired-t tests for selected cases are shown in Appendix B.

5.4 COAMPS Paired-t test results

The COAMPS model data, particularly for the 3-hour forecasts, were able to demonstrate that the mean differences were not significantly different for three cases compared to thermosonde data using the paired-t test. The .05 alpha level tests using the COAMPS data indicated a statistical lack of significant difference in 3 of 18 cases for the 3-hour data vs. 0 of 18 cases for the 15-hour forecasts, which suggests the means are significantly different 83 percent of the time. The forecasts that indicated a lack of significant differences between the means are shown in the Table 11. The paired-t test was also conducted for an alpha level of .10. These paired-t tests yield results that suggests a lack of significant differences in two cases as shown in Table 12. The COAMPS model shows a statistical lack of significant difference for an alpha level of .10 in 2 of 18 cases for the 3-hour forecasts and 0 of 18 for the 15-hour forecasts, which means it did indicate a significant statistical difference 89 percent of the time for the 3-hour forecasts. An alpha level of .01 was also checked, in which case the COAMPS model forecast showed a lack of significant differences between the means for 9 cases shown in Table 13. Using an alpha level of .01 the COAMPS data indicates a lack of significant difference in 5 of 18 cases for the 3-hour data vs. 4 of 18 cases for the 15-hour data. This results for an alpha level of .01 suggests that the thermosonde data and forecast data are different 72 percent of the time for the 3-hour forecasts and different 78 percent of the time for the 15-hour forecasts.

Table 12. Paired-t Test Results for Alpha level of .10

Launch	ACMES 3hr	MM5 15hr	COAMPS 3hr	COAMPS 15hr
19/0322Z	DIFFERENT	DIFFERENT	DIFFERENT	DIFFERENT
19/0508Z	DIFFERENT	DIFFERENT	DIFFERENT	DIFFERENT
19/2323Z	DIFFERENT	DIFFERENT	SAME	DIFFERENT
20/0115Z	DIFFERENT	DIFFERENT		DIFFERENT
20/0300Z	DIFFERENT	DIFFERENT	DIFFERENT	DIFFERENT
20/0444Z	DIFFERENT	DIFFERENT	DIFFERENT	DIFFERENT
20/2320Z	DIFFERENT	DIFFERENT	DIFFERENT	DIFFERENT
21/0235Z	DIFFERENT	DIFFERENT	DIFFERENT	DIFFERENT
21/0413Z	DIFFERENT	DIFFERENT	DIFFERENT	DIFFERENT
23/0115Z	DIFFERENT	DIFFERENT	SAME	DIFFERENT
23/0254Z	DIFFERENT	DIFFERENT	DIFFERENT	DIFFERENT
24/0114Z	DIFFERENT	DIFFERENT	DIFFERENT	DIFFERENT
24/0248Z	DIFFERENT	DIFFERENT	DIFFERENT	DIFFERENT
24/0430Z	DIFFERENT	DIFFERENT	DIFFERENT	DIFFERENT
25/0115Z	SAME	DIFFERENT	DIFFERENT	DIFFERENT
25/0253Z	SAME	DIFFERENT	DIFFERENT	DIFFERENT
26/0111Z	DIFFERENT	DIFFERENT	DIFFERENT	DIFFERENT
26/0249Z	DIFFERENT	DIFFERENT	DIFFERENT	DIFFERENT

Launch = Thermosonde Launch date and time

Different = Model is Statistically Different from Thermosonde data

Same = Model shows a lack of Statistical Difference from Thermosonde data

Shading = Paired-t tests where model and thermosonde data are not different

Blank Space = No model data available for comparison

The utility of these COAMPS model runs is that they suggest that temporal interpolation is not needed to get decent results. The gradient Richardson number algorithm was used for these COAMPS results. The COAMPS gradient Richardson number equation must be investigated further to see how this equation influences C_n^2 values when compared to the Dewan equation used by the MM5 and ACMES models. The COAMPS 3-hour forecasts did a better job of matching the thermosonde data based on statistical analysis when compared to the COAMPS 15-hour forecasts.

Table 13. Paired-t Test Results Alpha level .01

Launch	ACMES 3hr	MM5 15hr	COAMPS 3hr	COAMPS 15hr
19/0322Z	DIFFERENT	DIFFERENT	DIFFERENT	SAME
19/0508Z	SAME	DIFFERENT	DIFFERENT	DIFFERENT
19/2323Z	DIFFERENT	SAME	SAME	SAME
20/0115Z	SAME	DIFFERENT		SAME
20/0300Z	DIFFERENT	DIFFERENT	DIFFERENT	DIFFERENT
20/0444Z	DIFFERENT	DIFFERENT	SAME	DIFFERENT
20/2320Z	DIFFERENT	DIFFERENT	SAME	DIFFERENT
21/0235Z	SAME	DIFFERENT	DIFFERENT	SAME
21/0413Z	DIFFERENT	DIFFERENT	DIFFERENT	DIFFERENT
23/0115Z	DIFFERENT	DIFFERENT	SAME	DIFFERENT
23/0254Z	DIFFERENT	DIFFERENT	DIFFERENT	DIFFERENT
24/0114Z	DIFFERENT	DIFFERENT	DIFFERENT	DIFFERENT
24/0248Z	DIFFERENT	DIFFERENT	SAME	DIFFERENT
24/0430Z	DIFFERENT	DIFFERENT	DIFFERENT	DIFFERENT
25/0115Z	SAME	DIFFERENT	DIFFERENT	DIFFERENT
25/0253Z	SAME	DIFFERENT	DIFFERENT	DIFFERENT
26/0111Z	DIFFERENT	DIFFERENT	DIFFERENT	DIFFERENT
26/0249Z	DIFFERENT	DIFFERENT	DIFFERENT	DIFFERENT

Launch = Thermosonde Launch date and time

Different = Model is Statistically Different from Thermosonde data

Same = Model shows a lack of Statistical Difference from Thermosonde data

Shading = Paired-t tests where model and thermosonde data are not different

Blank Space = No model data available for comparison

The fact that the COAMPS 3-hour forecasts performed better statistically when compared to the 15-hour forecasts seemed a bit surprising because of the susceptibility of gravity wave noise contaminating any model forecast within the first 12 hours of model integration (Sashegyi and Madala 1993). All models try to achieve a state of dynamic balance, which can be disrupted due to data insertion (Harms et al. 1992a). Since 3 hours is a very short time to achieve dynamic balance vs. 15 hours, a condition with less dynamic balance and less propagated error could also occur in the model run. Due to the

forecast period being very short, if the model is initialized using “good” data, then there is also the possibility of less error in the 3-hour forecasts compared to 15-hour forecasts, which may be indicated in these results.

5.5 MM5 Paired-t test results

The MM5 model forecasts didn’t have any cases in which the observed and forecasted means showed a lack of significant differences for an alpha level of .05 or .10. The MM5 did show a lack of a significant difference between the means for the 19/12Z forecast for the 19/2323Z launch as shown in Table 13. The MM5 model shows a lack of significant statistical difference for the .01 alpha level in 1 of 18 cases for its 15-hour forecasts and 0 of 18 times for the .05 and .10 alpha levels as shown in Tables 11 and 12. This means we have a significant difference in the means 95 percent of the time for the .01 alpha level, and a 100 percent significant difference in the means for the other alpha levels.

5.6 ACMES Paired-t test results

The ACMES model data showed three cases where the forecasted means indicated a lack of significant difference from the observed means for an alpha level of .05 shown in Table 10. Using .05 alpha level, the ACMES shows a lack of significant statistical difference in 3 of 18 cases, which implies the means are significantly different 83 percent of the time. For a .10 alpha level the ACMES data indicated the best results in two cases listed in Table 12. The ACMES data suggests a lack of significant statistical difference for the .10 alpha level in 2 of 18 cases for its forecasts, which means it did not

correctly forecast optical turbulence 89 percent of the time. Using an alpha level of .01 the ACMES data indicated a lack of significant differences between the means in the five cases listed in Table 13. The .01 alpha level test for ACMES data shows a lack of significant statistical difference in 5 of 18 cases. This result suggests the model forecast and observed C_n^2 means are different 72 percent of the time for this thesis.

It is interesting to note that the ACMES C_n^2 forecasts for the launches 19/0322Z and 19/0508Z were orders of magnitude below the other models forecasts and the thermosonde data, but after this period became very comparable. There was a concern that the ACMES data may be utilizing temperatures much lower than the other models because of the order of magnitude difference in optical turbulence values it calculated for the first two launches compared to the other models. The temperature profiles did indicate a noticeable deviation above 14 km between the thermosonde temperatures and the ACMES model temperatures for the 19/0508Z launch. For the 19/0322Z launch the temperature profiles are comparable, so the reason for the differences in magnitude here requires further study.

5.7 Model to Model paired-t tests

Paired-t tests were also conducted on forecasts based on model output for each thermosonde launch. These paired-t tests were used to see if there were any differences between model forecasts. Theoretically, if there were not significant differences between forecasts of the various models, this would suggest that there are not major differences among the models. If the paired-t test results show forecasts based on model output have

significant differences, then there may be significant statistical differences between models. All paired-t tests comparisons for model runs were completed for the same valid time with an alpha level of .05 and are summarized in Table 14.

Table 14. Between Model Paired-t Test Results

Launch	A 3hr-M 15hr	A 3hr-C 15hr	A 3hr-C 3hr	M 15hr-C 15hr	M 15hr-C 3hr	C 15hr-C 3hr
19/0322Z	DIFFERENT	DIFFERENT	DIFFERENT	DIFFERENT	SAME	SAME
19/0508Z	DIFFERENT	DIFFERENT	DIFFERENT	SAME	DIFFERENT	DIFFERENT
19/2323Z	SAME	SAME	DIFFERENT	SAME	DIFFERENT	DIFFERENT
20/0115Z	SAME	SAME		SAME		
20/0300Z	SAME	SAME	DIFFERENT	SAME	DIFFERENT	DIFFERENT
20/0444Z	SAME	SAME	DIFFERENT	SAME	DIFFERENT	DIFFERENT
20/2320Z	SAME	SAME	DIFFERENT	SAME	DIFFERENT	DIFFERENT
21/0235Z	SAME	SAME	SAME	SAME	SAME	SAME
21/0413Z	SAME	SAME	SAME	SAME	SAME	SAME
23/0115Z	SAME	SAME	DIFFERENT	DIFFERENT	DIFFERENT	DIFFERENT
23/0254Z	SAME	SAME	DIFFERENT	DIFFERENT	DIFFERENT	DIFFERENT
24/0114Z	SAME	SAME	DIFFERENT	SAME	SAME	SAME
24/0248Z	SAME	SAME	DIFFERENT	SAME	DIFFERENT	DIFFERENT
24/0430Z	SAME	SAME	SAME	SAME	SAME	SAME
25/0115Z	DIFFERENT	DIFFERENT	DIFFERENT	SAME	DIFFERENT	DIFFERENT
25/0253Z	DIFFERENT	DIFFERENT	DIFFERENT	SAME	DIFFERENT	SAME
26/0111Z	SAME	SAME	DIFFERENT	SAME	DIFFERENT	DIFFERENT
26/0249Z	SAME	SAME	DIFFERENT	SAME	DIFFERENT	SAME

Launch = Thermosonde Launch date and time

Different = Model is Statistically Different from Thermosonde data

Same = Model shows a lack of Statistical Difference from Thermosonde data

Shading = Paired-t tests where model and thermosonde data are not different

Blank Space = No model data available for comparison

In Table 14, cases where the models show no statistical difference are highlighted. A

“same” value indicates there is a lack of statistical difference between each models

forecast for optical turbulence. A “different” value in Table 14 indicates that there is a

significant statistical difference between each models forecast for optical turbulence at the .05 alpha level. The ACMES 3-hour and COAMPS 15-hour data yield similar results. The ACMES 3-hour and MM5 15-hour forecasts also indicate similar results. Based on the ACMES 3-hour results being similar to both the COAMPS 15-hour and MM5 15-hour results, it's not real surprising that the COAMPS 15-hour and MM5 15-hour forecasts indicate similar results to each other overall. From the other comparisons, it seems that the COAMPS 3-hour forecasts are statistically different when compared to the other models data.

All vertically integrated 500 m layers were summed up for each model output valid time and compared to vertically integrated values for the equivalent thermosonde data. This integration of data was completed assuming an “onion skin” model of the atmosphere, in which the atmosphere is homogeneous in that layer. These vertically integrated values for the models are compared to the equivalent thermosonde values to see which model came closest to matching the thermosonde C_n^2 profile. These vertically integrated values are depicted in Table 15.

Table 15. Vertically Integrated Values of Profiles

Launch	Obs Cn2	ACMES 3hr	MM5 15 hr	COAMPS 15hr	COAMPS 3hr
19/0322Z	1.08E-15	2.06E-16	1.07E-15	1.78E-15	1.83E-15
19/0508Z	1.12E-15	4.28E-16	1.06E-15	1.83E-15	3.40E-15
19/2323Z	3.40E-16	9.66E-16	8.59E-16	3.22E-15	2.58E-16
20/0115Z	7.45E-16	8.67E-16	8.15E-16	3.22E-15	
20/0300Z	2.71E-16	8.86E-16	7.77E-16	1.61E-15	1.77E-15
20/0444Z	1.15E-15	9.19E-16	7.26E-16	1.69E-15	2.22E-15
20/2320Z	3.82E-16	1.08E-15	9.65E-16	3.10E-15	5.88E-16
21/0235Z	6.53E-15	1.07E-15	9.44E-16	1.56E-15	2.27E-15
21/0413Z	3.28E-16	1.07E-15	9.89E-16	1.71E-15	3.06E-15
23/0115Z	8.48E-16	8.81E-16	1.30E-15	3.86E-15	8.26E-16
23/0254Z	3.30E-16	8.91E-16	1.22E-15	5.32E-15	3.92E-15
24/0114Z	1.82E-15	2.36E-15	1.23E-15	8.99E-15	4.47E-15
24/0248Z	1.90E-15	1.78E-15	1.28E-15	7.82E-15	4.39E-15
24/0430Z	5.73E-16	1.28E-15	1.13E-15	3.81E-15	3.13E-15
25/0115Z	2.24E-16	2.03E-16	9.98E-16	4.46E-15	6.79E-16
25/0253Z	2.59E-16	2.11E-16	1.10E-15	2.13E-15	1.34E-15
26/0111Z	4.18E-16	1.12E-15	8.00E-16	4.54E-15	2.60E-16
26/0249Z	1.09E-16	1.07E-15	8.00E-16	5.93E-15	1.02E-15

Shading = Vertically Integrated Model value that is closest to the Vertically Integrated Thermosonde value

Launch = Thermosonde Launch date and time

Obs Cn2 = Vertically Integrated Thermosonde value

ACMES 3hr = Vertically Integrated ACMES 3 hr value

MM5 15hr = Vertically Integrated MM5 15hr value

COAMPS 15hr = Vertically Integrated COAMPS 15hr value

COAMPS 3hr = Vertically Integrated COAMPS 3hr value

The MM5 15-hour data suggests its vertically integrated values were closest to the thermosonde data compared to the other models for eight thermosonde launches. The COAMPS 3-hour vertically integrated data were closest to the actual thermosonde data

on five occasions, followed by the ACMES 3-hour integrated values, which yielded the closest vertically integrated results on four occasions.

5.8 Thermosondes

The thermosonde launches that occurred within the same 0-6 hour period show an overall similar vertical profile, but can be highly variable over short distances as seen by the figures in Appendix A. The thermosonde data are highly variable as seen in the profiles and suggests that the sensitivity of the models can only be expected to model overall high and low values due to the models not having the same vertical or horizontal resolution of the thermosondes. The ABL program is concerned with path integrated optical turbulence values approximately twice that of the CLEAR I profile. Vertically integrating or binning the thermosonde data and taking the mean value of these layers is a way of attempting to path integrate values of C_n^2 along a pseudo-horizontal path. More important than the highest values in a profile, values of optical turbulence along an integrated path in the atmosphere may be inferred, which may indicate regions of enhanced Rytov variance.

VI. Conclusions

6.1 Summary

Vertically path integrated mean layer comparisons between the models and thermosonde data using 500 m layers suggests that the COAMPS 3-hour data yield the best results. The COAMPS 3-hour data had better ME, MAE, RMSE and contingency table results when compared to the other models. The ACMES, MM5, and COAMPS 15-hour data had comparable results based on objective metrics and contingency table scores.

The optical turbulence averages across the entire domain are understandably smoother than the other profiles for both the MM5 and ACMES models. These domain averages seem to indicate the vertical structure of C_n^2 in the atmosphere. Domain profiles may be a way to characterize the general structure of optical turbulence for very large areas.

None of the model forecasts completely matches the structure of the thermosondes in the boundary layer, troposphere and stratosphere. When using the vertically integrated path technique these models do seem to forecast the general overall structure when compared to the thermosonde profile.

The paired-t tests used to compare models suggest that the 3-hour COAMPS model is different from the other models, and that the other models are statistically similar. Results of paired-t tests among the models indicate the ACMES 3-hour data shows lack of a significant difference when compared to the COAMPS 15-hour and MM5 15-hour data. The ACMES model output for the first two launches was an order of

magnitude below the thermosonde data. After the first two launches, the ACMES data results became very comparable to the other data sets.

The COAMPS model runs were not interpolated in time as the other models were and still produced the best ME, MAE, RMSE, contingency scores, and paired-t results. Using the nearest model output valid times that were closest to the actual launch times, the COAMPS 3-hour forecasts managed to achieve better results when compared to the other models. These results indicate that temporal interpolation may not be necessary.

The MM5 model runs did manage to suggest a lack of significant difference between forecasted and observed values using the paired-t test at the alpha level of .01 for only one case and none for alpha levels of .10 or .05. The MM5 results based on ME, MAE, RMSE, and correlations were comparable to the other models. Results of the paired-t tests among the models suggest the MM5 15-hour data are not significantly different from the ACMES 3-hour and COAMPS 15-hour data. The MM5 model yielded the best results when comparing model profiles near the tropopause associated with the strong jet stream event for the 20/2320Z, 21/0235Z, and 21/0413Z launches.

The ACMES method results indicate that it models optical turbulence data comparably to the MM5 and COAMPS mesoscale models. The ACMES data suggest this method can be used to model the climatology of optical turbulence in areas void of optical turbulence data.

Vertically integrated path values were computed by summing up all 500 m layers for each thermosonde launch and model output valid time. These vertically path integrated values suggest that the MM5 data are closest to the vertically integrated thermosonde data on more occasions than the other models. The COAMPS 3-hour data

and the ACMES 3-hour data were closest to the vertically integrated thermosonde data nearly the same number of times. Vertically integrating layers of thermosonde and model data can be adjusted to determine a pseudo-slant integrated optical turbulence path through the atmosphere.

The synoptic analysis conducted for this thesis lends support to the relationship between increased values of C_n^2 in the presence of the jet stream or strong temperature gradients. The ability of forecasters to predict synoptic scale phenomena is highlighted with the enhanced jet stream event mentioned previously.

6.2 Recommendations

Each of these models deserves continued study. Path integrated values of optical turbulence are what these models must forecast accurately. Higher values of C_n^2 are of particular interest along these integrated paths when compared to the thermosonde profile. Experimentally determining path integrated optical turbulence values in the atmosphere is an expensive proposition. Accurately modeling and visualizing optical turbulence will ultimately offset the cost associated with actual measurements. Vertical profiles based on the thermosonde data can be used to infer path-integrated values of optical turbulence assuming an “onion skin” atmosphere. Domain profiles may provide some insight into how C_n^2 might be inferred for large areas. MM5 3-hour forecasts should be compared to other models with 3-hour forecasts to see how they compare. Each model that is used in a comparison should have all its data available. This would help ensure that all models are manipulated and managed in a similar manner for consistency of comparisons. The differences in accuracy of each model based on

objective metrics may be due to the lack of spin up time in which the models are allowed to assimilate all parameters properly. Horizontal path integrations can be attempted among models if all model data are available.

Differences between the COAMPS 3-hour data and the other models may be due to how these models assimilate their data, initialize boundary conditions, and/or use algorithms to produce optical turbulence. The areas of initialization, assimilation, and parameterization schemes used in these models should be continued areas of focus regarding efforts in modeling optical turbulence.

Ultimately, extreme care must be used when forecasting optical turbulence with any of these models. These models cannot be expected to predict C_n^2 with a high degree of reliability at this time. One of the reasons these models don't forecast optical turbulence accurately when compared to the thermosonde is that the horizontal and vertical resolution of the models are much less than the resolution of the thermosonde. The models used in this thesis will provide more accurate optical turbulence forecasts as improvements in modeling and research continues.

The use of existing forecasting techniques cannot be overemphasized, when predicting areas of optical turbulence. Numerical weather prediction along with forecasting techniques are part of the suite of tools that should be used to provide better optical turbulence forecasts.

Appendix A. Synoptic Charts

This appendix contains selected surface, 500 mb, 300mb, 200mb, skew-t charts, infrared and water vapor satellite images. These images highlight weather conditions before, during, and after the increase in jet stream event between 21/00Z and 23/00Z. These figures also include binned profiles for all thermosonde launches and domain averages as well as selected temperature profiles.

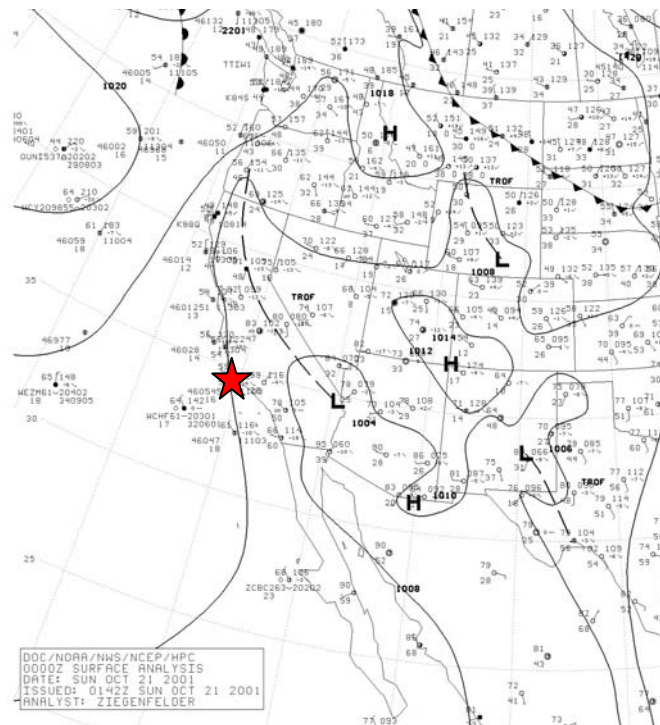


Figure A.1 Surface Analysis 00Z 21 October 2001, inverted trough to the east of Vandenberg AFB, CA. [Adapted from NCDC 2001]

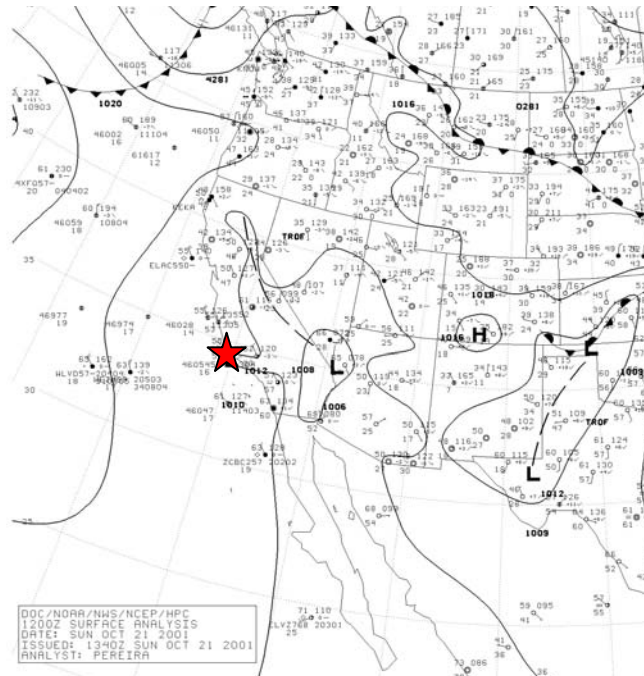


Figure A.2 Surface Analysis 12Z 21 October 2001, inverted trough moving eastward [Adapted from NCDC 2001]

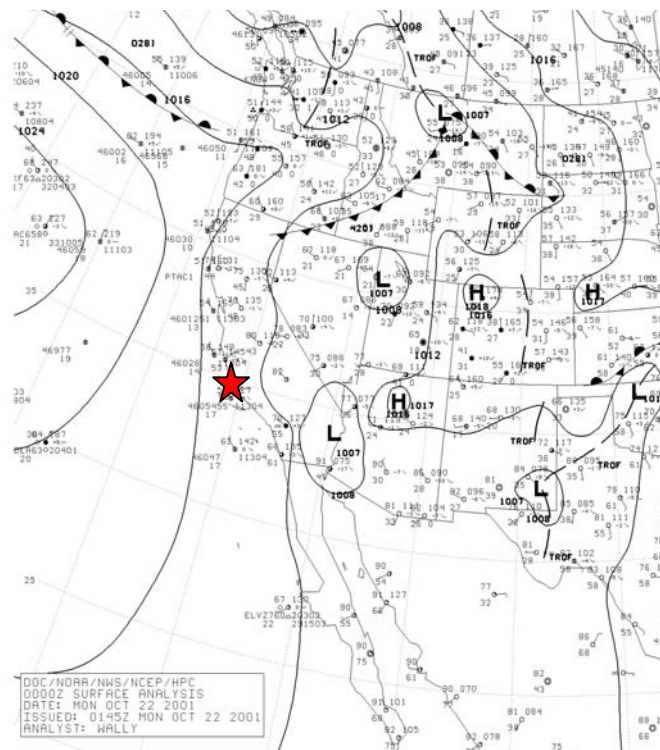


Figure A.3 Surface Analysis 00Z 22 October 2001, high pressure becoming dominant [Adapted from NCDC 2001]

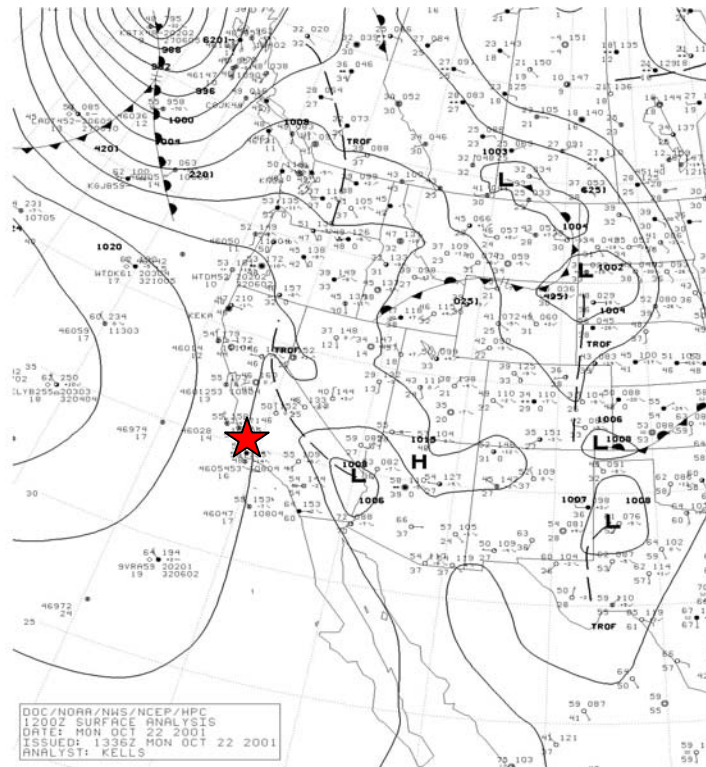


Figure A.4 Surface Analysis 12Z 22 October 2001, ridging to the west [Adapted from NCDC 2001]

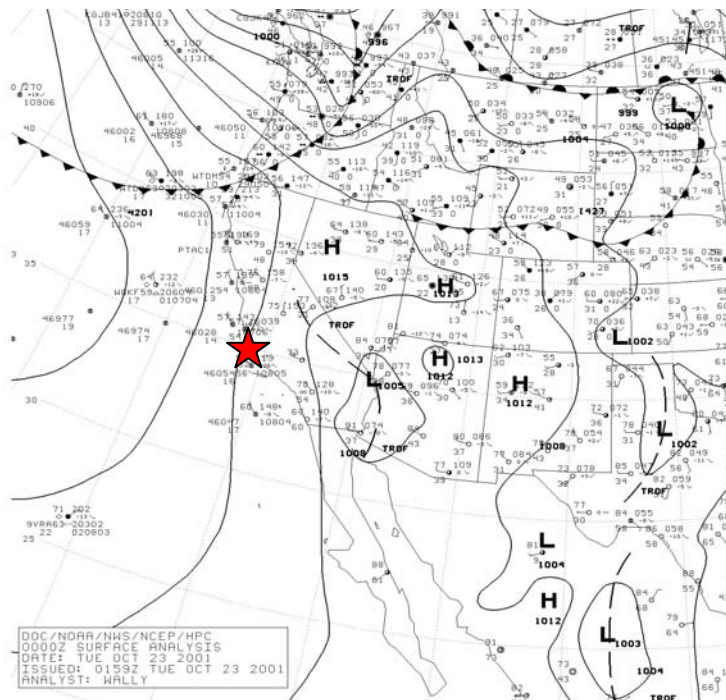


Figure A.5 Surface Analysis 00Z 23 October 2001, northerly flow around high pressure to the west [Adapted from NCDC 2001]

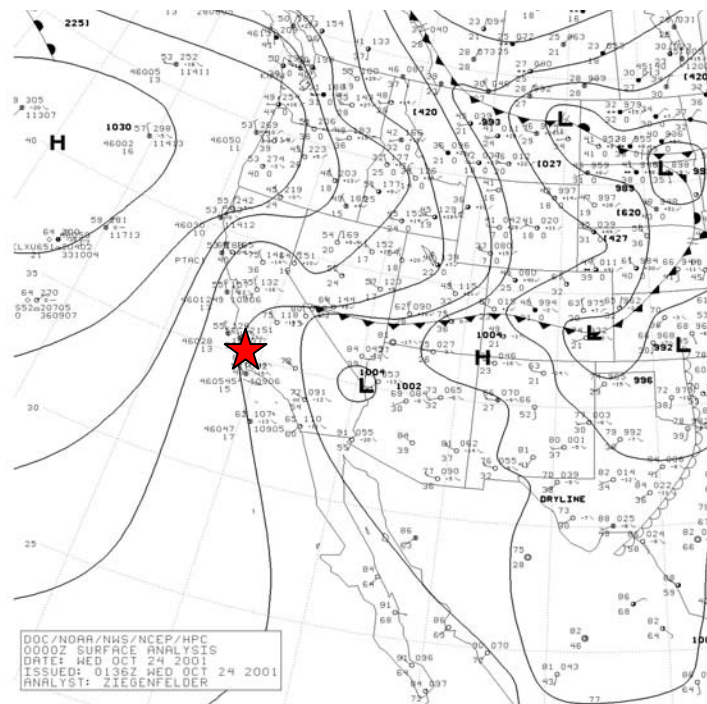


Figure A.6 Surface Analysis 12Z 23 October 2001, inverted trough axis to the east [Adapted from NCDC 2001]

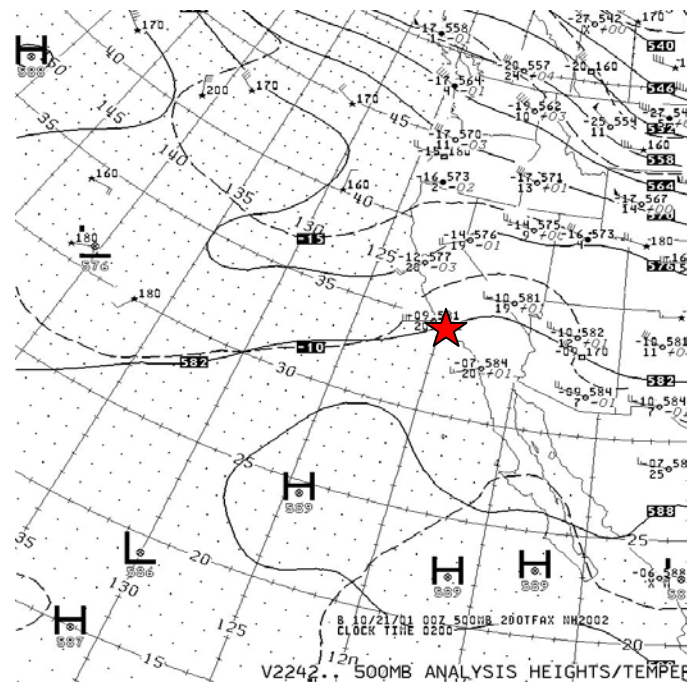


Figure A.7 500 mb Analysis Chart 00Z 21 October 2001, weak ridging with trough to NW [Adapted from NCDC 2001]

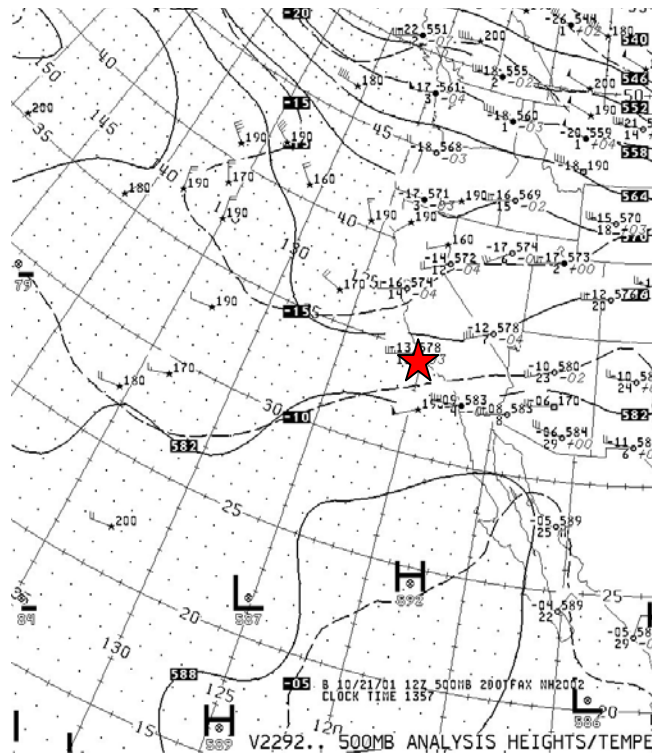


Figure A.8 500 mb Analysis Chart 12Z 21 October 2001, zonal flow [Adapted from NCDC 2001]

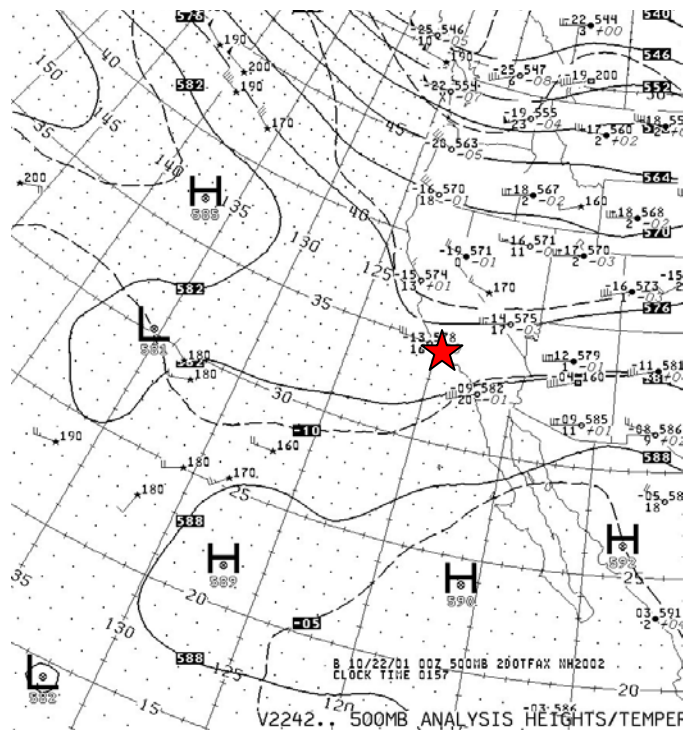


Figure A.9 500 mb Analysis 00Z 22 October 2001, zonal flow with trough to the west [Adapted from NCDC 2001]

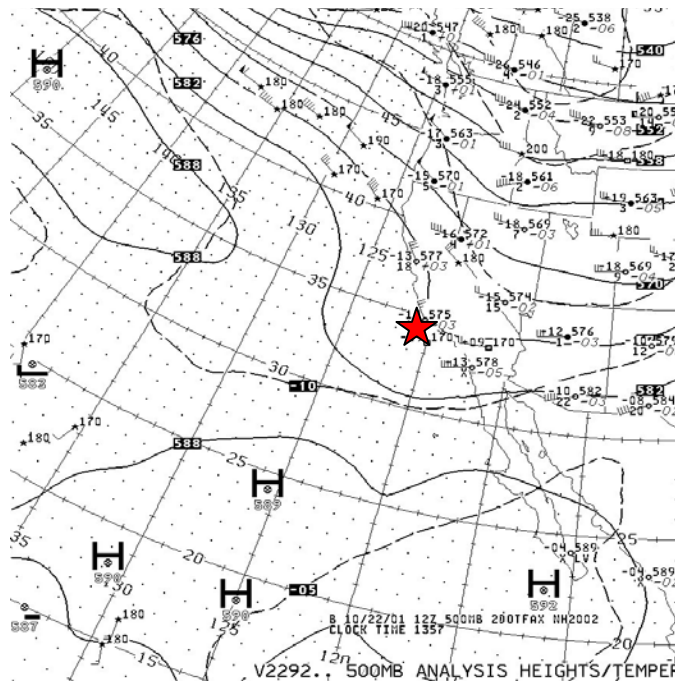


Figure A.10 500 mb Analysis 12Z 22 October 2001, trough Axis near Vandenberg AFB, CA. [Adapted from NCDC 2001]

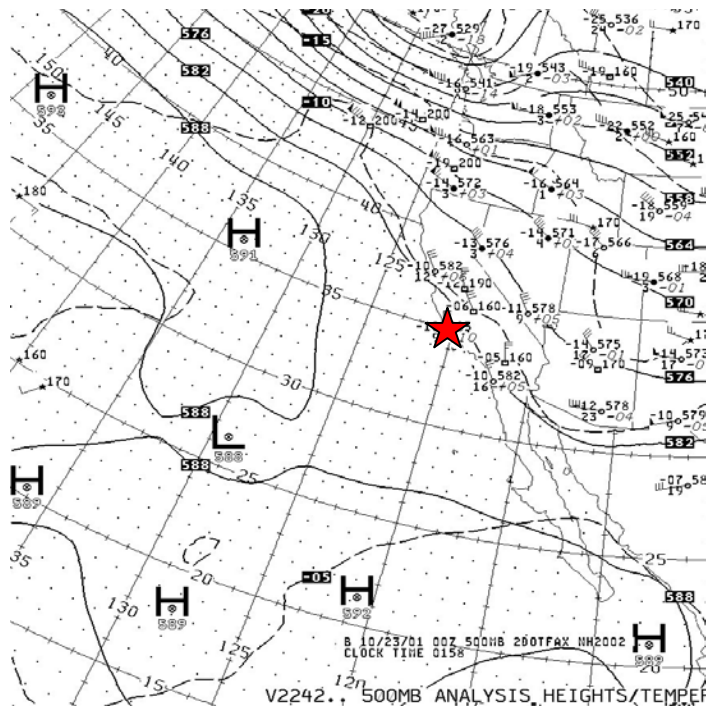


Figure A.11 500 mb Analysis 00Z 23 October 2001, ridge beginning to build into region [Adapted from NCDC 2001]

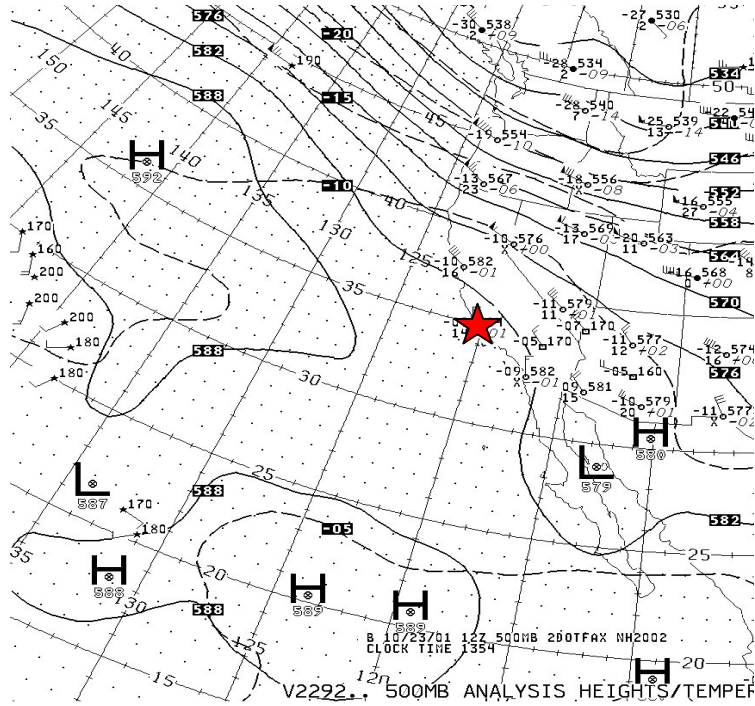


Figure A.12 500 mb Analysis 12Z 23 October 2001, NW flow around Pacific High [Adapted from NCDC 2001]

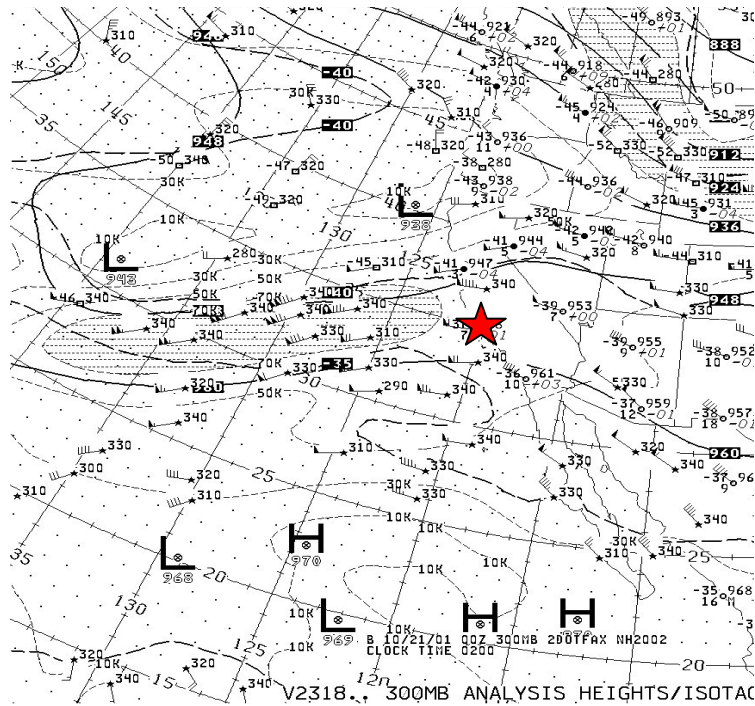


Figure A.13 300 mb Analysis 00Z 21 October 2001, jet maximum moving eastward into region [Adapted from NCDC 2001]

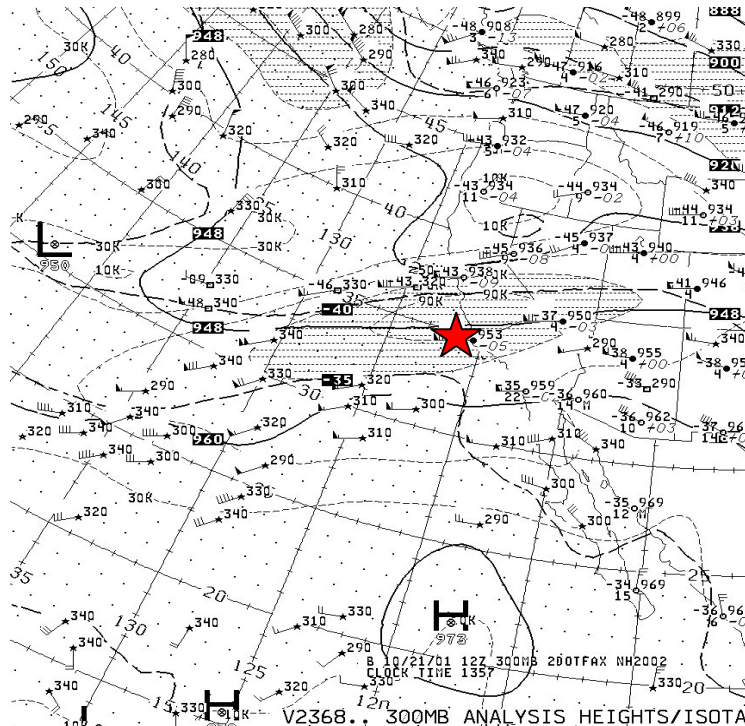


Figure A.14 300 mb Analysis 12Z 21 October 2001, jet maximum over Vandenberg AFB, CA. [Adapted from NCDC 2001]

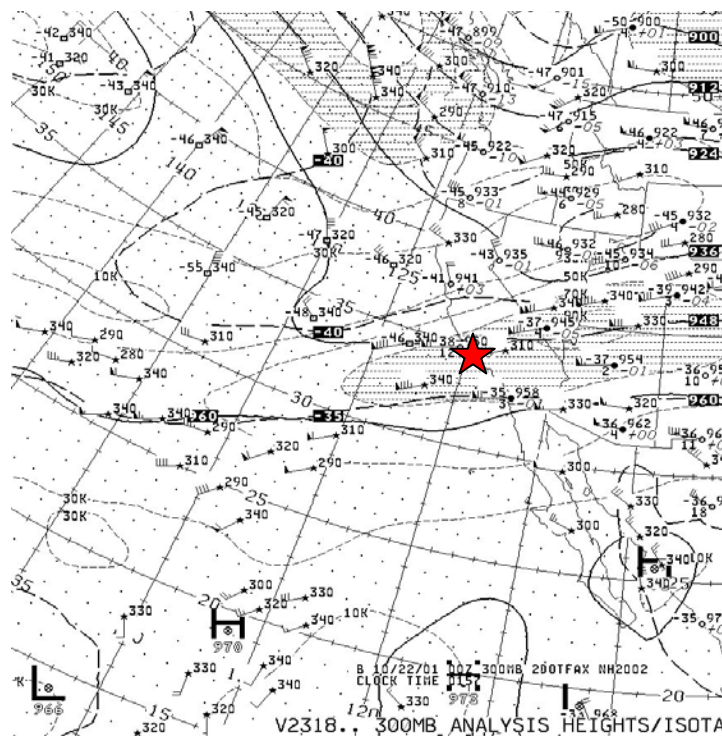


Figure A.15 300 mb Analysis 00Z 22 October 2001, jet maximum moving out of region [Adapted from NCDC 2001]

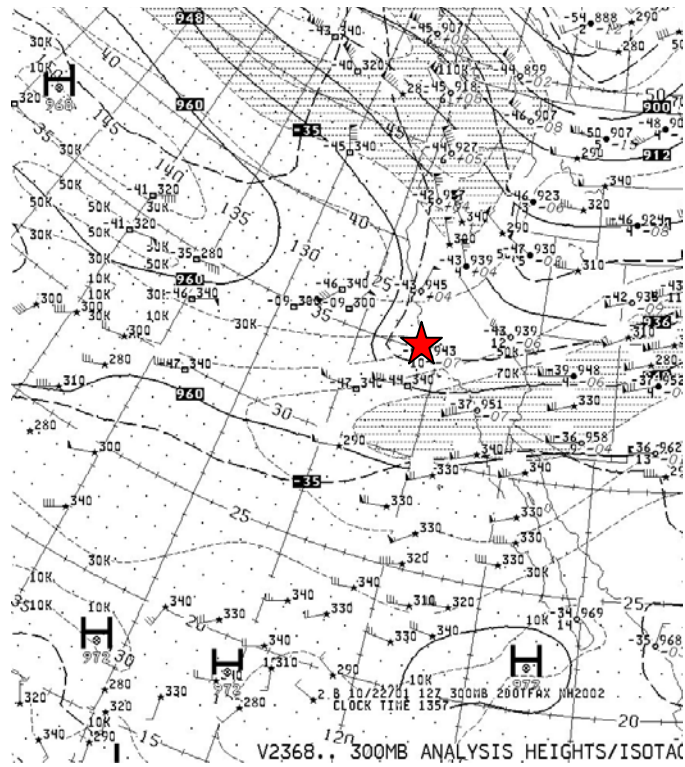


Figure A.16 300 mb Analysis 12Z 22 October 2001, trough axis in place as jet maximum moves south [Adapted from NCDC 2001]

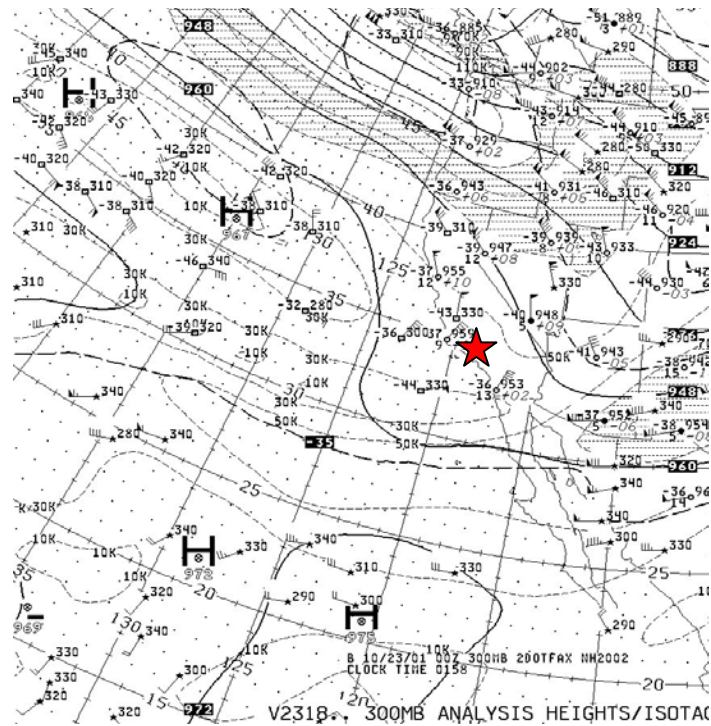


Figure A.17 300 mb Analysis 00Z 23 October 2001, weak trough axis with jet to SE [Adapted from NCDC 2001]

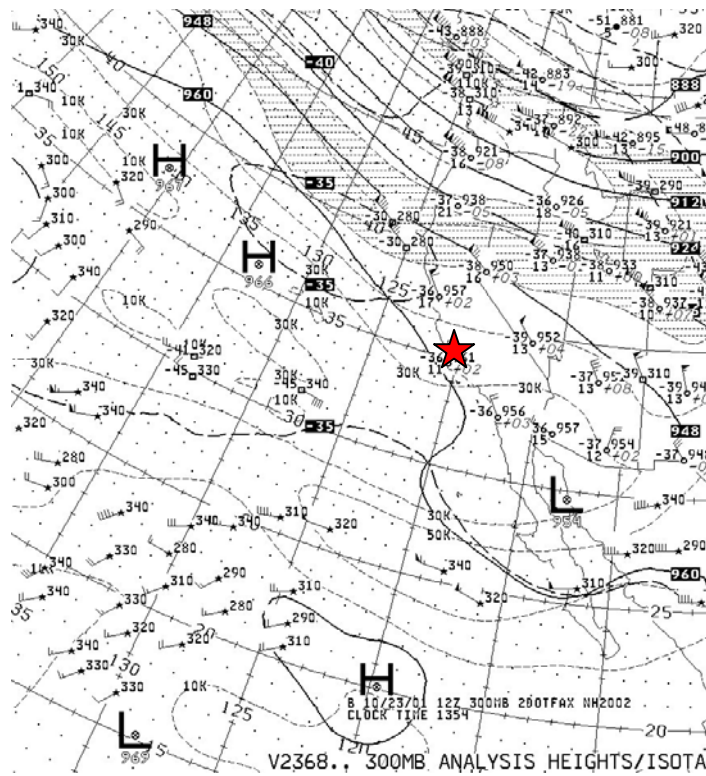


Figure A.18 300 mb Analysis 12Z 23 October 2001, NW flow around N. Pacific High [Adapted from NCDC 2001]

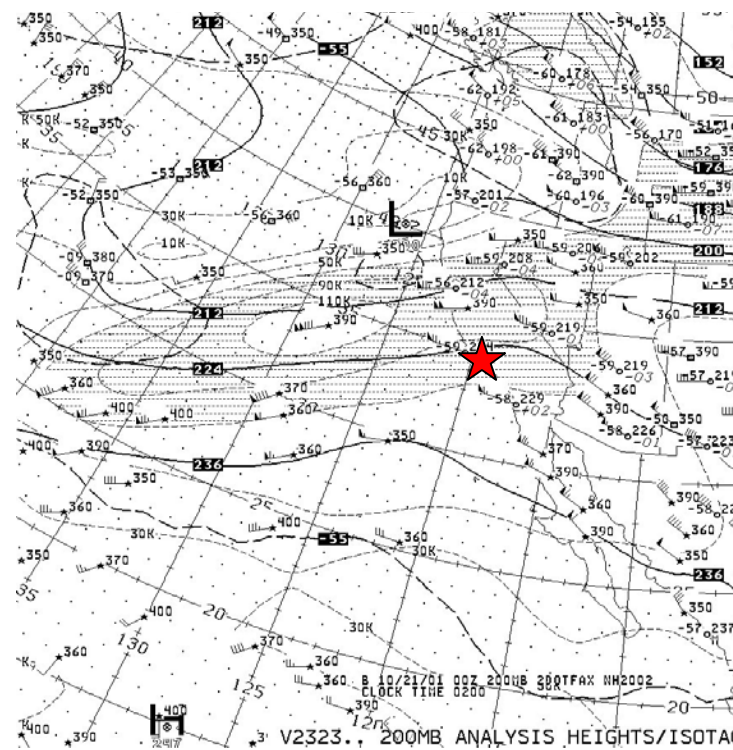


Figure A.19 200 mb Analysis 00Z 21 October 2001, jet maximum moving eastward [Adapted from NCDC 2001]

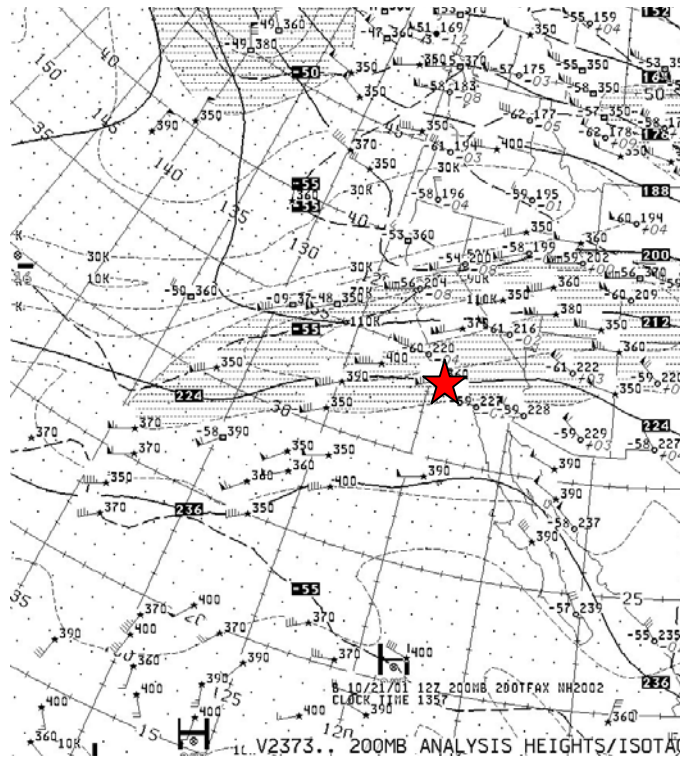


Figure A.20 200 mb Analysis 12Z 21 October 2001, jet maximum moving in place over Central and S. CA [Adapted from NCDC 2001]

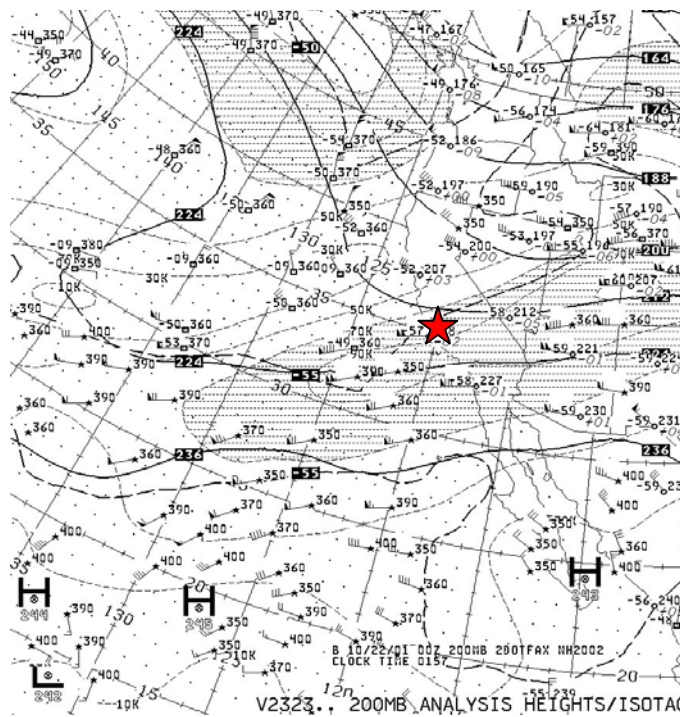


Figure A.21 200 mb Analysis 00Z 22 October 2001, jet maximum near Vandenberg AFB, CA [Adapted from NCDC 2001]

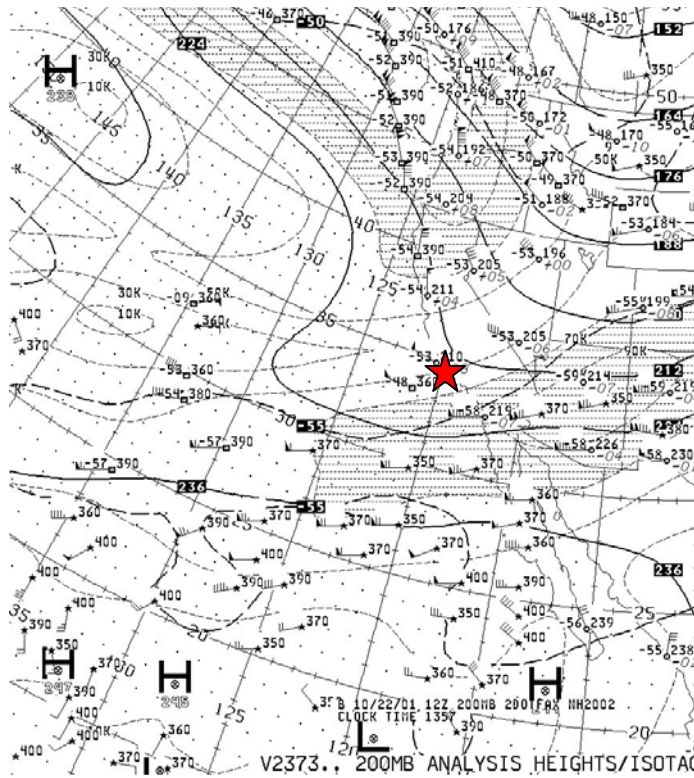


Figure A.22 200 mb Analysis 12Z 22 October 2001, jet maximum south of region [Adapted from NCDC 2001]

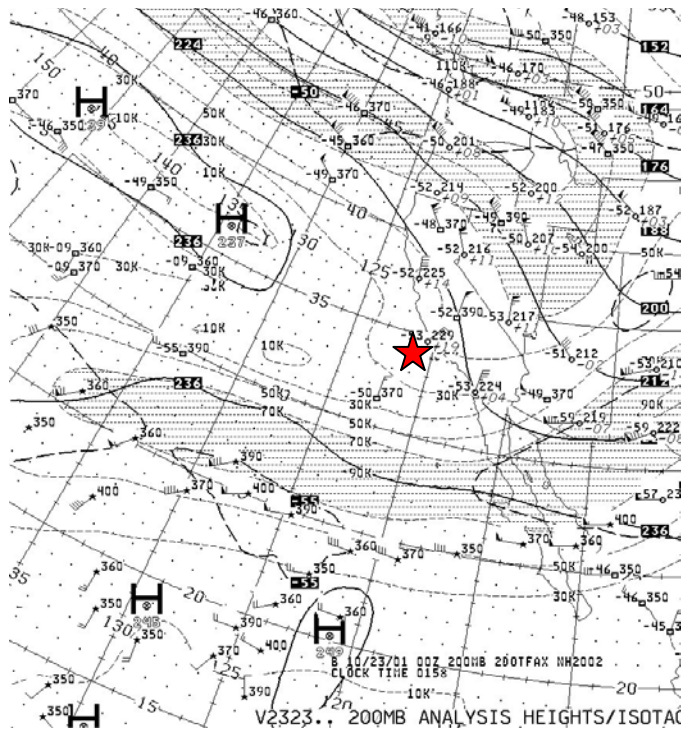


Figure A.23 200 mb Analysis 00Z 23 October 2001, trough axis moving to SE of region [Adapted from NCDC 2001]

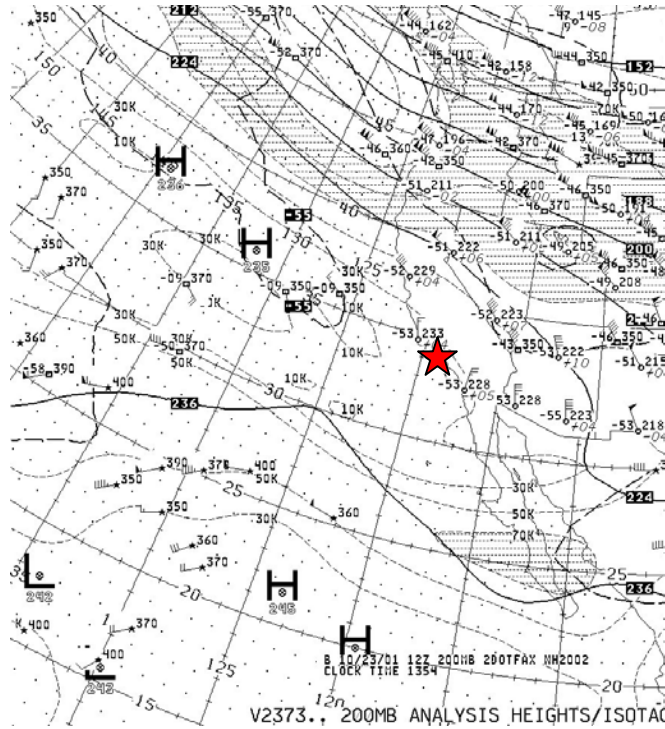


Figure A.24 200 mb Analysis 12Z 23 October 2001, NW flow around N. Pacific High [Adapted from NCDC 2001]

72393 VBG Vandenberg Afb

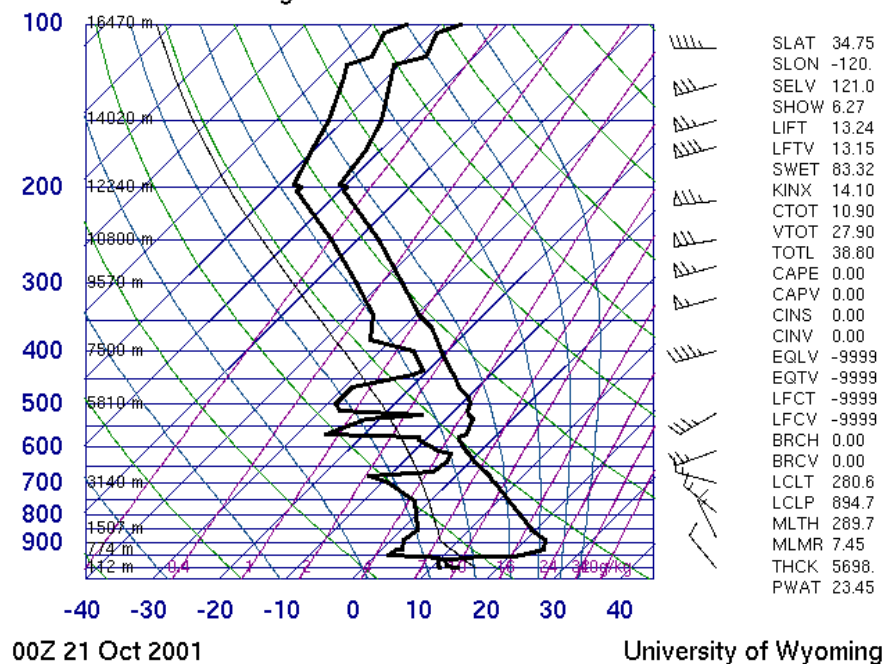


Figure A.25 Skew-T profile 00Z 21 October 2001, 85 kt jet maximum above tropopause near 200 mb
[Adapted from University of Wyoming 2001]

72393 VBG Vandenberg Afb

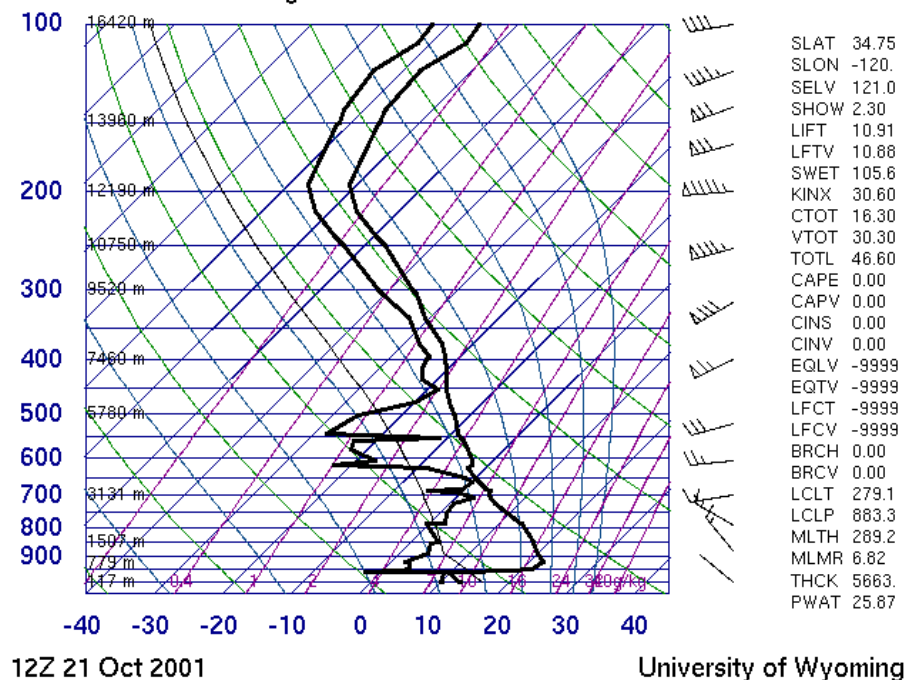


Figure A.26 Skew-T profile 12Z 21 October 2001, 95 kt jet maximum near 200 mb and tropopause
[Adapted from University of Wyoming 2001]

72393 VBG Vandenberg Afb

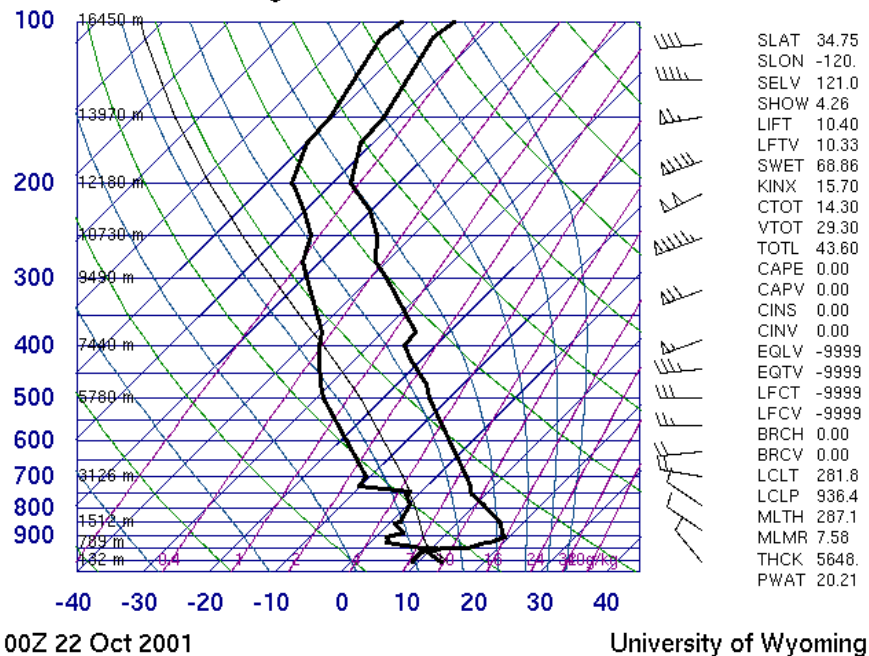


Figure A.27 Skew-T profile 00Z 22 October 2001, 100 kt jet maximum near 200 mb and below tropopause [Adapted from University of Wyoming 2001]

72393 VBG Vandenberg Afb

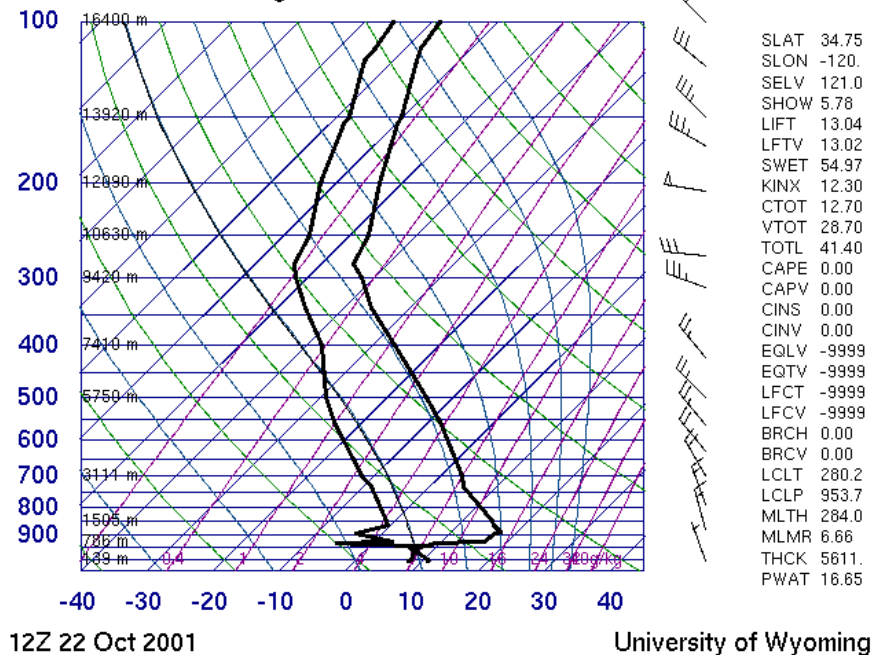


Figure A.28 Skew-T profile 12Z October 2001, 50 kt decrease in jet maximum at 200 mb with tropopause height lowering to just above 300 mb [Adapted from University of Wyoming 2001]

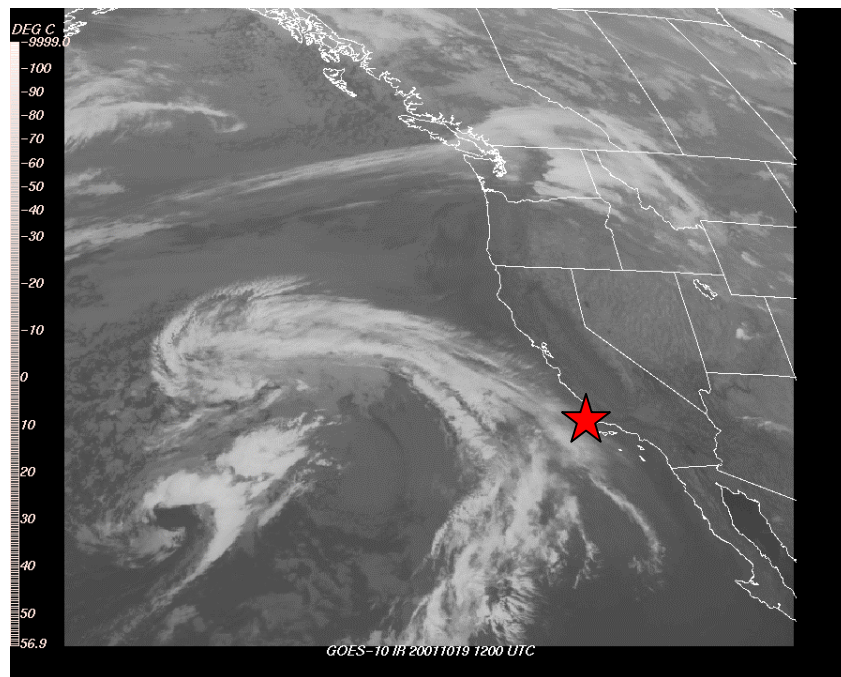


Figure A.29 Infrared Satellite Image 12Z 19 October 2001, weakening upper front with embedded vorticity maximum to the west [Adapted from NCDC 2001]

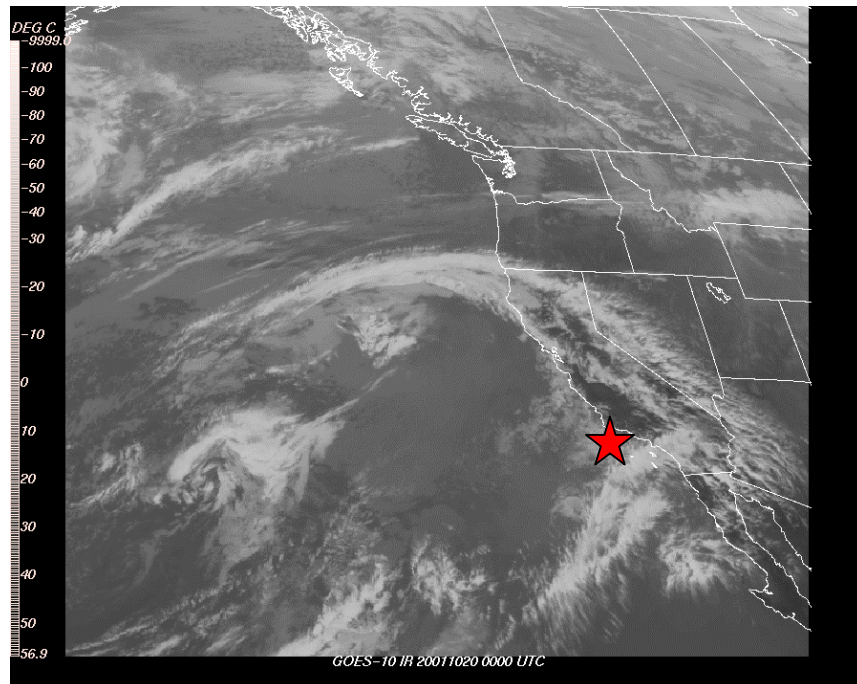


Figure A.30 Infrared Satellite Image 00Z 20 October 2001, weakening front moving inland as vorticity maximum decays to west [Adapted from NCDC 2001]

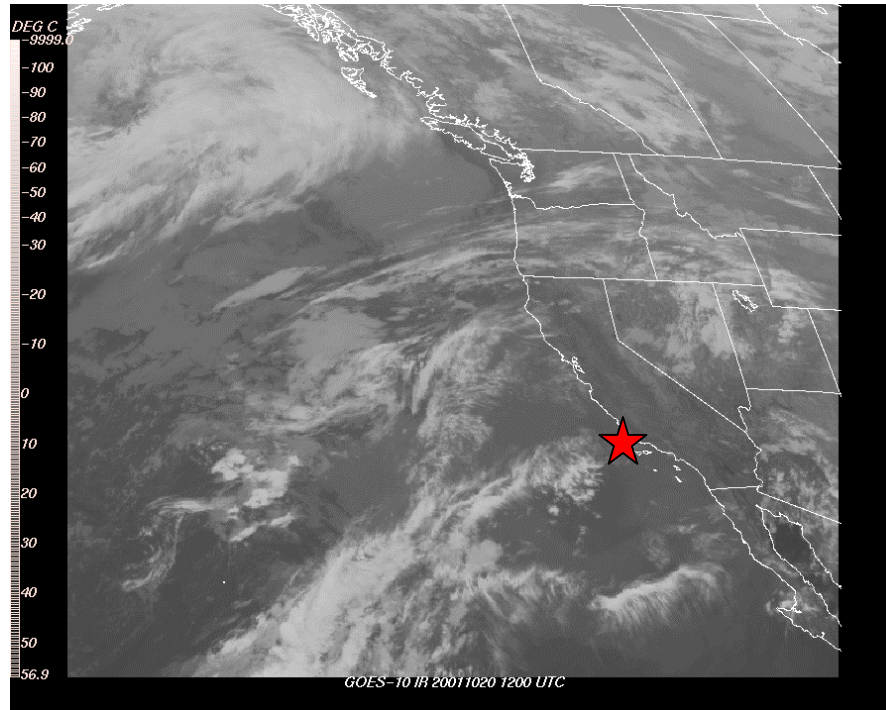


Figure A.31 Infrared Satellite Image 12Z 20 October 2001, moisture plume from SW [Adapted from NCDC 2001]

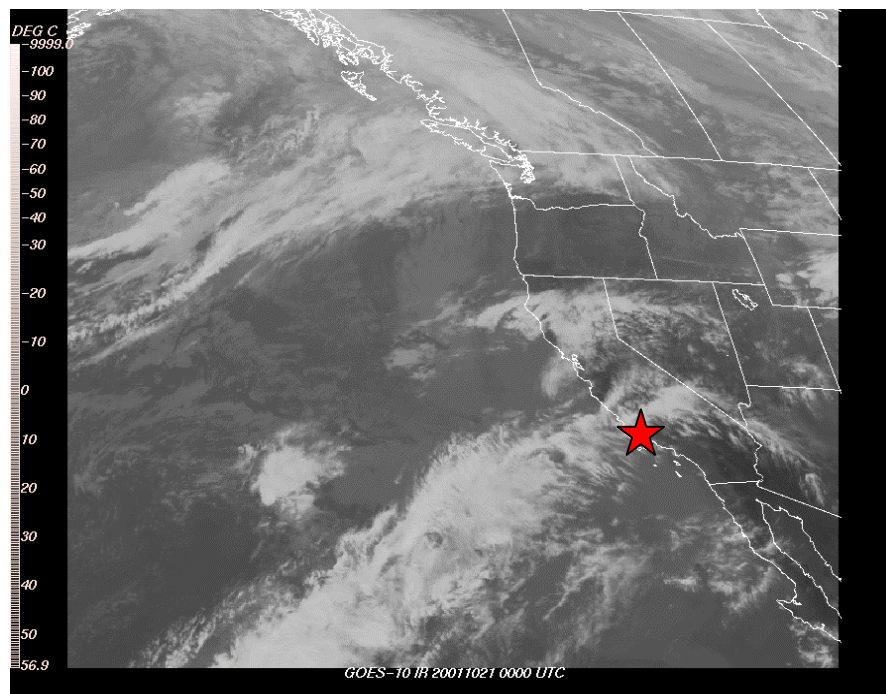


Figure A.32 Infrared Satellite Image 00Z 21 October 2001, moisture plume from SW [Adapted from NCDC 2001]

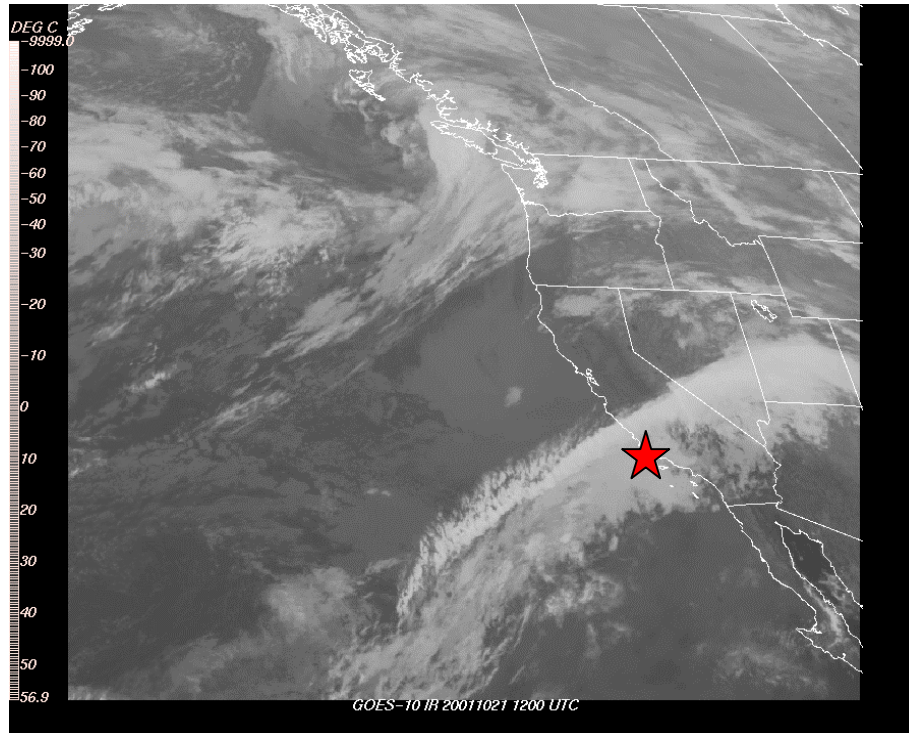


Figure A.33 Infrared Satellite Image 12Z 21 October 2001, jet axis just north of moisture plume [Adapted from NCDC 2001]

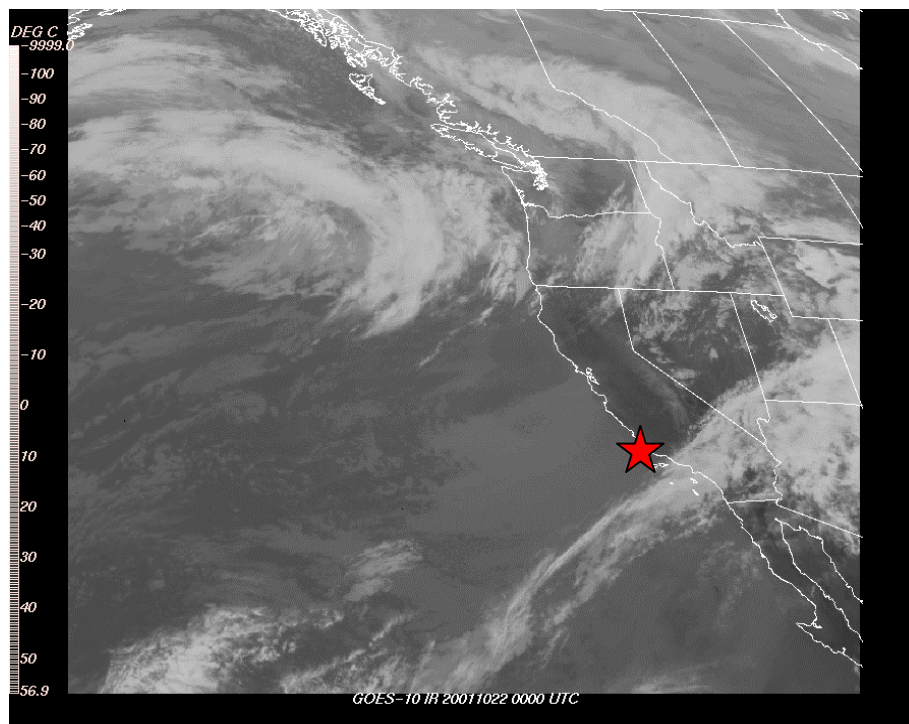


Figure A.34 Infrared Satellite Image 00Z 22 October 2001, high pressure builds as jet axis moves southward [Adapted from NCDC 2001]

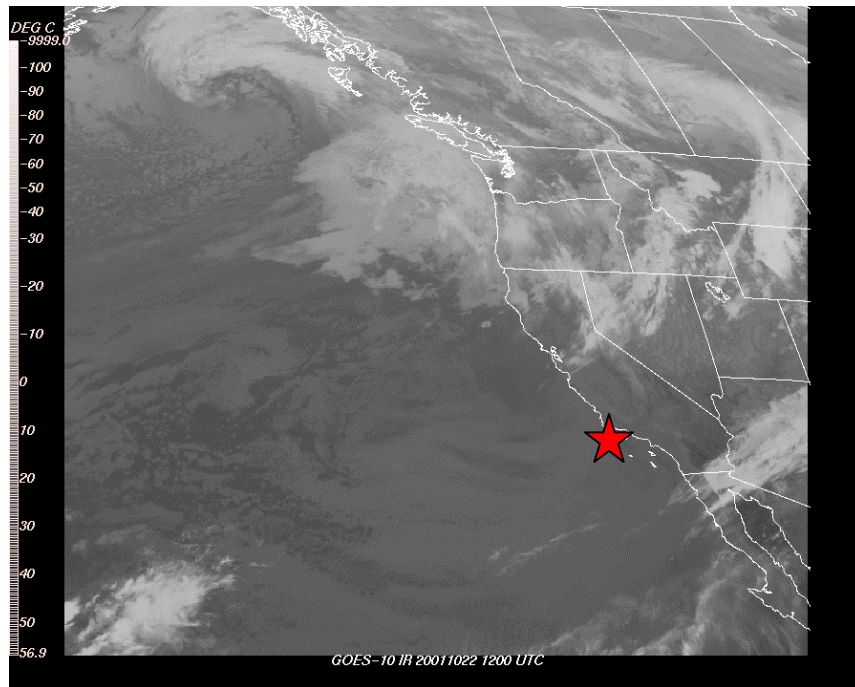


Figure A.35 Infrared Satellite Image 12Z 22 October 2001, high pressure dominant [Adapted from NCDC]



Figure A.36 Water Vapor Satellite Image 12Z 19 October 2001, upper front bringing moisture from SW [Adapted from NCDC 2001]

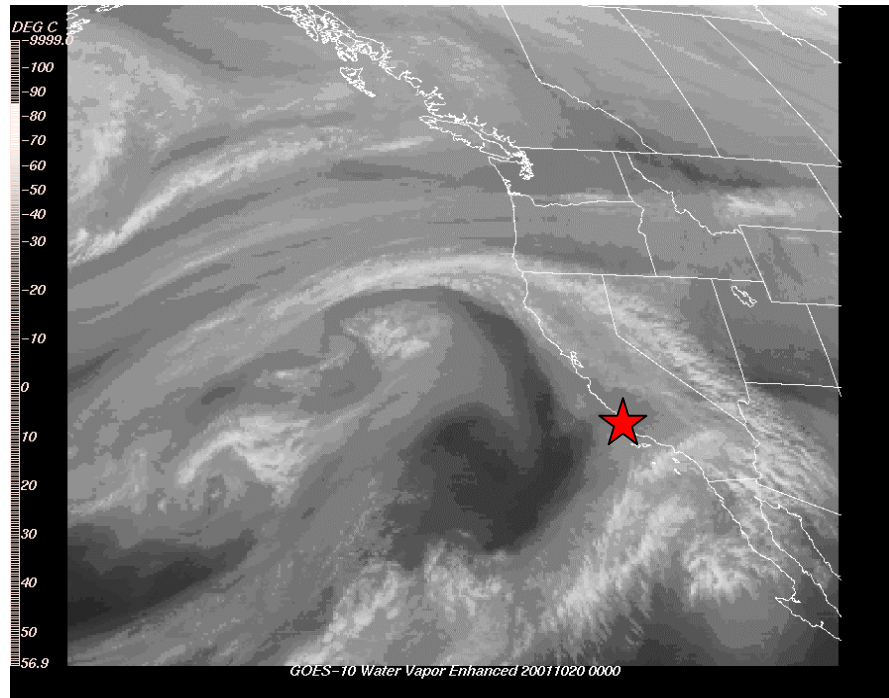


Figure A.37 Water Vapor Satellite Image 00Z 20 October 2001, upper boundary moving inland [Adapted from NCDC 2001]

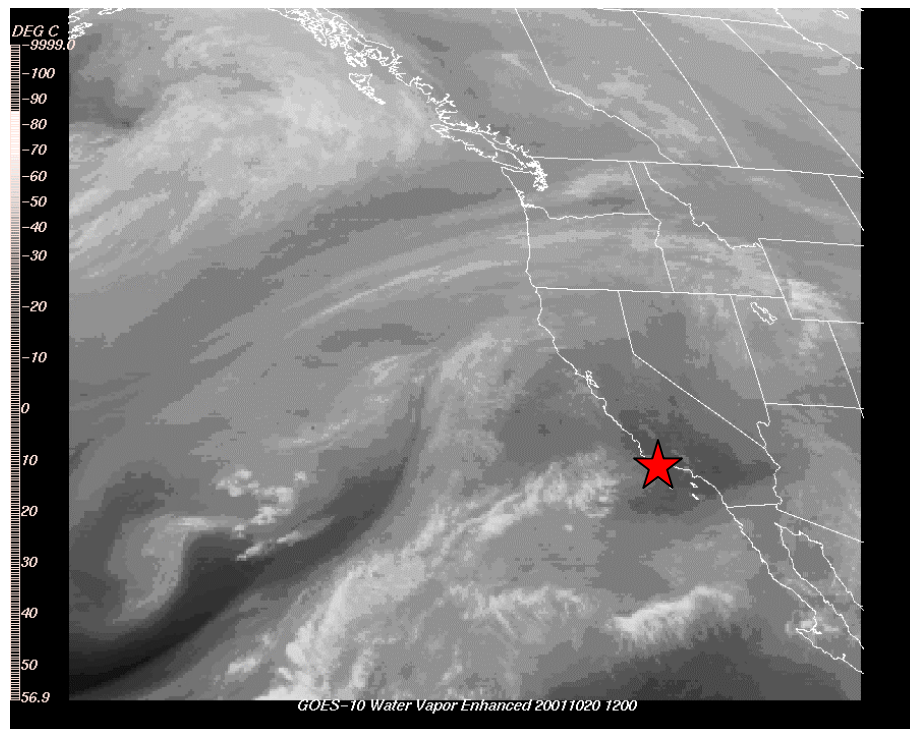


Figure A.38 Water Vapor Satellite Image 12Z 20 October 2001, moisture plume moving from SW around weakening vorticity maximum in Pacific [Adapted from NCDC 2001]

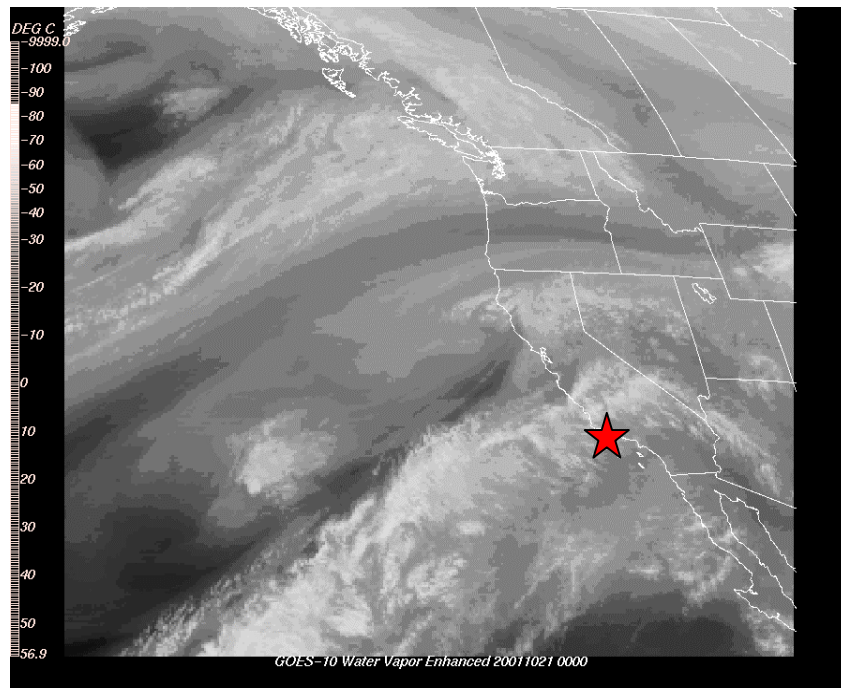


Figure A.39 Water Vapor Satellite Image 00Z 21 October 2001, moisture plume from SW evident as jet becomes more prominent from SW [Adapted from NCDC 2001]

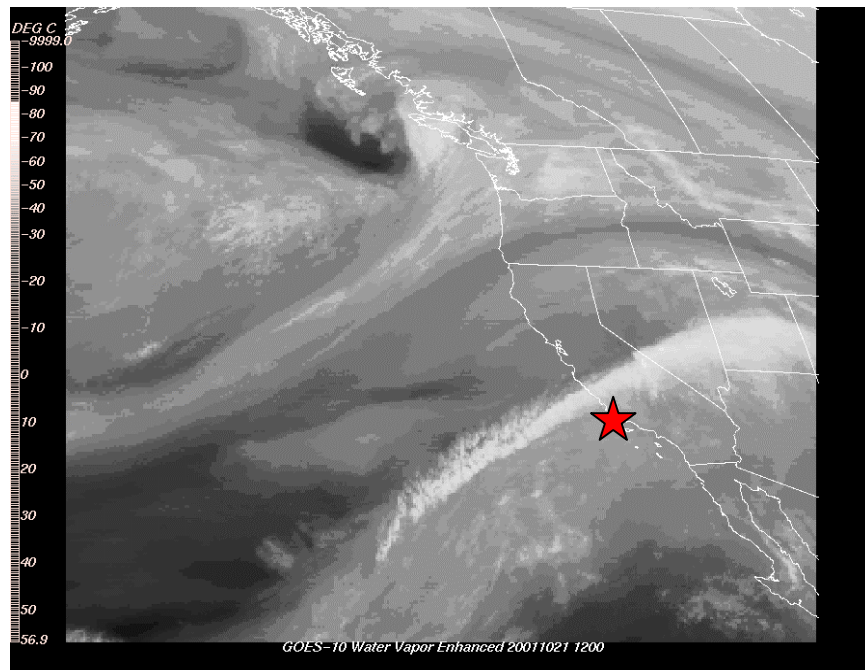


Figure A.40 Water Vapor Satellite Image 12Z 21 October 2001, jet evident over top of ridge outlining moisture plume [Adapted from NCDC 2001]

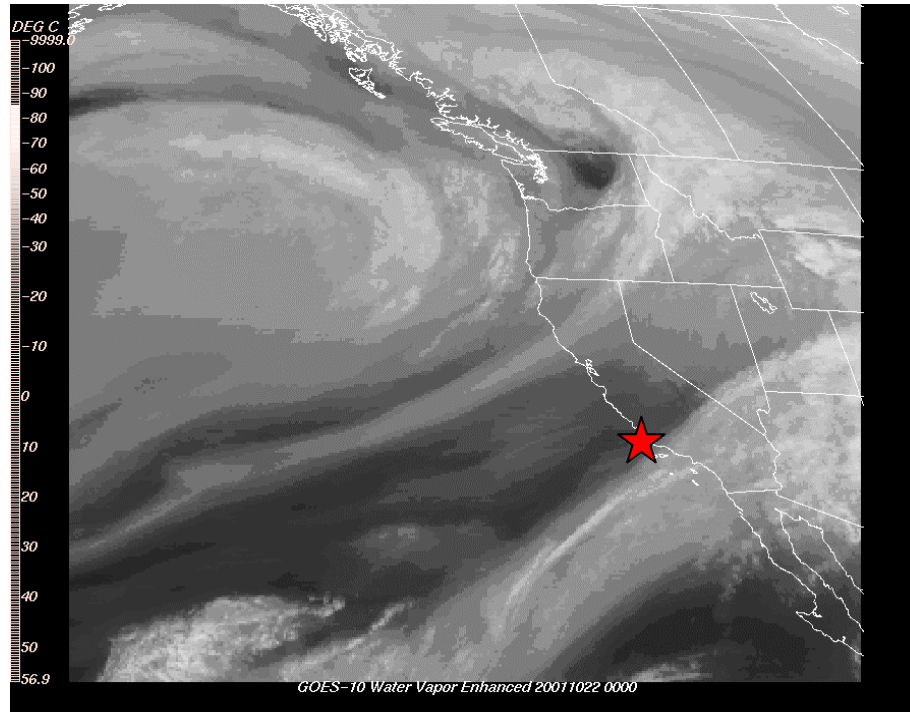


Figure A.41 Water Vapor Satellite Image 00Z 22 October 2001, maximum moving over region [Adapted from NCDC 2001]

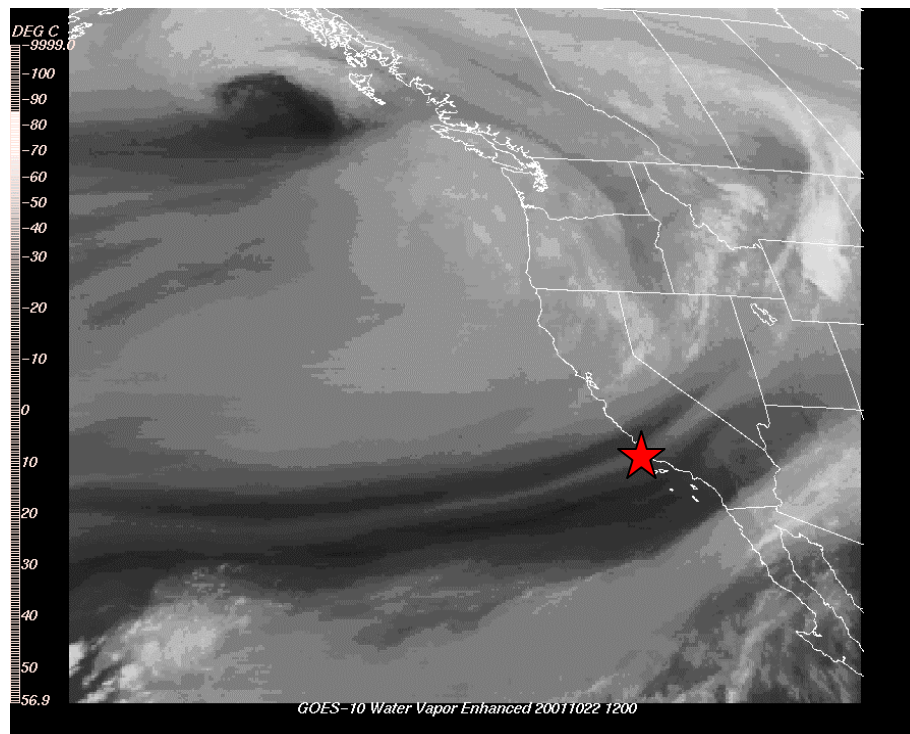


Figure A.42 Water Vapor Satellite Image 12Z 22 October 2001, jet maximum moving southward over S. California [Adapted from NCDC 2001]

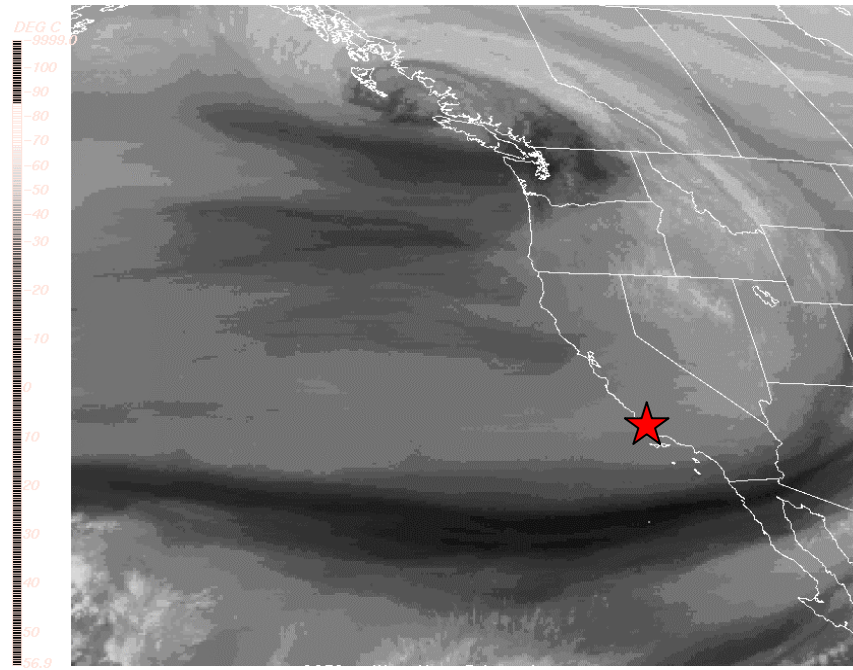


Figure A.43 Water Vapor Satellite Image 00Z 23 October 2001, zonal flow as jet maximum south of region
[Adapted from NCDC 2001]

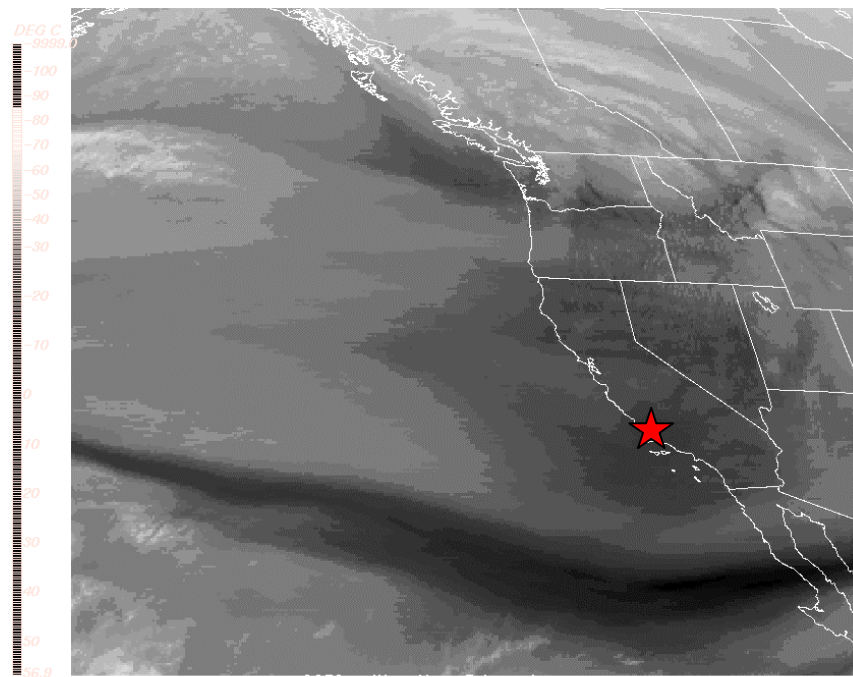


Figure A.44 Water Vapor Satellite Image 12Z 23 October 2001, jet maximum well south of region
[Adapted from NCDC 2001]

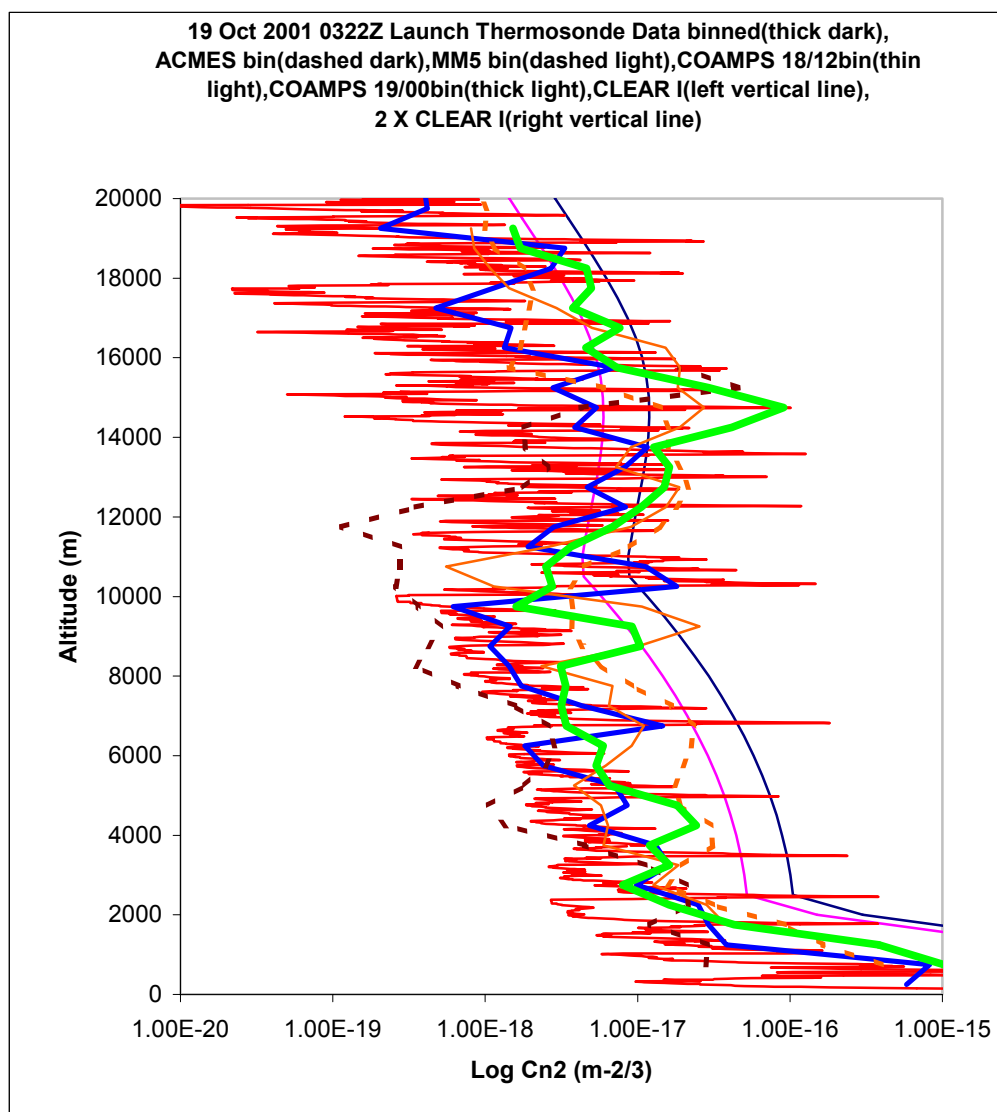


Figure A.45 Binned Vertical data Profiles for 19/0322Z Launch

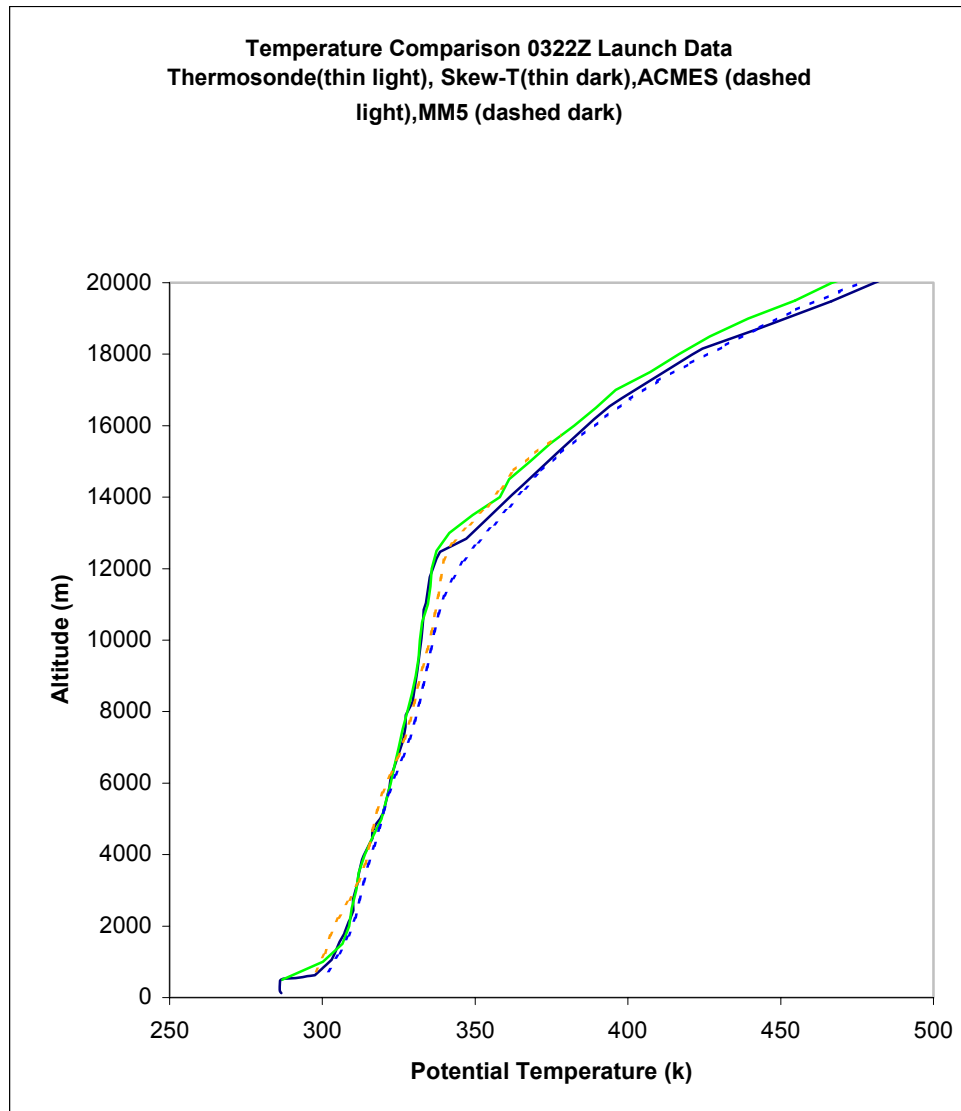


Figure A.46 Potential Temperature Profiles for 19/0322Z Launch

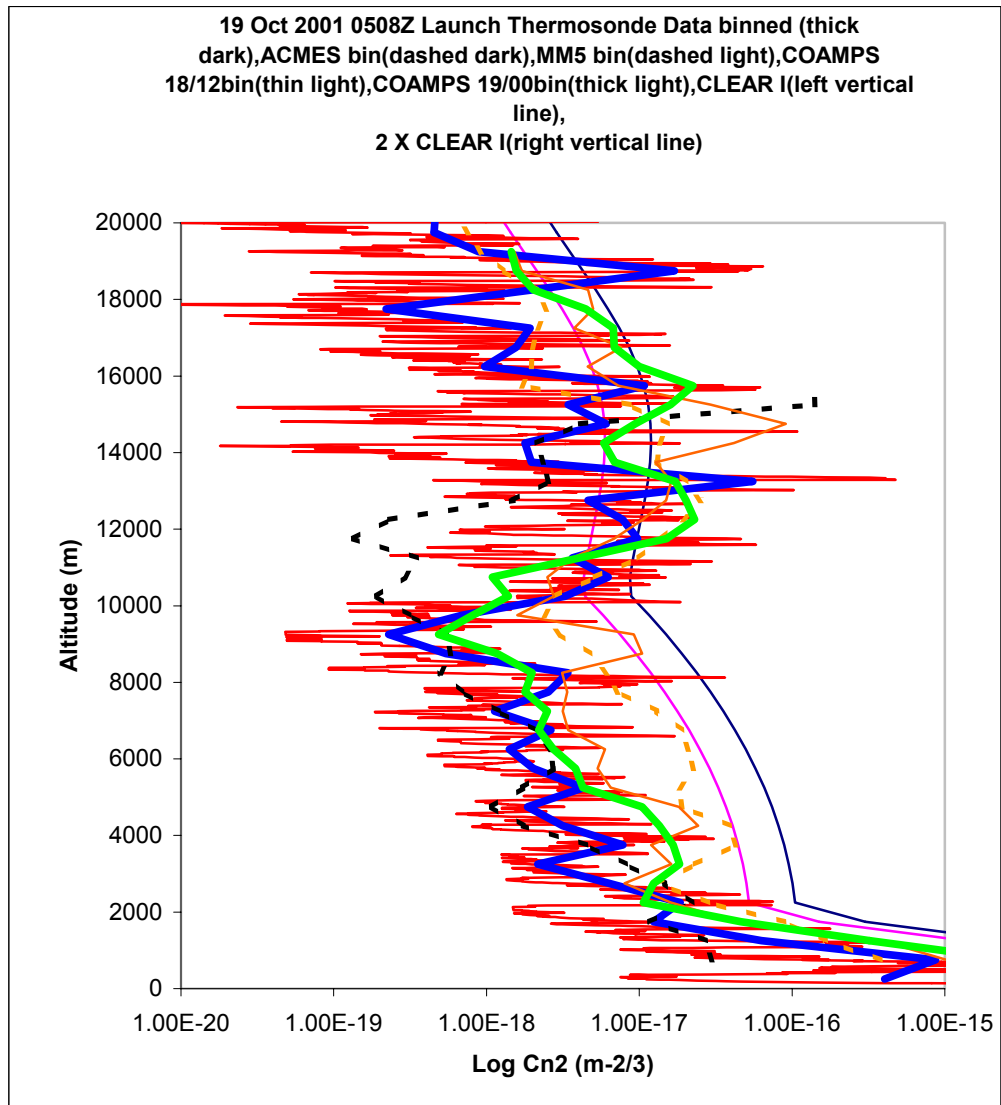


Figure A.47 Binned Vertical data Profiles for 19/0508Z Launch

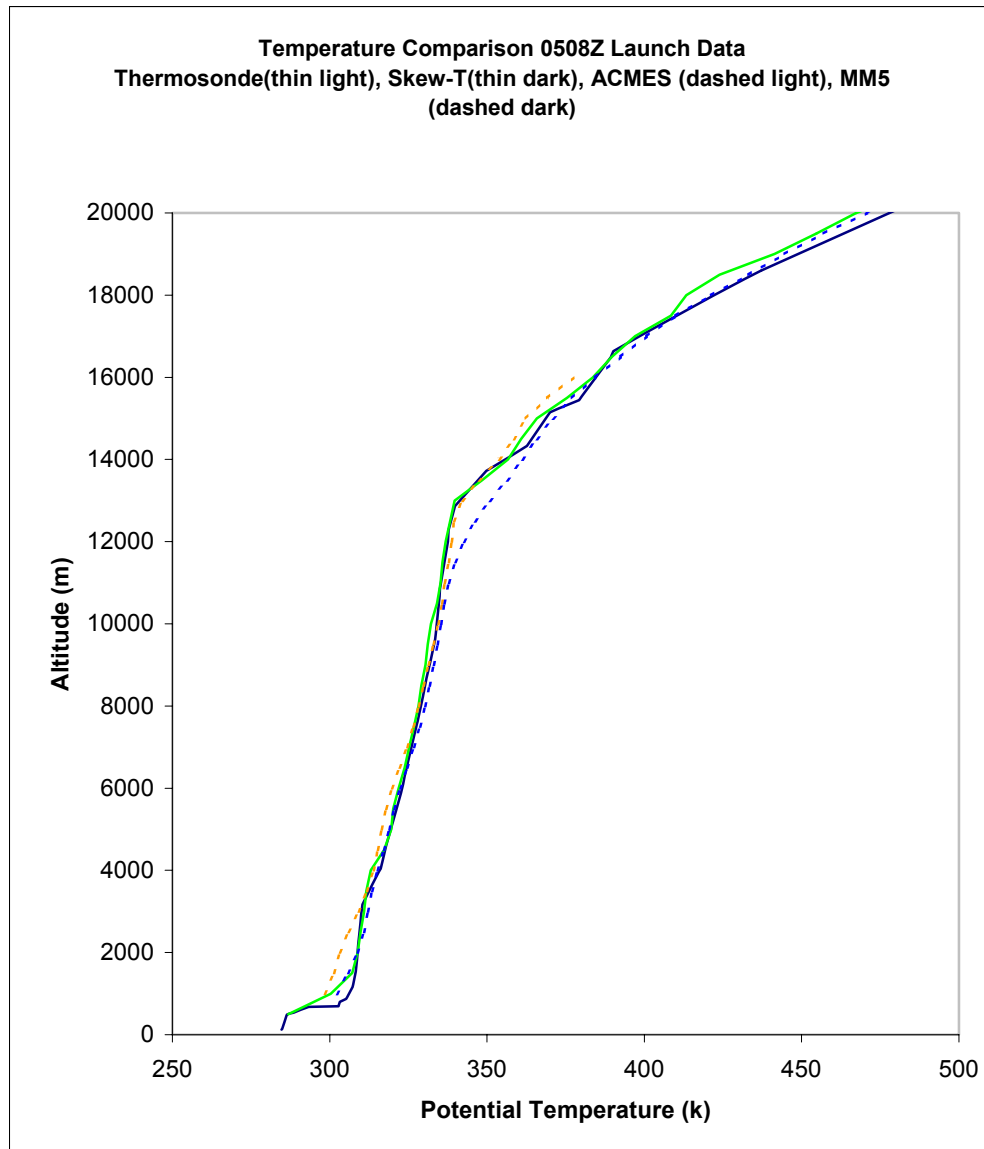


Figure A.48 Potential Temperature Profiles for 19/0508Z Launch

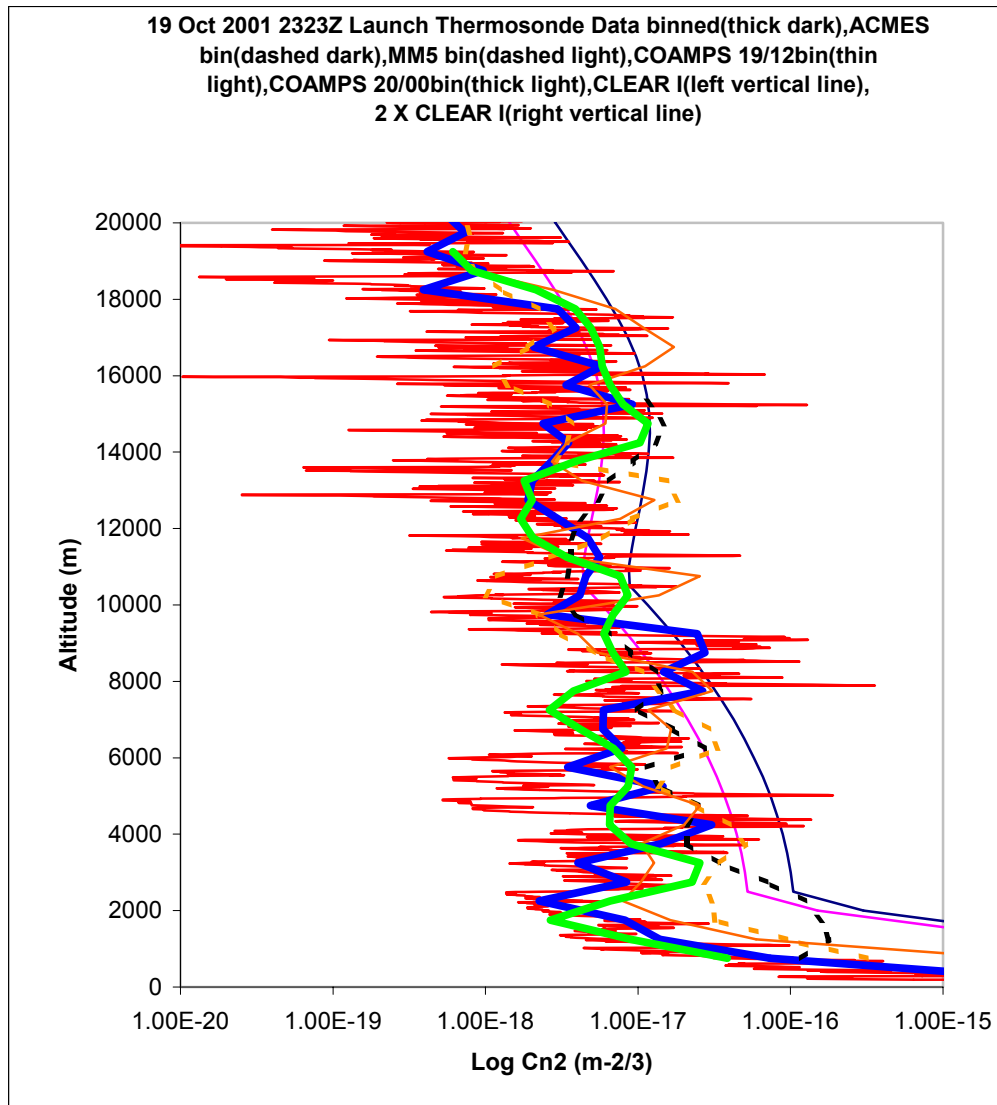


Figure A.49 Binned Vertical data Profiles for 19/2323Z Launch

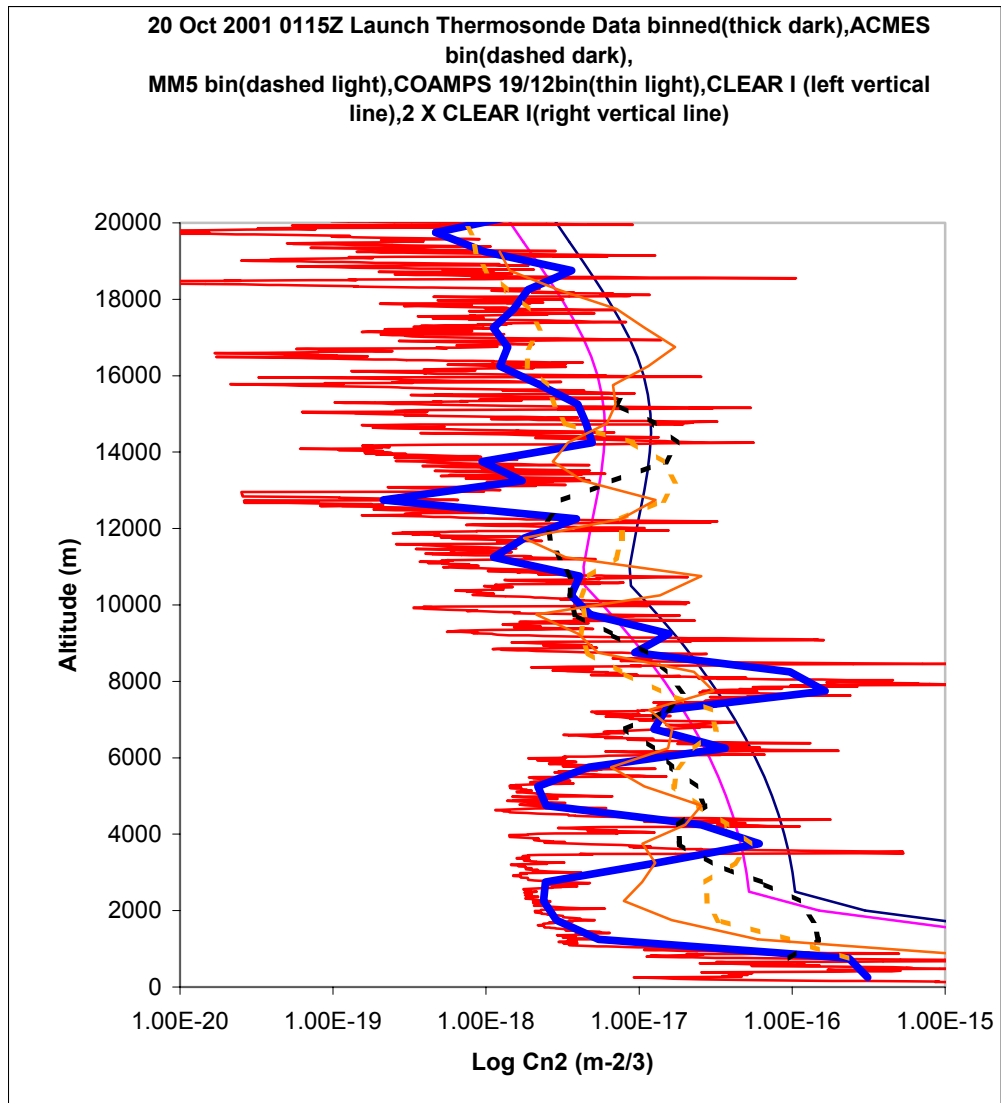


Figure A.50 Binned Vertical data Profiles for 20/0115Z Launch

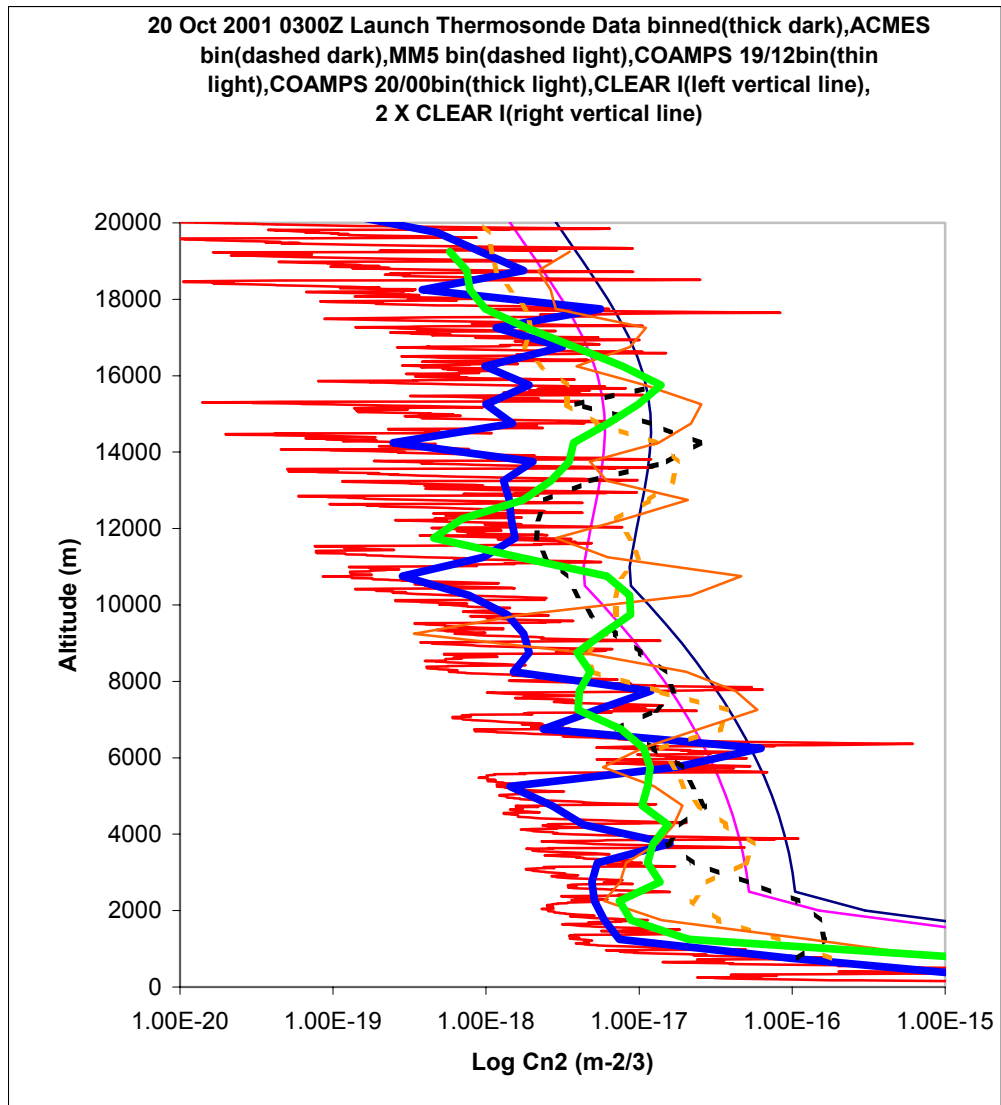


Figure A.51 Binned Vertical data Profiles for 20/0300Z Launch

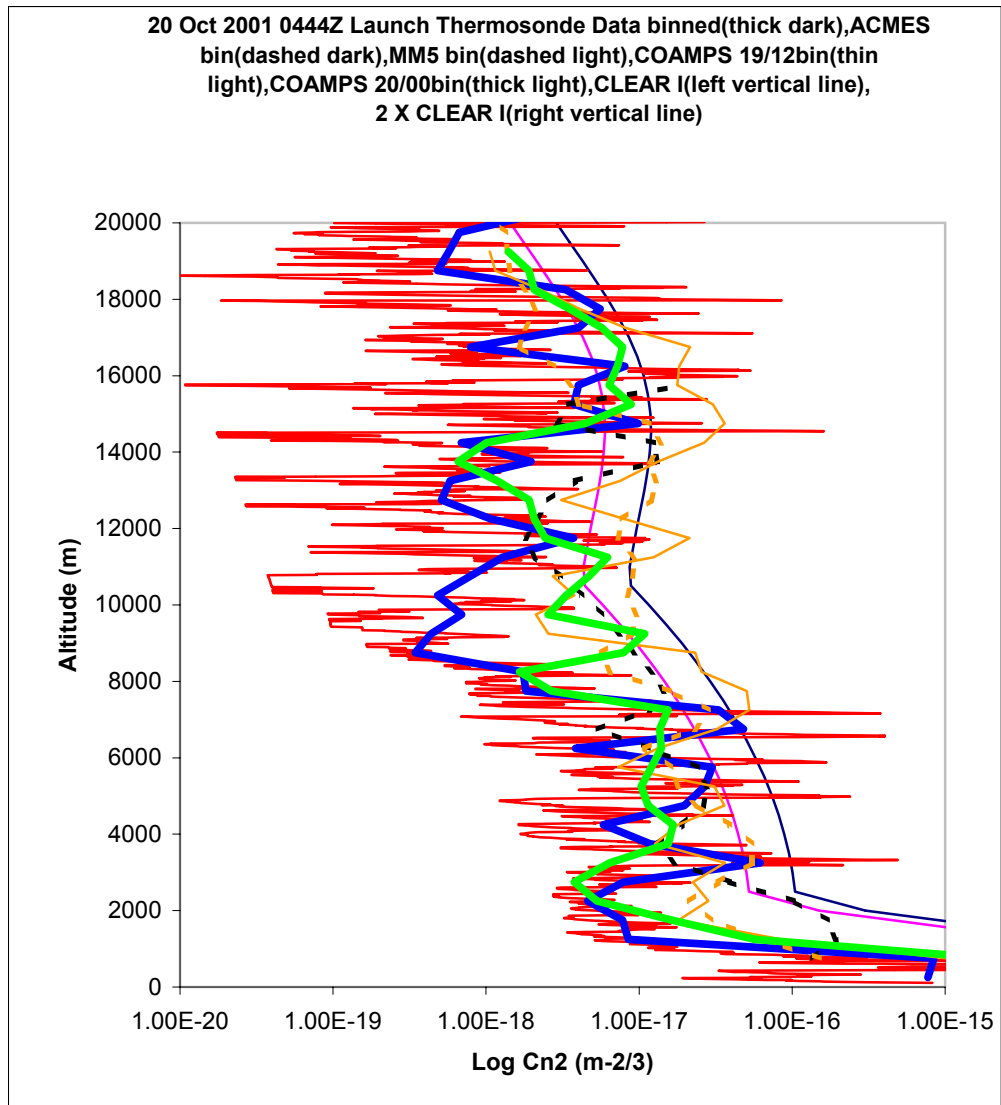


Figure A.52 Binned Vertical data Profiles for 20/0444Z Launch

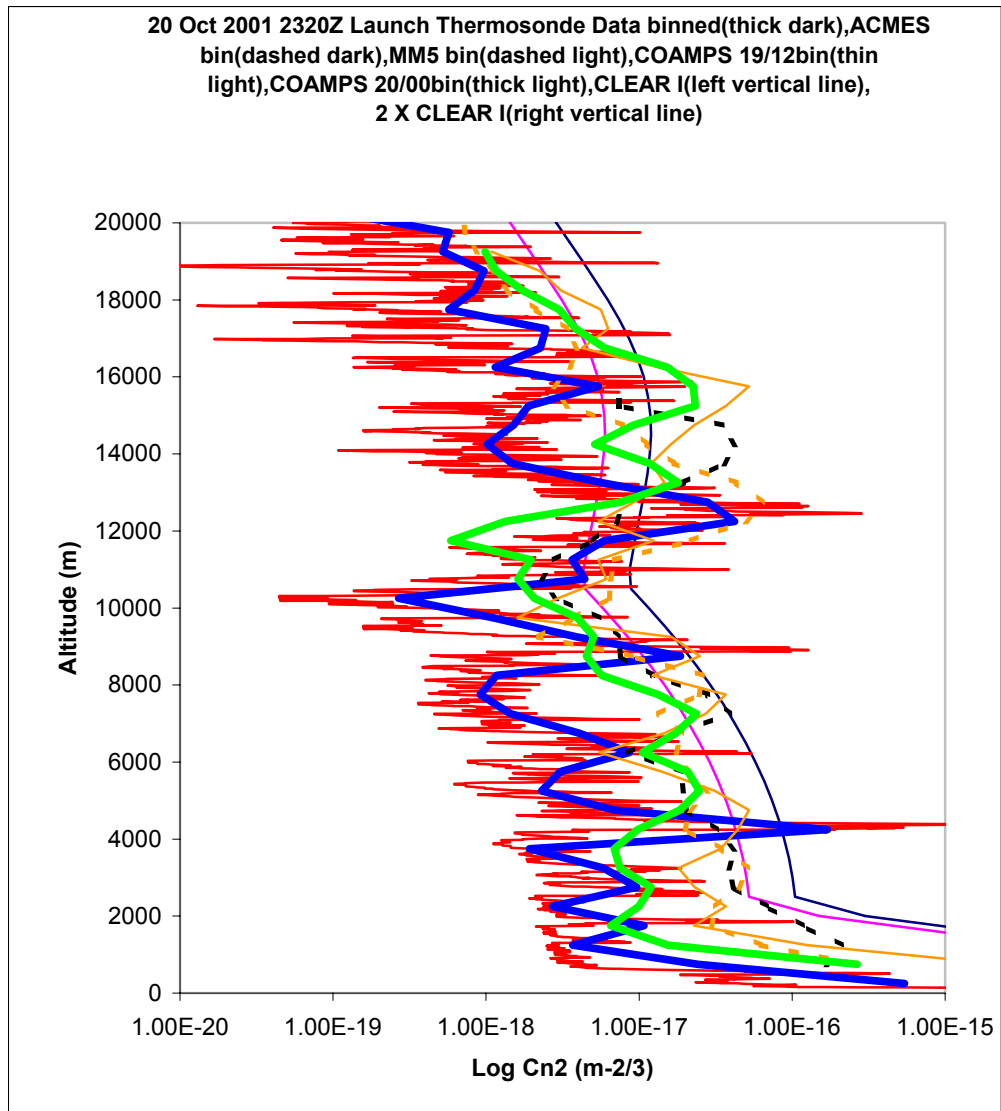


Figure A.53 Binned Vertical data Profiles for 20/2320Z Launch

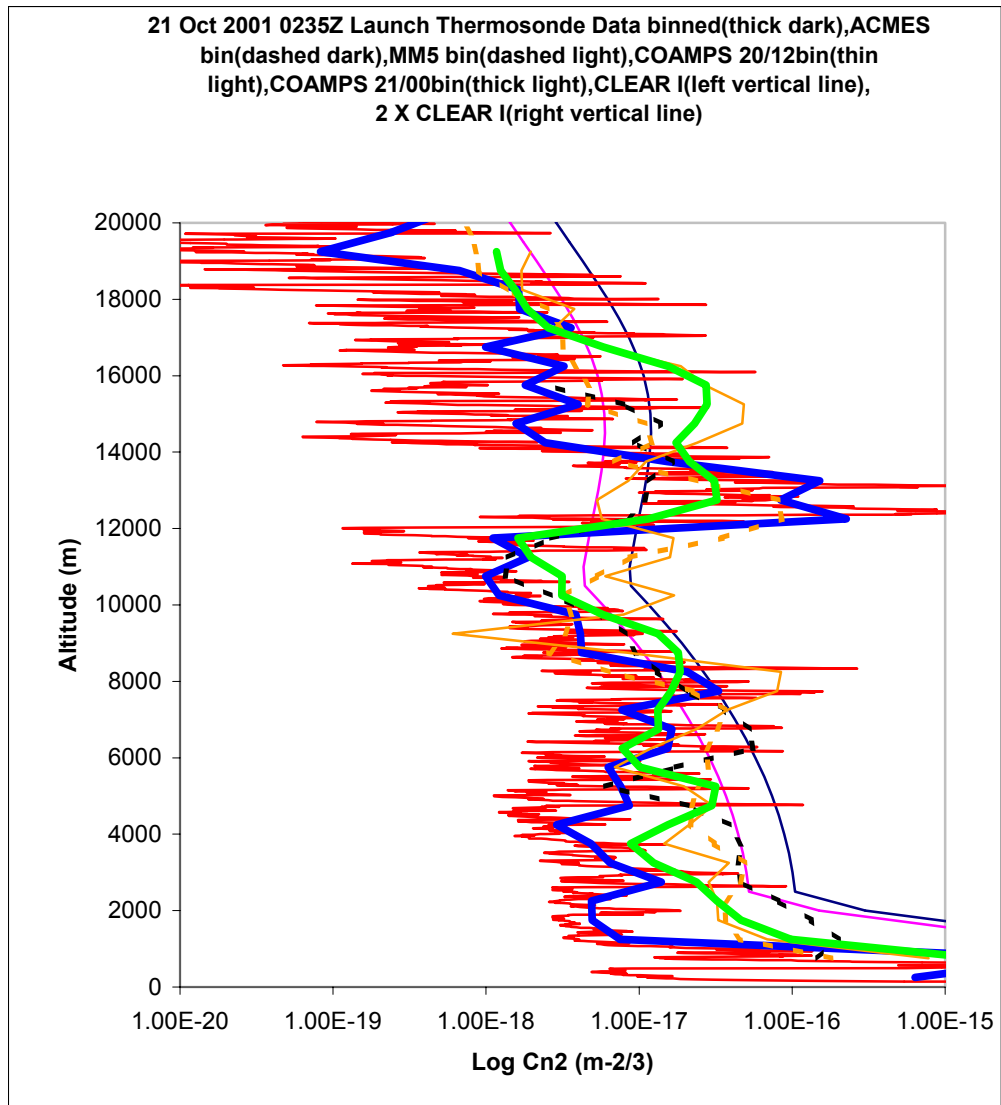


Figure A.54 Binned Vertical data Profiles for 21/0235Z Launch

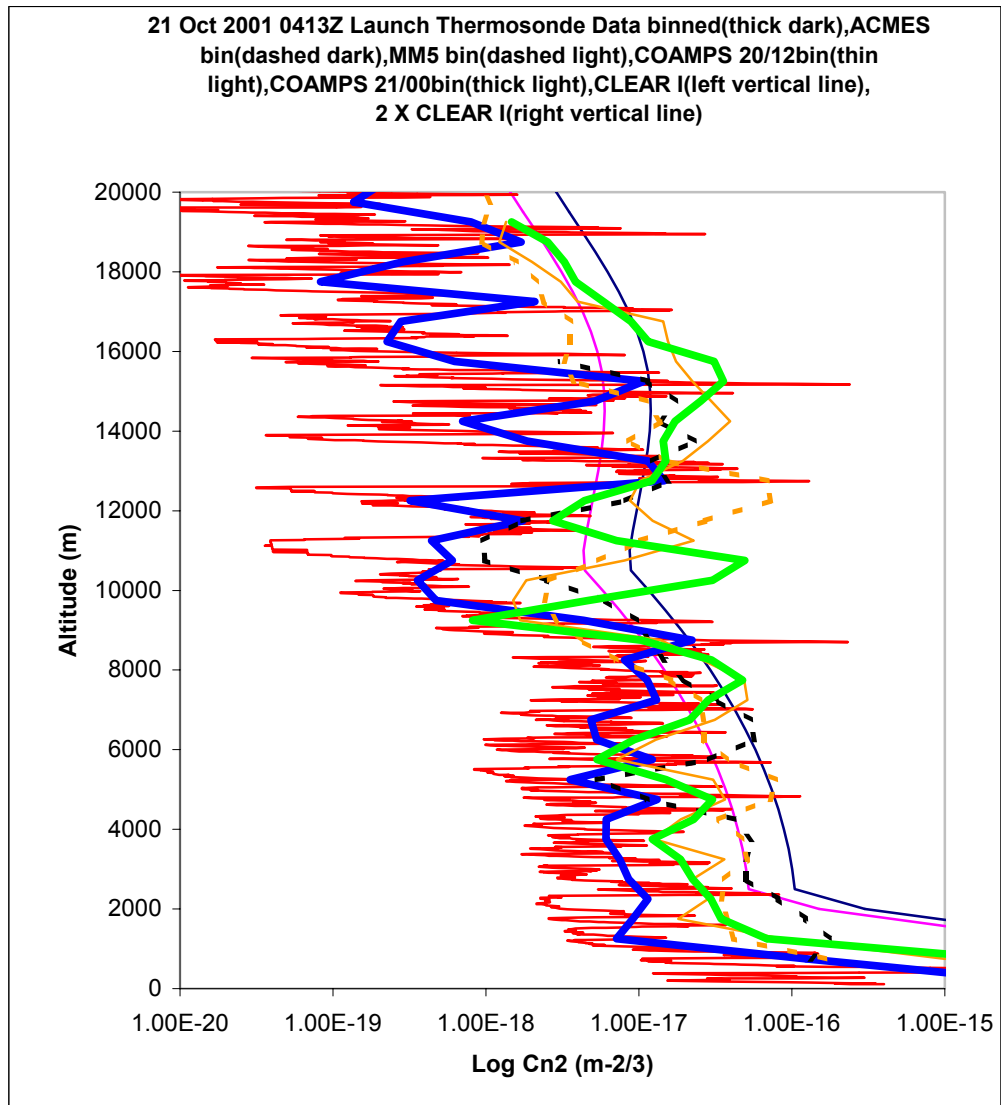


Figure A.55 Binned Vertical data Profiles for 21/0413Z Launch

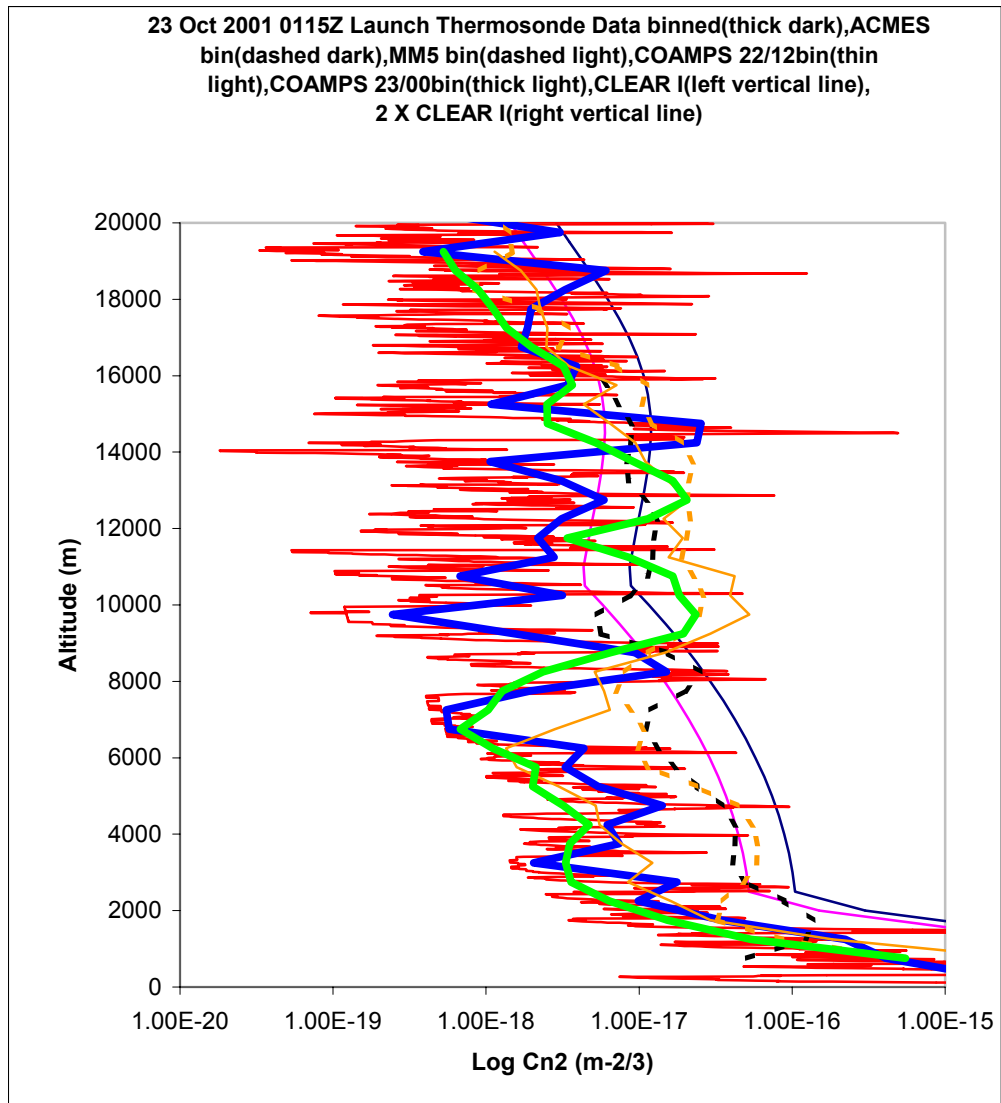


Figure A.56 Binned Vertical data Profiles for 23/0115Z Launch

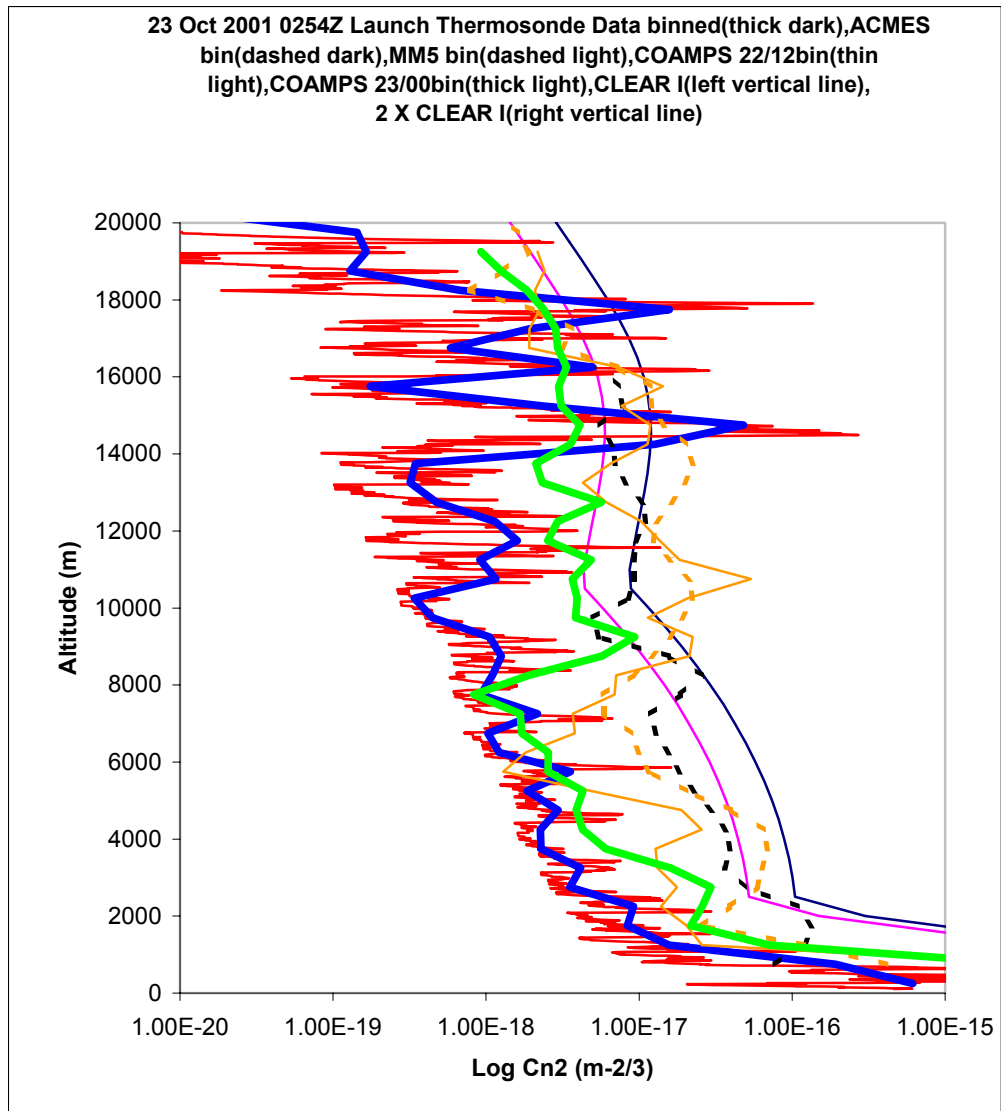


Figure A.57 Binned Vertical data Profiles for 23/0254Z Launch

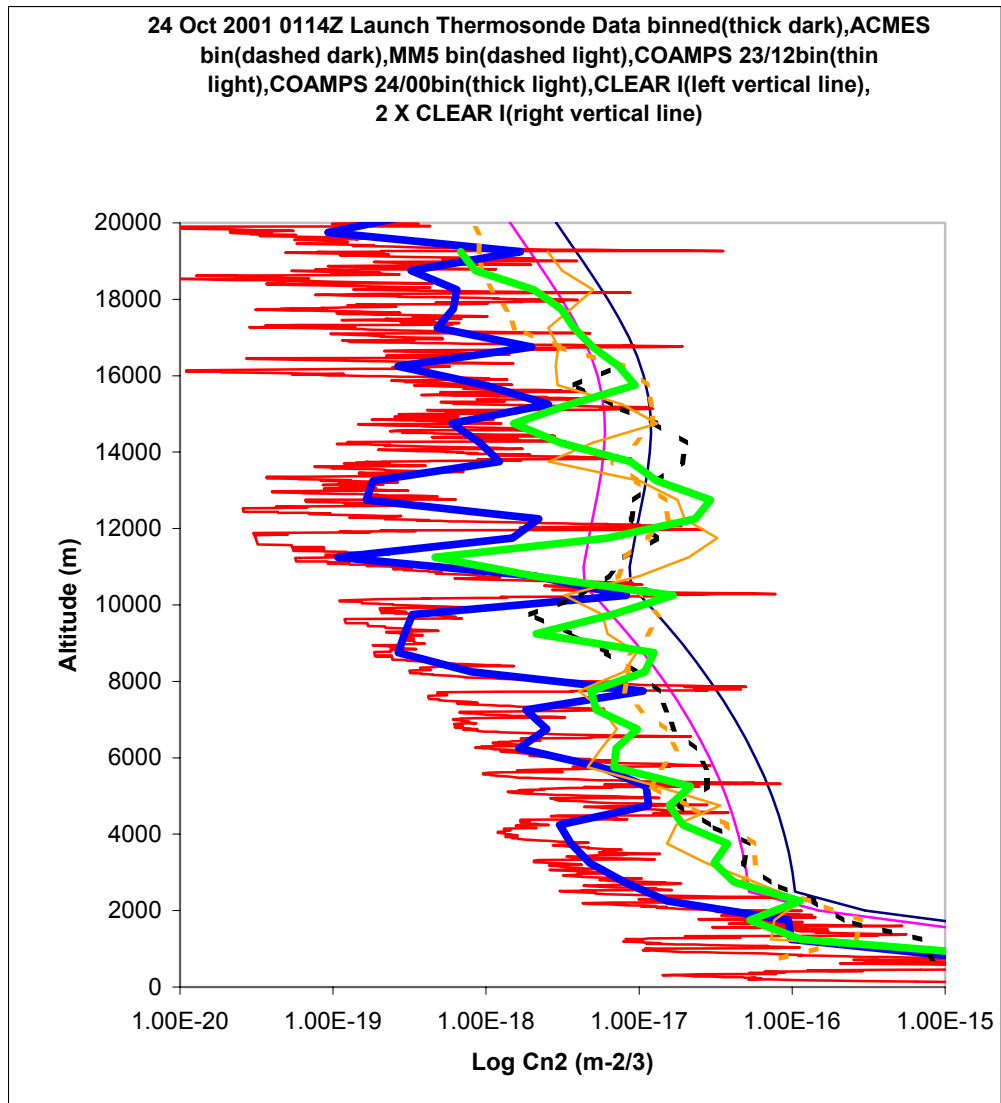


Figure A.58 Binned Vertical data Profiles for 24/0114Z Launch

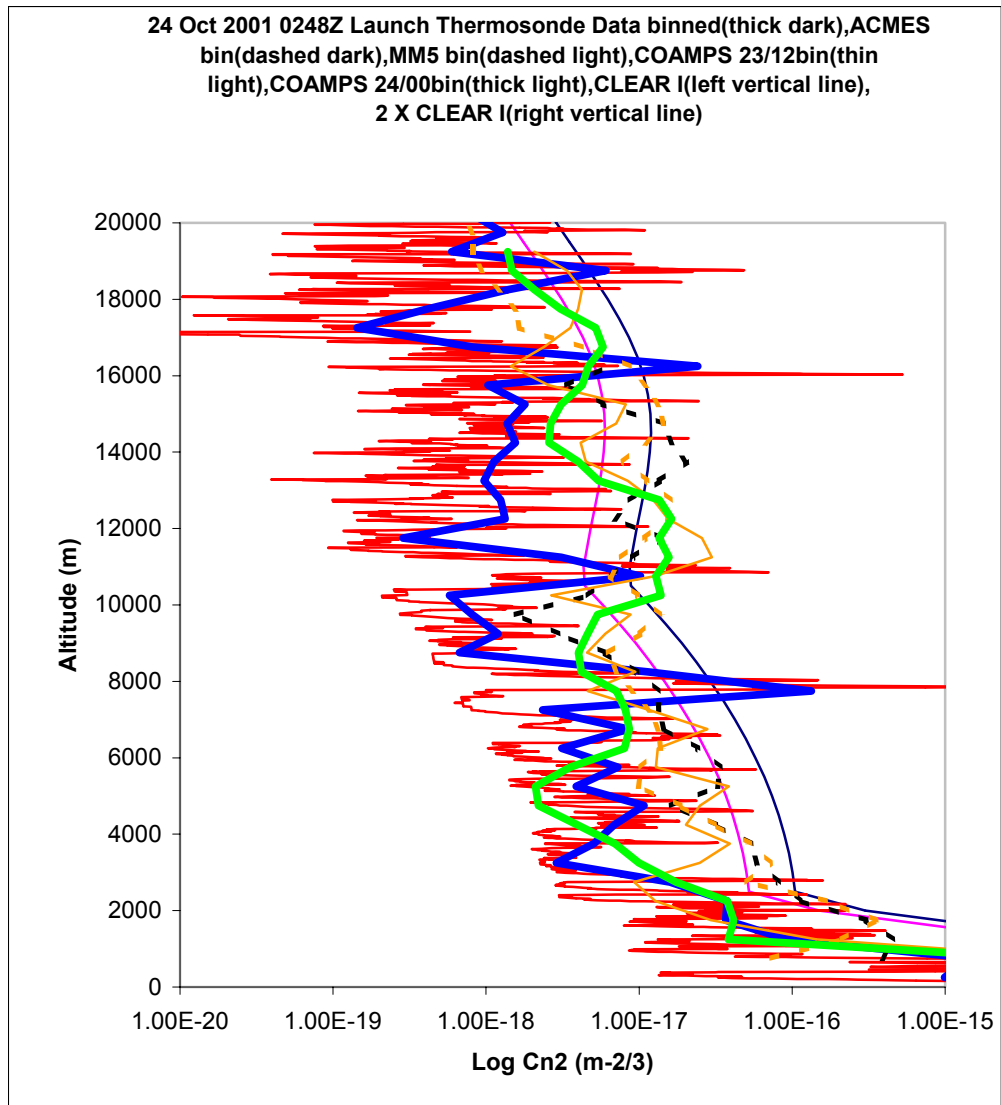


Figure A.59 Binned Vertical data Profile for 24/0248Z Launch

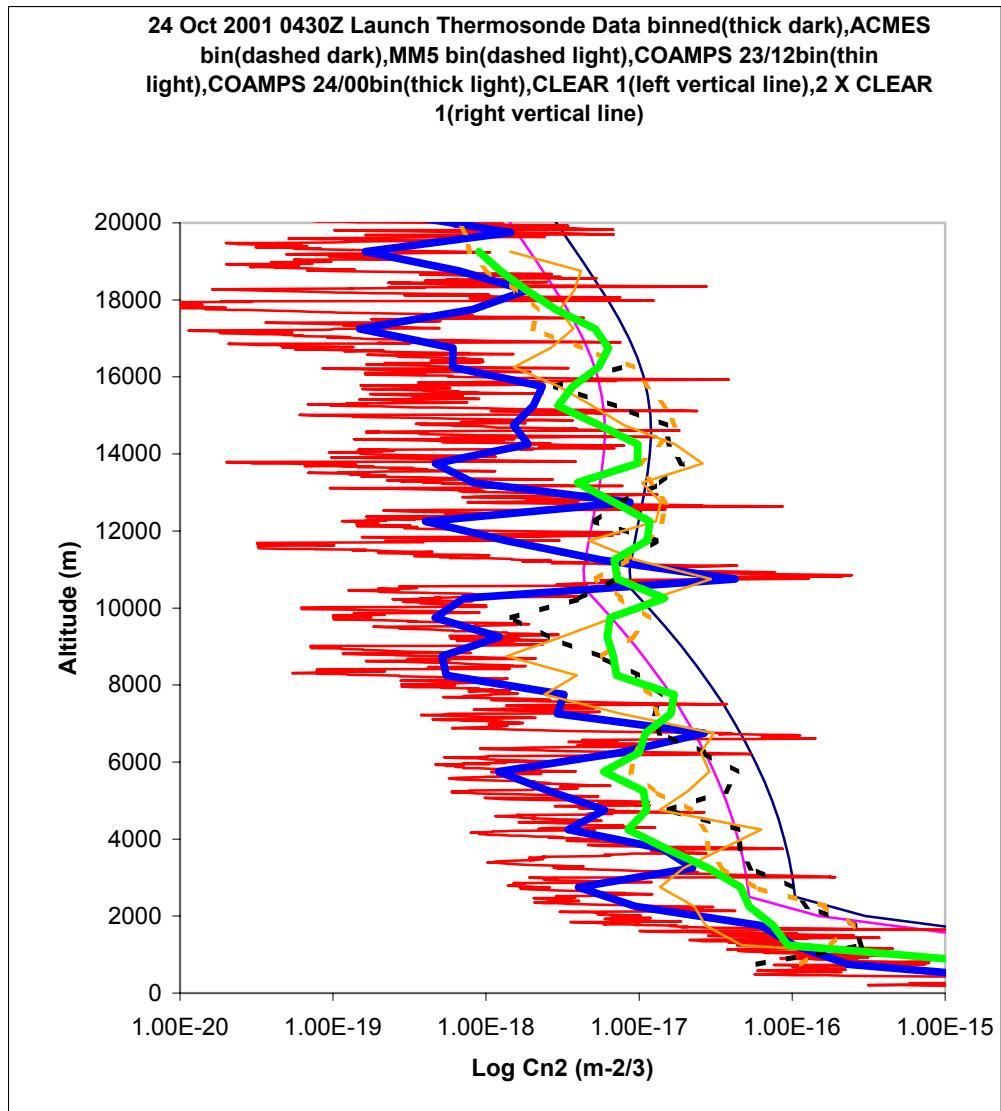


Figure A.60 Binned Vertical data Profile for 24/0430Z Launch

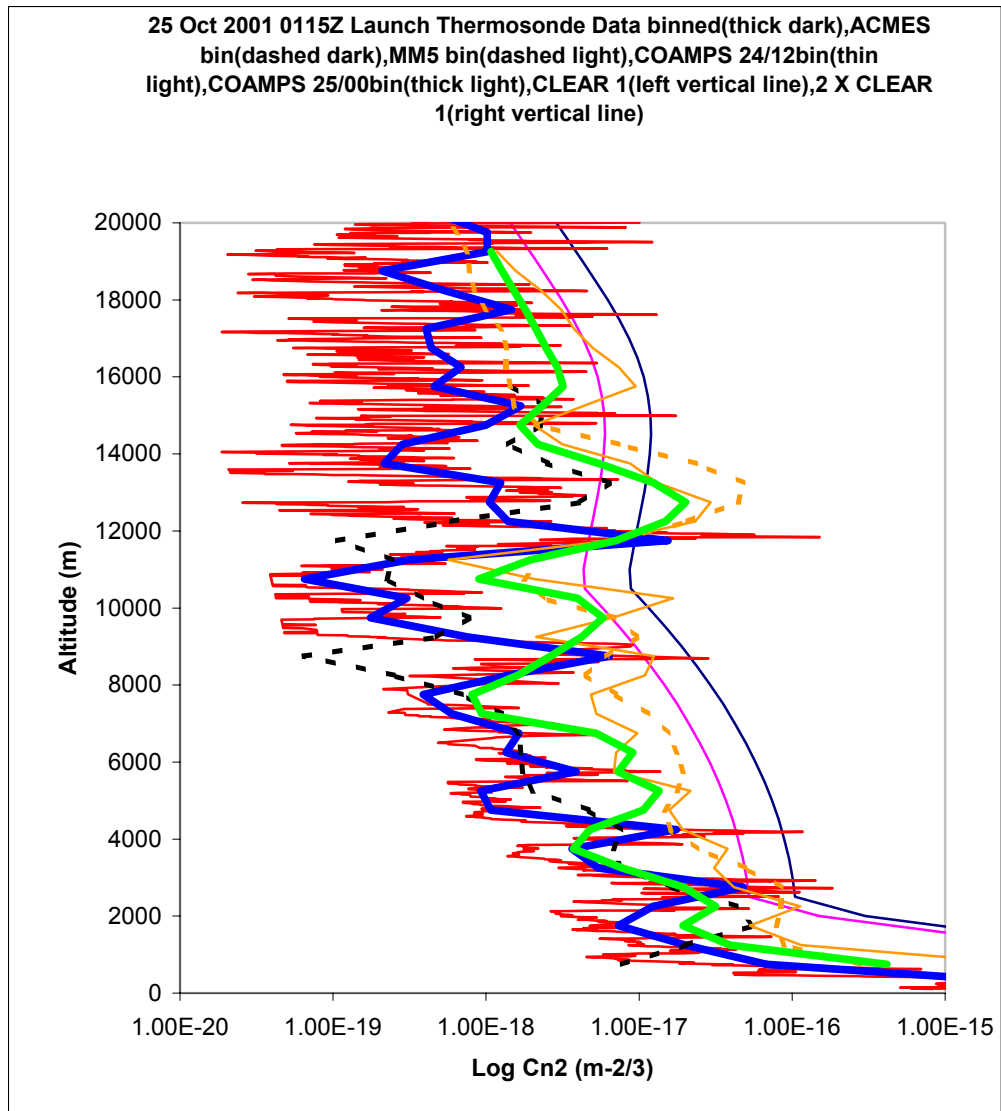


Figure A.61 Binned Vertical data Profile for 25/0115Z Launch

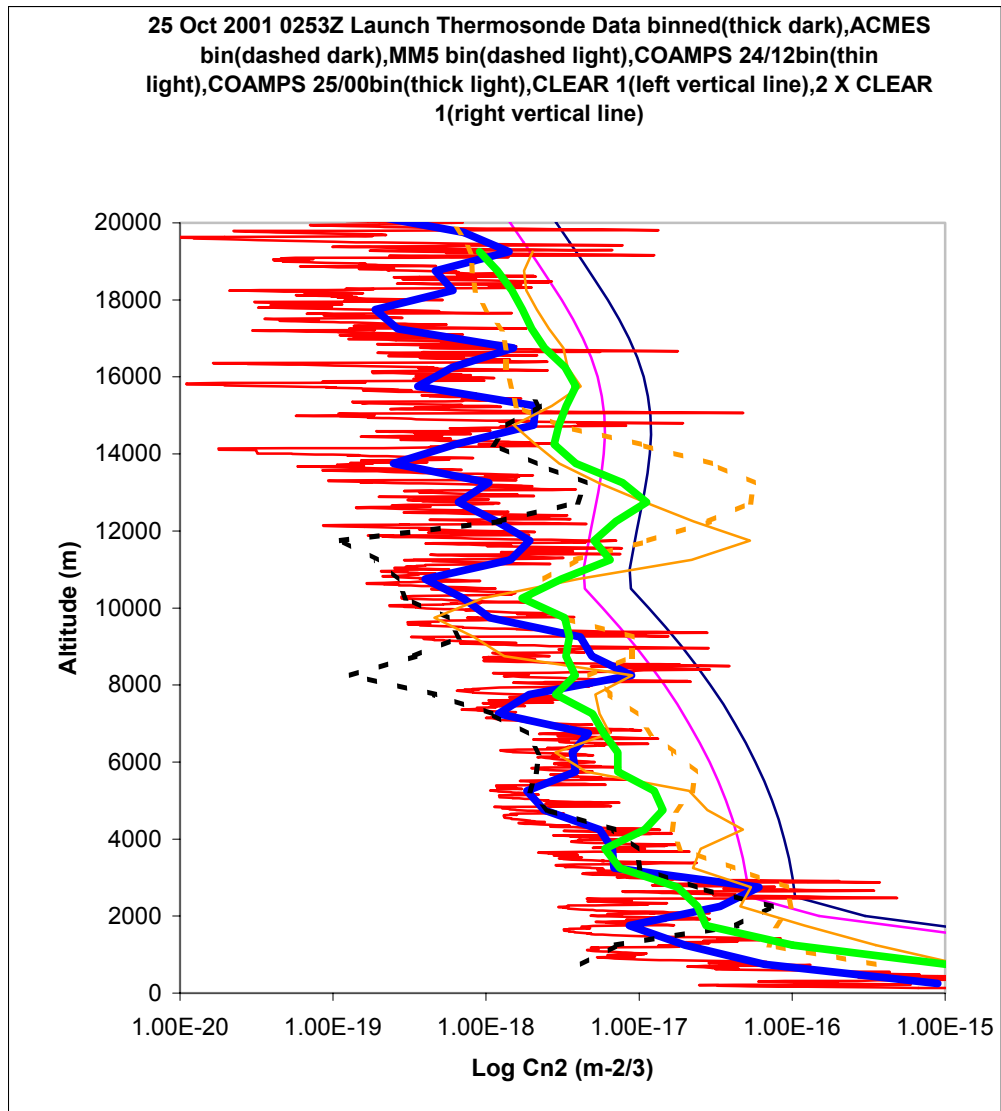


Figure A.62 Binned Vertical data Profile for 25/0253Z Launch

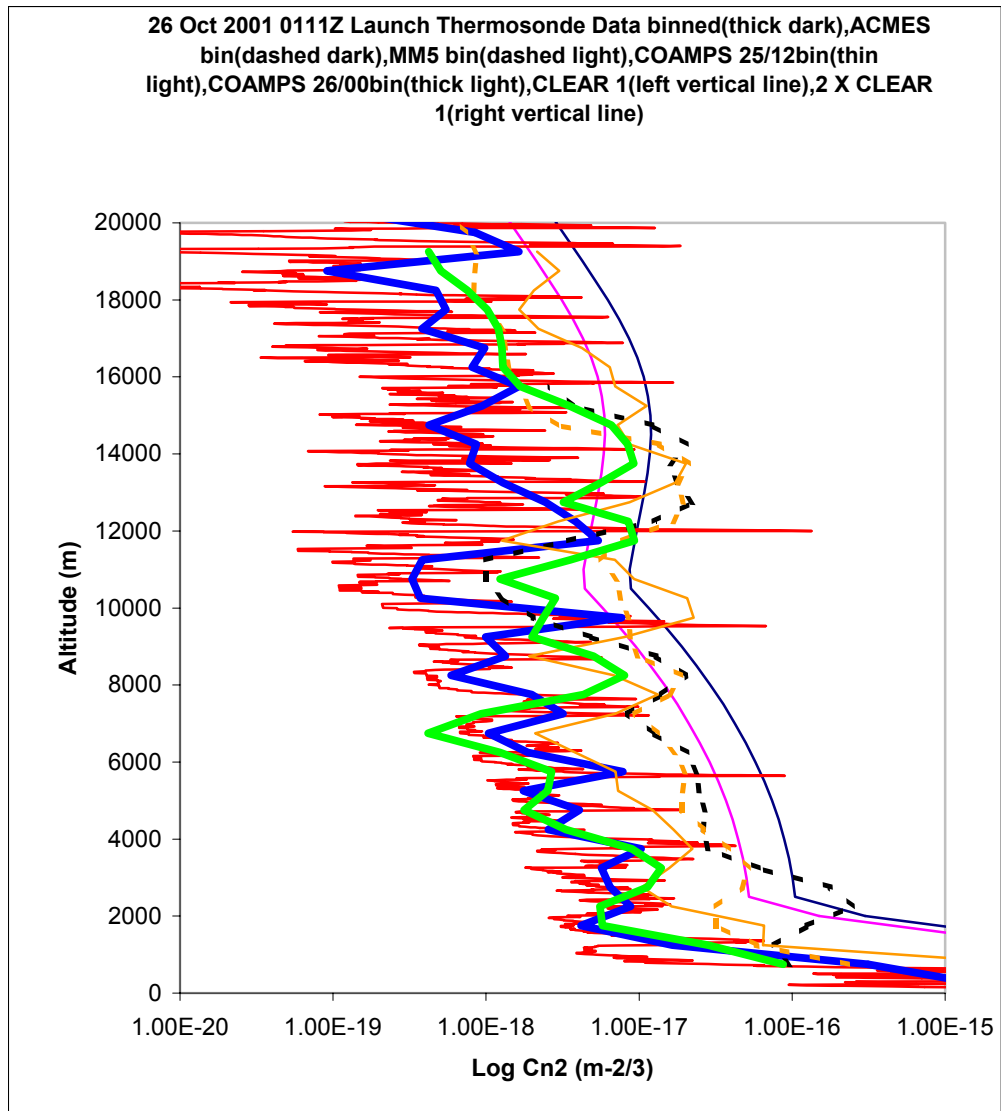


Figure A.63 Binned Vertical data Profiles for 26/0111Z Launch

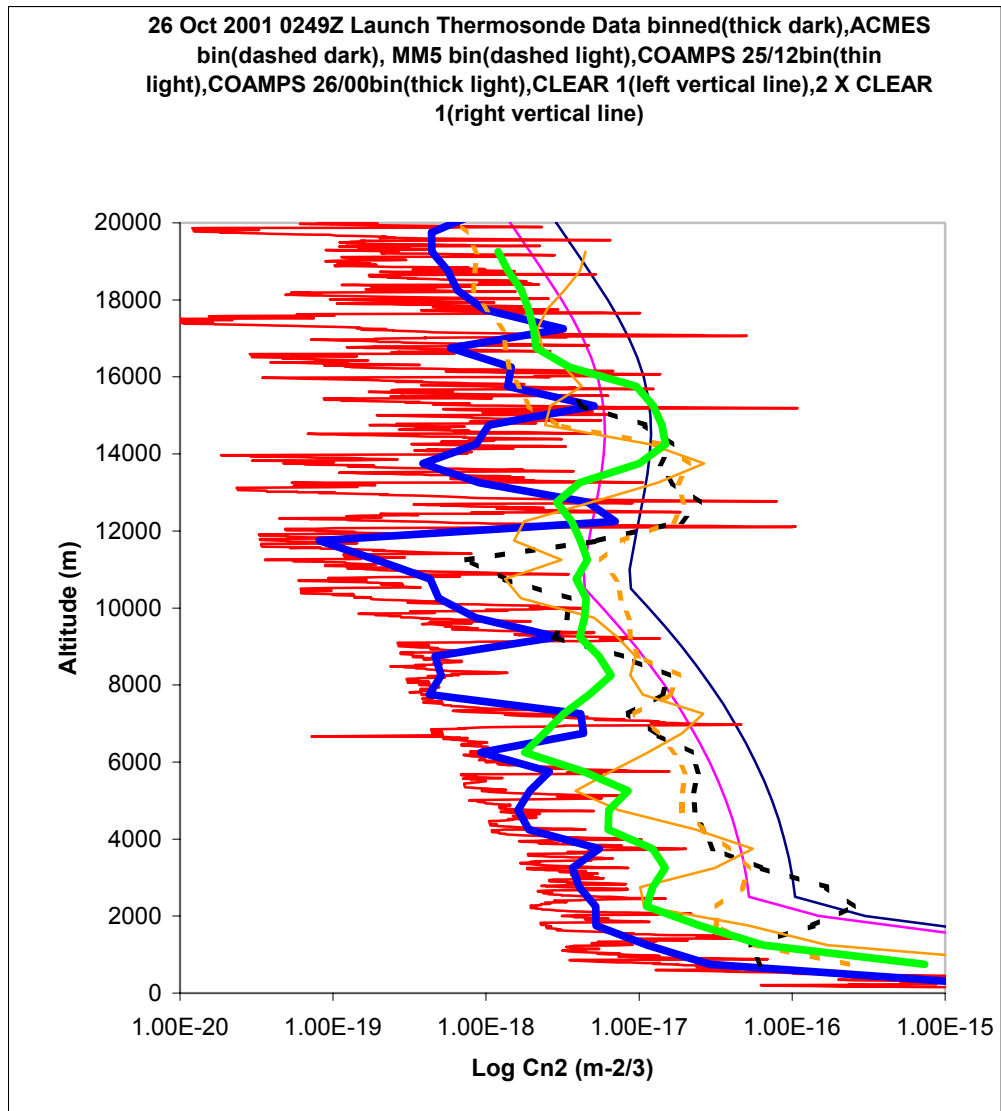


Figure A.64 Binned Vertical data Profiles for 26/0249Z Launch

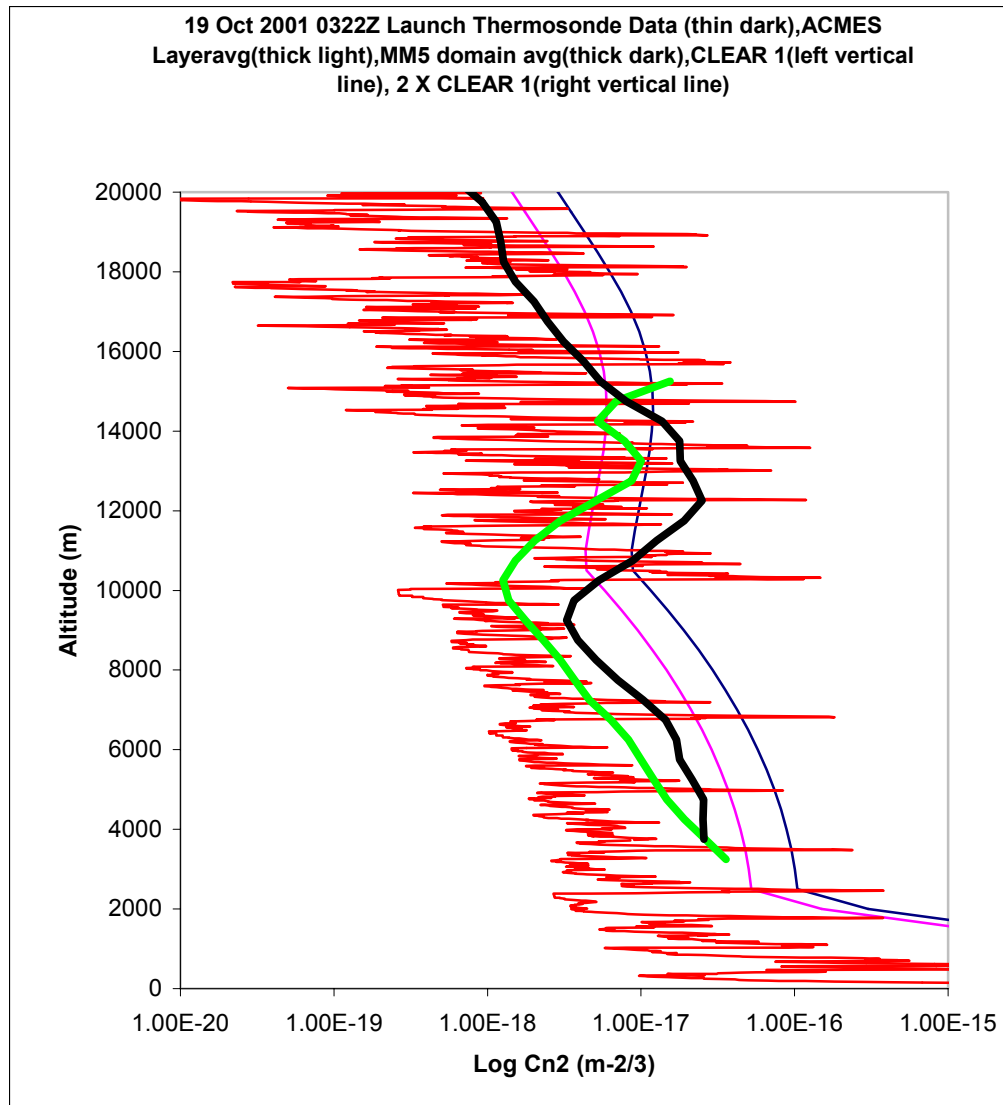


Figure A.65 Domain Average Profiles for 19/0322Z Launch

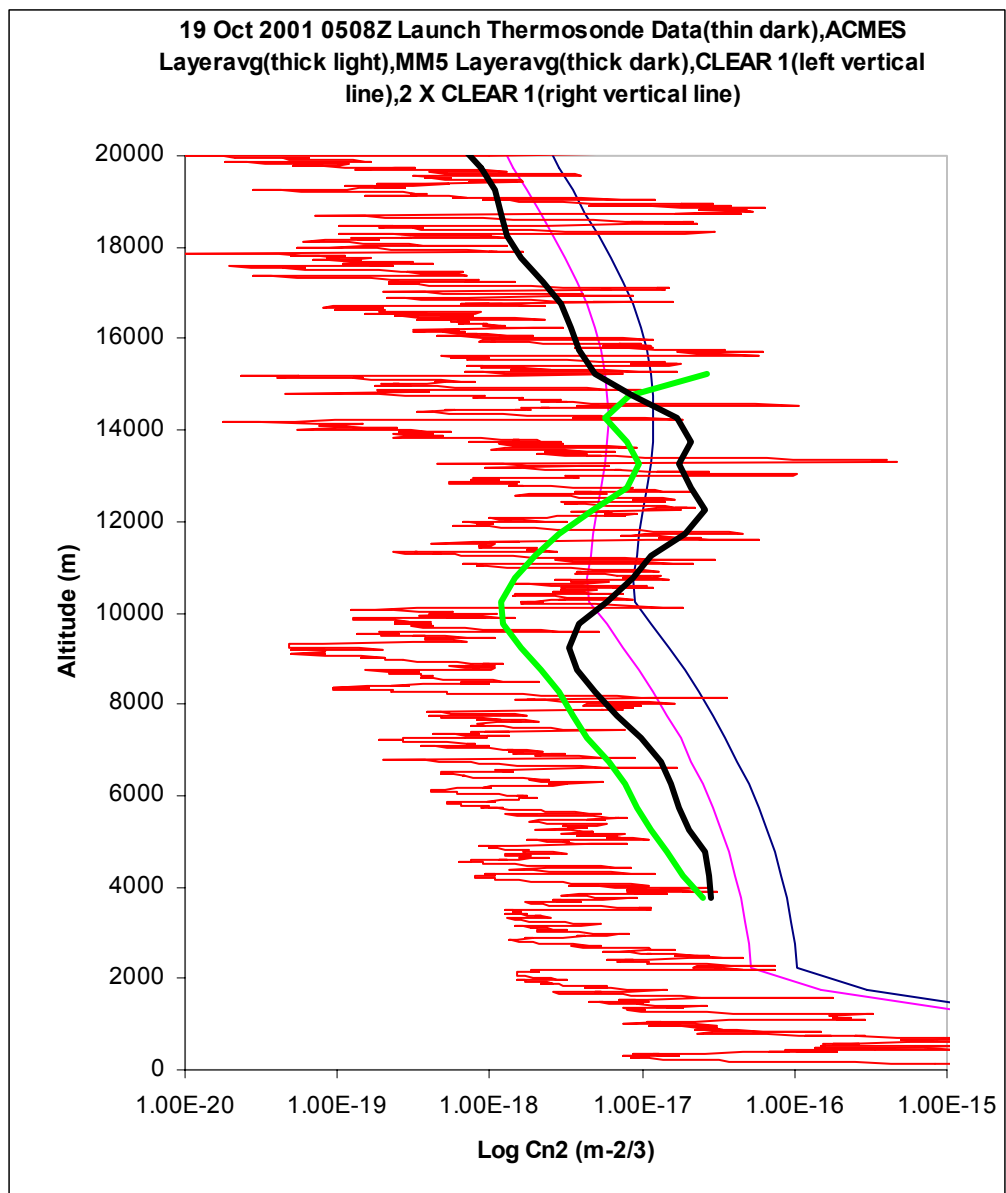


Figure A.66 Domain Average Profiles for 19/0508Z Launch

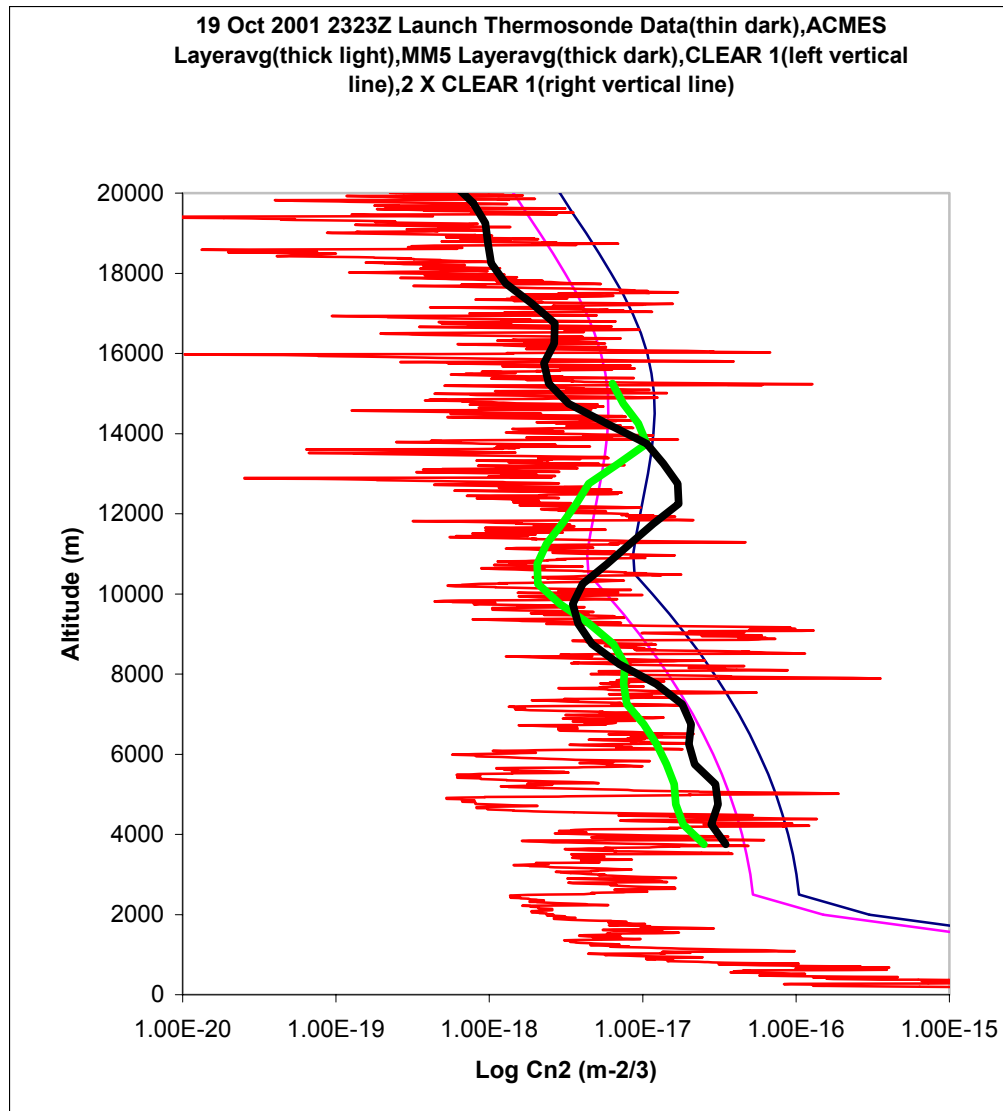


Figure A.67 Domain Average Profiles for 19/2323Z Launch

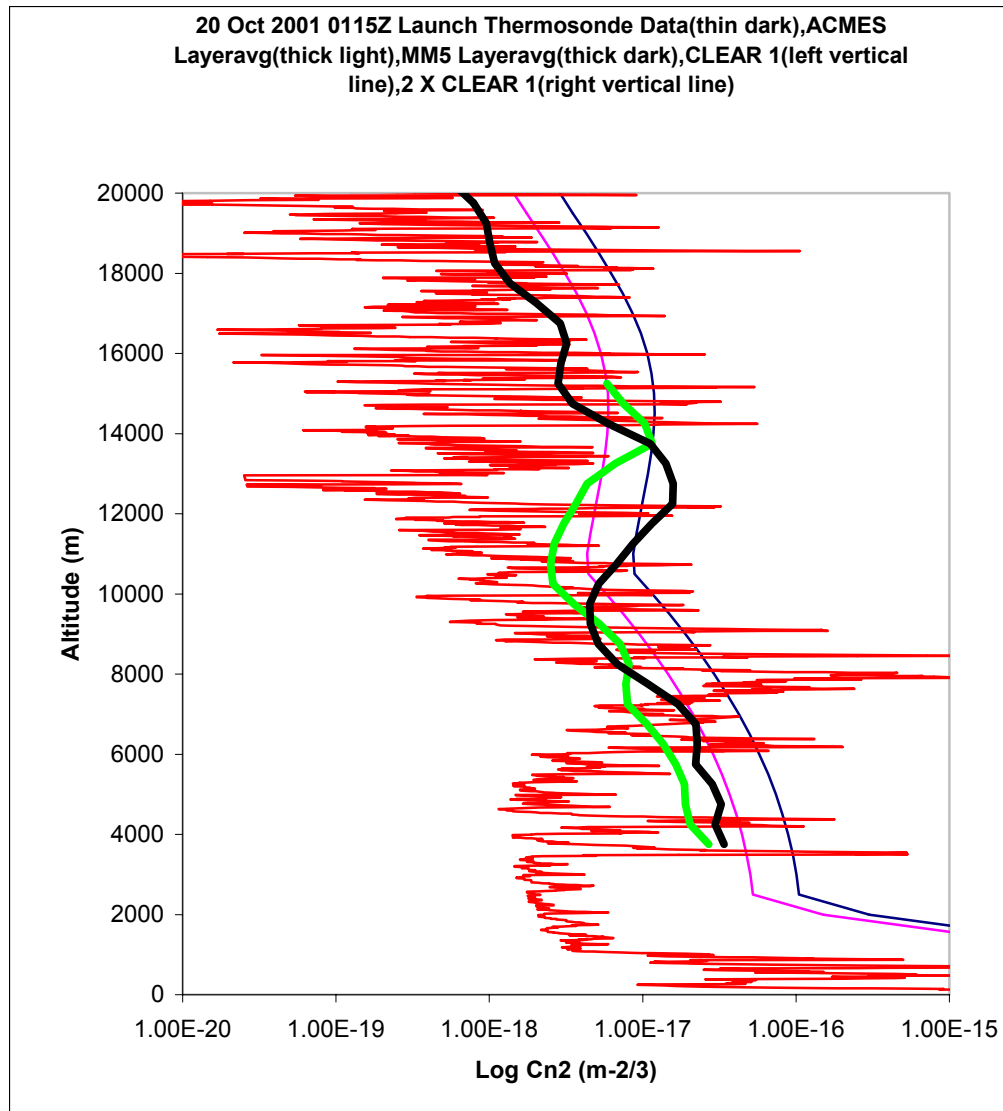


Figure A.68 Domain Average Profiles for 20/0115Z Launch

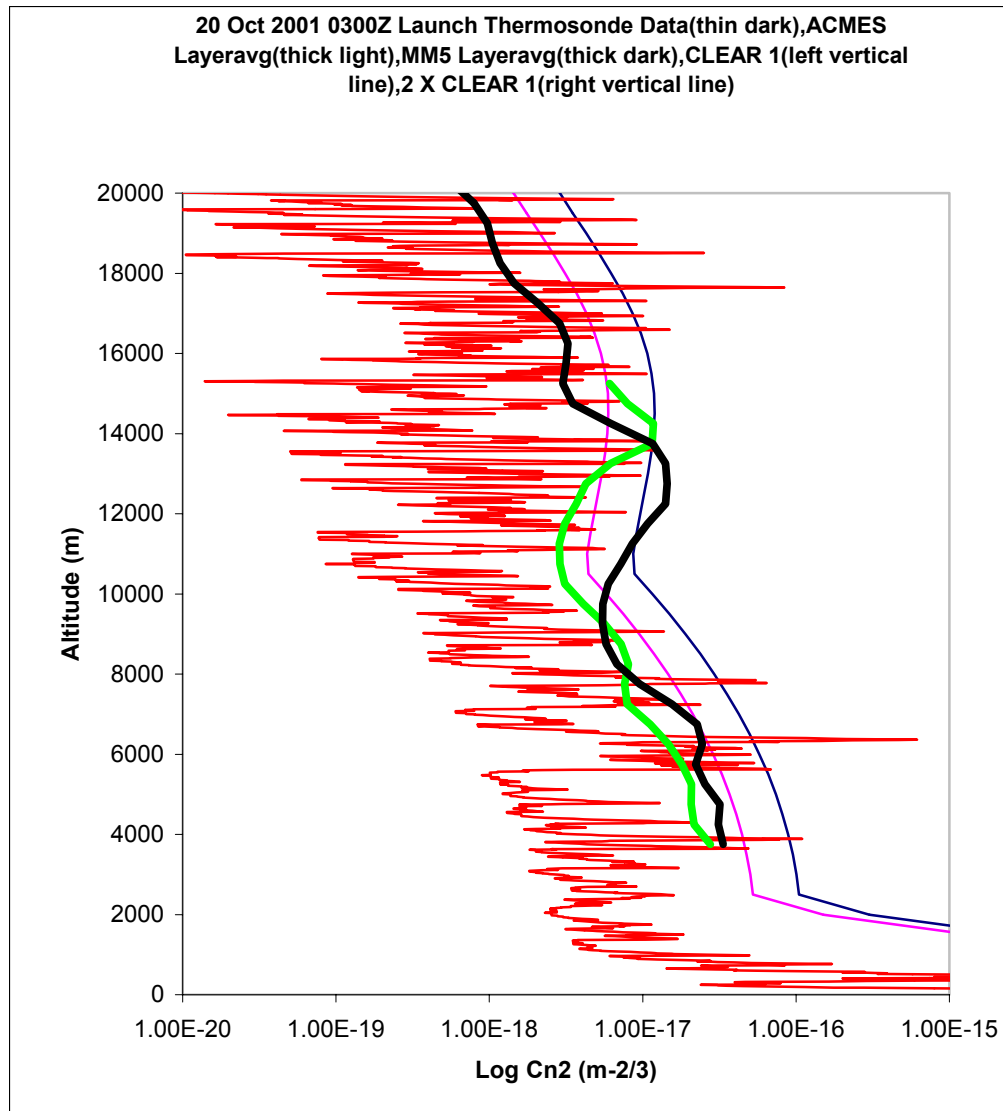


Figure A.69 Domain Average Profiles for 20/0300Z Launch

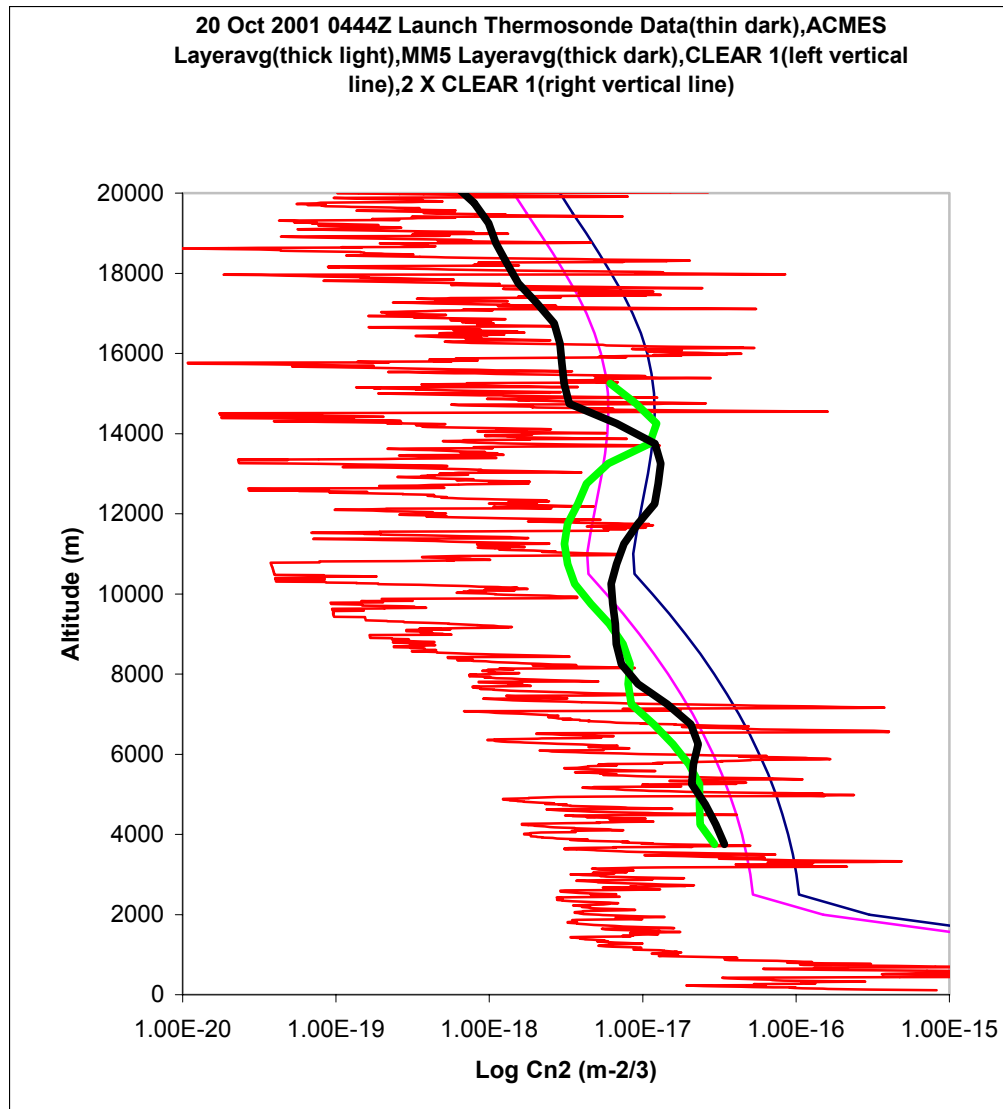


Figure A.70 Domain Average Profiles for 20/0444Z Launch

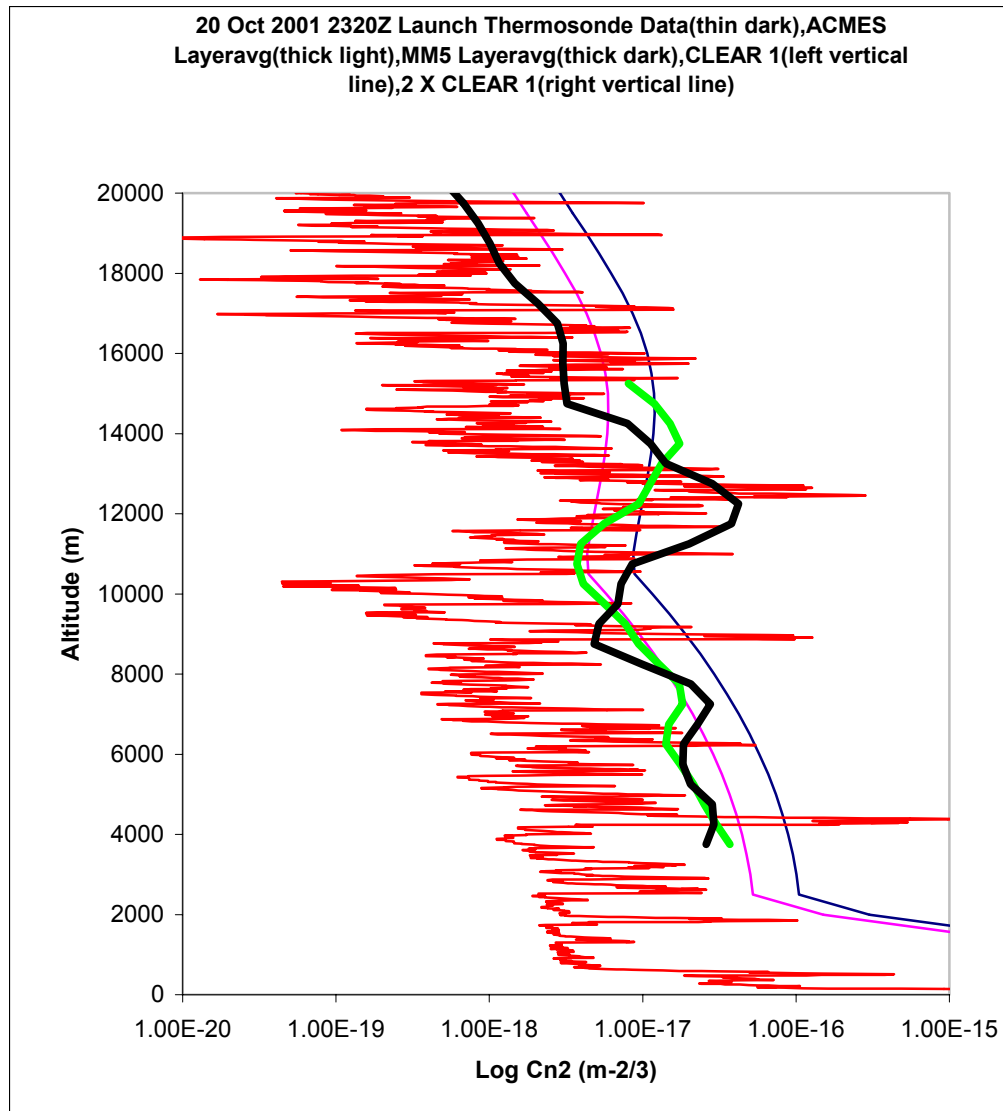


Figure A.71 Domain Average Profiles for 20/2320Z Launch

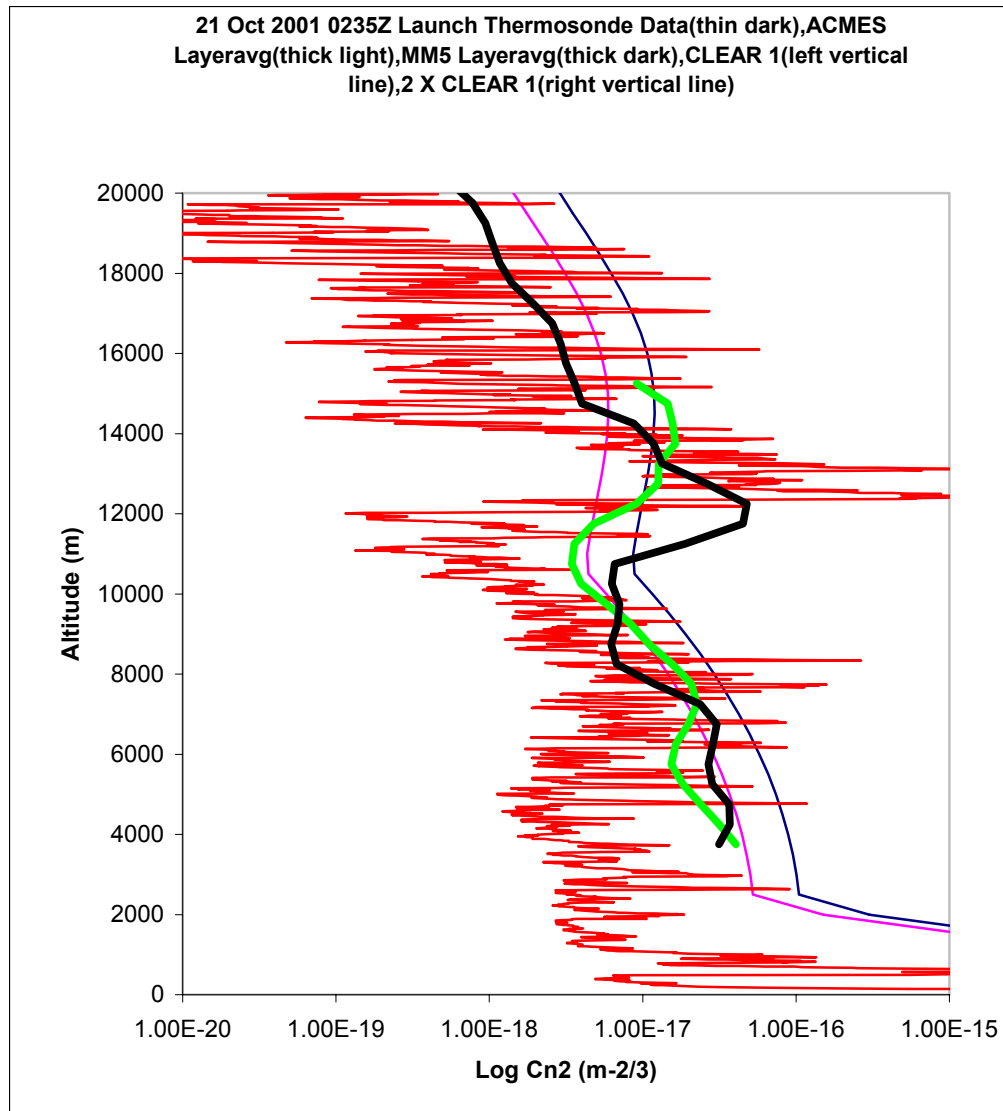


Figure A.72 Domain Average Profiles for 21/0235Z Launch

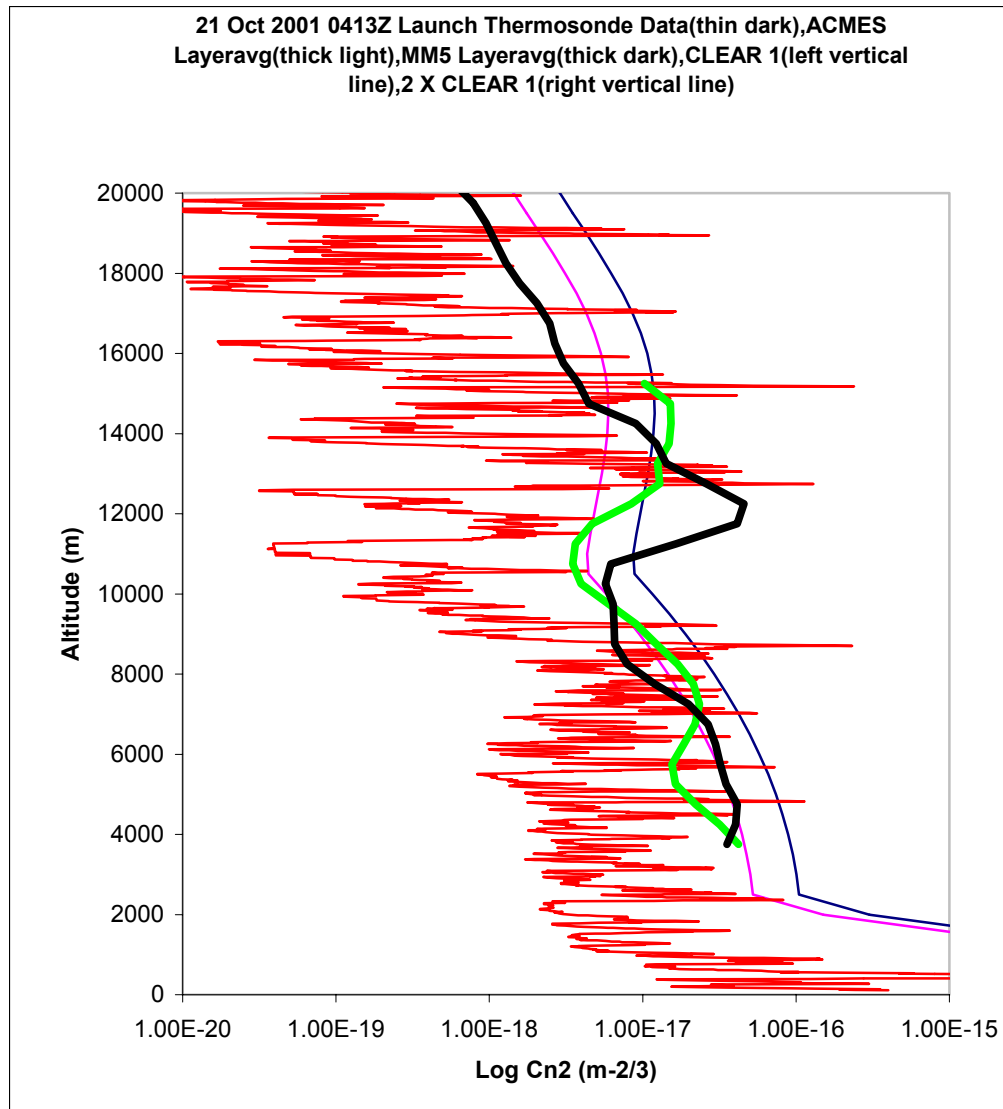


Figure A.73 Domain Average Profiles for 21/0413Z Launch

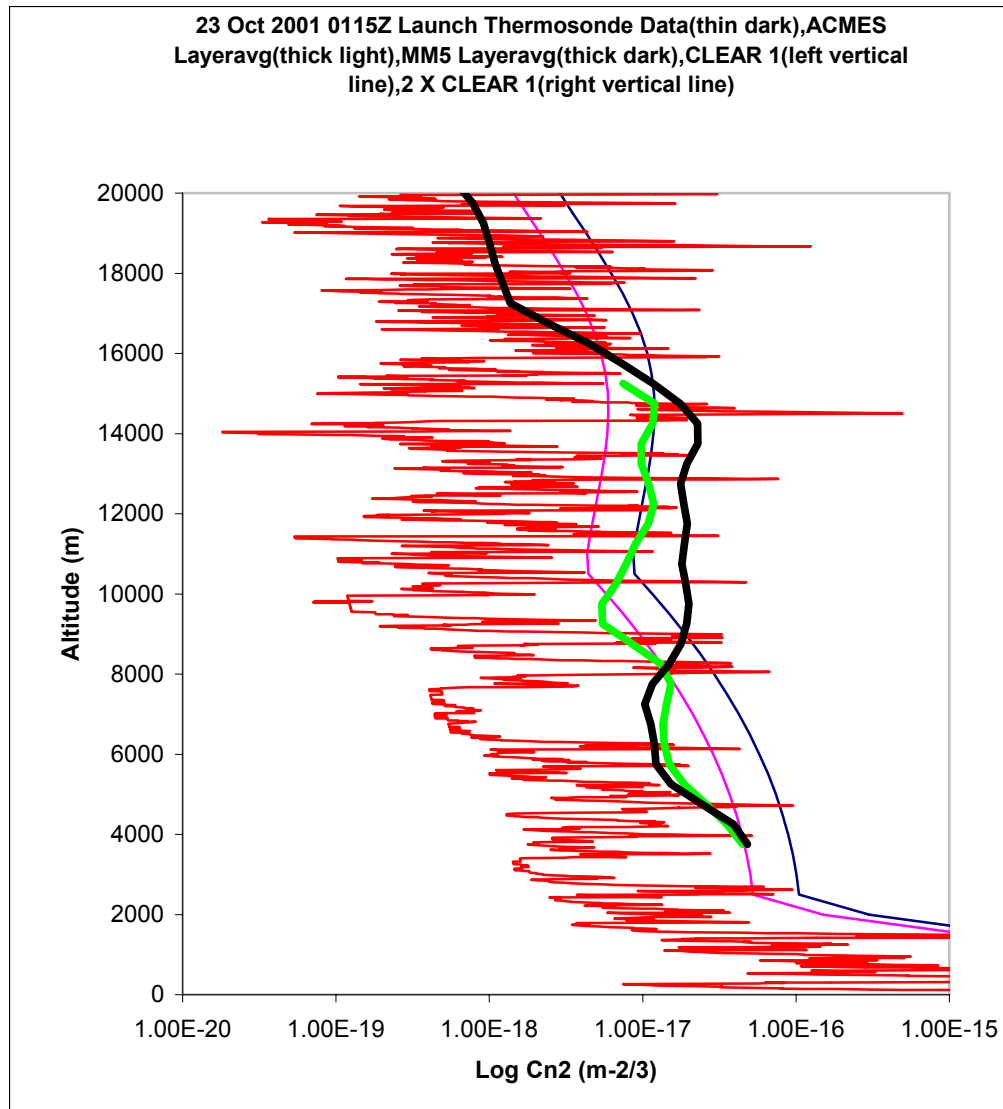


Figure A.74 Domain Average Profiles for 23/0115Z Launch

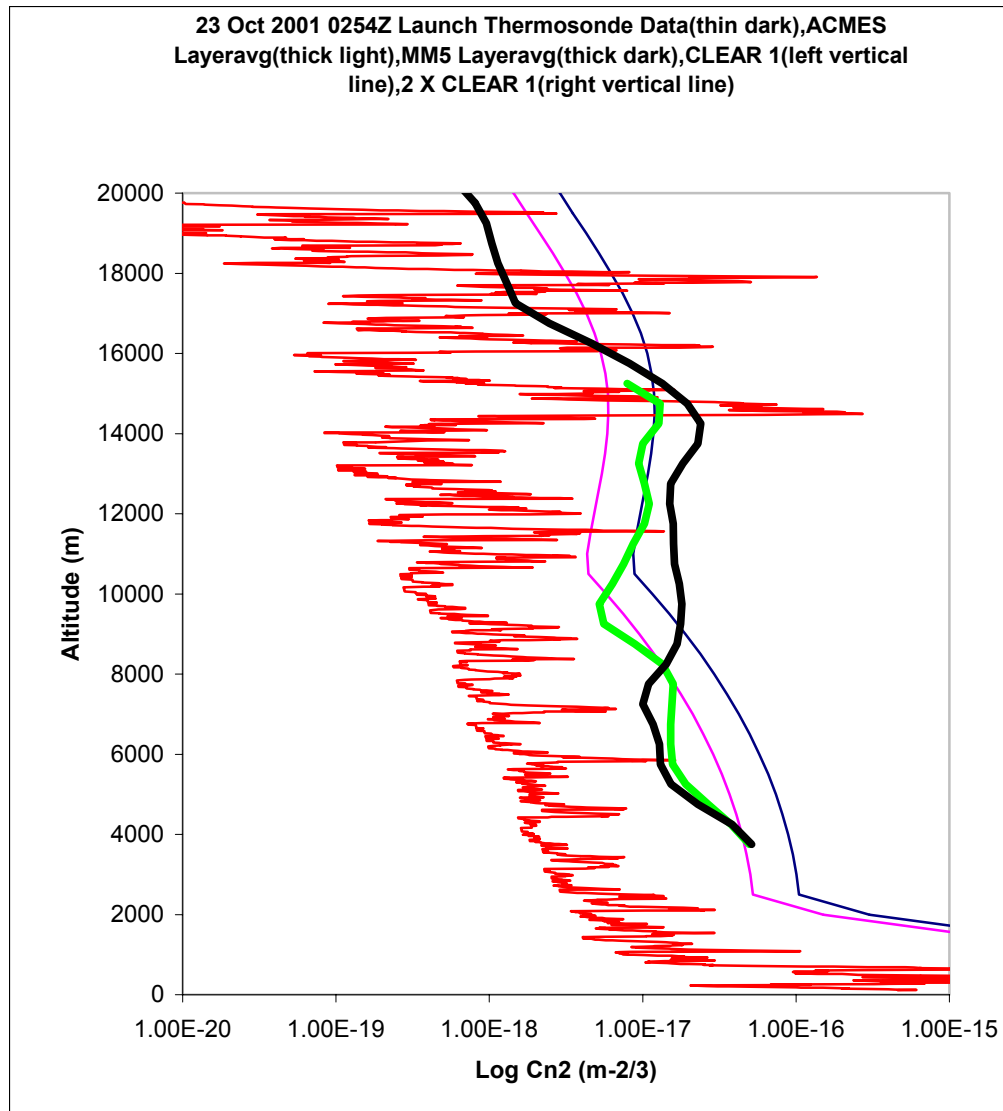


Figure A.75 Domain Average Profiles for 23/0254Z Launch

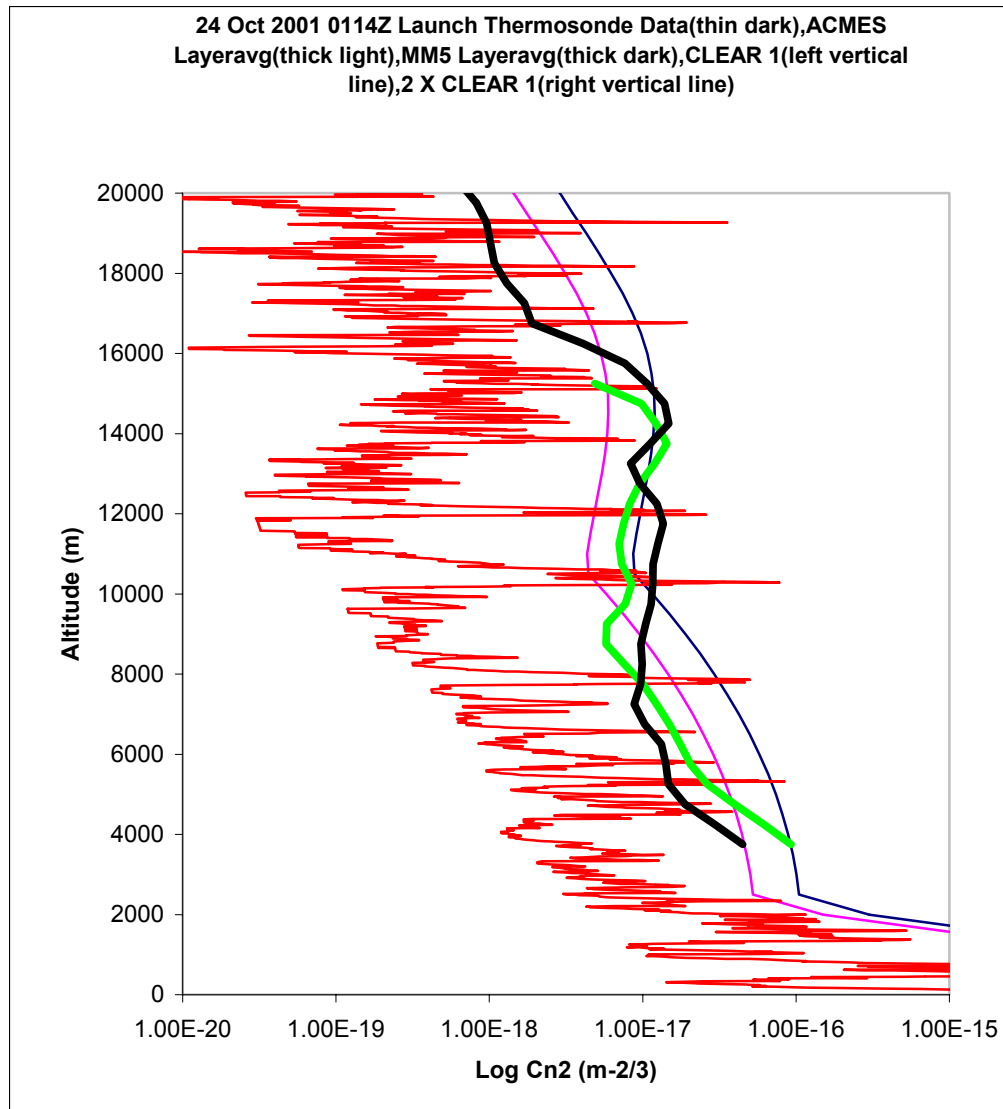


Figure A.76 Domain Average Profiles for 24/0114Z Launch

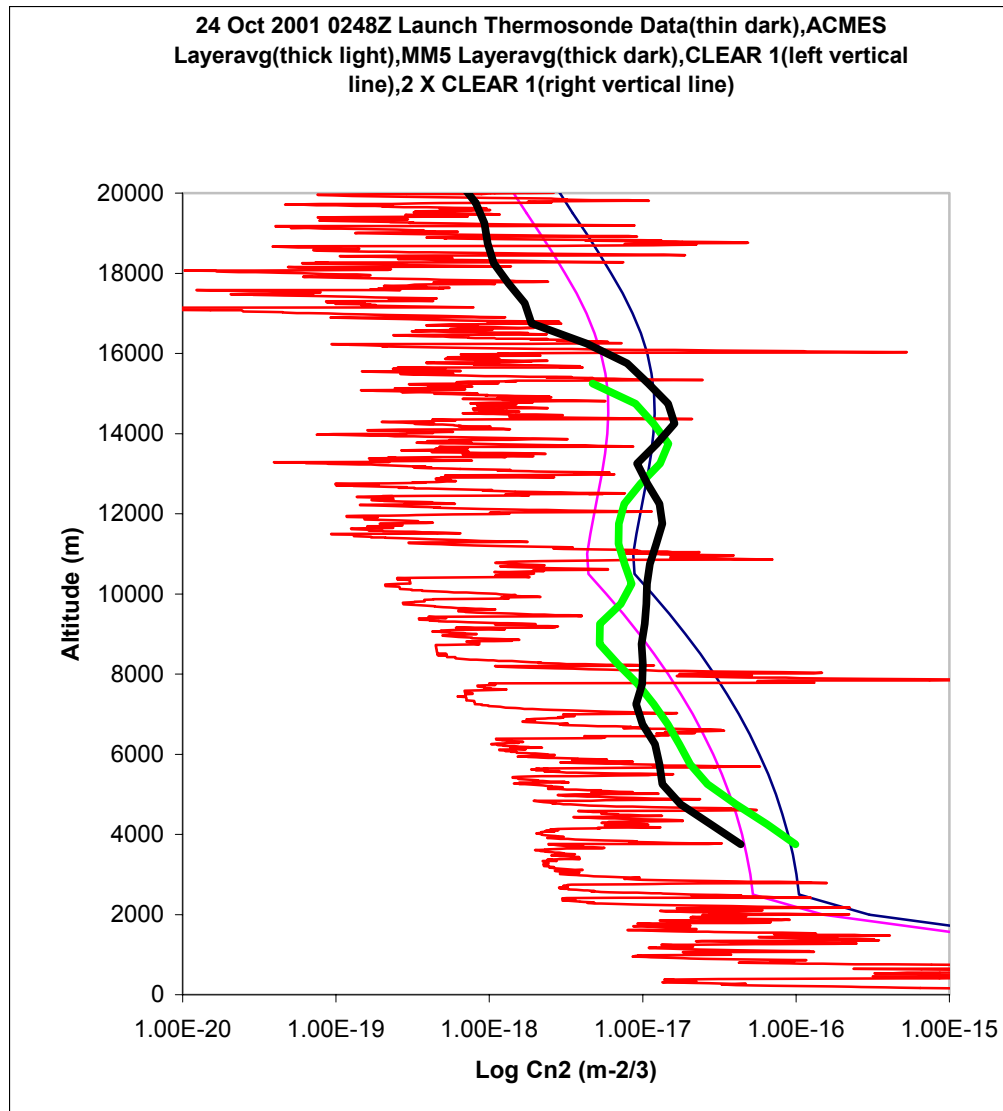


Figure A.77 Domain Average Profiles for 24/0248Z Launch

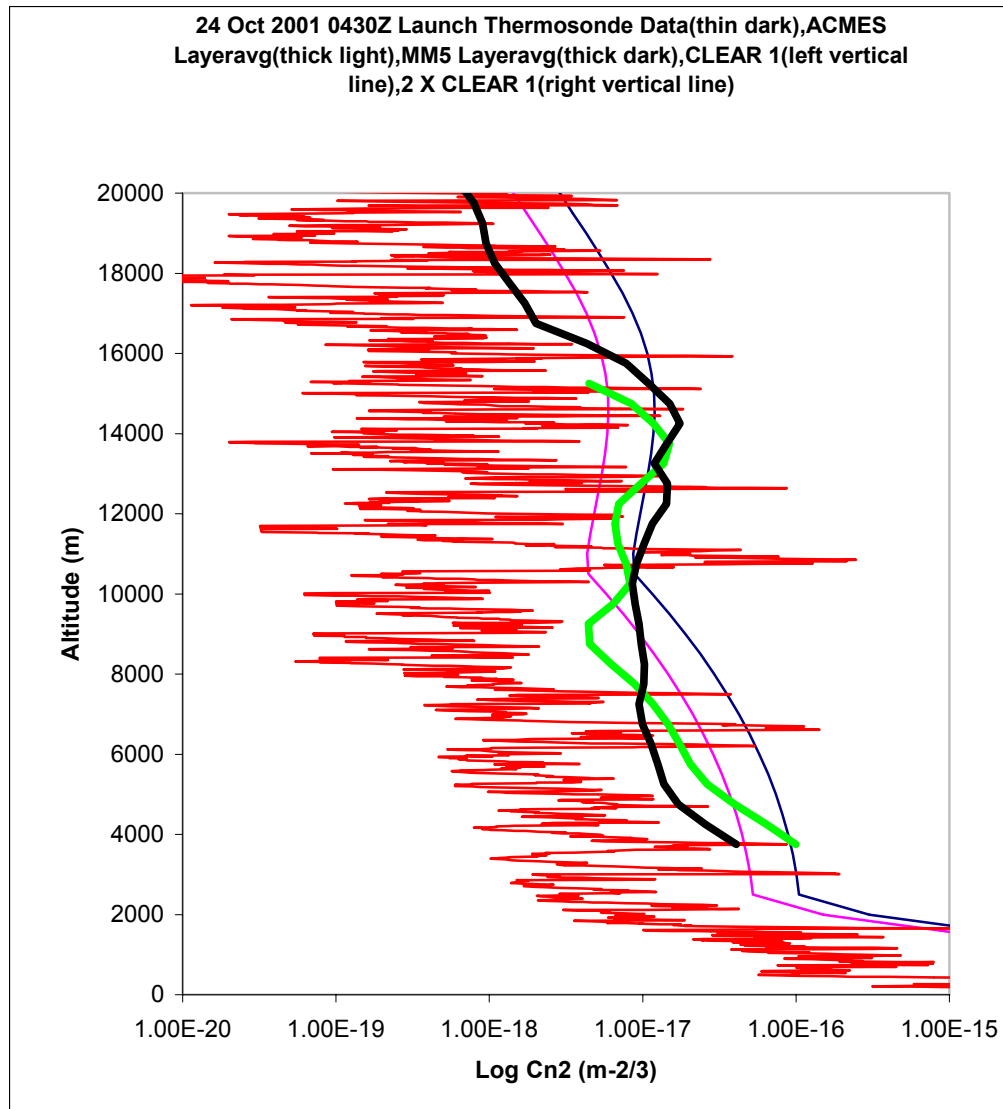


Figure A.78 Domain Average Profiles for 24/0430Z Launch

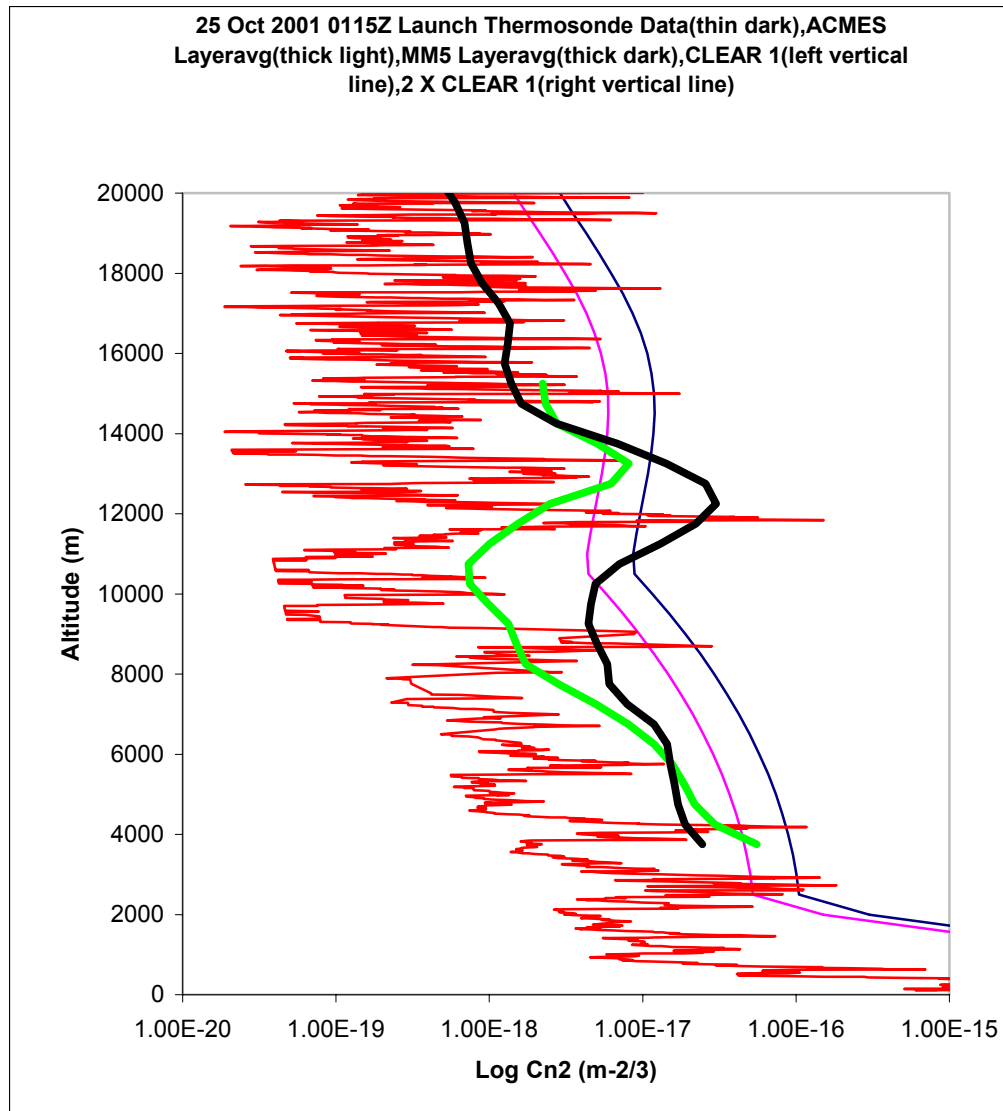


Figure A.79 Domain Average Profiles for 25/0115Z Launch

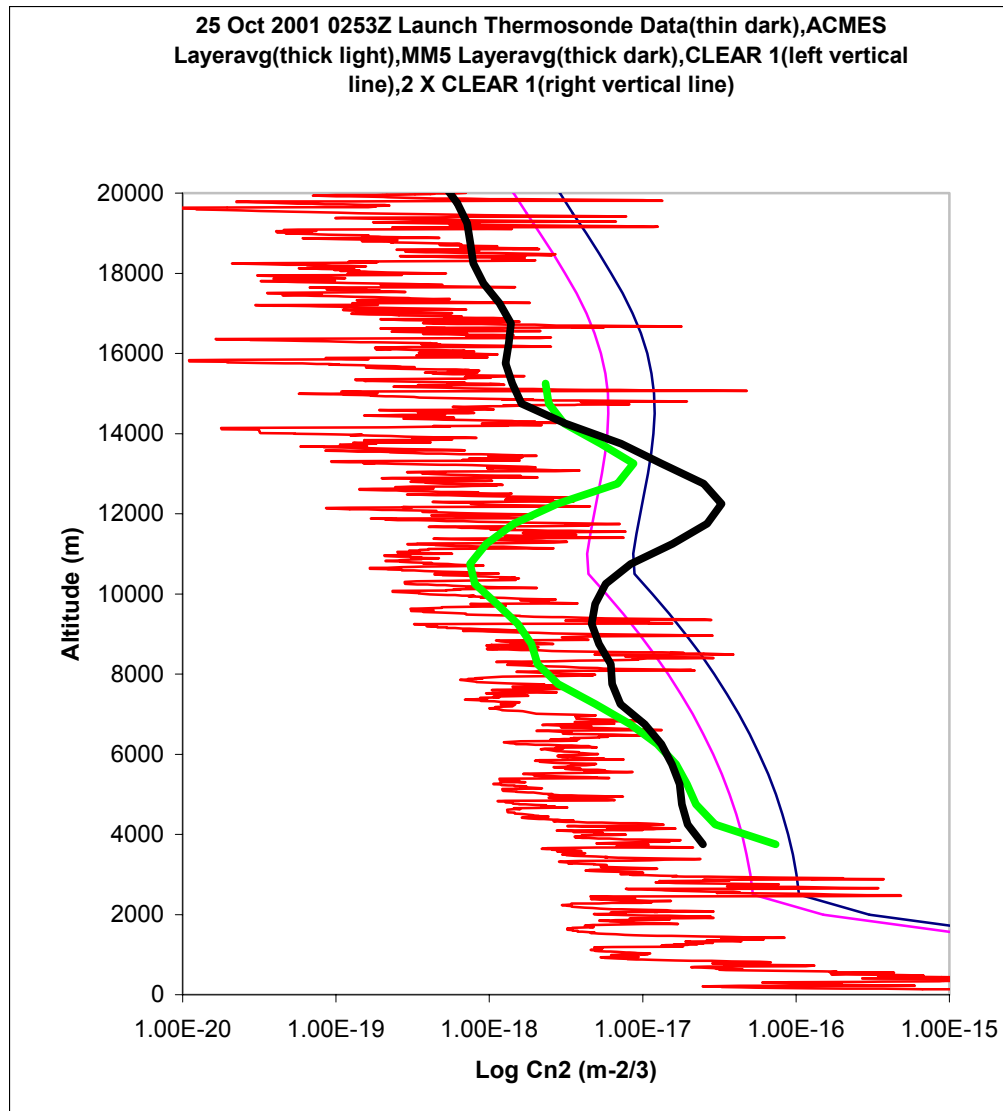


Figure A.80 Domain Average Profiles for 25/0253Z Launch

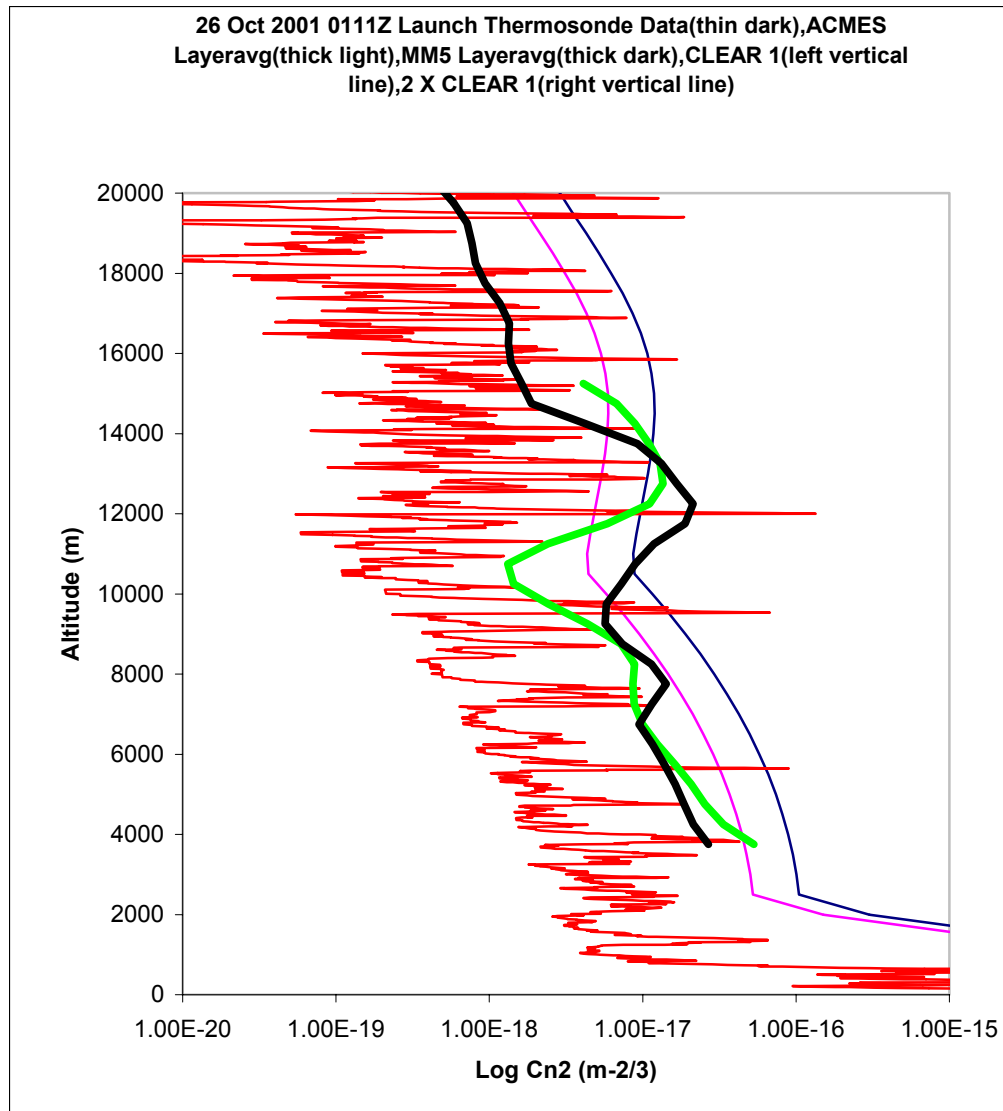


Figure A.81 Domain Average Profiles for 26/0111Z Launch

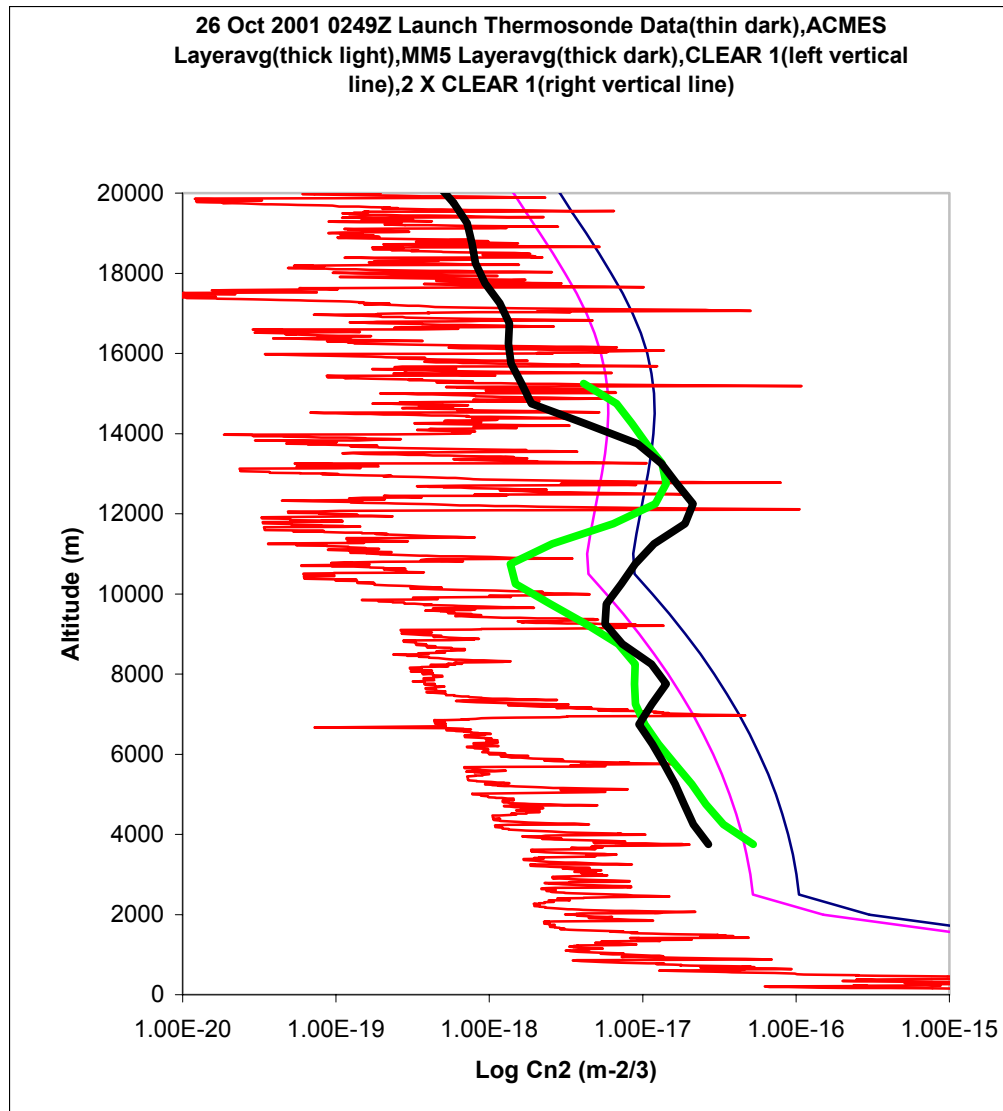


Figure A.82 Domain Average Profiles for 26/0249Z Launch

Appendix B. Statistical Charts

The statistical charts contained in this appendix are for the ACMES and COAMPS model runs in which the paired-t test indicated that the difference in means between the observed and modeled data was insignificant for an alpha level of .05.

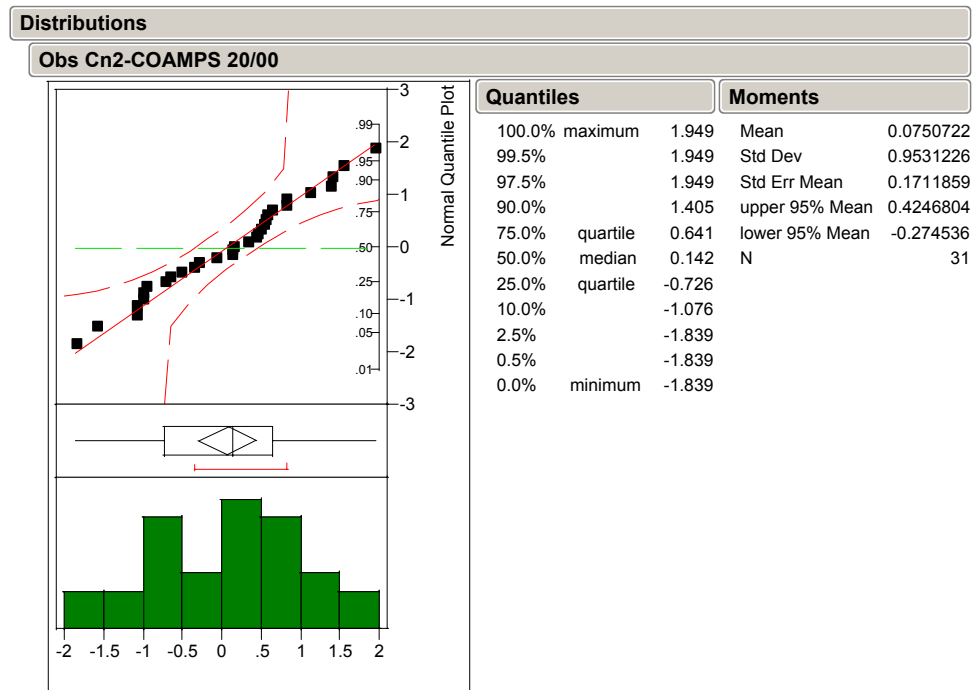


Figure B.1 Distribution Plot for differences between thermosonde data and COAMPS20/00Z data for 19/2323Z Launch

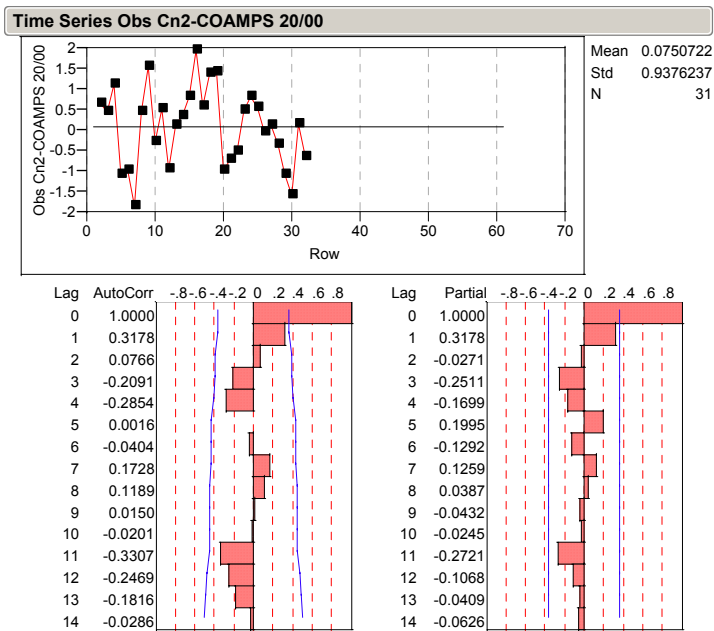


Figure B.2 Time Series Plot for differences between thermosonde data and COAMPS 20/00Z data for 19/2323Z Launch

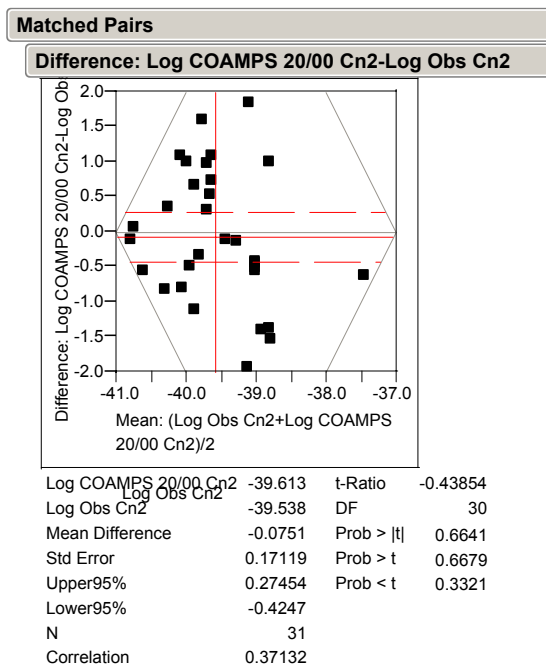


Figure B.3 Matched Pairs Plot for paired-t test of differences between thermosonde data and COAMPS 20/00Z data for 19/2323Z Launch

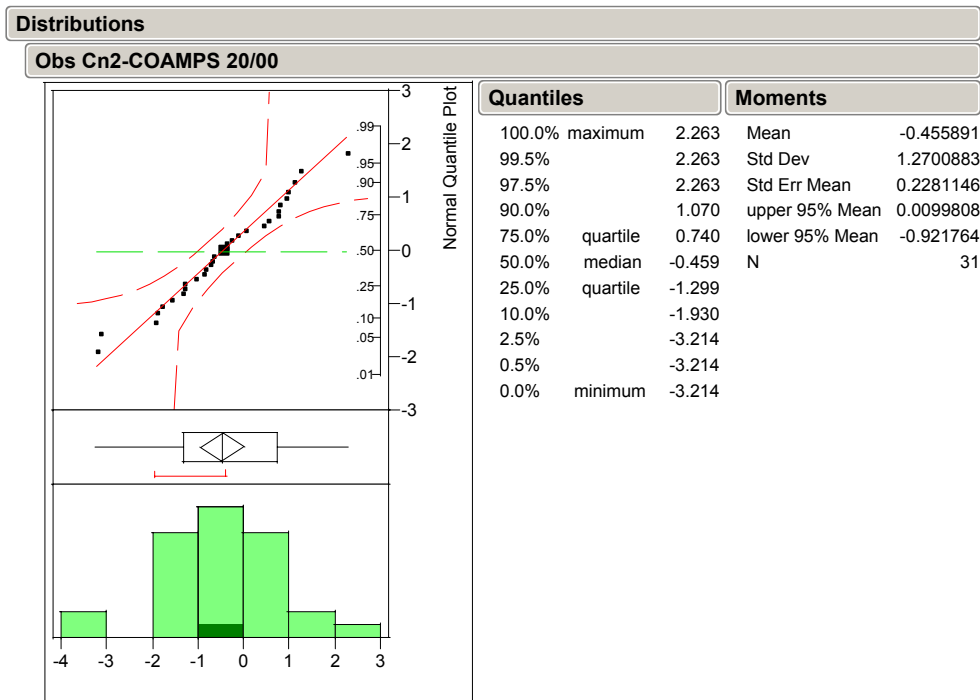


Figure B.4 Distribution Plot for differences between thermosonde data and COAMPS 20/00Z data for the 20/0444Z Launch

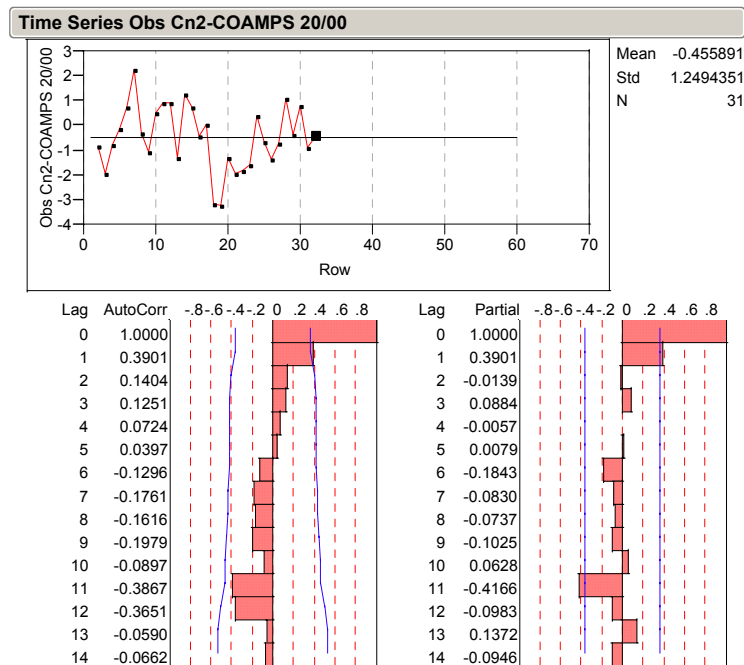


Figure B.5 Time Series Plot for differences between thermosonde data and COAMPS 20/00Z data for the 20/0444Z Launch

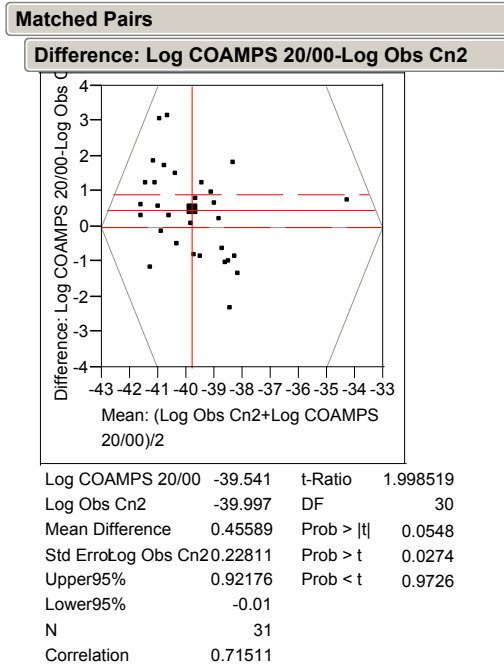


Figure B.6 Matched Pairs Plot for paired-t test of differences between thermosonde data and COAMPS 20/00Z data for 20/0444Z Launch

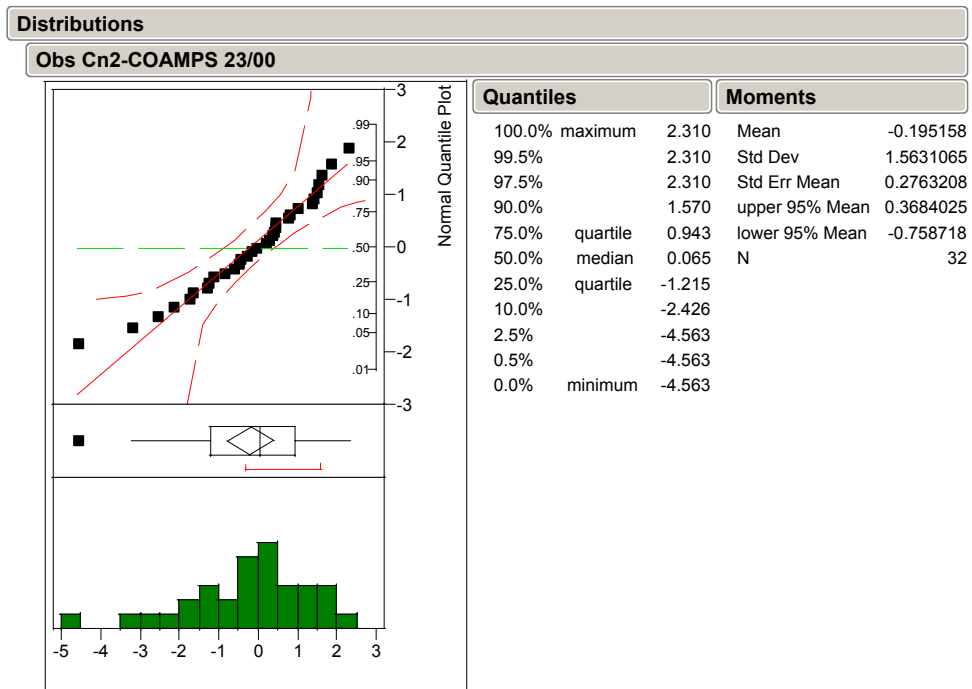


Figure B.7 Distribution Plot for differences between thermosonde data and COAMPS 20/00Z data for 23/0115Z Launch

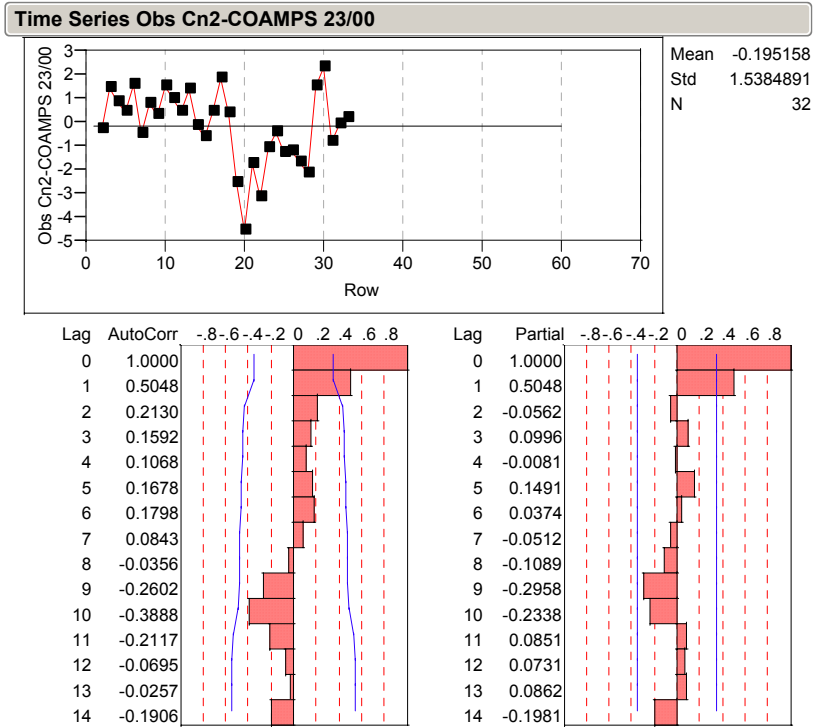


Figure B.8 Time Series Plot for differences between thermosonde data and COAMPS 23/00Z data for the 23/0115Z Launch

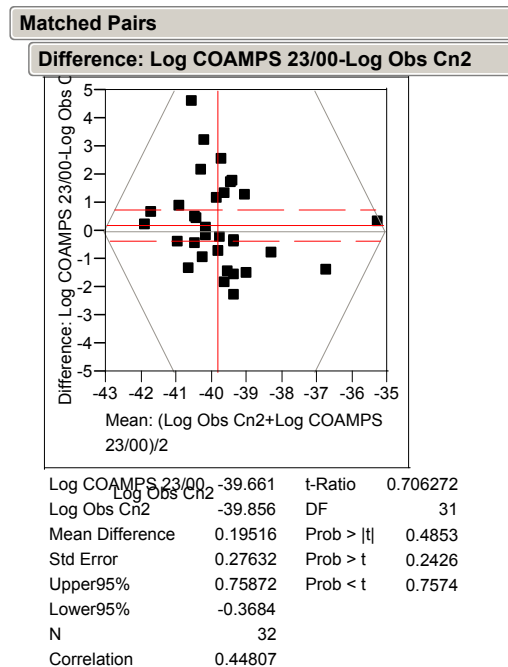


Figure B.9 Matched Pairs Plot for paired-t test of differences between thermosonde data and COAMPS 23/00Z data for 23/0115Z Launch

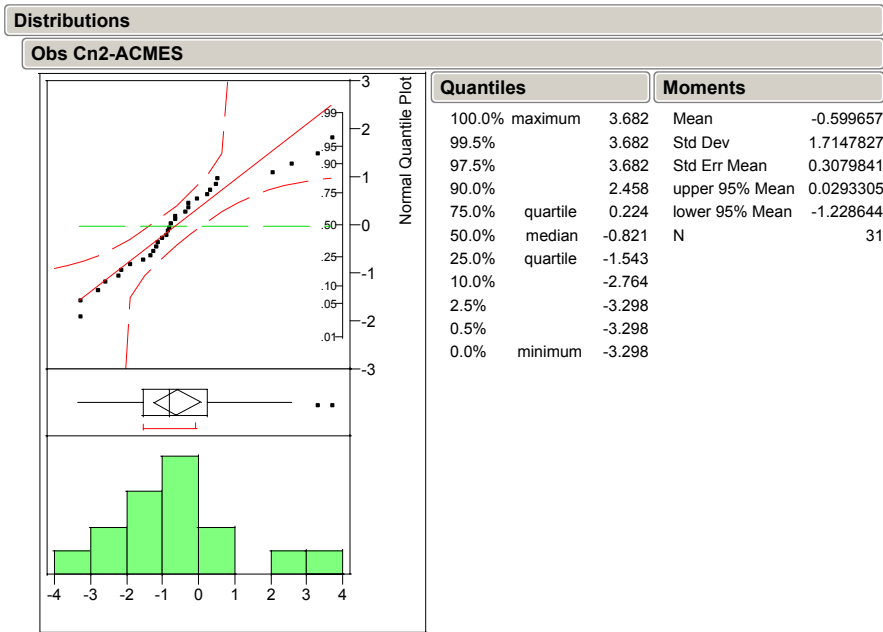


Figure B.10 Distribution Plot for differences between thermosonde data and ACMES data for the 21/0235Z Launch

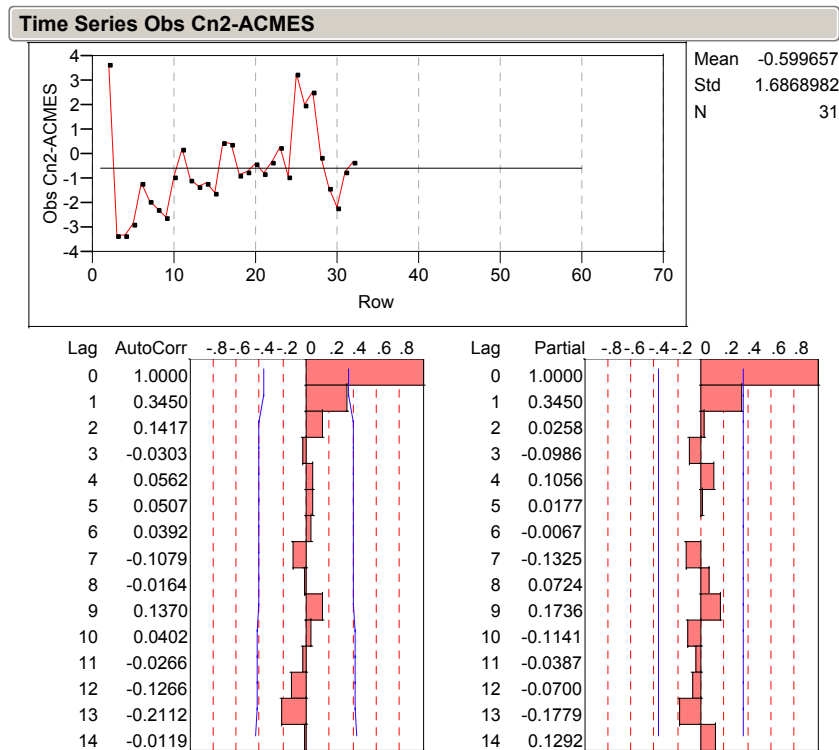


Figure B.11 Time Series Plot for differences between thermosonde data and ACMES data for the 21/0235Z Launch

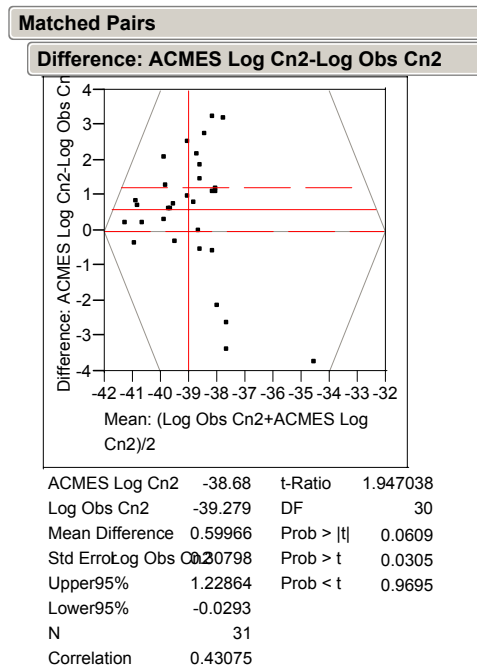


Figure B.12 Matched Pairs Plot for paired-t test of differences between thermosonde data and ACMES data for 21/0235Z Launch

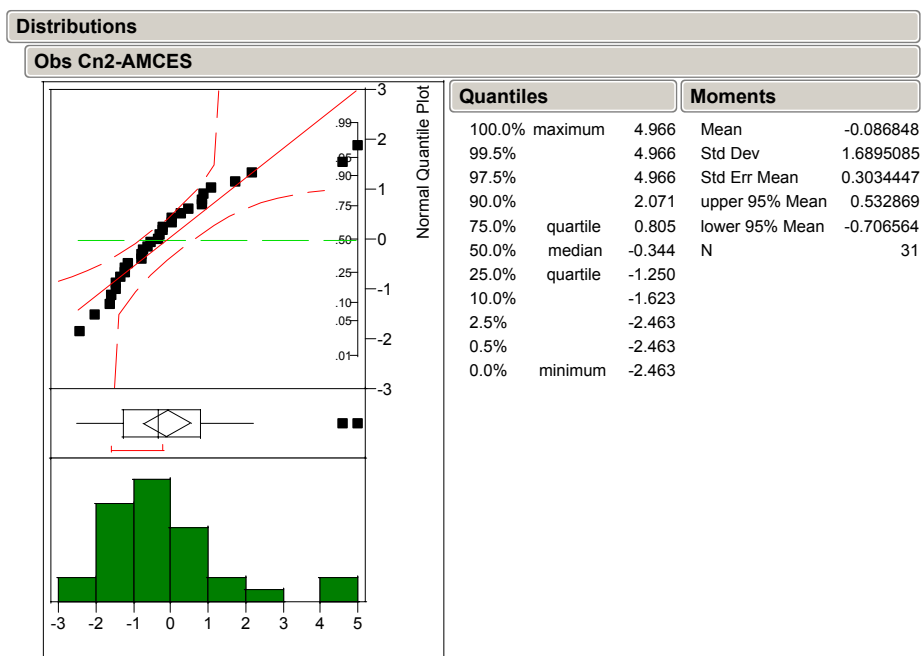


Figure B.13 Distribution Plot for differences between thermosonde data and ACMES data for the 25/0115Z Launch

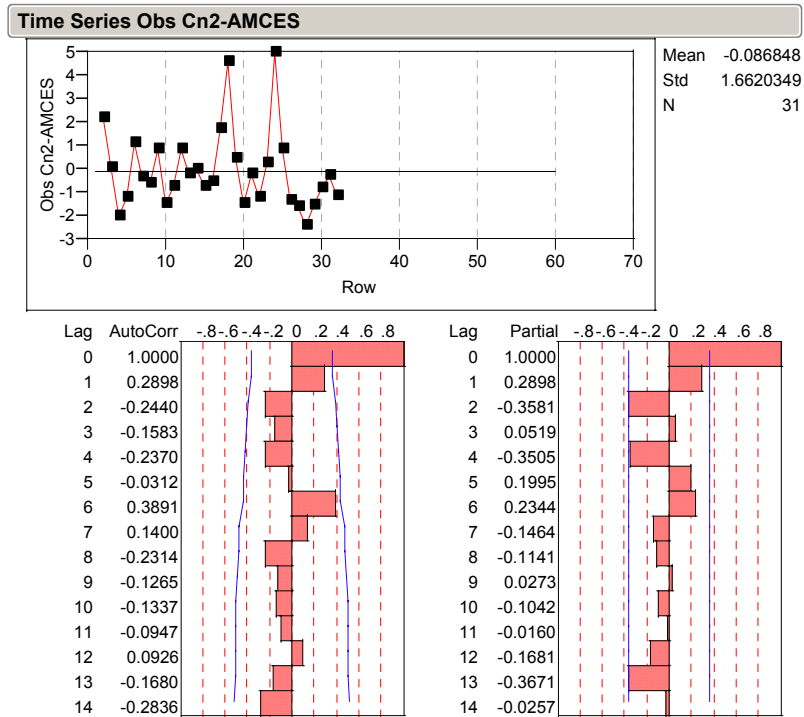


Figure B.14 Time Series Plot for differences between thermosonde data and ACMES data for the 25/0115Z Launch

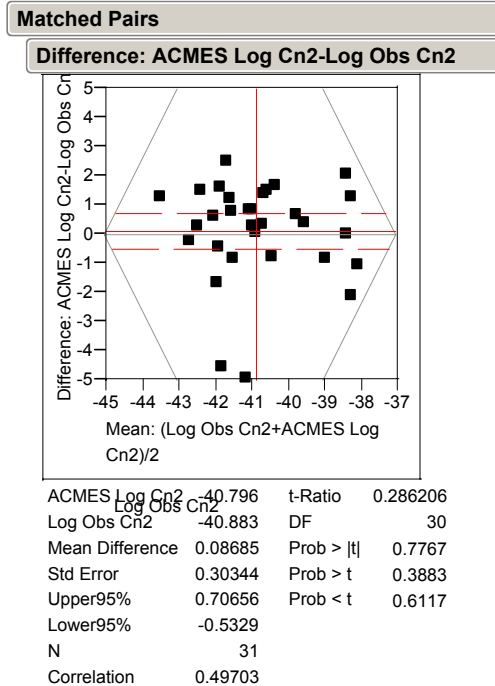


Figure B.15 Matched Pairs Plot for paired-t test of differences between thermosonde data and ACMES data for 25/0115Z Launch

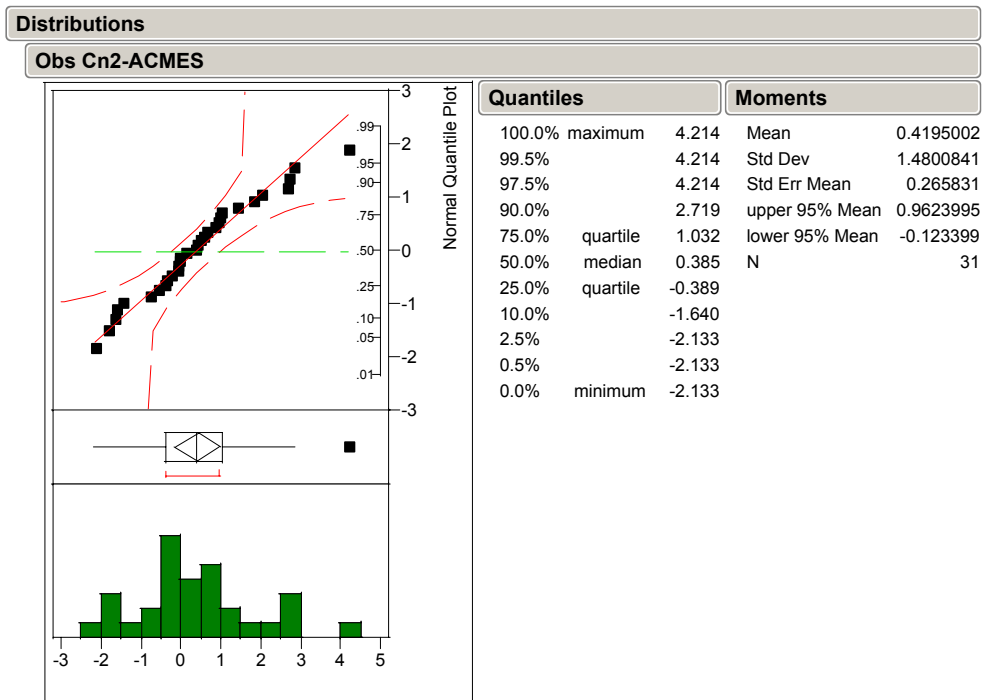


Figure B.16 Distribution Plot for differences between thermosonde data and ACMES data for the 25/0253Z Launch

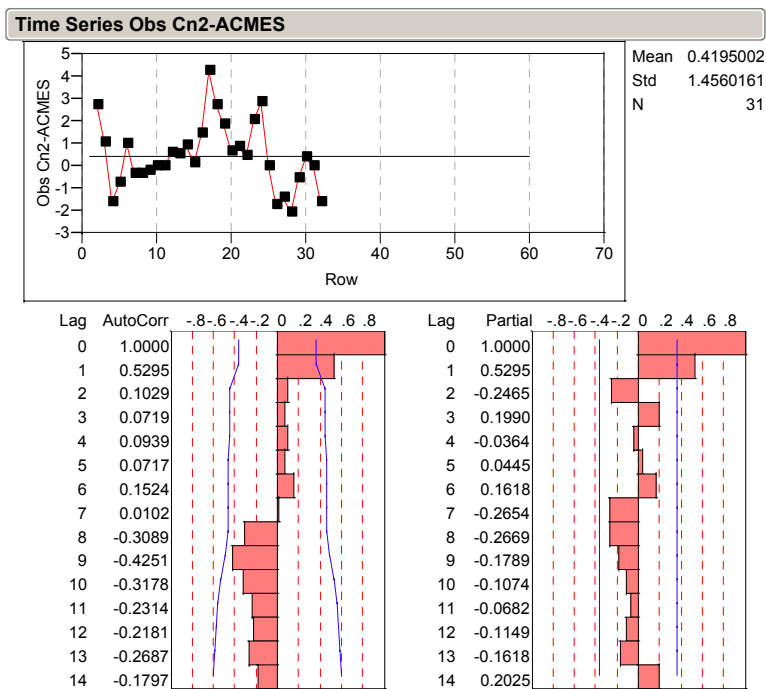


Figure B.17 Time Series Plot for differences between thermosonde data and ACMES data for the 25/0253Z Launch

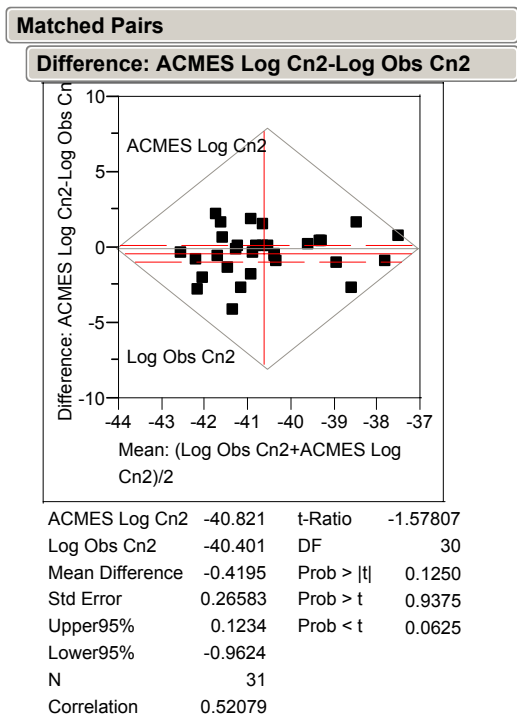


Figure B.18 Matched Pairs Plot for paired-t test of differences between thermosonde data and ACMES data for 25/0253Z Launch

References

- Advanced Climate Modeling Environmental Simulations (ACMES), 2001: ACMES General Information [available online at https://www2.afccc.af.mil/acmes_mil/]
- Airborne Laser System Program Office (ABL), 2002: Airborne Laser (YAL-1A) Fact Sheet [available online at <http://www.airbornelaser.com>]
- Air Force Research Laboratory (AFRL), 1998: Thermosonde picture [available online at <http://www.vs.afrl.af.mil/Factsheets/thermo.html>]
- Amrhein, E., 2002: *RE: ACMES ABL-VBG model runs*. Electronic Message 1841UTC, 22 November 2002
- Andrews, L.C., R.L. Phillips, 1997: *Laser Beam Propagation through Random Media*. SPIE Optical Engineering Press, 434 pp.
- Beland, R.R., 1993: Propagation through Atmospheric Optical Turbulence. *Atmospheric Propagation of Radiation, Vol.2, Smith, F.G.*, Environmental Research Institute of Michigan, 159-224 pp.
- Bougeault, P., C.D. Hui, B. Fleury, J. Laurent 1995: Investigation of Seeing by means of an Atmospheric Mesoscale Numerical Simulation. *Applied Optics.*, **34**, 3481-3488.
- Budai, J.W., 2001: Analyzing the effects of Meteorology on Radar measured index of refraction structure parameter. M. S. Thesis, AFIT/GM/ENP/01M-1, Department of Engineering Physics, Air Force Institute of Technology, 99 pp.
- Buften, J.L., 1975: A Radiosonde Thermal Sensor Technique for Measurement of Atmospheric Turbulence. NASA TN D-7867, pp. 41.
- Conover, W. J., 1980: *Practical Nonparametric Statistics*, 2nd Ed. John Wiley & Sons, 493 pp.
- Corrsin, S., 1951: On the Spectrum of Isotropic Temperature Fluctuations in an Isotropic Turbulence. J. Appl. Phys., **22**, 469-473.
- Coupled Ocean Atmosphere Mesoscale Prediction System (COAMPS), 1999: COAMPS General Information, [available online at <http://www.nrlmry.navy.mil/projects/coamps/>]
- Cressman, G., 1959: An Operational Objective Analysis System. Mon. Wea. Rev., **87**, 367-374

- Devore, J.L., 2000: *Probability and Statistics for Engineering and the Sciences*. 5th ed. Duxbury, 775 pp.
- Dewan, E.M., 1980: Optical Turbulence Forecasting a Tutorial, Air Force Geophysics Laboratory, ADA086863, pp. 70.
- Dudhia, J.,D. Gill, Y. Guo, K. Manning, W. Wang, 2001: PSU/NCAR Mesoscale Modeling System, Tutorial Class Notes and User's Guide: MM5 Modeling System Version 3. [Online at <http://www.mmm.ucar.edu/mm5/doc.html>]
- General Accounting Office (GAO), 1997: Theater Missile Defense: Significant Technical Challenges Face the Airborne Laser Program. World Wide Web, <http://www.gao.gov/new.items/ns98037.pdf>, 18 pp.
- Gibson, C.H., 1991: *Encyclopedia of Physics*. VCH Publishers, Inc., 1408 pp.
- Glickman, T.S., Managing Editor, et al., 2000: *Glossary of Meteorology*, Boston, Massachusetts, American Meteorological Society, 855 pp.
- Goda, M.E., 2002: Personal Interview 21 Nov 02 1700UTC.
- Golnik, G., 1993: Directed Energy Systems. *Emerging Systems and Technologies*, Vol. 8, Robinson, S.R., Environmental Research Institute of Michigan, 405-474 pp.
- Harms, D.E., S. Raman, R.V. Madala, 1992a: An Examination of Four –Dimensional Data-Assimilation Techniques for Numerical Weather Prediction. *Bull. Amer. Meteor. Soc.*, **73**, 425-440.
- Jumper, G.Y, H.M. Polchlopek, R.R. Beland, E.A. Murphy, P. Tracy, K. Robinson, 1997: Balloon-Borne Measurements of a Atmospheric Temperature Fluctuations. AIAA 1997-2353, 8 pp.
- Jumper, G.Y., R.R. Beland, 2000: Progress in the Understanding and Modeling of Atmospheric Optical Turbulence. AIAA 2000-2355, 9 pp.
- Kalnay, E., M. Kanamitsu, R. Kistler, W. Collins, D. Deaven, L. Gandin, M. Iredell, S. Saha, G. White, J. Woollen, Y. Zhu, A. Leetmaa, R. Reynolds 1996: The NCEP/NCAR 40-Year Reanalysis Project. *Bulletin of the American Meteorological Society*, **77**, 437-471.
- Kolmogorov, A.N., 1941: Dissipation of Energy in Locally Isotropic Turbulence. *Doklady Akad, Nauk SSSR*, 32.

- Kolmogorov, A., 1961: *In Turbulence, Classic Papers on Statistical Theory*. Interscience, 151 pp.
- Kundu, P.K., 1990: *Fluid Mechanics*. Academic Press, 638 pp.
- MacGovern, A.J., D.A. Nahrstedt, M. M. Johnson, 2000: Atmospheric Propagation for Tactical Directed Energy Applications. *SPIE-Int. Soc. Opt. Eng.*, **4034**, 128-139.
- Mesoscale Atmospheric Simulation System (MASS), 2001: MASS Reference Manual, MESO, Inc. Troy, NY [available online at <http://www.meso.com/mass-user/masshome.htm>] 133pp.
- National Climatic Data Center (NCDC), 2001: NCDC General Information [available online at <http://www.ncdc.noaa.gov/oa/ncdc.html>]
- Obukhov, A.M., 1941: On the Distribution of Energy in the Spectrum of Turbulent Flow. *Doklady Akad. Nauk SSSR*, **32**, 19 pp.
- Parker, S.W., 2002: Atmospheric Turbulence Comparison using MM5 and COAMPS Mesoscale Models. M.S. Thesis, ADB281596, Department of Physics, Naval Postgraduate School, 86 pp.
- Pries, T.H., 1980: Atmospheric Sensitivities of High Energy Lasers. AWS/TN-80/003 14 pp.
- Roadcap, J.R., 2002: Personal Communication. Electronic Message 1641UTC, 20 November 2002.
- Roadcap, J., D. DeBenedictis, F. Ruggiero, 2001: Case Study Analysis for 20-22 October 2001. ABL-AFOSR Workshop, Kirtland AFB, NM, 41 pp.
- Robinson, K., 2002: Personal Communication. Electronic Message 1714UTC, 22 November 2002.
- Ruggiero, F.H., D.A. DeBenedictis 2002: Forecasting Optical Turbulence HPC Users Group Conference 10-14 June 2002.
- Sashegyi, K.D., R. V. Madala 1993: Application of vertical mode initialization to a limited area model in flux form. *Mon. Wea. Rev.*, **121**, 207-220.
- Strohbehn, J.W. 1978: Topics in Applied Physics. Vol. 25, *Laser Beam Propagation in the Atmosphere*, Springer-Verlag , 325 pp.
- Tatarski, V.I. 1961: *Wave Propagation in a Turbulent Medium*. McGraw-Hill, 285 pp.

- Tennekes, H., J.L. Lumley 1972: *A First Course in Turbulence*. The MIT Press, 300 pp.
- Tjernstrom, M., 1993: Turbulence Length Scales in Stably Stratified Free Shear Flow Analyzed from Slant Aircraft Profiles. *Journal of Applied Meteorology*, **32**, 948-963.
- Tsvang, L., 1969: Microstructure of Temperature Fields in the Free Atmosphere. *Radio Science*, **4**, 1175-1177.
- University of Wyoming (UW), 2002: Skew-T data [available online at <http://weather.uwyo.edu/upperair/sounding.html>].
- Warner, T.T., R.A. Peterson, R.E. Russell, E. Treadon, 1997: A Tutorial on Lateral Boundary Conditions as a Basic and Potentially Serious Limitation to Regional Numerical Weather Prediction. *Bulletin of the American Meteorological Society*, **78**, 2599-2617.
- Walters, D.L., 2002a: Personal Communication. Electronic Message 0159UTC, 9 May 2002.
- Walters, D.L., 2002b: Personal Communication. Electronic Message 2247UTC, 27 November 2002
- Walters, D.L., K.E. Kunkel, 1981: Atmospheric Modulation Transfer Function for Desert and Mountain Locations: The Atmospheric effects on r_o . *J. Opt. Soc. Am.*, **71**, 397-405.
- Weaver, L.D., W. Brown, P. Kelly, E. Boll, M. Keltos, 2002: *ABLSTAR*. Air Force Research Laboratory, 249 pp.
- White, K.O., D.M. Garvey, W.A. Peterson, F.D. Eaton, 1985: Atmospheric Characterization at the HIDL site CLEAR I program 29 August to 28 September 1984. U.S. Army Atmospheric Sciences Laboratory, AD-B096 306, 70 pp.
- Wilks, S., 1995: *Statistical Methods in the Atmospheric Sciences*. The Academic Press, 467 pp.

Vita

Captain De Leon C. Narcisse is a member of the United States Air Force.

REPORT DOCUMENTATION PAGE				Form Approved OMB No. 074-0188	
<p>The public reporting burden for this collection of information is estimated to average 1 hour per response, including the time for reviewing instructions, searching existing data sources, gathering and maintaining the data needed, and completing and reviewing the collection of information. Send comments regarding this burden estimate or any other aspect of the collection of information, including suggestions for reducing this burden to Department of Defense, Washington Headquarters Services, Directorate for Information Operations and Reports (0704-0188), 1215 Jefferson Davis Highway, Suite 1204, Arlington, VA 22202-4302. Respondents should be aware that notwithstanding any other provision of law, no person shall be subject to a penalty for failing to comply with a collection of information if it does not display a currently valid OMB control number.</p> <p>PLEASE DO NOT RETURN YOUR FORM TO THE ABOVE ADDRESS.</p>					
1. REPORT DATE (DD-MM-YYYY) 02-28-2003		2. REPORT TYPE Master's Thesis		3. DATES COVERED (From – To) Jun 2002 – Mar 2003	
4. TITLE AND SUBTITLE COMPARISON OF THE REFRACTIVE INDEX STRUCTURE CONSTANT DERIVED FROM NUMERICAL WEATHER PREDICTION (NWP) MODELS AND THERMOSONDE DATA				5a. CONTRACT NUMBER	
				5b. GRANT NUMBER	
				5c. PROGRAM ELEMENT NUMBER	
6. AUTHOR(S) Narcisse, De Leon C., Captain, USAF				5d. PROJECT NUMBER	
				5e. TASK NUMBER	
				5f. WORK UNIT NUMBER	
7. PERFORMING ORGANIZATION NAMES(S) AND ADDRESS(S) Air Force Institute of Technology Graduate School of Engineering and Management (AFIT/EN) 2950 Hobson Way, Building 640 WPAFB OH 45433-7765				8. PERFORMING ORGANIZATION REPORT NUMBER AFIT/GM/ENP/03-04	
9. SPONSORING/MONITORING AGENCY NAME(S) AND ADDRESS(ES) SMC/TMSW Attn: Lt. Col. Randy Lefevre 3300 Target Rd Kirtland AFB, NM. 87117-5776				10. SPONSOR/MONITOR'S ACRONYM(S)	
				11. SPONSOR/MONITOR'S REPORT NUMBER(S)	
12. DISTRIBUTION/AVAILABILITY STATEMENT APPROVED FOR PUBLIC RELEASE; DISTRIBUTION UNLIMITED.					
13. SUPPLEMENTARY NOTES EN – Advisor: Lt Col Michael K. Walters					
14. ABSTRACT An accurate depiction of atmospheric turbulence is required for successful employment of a viable airborne laser for the Department of Defense (DOD). The ABL Special Program Office (SPO), which is tasked by the Missile Defense Agency (MDA) has not designated any particular numerical weather model that is used exclusively to model optical turbulence. This research compares CLEAR1, 2 X CLEAR 1 and thermosonde derived values of the refractive index structure constant to optical turbulence values derived from several numerical weather prediction models currently in use by the DOD. The models used were the Fifth Generation Mesoscale Model (MM5), the Coupled Ocean Atmosphere Prediction System (COAMPS), and the Advanced Climate Modeling and Environmental Simulation (ACMES) program. Comparisons are presented using thermosonde data collected at Vandenberg AFB, California during the period 19-26 Oct 2001 Universal Time Coordinated (UTC). Results indicate that the model-derived optical turbulence and the thermosonde derived optical turbulence values are statistically different in many cases.					
15. SUBJECT TERMS Optical Turbulence, Meteorology, Lasers, Directed Energy Weapons					
16. SECURITY CLASSIFICATION OF:			17. LIMITATION OF ABSTRACT SAR	18. NUMBER OF PAGES 185	19a. NAME OF RESPONSIBLE PERSON Lt Col Michael K. Walters, ENP
a. REPOR T U	b. ABSTR ACT U	c. THIS PAGE U			19b. TELEPHONE NUMBER (Include area code) (937) 255-3636, ext 4681

Standard Form 298 (Rev. 8-98)
Prescribed by ANSI Std. Z39-18

				Form Approved OMB No. 074-0188	
--	--	--	--	-----------------------------------	--